OAK RIDGE NATIONAL LABORATORY LIBRARIES
3 4456 0548158 2

CENTRAL RESEARCH LIBRARY
DOCUMENT COLLECTION

172

ORNL-3989
UC-20 – Controlled Thermonuclear Processes

THERMONUCLEAR DIVISION
SEMIANNUAL PROGRESS REPORT
FOR PERIOD ENDING APRIL 30, 1966

CENTRAL RESEARCH LIBRARY
DOCUMENT COLLECTION
LIBRARY LOAN COPY
DO NOT TRANSFER TO ANOTHER PERSON
If you wish someone else to see this document, send in name with document and the library will arrange a loan.

OAK RIDGE NATIONAL LABORATORY
operated by
UNION CARBIDE CORPORATION
for the
U.S. ATOMIC ENERGY COMMISSION

Printed in USA. Price $5.00 . Available from the Clearinghouse for Federal Scientific and Technical Information, National Bureau of Standards, U.S. Department of Commerce, Springfield, Virginia 22151

LEGAL NOTICE

This report was prepared as an account of Government sponsored work. Neither the United States, nor the Commission, nor any person acting on behalf of the Commission:

A. Makes any warranty or representation, expressed or implied, with respect to the accuracy, completeness, or usefulness of the information contained in this report, or that the use of any information, apparatus, method, or process disclosed in this report may not infringe privately owned rights; or

B. Assumes any liabilities with respect to the use of, or for damages resulting from the use of any information, apparatus, method, or process disclosed in this report.

As used in the above, "person acting on behalf of the Commission" includes any employee or contractor of the Commission, or employee of such contractor, to the extent that such employee or contractor of the Commission, or employee of such contractor prepares, disseminates, or provides access to, any information pursuant to his employment or contract with the Commission, or his employment with such contractor.

ORNL-3989

Contract No. W-7405-eng-26

THERMONUCLEAR DIVISION
SEMIANNUAL PROGRESS REPORT
For Period Ending April 30, 1966

AUGUST 1966

OAK RIDGE NATIONAL LABORATORY
Oak Ridge, Tennessee
operated by
UNION CARBIDE CORPORATION
for the
U. S. ATOMIC ENERGY COMMISSION

OAK RIDGE NATIONAL LABORATORY LIBRARIES

Contents

INTRODUCTION vii

ABSTRACTS xi

1. INJECTION AND ACCUMULATION: SINGLE-PASS EXPERIMENTS (DCX-1) 1
   - 1.1 Introduction 1
   - 1.2 Experiments in Weak Field Gradients 1
     - 1.2.1 RF Spectra 3
     - 1.2.2 Energy Spectra 5
     - 1.2.3 Other Features 6
     - 1.2.4 Discussion 8
   - 1.3 End Wall Experiments 9
   - 1.4 Historical Review 11

2. INJECTION AND ACCUMULATION: MULTIPLE-PASS EXPERIMENTS (DCX-2) 14
   - 2.1 Introduction 14
   - 2.2 Studies of the Central-Peak Plasma 15
   - 2.3 Other Gas Dissociation Experiments 17
   - 2.4 Energy Analyzer Beam and Plasma Measurements 21
   - 2.5 Hydrogen-Arc Experiments 24
   - 2.6 Attempt to Measure Cold-Plasma Density with a Microwave Interferometer 25
   - 2.7 Measurements of the Cold Plasma with Gridded Probes 26
   - 2.8 End-Injection Experiments 30

3. ELECTRON-CYCLOTRON HEATING 31
   - 3.1 Injection of Neutrals and Trapping on an Electron Resonant Environmental Medium (INTEREM) 31
     - 3.1.1 Introduction 31
     - 3.1.2 Neutral-Beam Injection Studies 31
     - 3.1.3 Transverse Scans of the Trapped Proton Population 33
     - 3.1.4 Vacuum Conditions 34
     - 3.1.5 Spectral Studies in INTEREM 35
   - 3.2 Electron-Cyclotron Heating Experiments in the ELMO Facility 35
   - 3.3 Flute Instabilities in the Physics Test Facility (PTF) 39

4. PLASMA PHYSICS 43

4.1 Beam-Plasma Interaction Experiments 43
4.1.1 In Burnout IV 43
4.1.2 In DCX-1 44
4.1.3 In Burnout V 46

4.2 Beam-Excited Ion-Cyclotron Oscillations 51
4.2.1 Introduction 51
4.2.2 Apparatus 51
4.2.3 Experimental Observations 52
4.2.4 Conclusions 54

4.3 An Electron-Collecting Probe as an Ion Wave Detector 55

4.4 Plasma Density Measurement in a Hollow-Cathode Arc by Arc Reversal 55

4.5 Use of an Ordinary Camera as a Streak Camera 56

4.6 A Cesium Plasma with No Short-Circuit Effects at the End Electrodes 58

4.7 Varying Plasma Electron Temperature in Discharge Tubes by a Simple Auxiliary Electrode 58

4.8 Hot-Electron Plasma Blanket 61
4.8.1 Introduction 61
4.8.2 Arc Electrode Modifications 61
4.8.3 Temperature and Density Measurements 61
4.8.4 Diffusion of the Plasma 63
4.8.5 Investigation of Magnetic Field Effects 65

4.9 A Curved Arc 67
4.9.1 Introduction 67
4.9.2 The J-Arc Facility 67
4.9.3 Results 70

4.10 Boundary Wall Treatment in the Penning Ion Gage 71

4.11 Further Studies of the Excitation Heating of Ions 74
4.11.1 Introduction 74
4.11.2 General Discussion 74
4.11.3 Results 76
4.11.4 Discussion of Results 76
4.11.5 Conclusions 77

5. ATOMIC AND MOLECULAR CROSS SECTIONS 78

5.1 Excited States of H, H_2, and H_3 78

5.2 Charge States of Atoms Following Readjustment to Inner-Shell Vacancies 80

5.3 Measurements of Kinetic Energies of H^+ and H Following Dissociation of H_2 by Electron Impact 81

5.4 High-Energy Charge-Exchange Cross Sections 82

5.5 Detection of Low-Energy Neutral Atoms 82

5.6 Pressure Measurements for Condensable Gases 87

5.7 The Atomic and Molecular Processes Information Center 87

6. HIGH-CURRENT ION-BEAM PRODUCTION AND INJECTION 89
6.1 Four-Electrode H_2^+ Source 89
6.2 Non-PIG Source Design 90
6.3 The DCX-2 End Injector 94
6.4 Intense D-T Neutron Generator 94
6.5 Neutral Beams 94

7. PLASMA THEORY AND COMPUTATION 95
7.1 Theoretical Interpretation of Some DCX-2 Observations 95
7.1.1 Introduction 95
7.1.2 Application of the Equations to DCX-2 96
7.1.3 Damping Due to Warm Plasma 97
7.1.4 Statistical Mechanics of the Waves 98
7.2 Some Implications of the Stability of the Energetic Plasma in DCX-2 99
7.3 Propagation Properties of Unstable Waves 101
7.3.1 Introduction 101
7.3.2 Real ω–Real k Solutions of Dispersion Relations: Wave Plots 101
7.3.3 Determination of Complex Roots of Dispersion Relations 103
7.4 Relativistic Instability in Hot-Ion Plasmas 105
7.5 Stability of DCX-1 Toward Drift-Cyclotron Instability at Low Density 106
7.6 Cold-Plasma Effects in Finite Length Plasmas 107
7.7 Parametric Excitation of Transverse Waves in a Plasma 108
7.8 Studies for DCX-3 108

8. MAGNETICS AND SUPERCONDUCTIVITY 109
8.1 New Compact Table for Magnetic-Coil Calculations 109
8.2 Ribbon Coil Development 110
8.3 Versatile, Large-Volume Coil Arrangement ("D Coils") 113
8.4 Ferromagnetic Flux Tube Spreaders 114
8.5 First Scale-up of the Iron-Core Electromagnet Producing a Magnetic Well with Non-zero Minimum 116
8.6 Some Surface Current Phenomena in Hard Superconductors 120
8.6.1 Introduction 120
8.6.2 Experimental Arrangement 121
8.6.3 Three Different Types of Experiments 121
8.6.4 Discussion 123
8.7 Influence of Surface Currents on AC Losses in Hard Superconductors 124
8.8 Superconductivity Research Directed Toward the Development of Large Superconducting Magnet Systems 126

9. VACUUM STUDIES 128
9.1 Mass Spectrometry Development 128
9.1.1 Introduction 128

9.1.2 Organic Peaks 128
9.1.3 Effect of Gage Tubulation on Pressure Readings 130
9.1.4 Scan Speed and Response Times 131
9.1.5 Sensitivity and Cracking Patterns 131
9.1.6 Conclusion 131

9.2 Observation of Pressure Pips in Vacuum Systems 132

10. SPUTTERING OF COPPER, MOLYBDENUM, 304 STAINLESS STEEL, AND TUNGSTEN BY DEUTERIUM IONS 134

11. DESIGN AND ENGINEERING: NOTES 135

11.1 Coxaial Electric Field Probes Constructed with Pyrolytic Boron Nitride as the Insulation Material 135

11.2 Failures of OFHC Copper Tubing in DCX-1 Service 136

11.3 Cast Crossovers 139

11.4 General Welding, Braze-Welding, and Brazing Developments for CTR Equipment 141

11.5 Heliarc Brazing of Copper Bus Tubing Used in Gas Arc Facility and ELMO Electromagnets 142

12. DESIGN AND ENGINEERING: SERVICE REPORT 144

PUBLICATIONS, ORNL REPORTS, PAPERS, AND TRAVELING LECTURE PROGRAM 145

Introduction

A. H. Snell

The main attention in DCX-2 has been devoted in the past few months to the so-called "central-peak" plasma. This is the component of the total plasma that contains most of the hot ions, with tremendous energy spread and with essentially all the ion energy in $v_{\perp}$. Its name bespeaks its contrast with the "side-peak" fast-ion component that corresponds to helical motion with a pitch angle of a few degrees as seen by the chosen method of observation, namely, a directional detector that registers the fast neutrals flying out as a result of charge exchange. There are two side peaks (Fig. 2.1), corresponding to the forward and backward motion between mirror coils. (The side peaks, however, are not to be confused with the molecular-ion beam; they come from genuinely trapped protons.) The central-peak plasma, meanwhile, has the convenient property that, because of its lack of axial motion, it does not encounter the injection snout. Here it is in contrast with the side-peak plasma, for in a low-pressure regime chosen to emphasize the side peaks, substantial direct loss of fast ions upon the snout seems indeed to take place. The central-peak plasma can be made to come and go according to subtle operating conditions (Sect. 2.2), but the interest of the moment lies in its stability. After injection is stopped, radio-frequency activity quickly ceases, and the central-peak plasma withstands instability much better than it should according to current theory. This matter is discussed in Sect. 7.2, where, despite allowances made for finite plasma size and the presence of cold plasma, the stability remains incompletely explained. With the feeling that a more precise understanding is important, attention is being devoted to the improvement of computer codes that will facilitate investigation of the growth of unstable wave modes (Sect. 7.3) to see if a more detailed treatment of the establishment of stability-instability boundaries can yield better agreement with the DCX-2 results.

The observation that radio-frequency activity ceases quickly after injection stops recalls older but similar observations in DCX-1. In that work the particular conflict with theory discussed above did not emerge, because the plasma was shorter in the direction along the magnetic field. However, in DCX-1 the occurrence of the radio frequency in bursts permitted an observation of different emphasis: the radio-frequency activity ceases, not directly because the injection has stopped, but because the *energy of the trapped protons has spread.* The plasma in fact is telling us how much energy spread is needed for stability. Thus the DCX-1 and DCX-2 results indicate that in the matter of the velocity-space instabilities, the relaxed energy distribution is of immediate importance and that it is more critical than a directional spread in velocities. Two philosophies can then arise. One states that the injected particle beam should have the energy spread built into it before it enters the storage volume, so that the energy source that drives the instabilities can never appear in the plasma. The other says that the plasma itself will spread the energy and that until one sees unaffordable losses accompanying the process, one cannot dismiss its possible exploitation if there are separate, desirable plasma characteristics to be gained.

Before leaving DCX-2, one should point to the rich spectrum of radiation in the ion cyclotron harmonics, with its peculiar behavior in that under some circumstances the even harmonics can be stronger than the odd harmonics (Fig. 2.9). In Sect. 7.1 a neat interpretation is offered in terms of wave-wave coupling.

Since the negative-mass instability was diagnosed in DCX-1, some exploratory work was undertaken to study the behavior of the instability under variation of some of the major parameters of the configuration. The investigation described in Sect. 1.2 describes what happened when the field index n was varied; in particular, the field was flattened to see how the instability behaved when DCX-1 became more DCX-2-like. Some undoubtedly striking similarities emerged in the plasma behavior in the two apparatuses, but to conclude from this alone that the negative-mass instability is present in DCX-2 may be premature.

Another interim use of the DCX-1 apparatus was a study of the influence of the reactive, segmented end walls upon the behavior of the trapped proton population. (This wall treatment had previously been found to have a strong stabilizing effect upon calutron beams.) The conclusion from the work in DCX-1 is that the reactance definitely couples into the total plasma oscillating system, and thus one has an easy measure of control over some of the plasma properties. However, despite a marked sensitivity of the radio-frequency emission from the plasma to the adjustments of the boundary impedance networks, the improvement in plasma density that could be realized was disappointingly small. Section 1.3 gives the pertinent discussion. A historical review of the different phases of the career of DCX-1 has been summarized in Sect. 1.4. We have learned a lot from DCX-1, not only in terms of plasma behavior, but also in its service through the years as a vehicle for the development of the techniques of plasma physics: arcs, instrumentation, magnetics, vacuum, and computation.

The boundary impedance networks are also found to produce a remarkable simplification in the complex radio-frequency pattern of the simple Penning ionization gage (Sect. 4.10), together with a lowering and flattening of the potential distribution.

In the neutral injection experiment INTEREM, instrumentation is developing, and we see trapping within the target electron-cyclotron plasma, an accumulated density of 2×10^7 fast protons/cm^3 at an injected H^0 beam current of 8 mA equivalent, and no energy spread (Sect. 3.1). In ELMO, a small, thin stainless steel cavity has permitted rather detailed observations of the diamagnetism of the 38-GHz electron-cyclotron plasma. Instabilities during decay can be induced that are strongly marked (Figs. 3.6 and 3.7), and are attributed to the formation of flutes as permitted by the gradual disappearance of cold plasma while warm plasma remains. In the 10.8-GHz electron-cyclotron plasma apparatus, PTF, grad B $m = 2$ controllable flutes are identified and found to be suppressed by cold plasma about 1/20 as dense as the warm-electron component in which the flutes form (Sect. 3.3).

A variety of topics in plasma physics is treated in Sect. 4. Beam-plasma interaction studies are treated in the further diagnosis of the ion-hot "burnout" plasmas, with photographic observation of the absence of light until impurities flood in and spectroscopic support for the earlier probe measurement $T_i \sim 1$ keV for the main body of the plasma (10^{12} density). Some new work is described in Sect. 4.2, where modulation of an electron beam passing through plasma gives some evidence of ion heating in the steady state. The large annular plasma of Sect. 4.8 is being developed toward densities higher than 10^{12} electrons/cm^3 by modification of the arc electrodes and by increasing the magnetic field strength. Two contributions to arc research appear; one is the demonstration that you can rather easily drive a vacuum arc of the Curran-Luce type around a U-bend (Fig. 4.23), and the other gives strong support to the suggestion that the 500-eV ionic temperatures in the carbon arc (as contrasted with $T_e \sim 10$ eV) may be due to collisions between metastably excited carbon ions. The support comes from the observation that metastable C^{2+} ions actually do comprise a strong fraction of the total ion population (Table 4.2).

In the matter of detection of neutral atoms in the difficult energy range of a few hundred electron volts, we note (Sect. 5.5) some remarkable yield curves of secondary-electron emission, with clear resolution of events that yield 1, 2, ... , 14 secondary electrons (Figs. 5.9 to 5.14). Inasmuch as the relative intensities of the groups are somewhat sensitive to the energy of the impinging primary particle, perhaps the ratio of the intensities of (say) the five-electron group to the one-electron group can be calibrated for use in inferring the mean energy of incident particles of a given kind. Plain copper surfaces would appear to give more linear and more reproducible results than Ag-Mg, although the latter material of course yields more secondary electrons.

The Ion Source and Accelerator Group adds to its battery of variants of the duoplasmatron source by reporting design and performance of sources

aimed at H_2^+ production. Their curve (Fig. 6.4) indicates 60 to 80 mA of H_2^+ ions and 70 mA of H^+ ions at 40 keV through a 1-in. aperture 42 in. from the focusing lens.

The projected plans for DCX-3 call for magnet coils of high current density, and for this we are at present pinning our hopes on the copper ribbon coils. Figures 8.3 and 8.4 show a small test coil, and Fig. 8.2 shows one that was tested to failure at a mean current density in the winding of about 200,000 A/in.^{2}. Ribbon coils have attractive features, but water flow problems will have to be solved, and a testing program must be undertaken before we will be confident of a final design for DCX-3. Other topics of interest in magnetics include a scale-up of the iron-pole "baseball seam" magnetic well to a sphere about 25 cm across (Figs. 8.9 and 8.10) with measurements that show under present conditions of shimming a central field of 3 kG, with an adequate axial mirror ratio and with so far a modest but improvable radial mirror ratio. The big "D-coil" for the magnet laboratory has been tested and installed (Fig. 8.5), strongly enough bound to enable its two halves to be connected as a cusp pair as well as a mirror pair.

Most of our work on superconductivity is done under contract with NASA, and only a summary is presented in Sect. 8.8 of the current investigations into the factors that influence the stability of superconductors in large coils. In Sects. 8.6 and 8.7, however, we show that surface currents are responsible for several phenomena encountered here and elsewhere in the sensitivity and lack of sensitivity of the flux in the body of the superconductor to changes in an applied external field.

The work on vacuum technology has been largely devoted to instrumental problems (Sect. 9). Spurious pressure and composition effects can be caused by gas sources close to the detecting instrument. The response time of a mass spectrometer has been increased by a factor of 20, so that a mass scan can now be recorded in 25 sec. Even this is much too slow to follow certain plasma phenomena that are observed in equipment such as DCX-2. Our report concludes with a few measurements of the sputtering of copper, molybdenum, stainless steel, and tungsten by deuterium ions (Sect. 10), and technical notes about high-temperature probes and important fabrication details for magnet coils (Sect. 11).

Abstracts

1. INJECTION AND ACCUMULATION: SINGLE-PASS EXPERIMENTS (DCX-1)

During this report period, the facility has been used for three widely divergent series of experiments:

1. The flexibility of variable magnetic field gradient acquired by the earlier installation of an additional coil pair was employed to obtain data for comparison with properties of the DCX-2 plasma. The properties of the two plasmas became more nearly alike as the DCX-1 field was flattened, but this mockup of the DCX-2 plasma omitted features required for unambiguous comparisons.

2. "Burnout" plasmas were operated in attempts to determine scaling relations for higher power inputs than were possible in prior burnout experiments. The details of this work are presented in Sect. 4.

3. A variety of reactive end walls were installed in the plasma chamber, and studies were made of the effects of these boundaries on plasma instability. The effects were negligible unless the walls were advanced into a portion of the volume normally occupied by the fast-proton plasma. At such positions certain boundary configurations exhibited significant effects upon rf signals, plasma density, and fast-proton energy spread. The end walls could partially damp or could augment instability, but under no condition was the plasma density higher than that obtained with the walls retracted to positions outside the fast-proton plasma.

Finally, there is included a historical review of the principal lines of investigations to which the facility has been devoted since its inception.

2. INJECTION AND ACCUMULATION: MULTIPLE-PASS EXPERIMENTS (DCX-2)

We have concentrated on gas dissociation experiments during this period with two motivations: (1) to study plasmas which may be related in a simple way to theoretical models and (2) to study the mechanism which results in the highly anisotropic, but relatively stable, plasmas which are produced. There are two energetic-proton plasma regimes with gas dissociation: the side-lobe-dominant regime discussed previously and the central-peak-dominant regime characteristic of arc dissociation.

Since the large volume ($\sim 7 \times 10^4$ cm^3), highly anisotropic ($T_\perp / T_\parallel \sim 10^3$) central-peak-dominant plasma fits theoretical models, these plasmas have been used to demonstrate the limitations of the current theories of ion-cyclotron instabilities through studies of the rf behavior following turnoff of the molecular-ion beam. It is found that when rf activity occurs after beam turnoff, it is associated with the streaming side-lobe plasmas. The central-peak plasma by itself is shown to be stable against ion-cyclotron instabilities after beam turnoff at densities about a factor of 40 above the usual rule of thumb instability threshold predicted by the infinite medium theory ($\omega_{pe} > \omega_{ci}$). The observed density is also approximately an order of magnitude higher than the instability threshold predictions of the Guest-Dory infinite medium theory, including finite electron temperature, an approximation to the observed velocity distribution, and wavelengths restricted to fit within the plasmas.

As the pressure is varied, transitions in the rf spectral patterns occur which are correlated with the appearance and disappearance of the central peak. Streaming instabilities associated with the molecular-ion beam and with the streaming protons are clearly seen.

Energy analyzer measurements have indicated that an anomalously high non-charge-exchange proton loss, generally absent, is large under certain conditions. Except for these conditions, the energy analyzer gives results which are consistent with other measurements. Measurements of the cold-plasma density have been made with a microwave interferometer as well as with gridded probes, but the two measurements yield inconsistent results.

Experiments have been started with an axially injected 200-mA beam of 100-keV protons. Initial experiments show no trapping. The rf generated does not include ion-cyclotron lines, and there is anomalous ion transmission at the mirrors.

3. ELECTRON-CYCLOTRON HEATING

As discussed in Sect. 3.1, the injected 20-keV neutral beam has been used for further proton trapping studies in the INTEREM facility. The energy spectrum of the trapped protons has been measured. No energy spread has been observed either with trapping on hydrogen gas or with electron-cyclotron plasma (ECP). The axial distribution of the trapped protons has also been measured. A slight amount of spreading occurs in the presence of the ECP, but this may be due to normal scattering processes rather than to an instability.

In Sect. 3.2 an experiment in the ELMO facility is described. An 8-mm ECP was formed in a 3.6-liter stainless steel cavity arranged to permit the measurement of fairly fast diamagnetic perturbations. This diagnostic along with a radial profile measurement of cold plasma streaming axially out of the hot plasma region has shown the principal electron constituent of the density to be of the order of 10^{12} electrons/cm^3 and to have an average energy of $\sim$1.5 keV. Instabilities observed after turnoff are well correlated with the decay of the conductivity-stabilizing cold plasma.

In Sect. 3.3 further work on the PTF is described. The large radial loss of hot electrons that is observed in the PTF plasma under some conditions is associated with perturbations that propagate azimuthally around the plasma surface with a phase velocity that is near the gradient-B drift velocity of 25-keV electrons. When the perturbations are fully developed, their wavelength is one-half the circumference of the plasma. However, it appears that the perturbations that grow initially are of much shorter wavelength. The instability can be suppressed by increasing the density of the cold plasma between the hot plasma and the conducting end walls. Stability is obtained when the cold plasma density is about 5×10^{-2} times the hot plasma density.

4. PLASMA PHYSICS

The "burnout" experiments were attempts to measure the ion density and temperature, to increase both of these by increasing the power density, and to measure D-D reaction products from the plasma.

In order to study the energy exchange between a beam and a plasma, it is necessary to produce strong oscillating electric fields. The use of a modulated high-current electron beam makes it possible to obtain large radio-frequency electric fields for plasma studies, and these electric fields are internal to the plasma.

It has been found that oscillations at the ion cyclotron frequency (ω_{ci}) may be excited in the beam-generated plasma when the beam is modulated at frequencies much higher than ω_{ci}. This effect is strongly dependent on the modulation depth and on pressure. It exhibits no dependence on modulation frequency. Further study is necessary in order to clarify the exact nature of the interaction.

An electron-collecting probe has been shown to be a supersensitive ion-wave collector. The plasma density in a hollow-cathode arc has been measured by reversing the arc and "sweeping out" and collecting the plasma. An ordinary hand-held camera has been used to take streak photographs of high time resolution. A cesium plasma with no short-circuit effects at the hot ion emitters has been produced. The plasma electron temperature in a discharge tube is being controlled by a simple auxiliary electrode.

The beam-plasma-generated hot-electron blanket is now well established as (1) a potentially useful environmental plasma or (2) a plasma which can be studied in a steady-state, pure form independent of the plasma source. We have evidence for the existence of several different electron distributions in the blanket. The first is a high-energy group of 100 keV mean energy and a density in the range of 10^9 to 10^{10} electrons/cm^3.

Possibly two intermediate-energy groups exist, both of which have sufficient energy to ionize the background gas but insufficient energy to produce x rays. Present experimental evidence indicates that one of these groups is about 2 keV in mean energy, with a density of about 1 to 5×10^{11} cm^{-3}. The other group is about 100 eV, with a density still open to question. A very-low-energy electron group of a few electron volts exists with a density greater than 10^{12} cm^{-3}.

Preliminary investigation with the use of iron for magnetic field shaping in the anode channel region indicates a method whereby the blanket-producing interaction may be made to exist at axial midplane magnetic fields in excess of 3 kG. Such field shaping has also allowed an increase in arc power input by a factor of 2, yielding our highest blanket densities at midplane fields in the neighborhood of 2 to 2.5 kG. A new anode and a field bucking coil are being assembled in order to test the operation at midplane fields up to 9 kG, which is the maximum of the 2:1 mirror coil system.

Direct-current, magnetically collimated vacuum arcs have successfully operated in an arrangement with a high degree of curvature. Gas-supported arcs have made a 180° turn with a radius of 7 in. A brief description is given of these observations as well as of the J-Arc Facility. This small apparatus possesses a number of unique engineering features which will greatly facilitate experimentation with curved systems. Two such features are the high pumping speed and unique freedom of access to toroidal discharges afforded by placing the confining field coils inside the vacuum enclosure.

The Penning ion gage seems to offer a simple device for testing various forms of the boundary impedance network. Preliminary observations made for the Penning ion gage in a glass vacuum system are reported.

Further studies have been made of the very long, magnetically confined energetic carbon arcs which exhibit hot ions ($T_{+\perp} \sim 500$ eV) in the presence of cold electrons ($T_{-} \sim 5$ eV). The densities of the ionic species C^{2+}, C^{2+*}, and C^{3+} have been determined by vacuum ultraviolet absorption spectroscopy and provide additional evidence in support of the excitation-heating theory.

5. ATOMIC AND MOLECULAR CROSS SECTIONS

Additional measurements have been made of the electric field ionization of the excited electronic quantum states of H, H_2, and H_3. The experimentally determined magnitude of the H_2 and H_3 state population was less than that of H, mainly because of secondary ionization and dissociation processes which occurred in the electric field region. Excited H state population formed by electron capture collisions of protons in H_2 gas was dependent on particle energy. For H energies greater than 60 keV the population was approximately constant; whereas for lower energies the population decreased, indicating a steeper dependence than the predicted n^{-3}.

Silicon surface-barrier detectors are now used routinely, with energy resolution of 1.8 keV. A new neutral particle detector has been developed which uses the high-resolution silicon barrier detectors to measure secondary electrons from a 15-kV negatively biased copper target. Pulse spectra were composed of several resolved groups, with each group corresponding to the number of secondary electrons emitted per incident neutral. Comparison of the ratio of the magnitudes of each group indicated the average particle energy, while the total count rate was a quantitative measure of the incident particle flux. The detector system was used also for a detailed study of secondary emission.

Progress is reported on the following projects: (1) measurements of kinetic energy of H^+ and H following dissociation of H_2 by electrons; (2) high-energy charge-exchange cross sections; (3) charge states of atoms following inner-shell ionization; (4) absolute vacuum measurements; and (5) the Atomic and Molecular Processes Information Center.

6. HIGH-CURRENT ION-BEAM PRODUCTION AND INJECTION

An unusually diversified program has been pursued during this report period. The four-electrode H_2^+ ion source was studied over an energy range of 10 to 600 keV. A 100-kV non-PIG accelerator was designed and successfully tested, and a similar 600-kV accelerator was designed. The DCX-2 end injector (100 keV, ~500 mA) was installed and tested. The ion source and accelerator for

a 150-kV, 500-mA dc neutron generator was completed and operated successfully for typical 4-h operation periods. A low-energy (0 to 40 keV) ion beam test stand was completed. In conjunction with the DCX-1 group, a program has been started to evaluate various neutral-forming cells with intense hydrogen ion beams in the energy range 20 to 60 keV.

7. PLASMA THEORY AND COMPUTATION

In this report period the principal theoretical investigations have centered on questions raised by two aspects of the DCX-2 program: (1) the detailed study of radio-frequency emissions during steady-state operation and (2) studies of the stability properties of the "central-peak plasma" after the beam is turned off. The rich spectrum of spontaneous emissions observed in the first class of experiments offers a possible insight into the nonlinear plasma phenomena which are invoked to explain the generation of many high harmonics of the ion gyrofrequency. This viewpoint provides a promising tentative explanation for the disappearance, under some circumstances, of odd-numbered harmonics of the proton gyrofrequency from the rf spectrum. From the second class of experiments has come the observation of stable plasma behavior in apparent contradiction to conventional stability analysis, emphasizing the necessity of examining the details of the propagation of unstable waves in order to determine more realistic instability thresholds. The analysis required to determine the important characteristics of the unstable waves is lengthy, difficult, and almost entirely numerical, so that work in this area has been concerned largely with the development of computer codes. The intensive effort devoted to the development of these analytical tools stems from the implication, drawn from the DCX-2 experiments, that more complete understanding of the nature of growing waves may lead to a partial relaxation of some predicted instability thresholds.

A number of rather specific questions relating to plasma stability have been investigated, several of which are reported here. The possible importance of an instability related to the relativistic change in gyrofrequency for fast ions was explored, even though for ion energies of interest to controlled fusion plasmas such relativistic shifts would be very small. New insight into one class of "drift-cyclotron" modes was obtained by studying the region of overlap of two very dissimilar models of the diamagnetic response of a plasma of finite radial extent. The stabilizing effects of cold plasma were analyzed for those experiments which might shed light on the accuracy of the model under study, and substantial agreement between theoretical predictions and experimental observations was found.

Theoretical calculations reveal that transverse electron plasma oscillations can be set up by parametric longitudinal oscillations at other than the plasma frequency.

A number of computations related to design problems in the proposed DCX-3 configuration have been carried out by the computer group.

8. MAGNETICS AND SUPERCONDUCTIVITY

For various applications it appeared necessary to calculate new tables of the ratio B_0/B_{max} for magnet coils with rectangular cross section and uniform current density. This seemed to be an almost trivial task; however, it turned out that for the desired, very large range of the normalized coil dimensions, a straightforward application of existing codes was not sufficient. Especially for very narrow coil shapes, errors up to 7 or 8% can occur. Furthermore, the steps of the variables should be chosen small enough to allow linear interpolation, but without making the table unnecessarily voluminous. The short description of the work needed to reach this goal is a good example of the intricacies involved in making reliable "compact tables" of magnet field quantities.

The 7-MW 13-in.-ID "D coil," which produces in Helmholtz configuration a field of 62 kG and which can be operated in cusp configuration, has been assembled. Electrical and mechanical tests preceding regular operation are progressing. Development work on the "ribbon coil" has been continued. This new design is supposed to be used for plasma physics experiments in which the restricted space calls for magnet coils with very high current densities. Recent tests showed that the previously attained value of about 90,000 A/in.^{2} can be almost doubled. The test arrangements described here consider carefully the necessity to use small header volumes. This devel-

opmental work is of special interest, since it is hoped that similar design principles can be applied not only to mirror and cusp coils but also to Ioffe and shear bars.

For various applications the use of iron to shape magnet fields is very convenient. Recent work in this line is the development of ferromagnetic flux tube spreaders for the Beam Plasma Facility; test results are described here. Our iron-core minimum-*B* magnet has been successfully scaled up to give a minimum at 3 kG in the center of a spherical volume 10 in. in diameter.

Superconductivity research has been continued. We studied surface current phenomena on cylindrical samples of hard superconductors in longitudinal external fields. Under special conditions, samples in "mixed state" (external field between lower and higher critical field) showed no changes of the bulk flux density distribution when the external field was varied within certain finite limits. We made these experiments with Nb-Zr and Pb-In samples, with sample surfaces unpolished, polished, and plated after polishing. Our results are in qualitative agreement with those obtained in different ways by other authors. These surface phenomena are of importance for the understanding of measurements using ac fields of large amplitudes and low frequencies. Previously, there were deviations of up to 70% when Bean's theory was applied to the evaluation of magnetic hysteresis loss measurements with high-field superconductors. It is shown here that these discrepancies can be removed when the surface currents are appropriately considered.

The work on superconductivity in this Division is sponsored by the Thermonuclear Branch of the AEC and by the George C. Marshall Space Flight Center of NASA. It is, of course, not possible to separate clearly the two respective areas of our activities. Our reports prepared for the latter governmental agency describe in detail our current research efforts directed toward the development of large superconducting magnet systems. In order to avoid duplication, we restrict ourselves here to presenting only a short abstract of this kind of work done during the last semiannual report period.

9. VACUUM STUDIES

Diagnosis of vacuum system quality is generally made using ionization gages or mass spectrometers. Two of the perennial problems in interpretation of data from these instruments have received additional study during this period. These are the questions of the significance of organic peaks in the spectrum of an unbaked system and the frequently noted discrepancy between nude and normally enveloped ion gages.

Organic peaks in a test vacuum system were found to be local to the ion source of the mass spectrometer and could be markedly decreased in magnitude by operating the spectrometer at an elevated temperature (about 125 to 150°C) continuously.

The discrepancy between a normally enveloped gage and a nude gage was found to be more strongly influenced by the off-gassing from the surfaces near the gage or its tubulation than by any other factor.

Improvements were made in the response time of the mass spectrometer used in the vacuum studies, which allowed mass analysis to be made of pressure pips of a variety of types. The pips which have been observed appear to originate with gasketed seals and may be air or off-gassing products. Both elastomer and metal gaskets in the presence or absence of oil have been observed to yield the periodic pressure bursts.

10. SPUTTERING OF COPPER, MOLYBDENUM, 304 STAINLESS STEEL, AND TUNGSTEN BY DEUTERIUM IONS

Copper was sputtered with D^+ and D_2^+ ions to check new equipment which we hope will enable us to attain 80 to 100 keV energy. Results of sputtering measurements for this report period are given.

11. DESIGN AND ENGINEERING: NOTES

Progress in the consideration of a few of our technological problems is briefly discussed. Development of high-temperature coaxial probes has

continued, and means have been found to pyrolytically deposit boron nitride on wires down to 0.1 mm diameter and then deposit tungsten on the boron nitride, resulting in very small probes which can withstand a 3000°K environment. Further progress in the understanding of early failure of copper tubing used in DCX-1 liners is discussed. Additional improvements in the design of hollow-conductor water-cooled electromagnets are described, including the progress of a cast-to-shape copper crossover and some techniques for Heliarc brazing of conductors in the proximity of insulating materials. Additionally, some general improvements in welding, braze-welding, and brazing of CTR equipment are discussed.

12. DESIGN AND ENGINEERING: SERVICE REPORT

The design and engineering activities are generally reported incidentally with the research efforts of other groups of the Division. These activities include execution or coordination of engineering design, shop fabrication, building operations, and maintenance. During this interval, members of the Engineering Services Group have engaged in a modest amount of technology developments.

1. Injection and Accumulation: Single-Pass Experiments (DCX-1)

J. L. Dunlap
R. S. Edwards
L. A. Massengill
H. Postma
R. G. Reinhardt
W. G. Schill
E. R. Wells

1.1 INTRODUCTION

The past several semiannual reports have given emphasis to the detailed features of microinstabilities in the DCX-1 plasma and to the density limitation caused by these instabilities with operation at very low pressures and trapping by Lorentz dissociation. The previous report[1] described a number of experiments which led to the conclusion that the negative mass instability was primarily responsible for the direct losses of energetic protons that limit the density of the protons to $(1-2) \times 10^8$ cm^{-3}. Some of these experiments involved controlled manipulation of energy spread and spatial anisotropy, and it was shown that these manipulations could produce 100-fold increases in threshold density for the instability. Unfortunately, with highest threshold the density limitation was relaxed by a factor of only 2.

At the beginning of this report period, it was clear that the detailed studies described in the past several reports had progressed to a point of diminishing return. The reader will note the effects of this assessment in the survey nature of the experiments to which the facility has recently been devoted.

During this report period, the facility has been used for three widely divergent series of experiments. In the first, we employed the newly acquired flexibility of variable radial field gradient[1] to obtain instability data with a nearly flat field for comparison with properties of the DCX-2 plasma. The second series of experiments involved operation of "burnout" plasmas in attempts to determine density scaling relations for higher power inputs than were possible in prior burnout experiments. The third series involved the use of reactive end walls in the plasma chamber and were studies of the stabilizing effects of these boundaries. The burnout experiments are described in Chap. 4 of this report. Details of the flat-field comparisons and of the work with reactive end walls are given in Sects. 1.2 and 1.3.

Since studies of the DCX-1 plasma have nearly arrived at a logical point for termination, we review in Sect. 1.4 the principal lines of investigation to which the facility has been devoted since its inception.

1.2 EXPERIMENTS IN WEAK FIELD GRADIENTS

There are several very obvious mechanical differences between DCX-1 and DCX-2:

1. The DCX-2 plasma is longer than that in DCX-1 by a factor near 30.
2. DCX-2 employs a multiple-pass H_2^+ beam which itself spends 10 μsec traveling down and back, while that of DCX-1 is a single-pass H_2^+ beam, spending 0.1 μsec in the machine.

[1] *Thermonuclear Div. Semiann. Progr. Rept. Oct. 31, 1965*, ORNL-3908, pp. 1–17.

3. DCX-2 has a magnetic field that is nearly uniform over a large extent. The DCX-2 field index,

$$n = \frac{-r}{B_z}\frac{dB_z}{dr},$$

varies through positive and negative values, but on the average it is about 0.0002 in the central section. The standard DCX-1 field is characterized by $n = 0.09$ in the region of the circular proton orbit.

4. DCX-2 proton orbits are precessive, while the standard injection trajectory of DCX-1 produces both circular and precessive orbits.

One of the differences, the magnetic field gradient, can be greatly reduced by using in DCX-1 the auxiliary coil set first employed in experiments described in the previous report. The auxiliary coil set (Fig. 1.1) can be energized to produce field indices varying from 0.002 to 0.052 while maintaining a field value of 9.6 kG at $r = 3.25$ in. on the median plane. This field value is that for a circular proton (300 keV) orbit radius of 3.25 in. (the usual value), and over the indicated range of n values, H_2^+ can be injected with beam turnaround tangent to this circular orbit.

It appeared that data on instability properties in DCX-1 operating with very weak field gradients might be useful for comparison with properties of the DCX-2 plasma. Therefore it was decided to make survey observations of the DCX-1 plasma as a function of field index, H_2^+ beam current, and pressure. To be more specific, data were obtained from experiments with gas dissociation for field indices of 0.052, 0.012, 0.004, and 0.002, with 600-keV H_2^+ currents of 0.1 to 5.0 mA, and with pressures from 5×10^{-8} to 2×10^{-4} torr (hydrogen leak). Observations were made with the following probes:

1. A charge-exchange neutral detector centered on the median plane at $r = 12$ in.
2. A solid-state energy analyzer on the median plane.
3. A "crown" rf probe on median plane at $r = 10$ in. for determining magnetic components of the rf fields.
4. A gridded cold-plasma probe at $z = 19$ in. (near the center of a mirror coil).

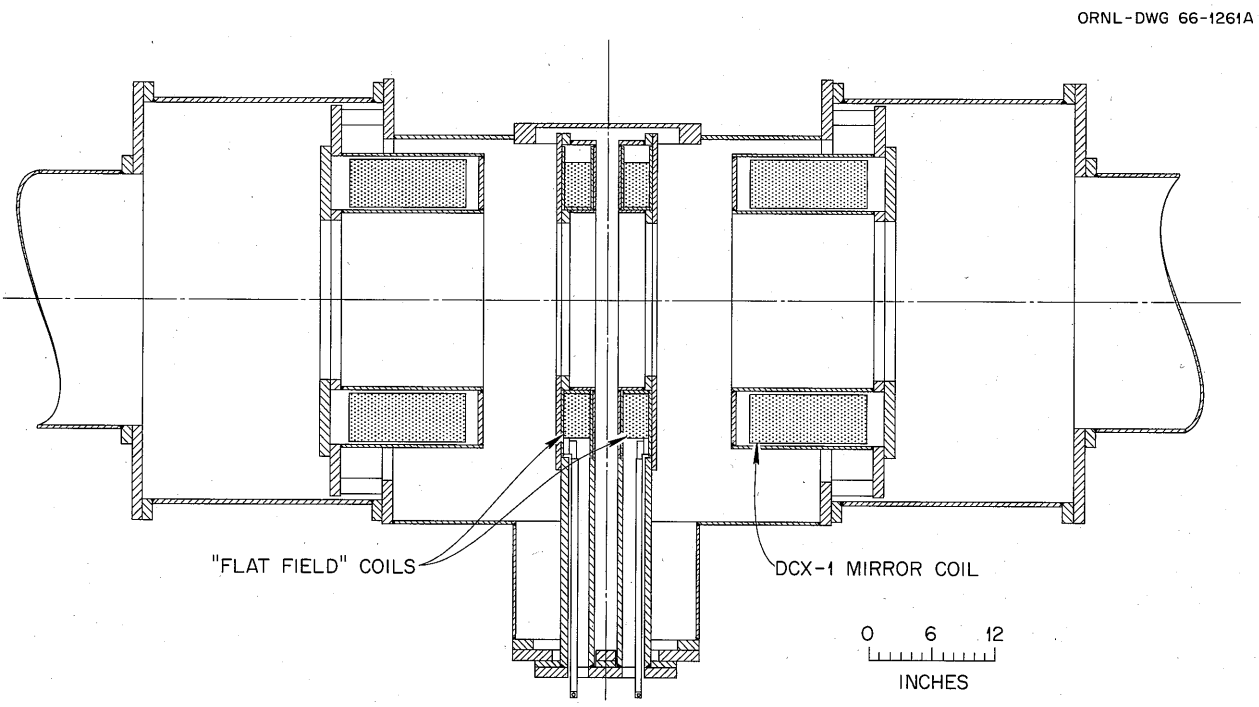

Fig. 1.1. Axial Section of the DCX-1 Facility, Showing Locations of the Flat Field and Mirror Coil Pairs.

5. An electrostatic probe on the median plane at $r = 7.5$ in. (just outside the plasma radius) for monitoring rf radial electric fields. The probe was connected to a Hewlett-Packard 8551A spectrum analyzer through low-loss high-frequency cable. In all essential respects this setup was identical to that employed for the corresponding measurements on DCX-2.
6. A movable radial scraper.

The data obtained included scans of rf spectra, spectral response to changes in plasma radius (through use of the scraper), energy analysis of escaping charge-exchange neutrals, cold-plasma saturation currents and ion energy, and fast-proton density and containment times. The experiments were restricted to gas dissociation.

1.2.1 RF Spectra

The rf line intensities show transitions at $(1-2) \times 10^{-5}$ torr, which are more pronounced with flat field. Maximum intensities shift from low harmonic numbers at low pressures to high harmonic numbers at high pressures (Figs. 1.2 and 1.3). With flat-field operation above transition pressure, even harmonics are stronger than odd harmonics by about 10 db (Fig. 1.2), the amplitude of the fundamental is much reduced (Figs. 1.2 and

PHOTO 83736A

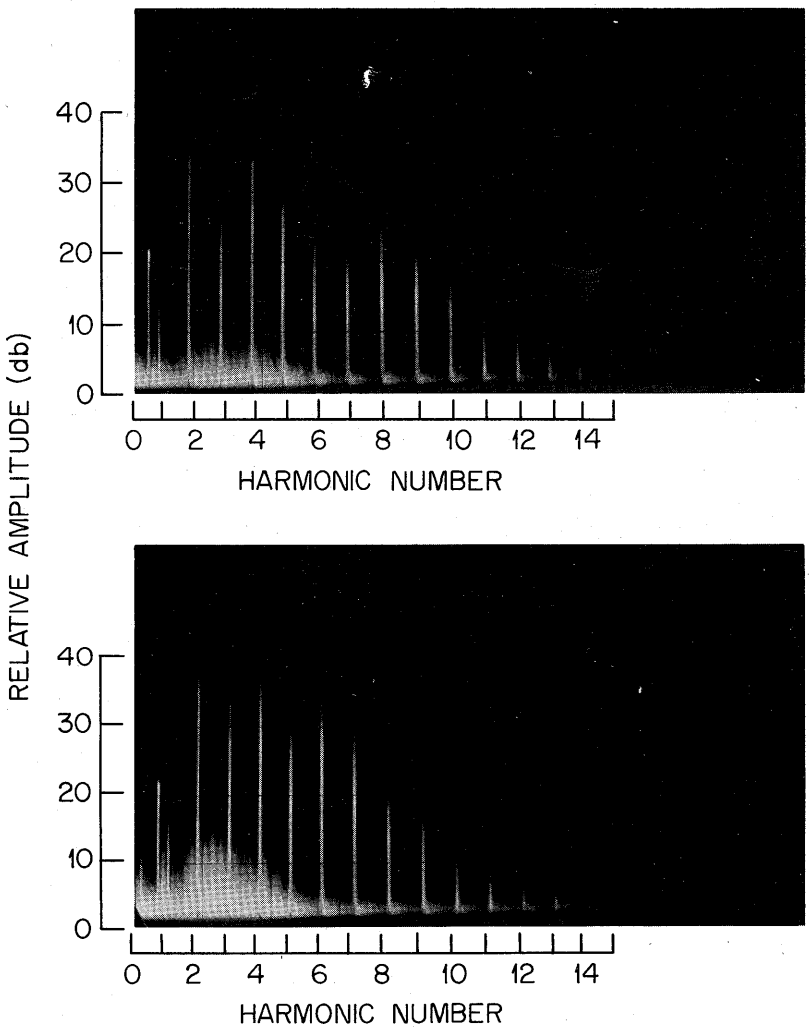

Fig. 1.2. Comparisons of the Harmonic Structure of Electrostatic Probe Signals from DCX-1 Operated with Two Values of Field Index. The signals which appear below ω_{ci} are generated in the spectrum analyzer, not in the plasma. The broad band extending up to about $n = 6$ is response to H_2^+ beam, not plasma.

PHOTO 83735A

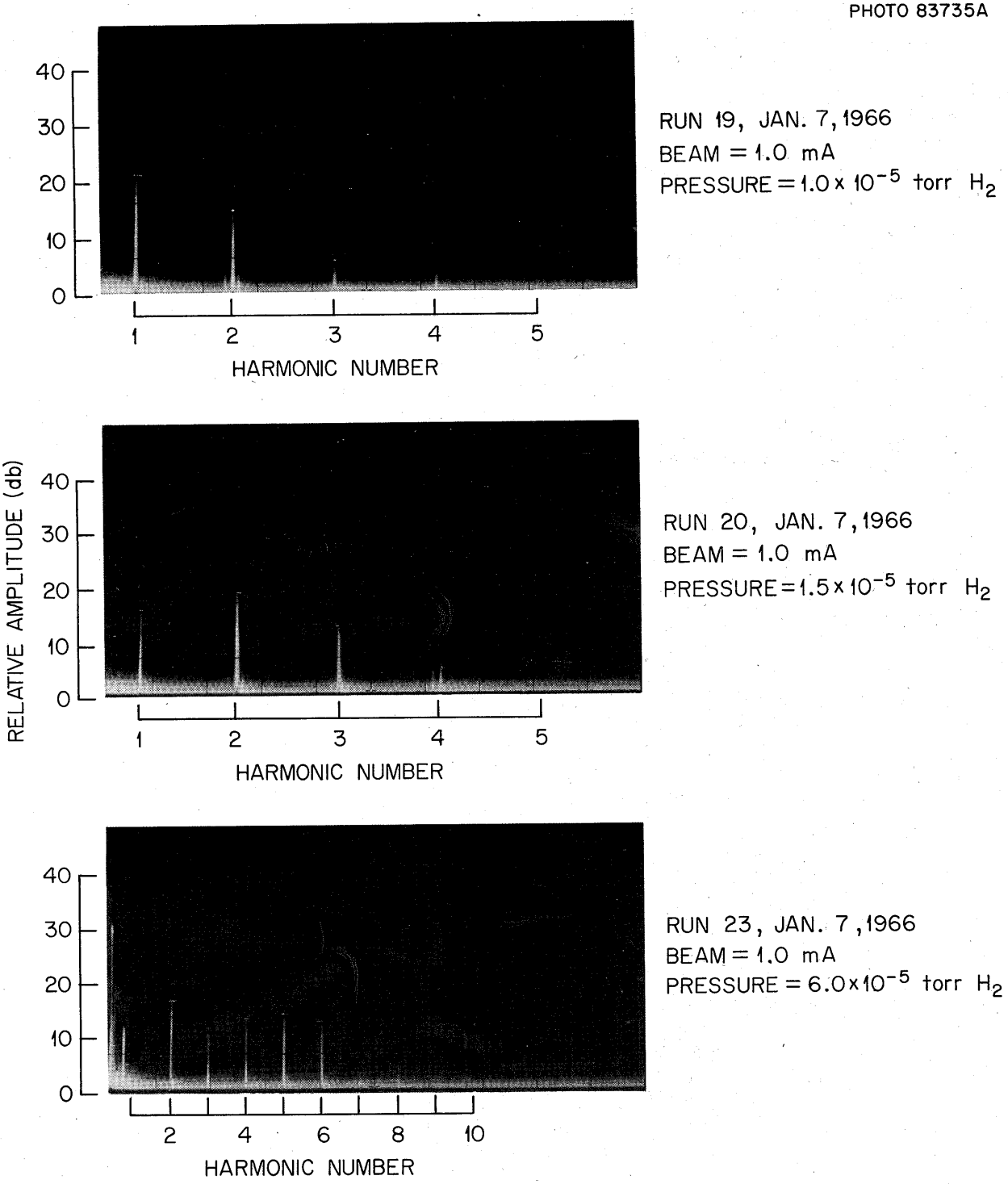

Fig. 1.3. Comparisons of the Harmonic Structure of Electrostatic Probe Signals from DCX-1 for Pressures near the Transition Pressure and a Field Index Value of 0.002.

PHOTO 83970

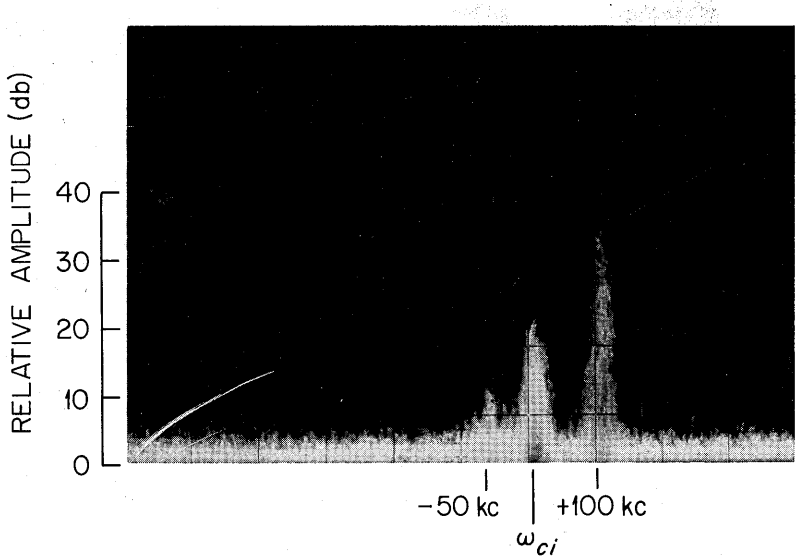

RUN 31, JAN. 7, 1966
BEAM = 1.0 mA
PRESSURE = 1.5×10^{-5} torr H_2
(AT TRANSITION)
FIELD INDEX = 0.002

Fig. 1.4. Spectrum Analyzer Display of Electrostatic Probe Signals near ω_{ci}, Showing Higher and Lower Frequency Components That Are Present Above Transition Pressure with a Field Index Value of 0.002. Steady-state operation, 5 sec exposure, 3 kc bandwidth, and 3 msec/cm sweep speed. Similar scans of higher harmonics show proportional frequency shifts.

1.3), and the fundamental band shows a splitting with additional components at −50 and +100 kc (Fig. 1.4). The higher harmonic bands show proportional splits.

At both high and low pressures, rf signal amplitudes and the number of observable harmonics increase as the field is flattened. With flat field and high pressure, up to 18 harmonics of the H^+ gyrofrequency are observed. No harmonics of H_2^+ and no frequency shifts after beam cutoff are observed under any conditions.

The spectral distribution of rf amplitudes is quite steady with $n = 0.002$ at low pressures. It becomes choppy with $n = 0.002$ at high pressures and with $n = 0.052$ at all pressures.

Additional data are provided by Figs. 1.5–1.9, which show the variation of peak amplitude of several harmonics with beam current, pressure, and field index.

1.2.2 Energy Spectra

In DCX-1, protons are initially trapped with a very small axial energy component, and, unlike DCX-2, there is no evidence of any organized central peak having less than the initial axial

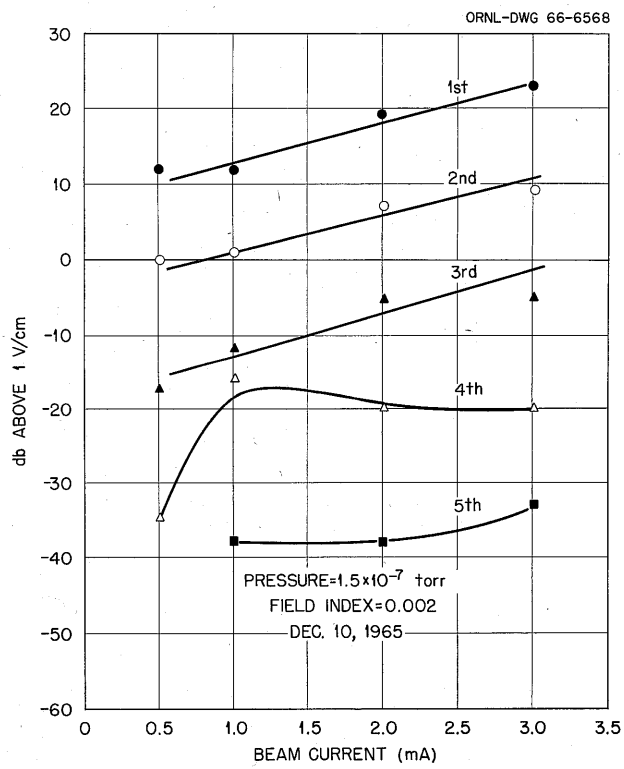

Fig. 1.5. Peak Amplitude of Electrostatic Probe Signals as a Function of Injected Molecular-Ion Current.

energy. The most impressive feature of the DCX-1 energy spectra obtained in these studies is the large increase in energy spread that accompanies operation with a nearly flat field. Figure 1.10 is a dramatic display of this dependence.

1.2.3 Other Features

For fixed beam and pressure, below $(1-2) \times 10^{-5}$ torr, the cold-plasma studies in DCX-1 show plasma potentials (here defined as the bias voltage required to repel half the ion saturation current) about three times greater with $n = 0.002$ than with $n = 0.052$. For $n = 0.002$, typical values for 1 mA H_2^+ (1×10^7 cm^{-3} fast-proton density) are 130 V at 1×10^{-6} torr and 20 V at slightly less than 1×10^{-5} torr. Unexplained experimental difficulties prevented acquiring reliable data above about 1×10^{-5} torr. This pressure was characterized by transitions in plasma properties, with evidence that cold-plasma currents increased more rapidly than pressure in the transition region. The transitions were most obvious in the case of the flat field.

Earlier determinations of the portion of the total trapped proton population of DCX-1 that actually participates in the instability (and

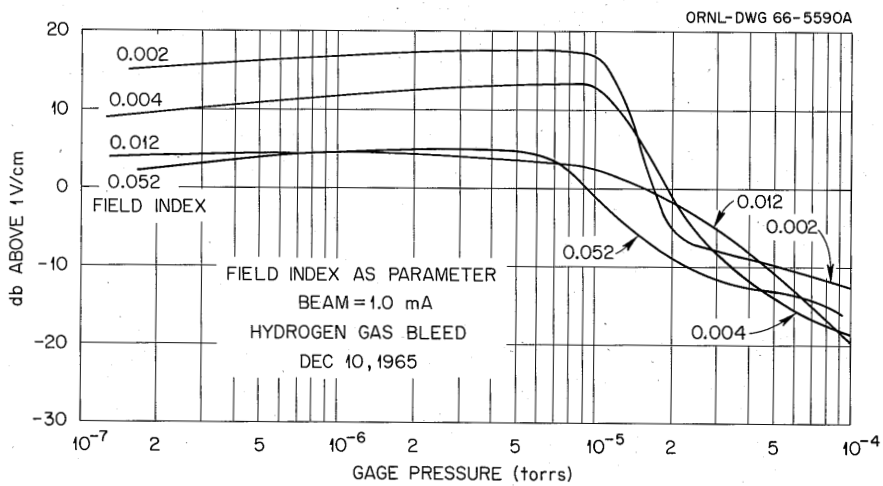

Fig. 1.6. Peak Amplitude of Electrostatic Signal First Harmonic as a Function of Pressure for Several Values of Field Index.

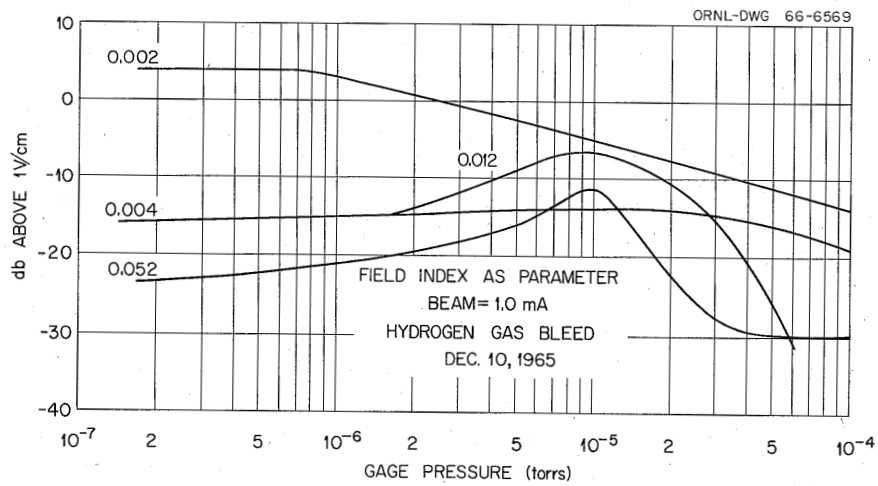

Fig. 1.7. Peak Amplitude of Electrostatic Signal Second Harmonic as a Function of Pressure for Several Values of Field Index.

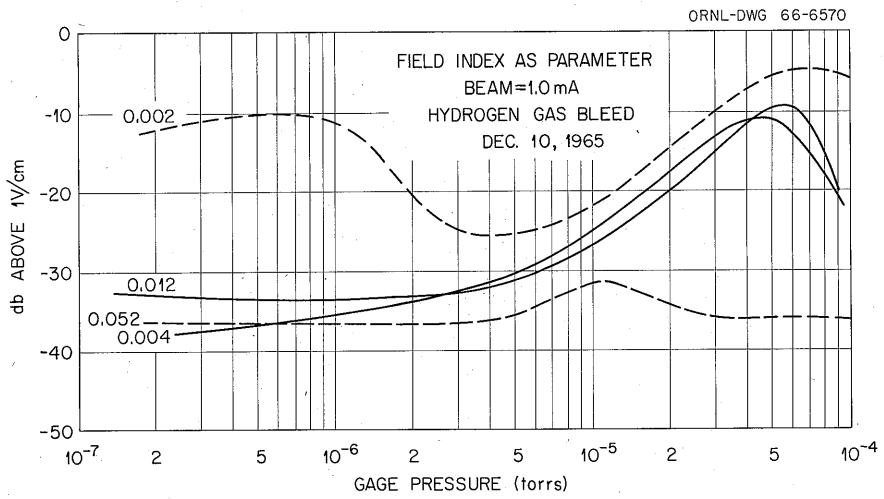

Fig. 1.8. Peak Amplitude of Electrostatic Signal Third Harmonic as a Function of Pressure for Several Values of Field Index.

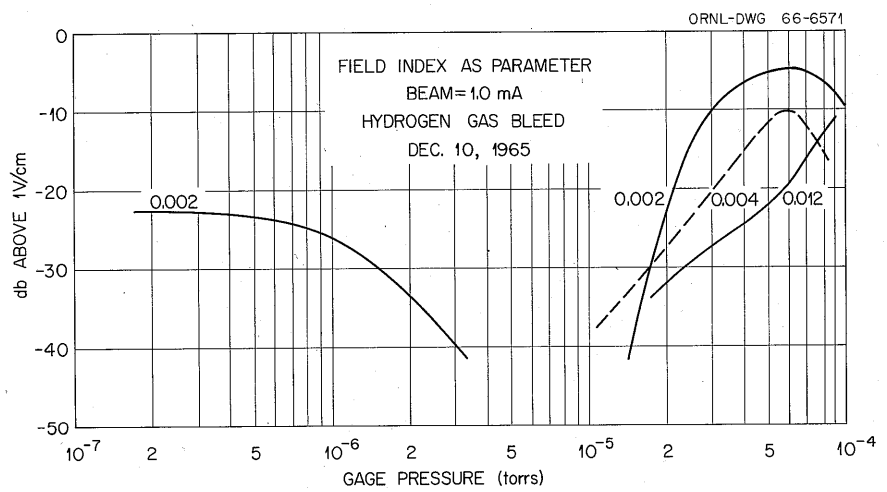

Fig. 1.9. Peak Amplitude of Electrostatic Signal Fourth Harmonic as a Function of Pressure for Several Values of Field Index.

therefore in rf generation) have been reported.[2] For field index values of 0.009, 0.06, and 0.019, the unstable proton population constituted only 2 to 3% of the total. This unstable portion consisted of those protons on nearly circular orbits, and the amplitude of the rf signals was not affected by moving in a radial scraper that reduces the radius until this scraper was close to the circular orbit.

With the very flat field characterized by an index of 0.002 and low pressures, a similar scraper experiment almost immediately produced a decrease in rf signal amplitude. We concluded that with the flat field, the portion of the trapped population participating in the instability is much greater, of the order of 50%. This behavior is consistent with continued interpretation of the dominant low-pressure instability as negative mass. The basic stabilizing effect for this instability is spread in ion gyrofrequency, and a flat magnetic field should therefore allow more trapped protons to participate.

[2] *Thermonuclear Div. Semiann. Progr. Rept. Oct. 31, 1965*, ORNL-3908, pp. 8 and 10–11.

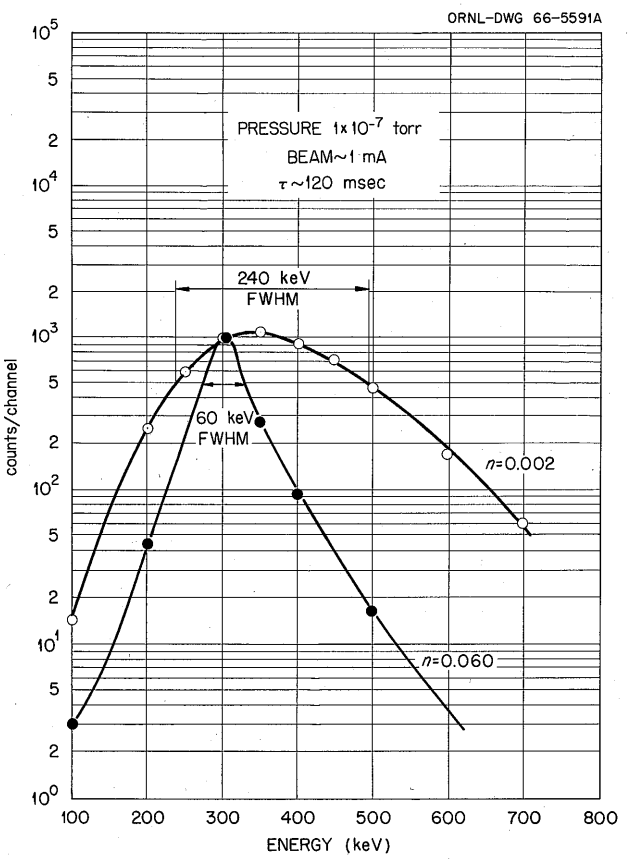

Fig. 1.10. Energy Spectra of Trapped Protons as a Function of Field Index.

Lorentz trapping in DCX-1 was of little consequence with flat-field operation. The maximum fast-proton densities obtained in DCX-1 during these experiments were (3–5) $\times$ 10^7 cm^{-3}, which is somewhat less than densities at which instability-driven proton losses are observed with the usual magnetic field gradient. Such losses were not observed in the experiments reported here, although evidence of strong instability was present.

1.2.4 Discussion

The existence of two pressure regimes seems to be a fundamental property of both the DCX-1 and DCX-2 plasmas, since complex transitions are observed in DCX-2 in the pressure range (3–6) $\times$ 10^{-6} torr.[3] Cold plasma very likely controls the transitions, and the transitions may denote shifts in the dominant instability mechanisms from those at low pressure, which involve primarily interactions among the hot ions alone, to those at high pressure, which involve cold plasma to a much larger extent. Fowler and Rankin[4] have suggested a mechanism for cold-plasma buildup in these facilities, and the observed transitions occur in the general range of pressures indicated by their calculations.

We believe that the dominant low-pressure instability in DCX-1 continues to be negative mass as the field is flattened. Operation with the smallest value of field index results in a significantly larger portion of the trapped proton population participating in the instability. Some effects of instability (rf signal amplitudes, proton energy spread, and plasma potential) are enhanced, and the magnitude of these effects becomes more like those observed in DCX-2.

At high pressures, operation of DCX-1 with flat rather than normal fields again results in plasma properties (suppression of rf signals at ion gyrofrequency, shift of harmonic structure to dominant even harmonics, lowered plasma potential, and enhanced cold-plasma flow) more similar to those of DCX-2. Detailed instability-mode studies have not been made in DCX-1 at pressures above transition. In view of the earlier suggestion that the instability in this regime may involve cold plasma, we have considered the two-component ion plasma instability of Hall, Heckrotte, and Kammash.[5] This instability does not appear to be involved. It can account only for an *upward* frequency shift from the ion gyro-*fundamental,* while in practice both higher and lower frequency components are observed for the several harmonics.

Although flat-field operation of DCX-1 yields plasma properties more similar to those of DCX-2 than does operation with normal field, a number of dissimilarities exist at both high and low pressures, and the similarities may be only superficial. We conclude that single-pass injection into the DCX-1 flat field does not simulate enough of the essential features of the DCX-2 plasma to permit unambiguous comparisons of the two plasmas.

---

[3]See sect. 2.3 of this report.

[4]T. K. Fowler and M. Rankin, *J. Nucl. Energy, Pt. C* 4, 311 (1962).

[5]L. S. Hall, W. Heckrotte, and T. Kammash, *Phys. Rev.* 139, A1132 (1965).

1.3 END WALL EXPERIMENTS[6]

A number of experiments were performed, mostly in the standard magnetic-field geometry, to investigate possible stabilizing effects of a variety of end-wall configurations. The experiments were essentially continuations of those previously reported,[7] but they employed three configurations suggested by more recent work on suppression of the calutron instability.[8]

Each set of end walls consisted of two identical structures, one for each end of the plasma chamber. The walls were basically circular, with a diameter of $19\frac{3}{4}$ in. They were mounted within the plasma chamber, parallel to the median plane, and were independently movable in azimuth and in displacement from the median plane. The metallic elements were of copper.

The three sets were of the general type illustrated in Fig. 1.11. Thirty-two radial sectors were supported by insulators from a grounded plate. Near the center of the configuration, certain sectors made contact with the inner conductor of a coaxial cable which, after a 3-m run, was accessible from outside the machine. The other sectors had coils wound around the insulators to produce resonance in a desired frequency range. In sets 1 and 2, every other sector was tied to the central cable, and the sectors with coils were alternately tuned to resonance at high- and low-frequency bands. In set 1 the bands were 70 to 80 and 18 to 21 MHz; in set 2 they were 55 to 60 and 14 to 16 MHz. Set 3 had only four tuned elements. These were equally spaced in azimuth and were resonant from 14 to 16 MHz.

The initial experiments were restricted to the use of set 1, a magnetic-field index of 0.002, and gas dissociation at pressures of about 1×10^{-7} torr (1-sec lifetimes and $n_+ \approx 10^7$ cm^{-3}). As usual there was ample evidence of the instability in the form of rf signals but no direct loss of protons. The rf spectrum from 5 to 100 MHz was observed by use of a DCX-2 electrostatic antenna and a wide-band, low-loss cable tie to a Hewlett-Packard 8551A spectrum analyzer. A variety of end-wall cable terminations (reactive, resistive, and ground) were employed, and the azimuthal and axial (to maximum displacements of $Z = \pm 4\frac{1}{2}$ in.) positions of the walls were varied. The nature of the cable terminations had little effect on the rf spectrum, and most experiments were with terminations to ground. Varying the positions of the end walls had little effect unless *both* walls were advanced close enough to the median plane to intercept part of the hot plasma. With the walls so advanced, variation of the relative *azimuthal* positions of the walls indicated positions capable of increasing and of decreasing rf signal amplitude. From the point of view of rf suppression, the most effective axial position was $Z = \pm 2$ in. There, at certain of the azimuthal positions for which sectors resonant at high frequencies faced those resonant at low frequencies, all signals in the 5- to 100-MHz range were reduced to noise level. The principal effect was on the gyrofrequency, and as a function of azimuthal position, the amplitude of this signal varied from noise level to 20 db above noise. The plasma density was reduced by about 20% by collisions with the end walls at $Z = \pm 2$ in., but there was no correlation of density fluctuation with rf amplitude.

Because of the rf suppression observed in these experiments, the studies were extended to instability-loss-dominated plasmas established by Lorentz trapping at low pressures in the standard magnetic field (index = 0.09). The usual DCX-1 crown probe was substituted for the DCX-2 probe. The former has a lower noise level and can be used for detection of electrostatic or magnetic signals. Diagnostics were expanded to include energy analysis of the trapped protons. Tests similar to those just described were made of all three end-wall configurations.

The exact nature of the results depended upon the wall configuration, the axial spacing, and the relative azimuthal positions. Since a detailed report of these observations would be hopelessly complex, we point out the following general features:

1. With these walls retracted from the fast-proton plasma, the plasma properties were those commonly obtained with the usual chamber walls.

[6] With E. D. Shipley and O. C. Yonts.

[7] *Thermonuclear Div. Semiann. Progr. Rept. Apr. 30, 1964*, ORNL-3652, pp. 8–14.

[8] *Thermonuclear Div. Semiann. Progr. Rept. Oct. 31, 1964*, ORNL-3760, pp. 45–46.

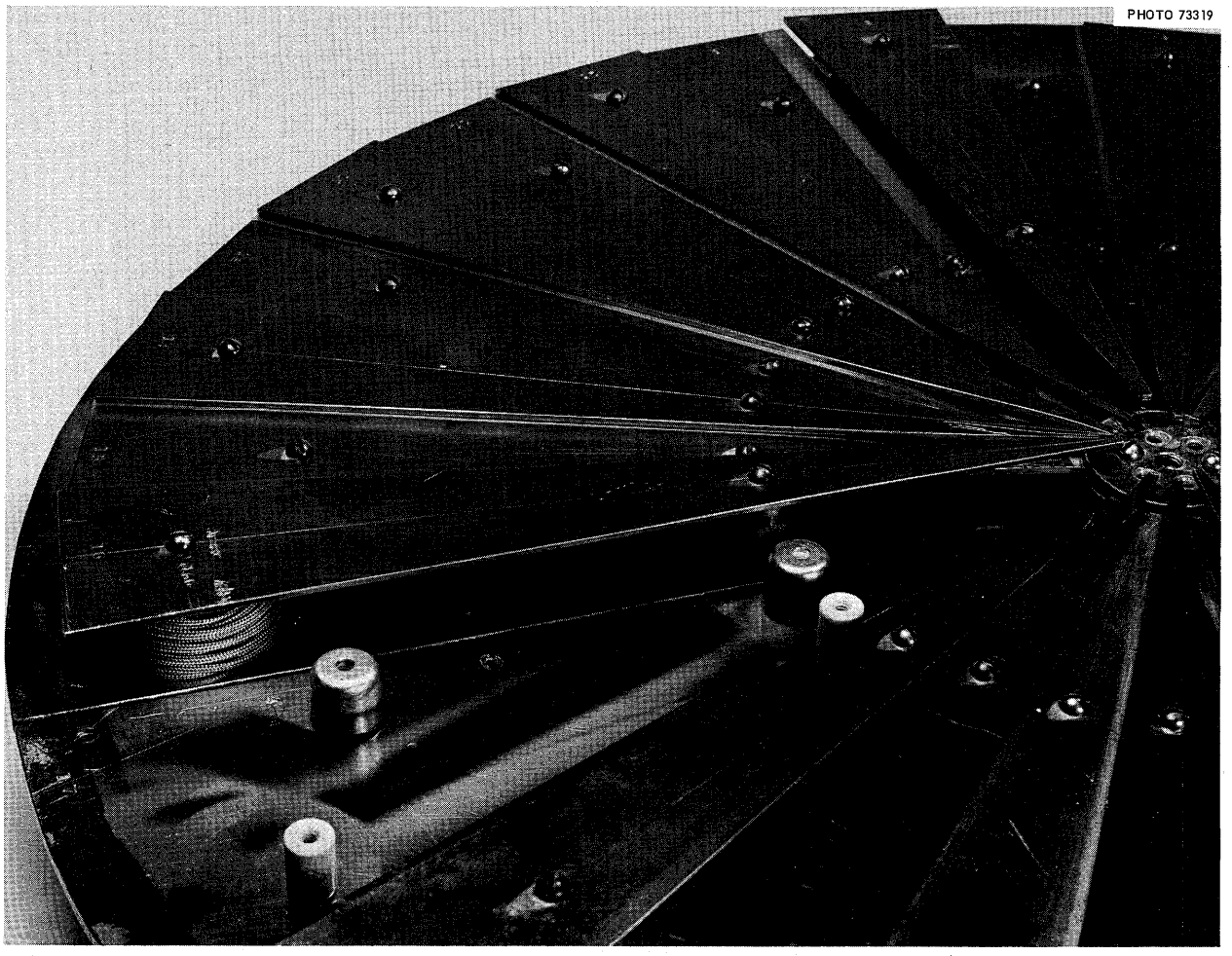

Fig. 1.11. Reactive End Wall Configuration No. 1. One sector has been removed to show a coil.

2. Again both end walls had to be advanced somewhat into the volume normally occupied by the fast-proton plasma in order to observe effects of the end walls on the instability.
3. For axial positions within the effective range, rf signal amplitudes were a function of relative azimuthal position. The signals from negative mass instability and from the axial instability varied in the same sense, but the effects on axial instability signals were generally the more pronounced. The effects on negative mass instability were most pronounced at the fundamental. The rf signals could not be reduced to noise level, but variations with azimuthal position of up to 30 db (fundamental band) were observed. With sets 1 and 2 the lowest rf amplitudes occurred when sectors resonant at high frequencies faced those resonant at low frequencies, and the largest amplitudes were those with reactive elements facing grounded elements. With set 3, lower rf amplitudes occurred with reactive elements in opposition.
4. The variations of proton energy spread and rf amplitude with azimuth were in the same sense (measurements made only with set 1).
5. Dependence of plasma density on relative azimuthal position was found only in the case of set 3. The variations of proton density and rf signal amplitude with azimuth were in the opposite sense (see Fig. 1.12). As usual, density was assessed from the product of neutral particle detector amplitude and decay time. The variation of density with azimuth was primarily the result of amplitude change.

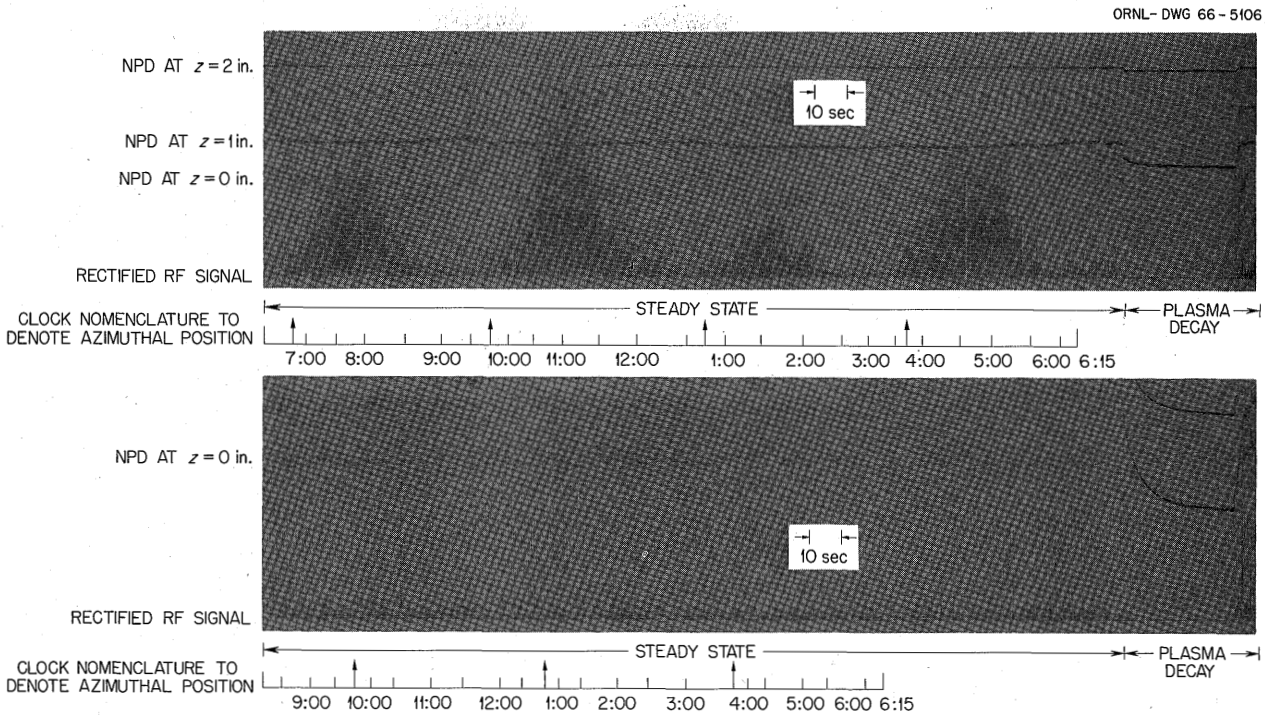

Fig. 1.12. Rf Amplitude and Charge-Exchange Signal (NPD) Variation with Azimuthal Orientation (One Cycle) of Reactive End Wall Set 3. The rf signal is a mixture of electrostatic and magnetic components, but is mostly the magnetic component generated by the axial instability. The end-wall axial positions were $Z = \pm\frac{3}{4}$ in. (upper display) and $Z = \pm 4\frac{1}{2}$ in. (lower display). $p = 8 \times 10^{-9}$ torr, H_2^{+*} current = 200 μA. Vertical arrows denote positions for aligned reactive elements. The four alignment positions do not produce identical effects, probably the result of the spread in reactance values.

The strongest variations were observed with the walls at $Z = \pm\frac{3}{4}$ in. The variations with $Z = \pm 2$ in. were barely observable.

6. Plasma densities were always lower than those obtained with the walls retracted to ineffective positions outside the volume normally occupied by the fast-proton plasma.

From these observations, it is evident that the end walls do couple to plasma instability. Coupling has been demonstrated in the earlier work by virtue of pronounced changes in the spectral distribution of rf signals.[7] The changes in proton energy spread and trapped proton density reported here represent new results.

The principal difficulty with the reactive end walls is that coupling takes place only under circumstances detrimental to plasma density (items 2 and 6). There is reason to believe that these walls are analogous to an impedance contributed by a layer of cold plasma between the energetic plasma and grounded end walls.[9] If the energetic plasma is to be strongly coupled to the reactive end walls, the conductance of the intervening space must be large. In this context the experiments have demonstrated that the conductance provided by the cold-plasma flow out of the DCX-1 energetic plasma is not sufficient for strong coupling and that for such coupling the reactive end walls must also be in substantial contact with energetic plasma. Such contact is objectionable for obvious reasons.

A more suitable plasma for testing the reactive end walls would be one that generates cold plasma in copious quantities.

1.4 HISTORICAL REVIEW

Experiments with the DCX-1 facility are in a terminal phase, and it is appropriate to review

[9] G. E. Guest and C. O. Beasley, Jr., "Cold Plasma Effects in Finite Length Plasmas," to be published in *Physics of Fluids*.

the principal lines of investigation to which the facility has been devoted.

As originally conceived, the facility was to be used for investigating the accumulation of hot ions formed by the dissociation of H_2^+ on a carbon arc operated along field lines so as to intercept the molecular beam at the proton circular orbit radius. The initial experiments therefore emphasized carbon-arc dissociation. Plasmas established by gas collisional dissociation were also studied, not so much for their own worth as to form a basis on which to evaluate the arc dissociation data.

These experiments constituted the bulk of those performed from 1958 to 1961. We found that the carbon arc was an efficient dissociator; in some of its configurations it could convert 30% of the H_2^+ current into protons. However, the arc constituted a poor environment for long-term containment of these energetic protons. Circulating protons lost energy to the cold electrons of the arc column at a rapid rate, 10 to 20 keV/msec. Since the cross section for charge exchange of trapped protons with gases varies as E^{-4} in the region around 300 keV, this energy loss seriously reduced the confinement time. Worse yet, the partially stripped carbon ions constituted additional charge-exchange centers, and at base pressures (then about 5×10^{-7} torr) essentially all the protons were lost by charge exchange in the arc itself. The best performance figures for these experiments were as follows:

Dissociation	n_+ (cm^{-3})	τ(msec)
Arc	$\sim 3 \times 10^9$	3–5
Gas	$\sim 3 \times 10^7$	10–15

Further reductions in pressure could have increased the proton lifetimes with gas dissociation, but would have had little effect on those with arc dissociation.

Hydrogen arcs, which have been developed elsewhere in the Division, were then investigated with the hopes of providing a dissociator with a much reduced concentration of charge-exchange centers. Despite baffling of the arc column and disposing of the large gas loads released at the electrodes with high-speed pumps, the pressure in the plasma region could not be reduced below 1×10^{-5} torr. At this pressure the performance of the system was dominated by the neutral-gas background. Diagnostic work on these arcs continued elsewhere in the Division, and it was eventually demonstrated that the arcs are subject to flutelike instabilities. Such instabilities account for the abnormally high pressures observed in the plasma chamber.

From 1961 to 1963 the emphasis shifted to detailed studies of the properties of plasmas established by gas dissociation. There were two significant reductions in base operation pressure: to $\sim 1 \times 10^{-8}$ torr by titanium evaporation and liquid-nitrogen cooling and then to $\sim 1 \times 10^{-9}$ torr upon discovery of the advantages of temperature cycling of such pumping surfaces. This period saw the development of most of the diagnostic equipment that we presently employ. Microinstabilities were evidenced by rf emission at ion-cyclotron harmonics, and correlated with these rf signals were plasma potential changes of hundreds of volts, rapid ejections of electrons from the plasma, dispersion of the proton energy distributions, and axial scattering of the plasma. The principal detrimental effects of instability were at low pressures. There they reduced mean containment time (because of changes in the energy distribution) and further diluted the density (because of axial expansion of plasma volume). They did not, however, result in any significant direct loss of protons; charge exchange continued to dominate. In this period, maximum densities of 1×10^8 cm^{-3} and maximum plasma lifetimes of 60 sec (since extended to 150 sec) were realized.

Early in 1963 the facility was altered to allow injection of H_2^+ generated from H_3^+ in a water-vapor cell, since such a beam has an excited-state population that favors Lorentz-force trapping. At base pressures this trapping technique provided proton input rates to the plasma more than an order of magnitude greater than those available with gas dissociation. For a stable plasma the density should have accumulated to about 5×10^9 cm^{-3}. Instead, by mid-1963 it was found that the density did not rise above 2×10^8 cm^{-3}. In addition to volume expansion and energy changes, microinstability-driven direct losses of protons were indicated. Stabilization by electron-cyclotron heating and also by reactive end-wall configurations was attempted during the latter half of 1963, but the density limitation remained.

Essentially all of 1964 and most of the first half of 1965 were devoted to detailed studies of the density limitation. Flutes and possible explanations not associated with instability were excluded. Radial and axial losses of fast protons were detected and were correlated with specific rf signals from instability, thereby demonstrating that the limitation was indeed the result of microinstability.

In the second half of 1965, the density threshold of the dominant microinstability and the limiting plasma density were studied as functions of deliberately induced changes in proton energy spread and spatial anisotropy. The changes relaxed the density limitation only slightly, but had profound effects on the instability threshold. These experiments and others expressly designed as mode identification studies resulted in identification of the dominant instability as negative mass. The more recent experiments are described in Sects. 1.2 and 1.3 of this report.

The principal contributions of DCX-1 have been in the field of detailed diagnostics of microinstabilities and are reported in two papers published during this report period.[10,11] In addition, a number of techniques developed during the course of these investigations (energy analysis by charge-changing spectrometer and by solid-state detectors, plasma potential measurements by lithium ion beam transmission, field component determinations by rf probes, instability damping by electron-cyclotron heating, and instability damping and mode identification through controlled variation of plasma anisotropy) have been recognized as significant contributions in themselves.

---

[10] J. L. Dunlap, G. R. Haste, C. E. Nielsen, H. Postma, and L. H. Reber, *Phys. Fluids* **9**, 199 (1966).

[11] H. Postma *et al.*, *Phys. Rev. Letters* **16**, 265 (1966).

2. Injection and Accumulation: Multiple-Pass Experiments (DCX-2)

P. R. Bell
J. S. Culver
R. C. Davis
S. M. DeCamp
J. C. Ezell
J. E. Francis
C. F. Harrison[1]
G. G. Kelley
N. H. Lazar
J. F. Lyon
E. C. Moore
O. B. Morgan
T. F. Rayburn
R. F. Stratton
C. W. Wright

2.1 INTRODUCTION

As we have mentioned in the past, two distinct components of the energetic plasma exist in the DCX-2 volume. These components may be identified by the pitch-angle distribution of the trapped protons. At the highest densities seen in DCX-2, that is, with lithium-arc dissociation (8×10^9 ions/cm^3), most of the density is contained in what has been called the "central-peak plasma." That is, most particles have $v_{\parallel} \sim 0$ and are therefore trapped in a very shallow mirror produced about the midplane of the DCX-2 magnetic field. In addition, of course, the "side-lobe plasma," comprising particles with axial energy nearly equal to the injected axial energy, was present but in a considerably smaller density. A similar behavior is seen with hydrogen-arc dissociation, but somewhat lower densities were obtained ($n_+ = 2 \times 10^9$ ions/cm^3). In gas dissociation the situation in the past has been more clouded. Under some conditions a central-peak plasma has been observed, and in the same pressure range at other times none could be detected. The energetic-ion densities in these two regimes are not very different. The necessary experimental parameters for obtaining these two conditions were not well defined, although the criticality of the shape of the magnetic field was recognized. The specific instability mode that caused the observed plasma, of course, was not identified.

During this report period additional gas dissociation experiments have been carried out with two motivations: (1) to study plasmas which may be related in a simple way to theoretical models and (2) to study the mechanism which results in the highly anisotropic, but relatively stable, plasmas which are produced. The first motivation has led to some success in understanding the limitations of the theories of ion-cyclotron instabilities. The second is still in an uncertain realm, with some empirical results available but the basic physical process not yet illuminated. In particular, variations in intuitively noncritical parameters change the observed trapped pitch-angle distribution from the one which shows a prominent central peak to one without a central peak. These variations still occur in an incompletely controlled way. Despite this uncertainty, we have been able to isolate a class of streaming instabilities associated with the molecular-ion beam and present some evidence that such modes exist in the proton spectrum as well. These modes probably contribute to the observed nonlinear behavior, but we have not yet established their relative importance.

To obtain these results we operate DCX-2 in much the same manner as we have in the past. The midplane field is 11.4 kG, and the injection energy is generally 540 keV. The injected H_2^+ beam current may be varied from less than 10 mA to 40 mA. The base pressure has been reduced to

[1]Analytical Chemistry Division.

2×10^{-8} torr by extensive cleaning of the vacuum components.

2.2 STUDIES OF THE CENTRAL-PEAK PLASMA

A very interesting plasma is produced by an instability when the pressure is raised by adding either hydrogen or nitrogen to the background gas. At equilibrium the pitch-angle distribution determined by scanning the collimated energy-sensitive barrier detector parallel to the axis shows the customary three-peaked distribution (see Fig. 2.1). In these experiments the detector is situated, as in the past, at the midplane and restricted in vertical angle to ±18° and does not view the dissociation neutrals from the beam. The axial energy of the two side lobes has been shown to correspond within the experimental error to the injected axial energy.[2] The total energy distribution of these particles is shown in Fig. 2.2. The more interesting group of particles are those from the central peak, since the density associated with them is, in general, somewhat higher than that in the side lobes. Further, their energy spread is considerably larger than that of the particles in the side-lobe plasma (Fig. 2.3). Taking the mean energy and the average spread of the central peak, we obtain an average axial "temperature" of 0.40 keV. Implicit in this definition of axial temperature is the assumption that the particles of all energies are uniformly distributed in pitch angle throughout the distribution. For the comparisons with theory which follow, this is, fortunately, not a critical parameter. It is possible to obtain the true mean axial energy by electronically selecting various energy intervals and, for each energy interval, scanning in the usual way, but this has not yet been done for this set of operating parameters.

As the pressure is varied, we find that the ratio of the intensity of the central peak to the side lobes varies; in particular, at the lowest pressures ($\sim 2 \times 10^{-7}$ torr with the beam injected), the primary component is the central peak, but the density contained in it is quite small, $\sim 1 \times 10^{7}$ ions/cm^3. As the pressure is raised, the density and the energy spread in the central-peak plasma increase. The maximum density and energy spread

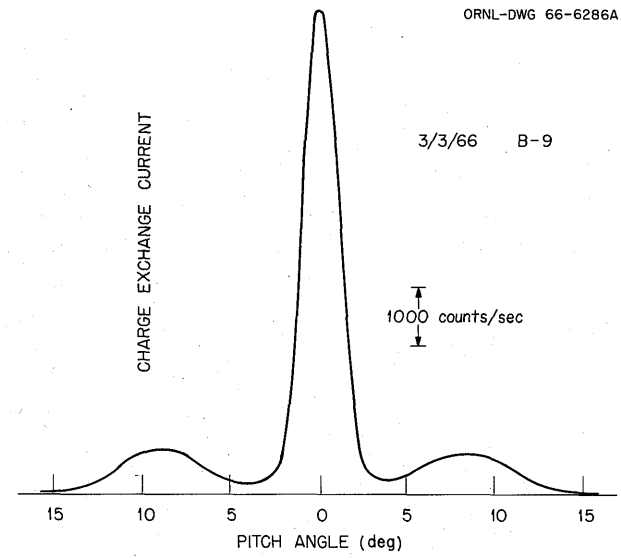

Fig. 2.1. Pitch-Angle Distribution of Charge-Exchange Neutrals. The detector response width was 0.1 by 36°. Neutral particles of all energies above ~75 keV were accepted.

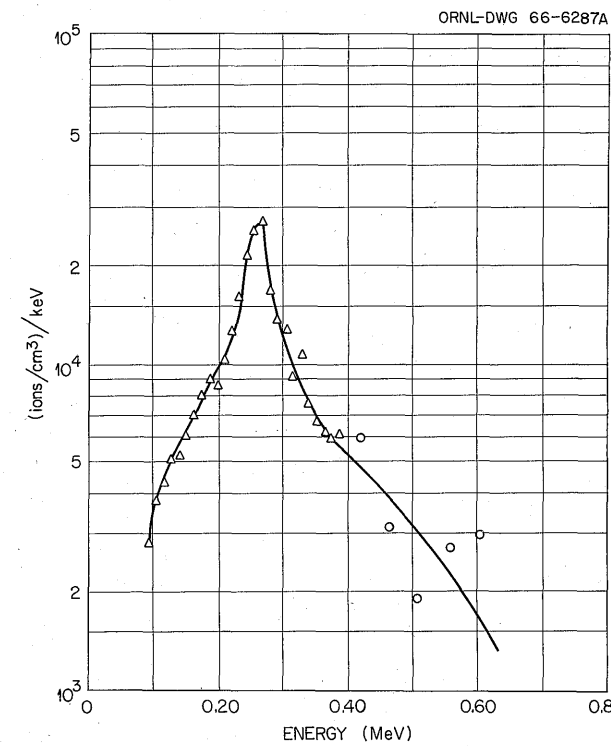

Fig. 2.2. Total Energy Spectrum of the Side-Lobe Plasma Ions. This is the energy distribution of the ion population derived from the energy spectrum of the escaping charge-exchange neutrals. The circled points are averages of several channels to improve statistics.

[2] *Thermonuclear Div. Semiann. Progr. Rept. Oct. 31, 1964*, ORNL-3760, p. 20.

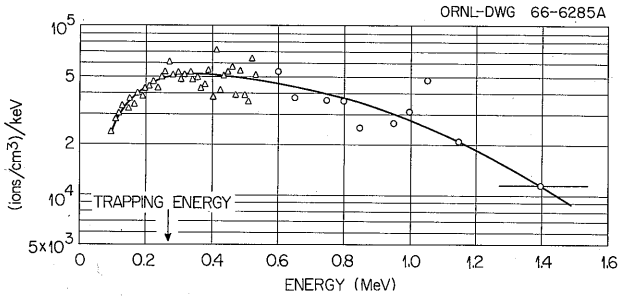

Fig. 2.3. Total Energy Spectrum of the Central-Peak Plasma Ions. The circled points are averages of several adjacent channels to improve statistics.

are obtained at a pressure of 3.3×10^{-6} torr with hydrogen gas fed into the vacuum liner. A probe was inserted into the vacuum liner in the far magnetic dip, which absorbed any energetic plasma trapped in that region as well as the side-lobe plasma without absorbing the central-peak plasma. Surprisingly, the density of the central peak increased by a factor of 3 to 5. Under these conditions the density in the central peak reaches $\sim 0.8 \times 10^8$ ions/cm^3. This value is determined by examining the time integral of the charge-exchange flux emitted to the walls and is observed with a foil detector in the midplane (Fig. 2.4). The axial extent of this plasma may be estimated from the observed currents to the detectors. Since almost no current is collected at $z = 120$ cm and the total charge observed at $z = 33$ cm is approximately one-half that at $z = 0$, we estimate the plasma length as ~ 100 cm. By scanning the plasma in the plane perpendicular to the axis, we have estimated the central-peak plasma radius to be roughly 15 cm. Thus the volume containing the plasma is quite large, $\sim 7 \times 10^4$ cm^3. From the energy distribution shown above, we note that the central-peak plasma is highly anisotropic, $T_\perp/T_\parallel \sim 10^3$, with $T_\perp$ of the order of 500 keV. This highly anisotropic plasma is contained in a sufficiently large volume so that theoretical models may be considered applicable. At present the most meaningful comparisons with theory may be made after the beam is turned off.

We have searched for the presence of rf fields at the ion cyclotron frequency and its harmonics after the beam is off and have found that the observed fields decay rapidly (less than a few milliseconds) and do not reappear, while the density has not changed by 10% in these times. The electron density is probably greater than the energetic-ion density. An estimate of the cold-plasma density after the beam is off was made by taking the ionization rate for protons with a mean energy of 500 keV and the observed ion density. We estimate the cold-plasma density as 3×10^8 ions/cm^3, assuming that the cold ions stream through the mirrors at a velocity of 2×10^5 cm/sec. Efforts at a direct measurement of the cold-plasma ion and electron energies and densities using a 3-cm interferometer and gridded probes have their difficulties, as described below. However, the data obtained by use of these tools do not rule out cold-plasma densities this high.

The usual rule of thumb criterion for onset of ion-cyclotron instabilities based on an infinite

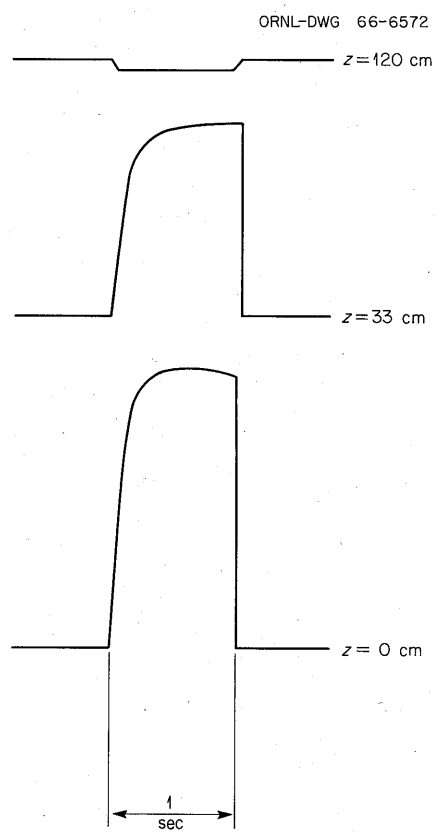

Fig. 2.4. Integrals of the Charge-Exchange Neutral Current After Beam Cutoff. These were measured at the indicated distances from the DCX-2 midplane. The leakage current is compensated for by a small dc drag current; the offset in the top trace and the slope at the top of the bottom trace reflect slight miscompensation due to drift. The zero of each integral is at the baseline. Each is the same relative scale.

medium theory is $\omega_{pe} > \omega_{ci}$. In DCX-2 this threshold yields a density of 4×10^6 electrons/cm^3. The absence of radio frequency at electron densities exceeding at least 10^8 electrons/cm^3 indicates clearly that this criterion is inapplicable. Soper and Harris[3] and Guest and Dory[4] have modified the infinite medium theory to include anisotropic velocity distributions and finite electron temperature. These considerations applied to DCX-2 do not change the criterion appreciably; therefore the difficulty probably lies in the finite size of the plasma.

An attempt has been made to model a finite-size plasma using the infinite medium theory by restricting the wavelengths which may propagate to those which can fit within the plasma. This approach, although reasonable, is certainly no substitute for finite plasma calculations. In fact, inclusion of finite size will automatically introduce other modes, such as drift modes. Using $k_r \gtrsim \pi/R$, where R is the plasma radius, the density threshold for the DCX-2 plasma is estimated as $\omega_{pe}/\omega_{ci} = 2$ or an electron density equal to 2×10^7 electrons/cm^3. We have exceeded this threshold by almost an order of magnitude. Further, the axial length of the plasma does not seem to constitute a limit since $L = 5\pi/k_{\parallel}$, where L is the axial length of the plasma and $k_{\parallel}$ is the axial wave number at the threshold density. Further discussions of the implications of the observed stability will be given in Sect. 7.2 of this report.

2.3 OTHER GAS DISSOCIATION EXPERIMENTS

As mentioned above, interpretation of gas dissociation experiments has been clouded by the appearance of different regimes of the instability-generated plasma. In particular, the central-peak plasma is present under some conditions and not under others. It is still not clear what causes the transition from one regime to the other, and extensive measurements have not completely determined the critical parameters. The one most critical parameter which seems to affect the presence or absence of the central peak is the relative position of the injector and the dip in the magnetic field. Small changes in these parameters have been forced upon us by shorts in the mirror coils which are compensated to produce a flat field over the central portion of the vacuum chamber but are not exactly compensated in the dip regions. Further, small mechanical motions of the injector have been made inadvertently which have affected the presence or absence of the central-peak plasma. Despite these uncontrolled changes in modes of operation, the behavior in each mode is reproducible and well defined. That is, the density, energy spread, and radio-frequency properties as a function of pressure, for example, are now well documented and predictable in each mode.

When the central peak is absent, the behavior of the plasma as a function of pressure is as described in the previous semiannual report.[5] That is, the density passes through a peak in the pressure range from 5×10^{-7} to 5×10^{-5} torr. This peak has been shown to result from energy spread of the trapped protons, which causes a relative reduction in the charge-exchange loss rate. It now appears that the side-lobe plasma which is produced under these operating conditions is also trapped in the weak magnetic dip in the center of the machine. Support for this conclusion has been recently derived by inserting obstacles in the far dip at $z = 120$ cm which had no effect on the contained density and energy distributions. It is interesting to note that when the beam is turned off with this pitch-angle distribution, rf persists for times as long as several tens of milliseconds. The rf is seen in bursts during this interval. The rf spectral patterns are not identical in the two regimes for the lower pressure ranges, although similarities at the higher pressures exist; in particular, the odd-even harmonic intensity variation is present in both cases. A comparison of two spectra at 1×10^{-5} torr is given in Fig. 2.5.

In the regime with a central-peak plasma, the maximum density was obtained at a pressure of 3.3×10^{-6} torr. Since the pitch-angle distribution observed under these conditions is so different from the injected pitch-angle distribution, it appears very clear that an instability must be present at equilibrium which produces this distribution. The radio frequencies associated with this instability are shown in Fig. 2.6 and are similar to

[3] G. K. Soper and E. G. Harris, *Phys. Fluids* **8**, 984 (1965).

[4] G. E. Guest and R. A. Dory, *Phys. Fluids* **8**, 1853 (1965).

[5] *Thermonuclear Div. Semiann. Progr. Rept. Oct. 31, 1965*, ORNL-3908, pp. 18–28.

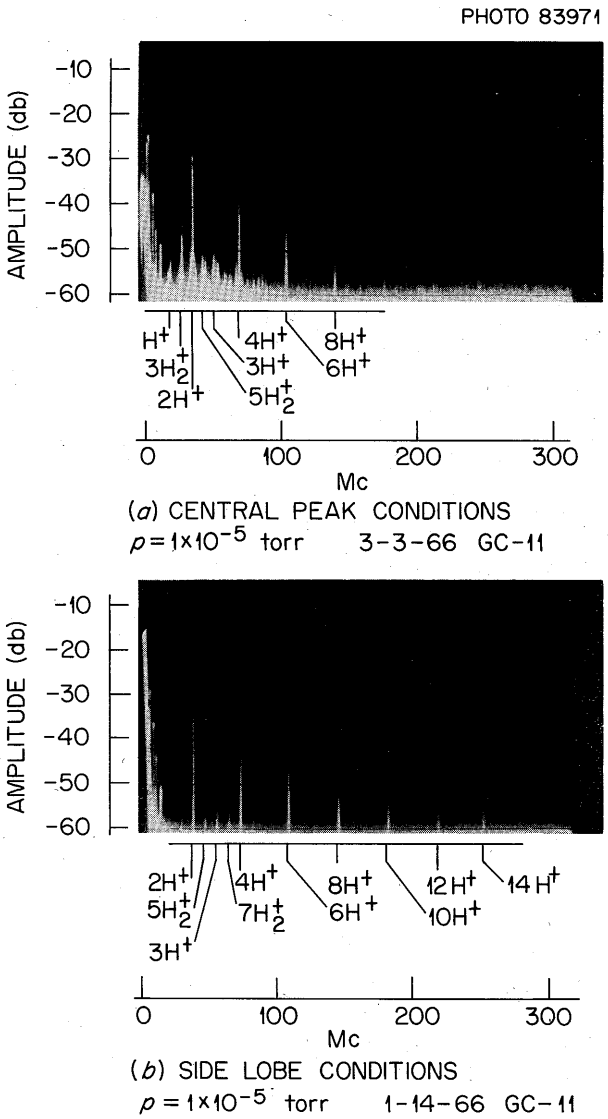

Fig. 2.5. Radio-Frequency Spectra from 0 to 300 Mc. The taller lines are the even harmonics of H^+, beginning with the second at 34.8 Mc.

many of the rf spectral patterns observed in the past with gas dissociation. We have determined that a number of transitions in the rf spectra occur as the pressure is raised and that at least in some cases more than one instability must be playing a role in the determination of the pitch-angle distribution. Surprisingly, only very small changes in pressure are required to change the rf spectral distribution, and, associated with these changes, we observe variations in the central-peak plasma. Some of these changes are illustrated in Fig. 2.7. Below 3×10^{-6} torr the equilibrium rf spectral distribution is characterized by strong H^+ signals, with the higher harmonics falling off rapidly. At a pressure of 4×10^{-6} torr the fundamental and odd harmonics of the proton gyrofrequency abruptly decrease in intensity. Associated with this abrupt change is the abrupt disappearance of the characteristic central-peak plasma. In its place we observe a double-peaked distribution. The side-lobe plasma has increased as well (Fig. 2.7*b*). As the pressure is raised to $\sim 1 \times 10^{-5}$ torr, a gradual change takes place during which time the odd harmonics appear sporadically. The central-peak plasma reappears but is much weaker relative to the side-lobe plasma. As the pressure is raised still further, the side-lobe plasma is increased, the total trapped density increases, and the rf spectra show the typical odd-even effect reported previously.[6]

It may be appropriate to mention at this point the similarity of the high-pressure results, reported by the DCX-1 group in this report, to these high-pressure observations. It is clear, however, that observations at lower pressure show distinct differences from the performance of DCX-1.

[6] *Ibid.*, pp. 27–28.

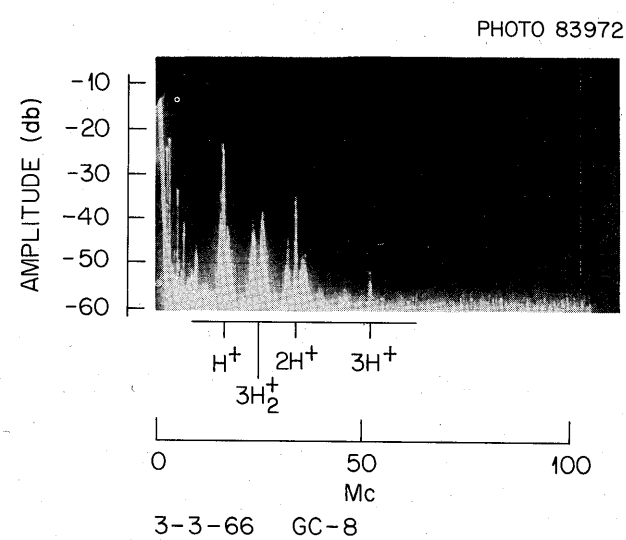

Fig. 2.6. Radio-Frequency Spectrum for Conditions of Maximum Central-Peak Plasma with Gas Breakup. Note that the molecular-ion harmonic lines are double. At the lower end of the spectrometer response (0 to 10 Mc) there are a few spurious lines. These can be seen clearly in all the figures in Fig. 2.7 as well.

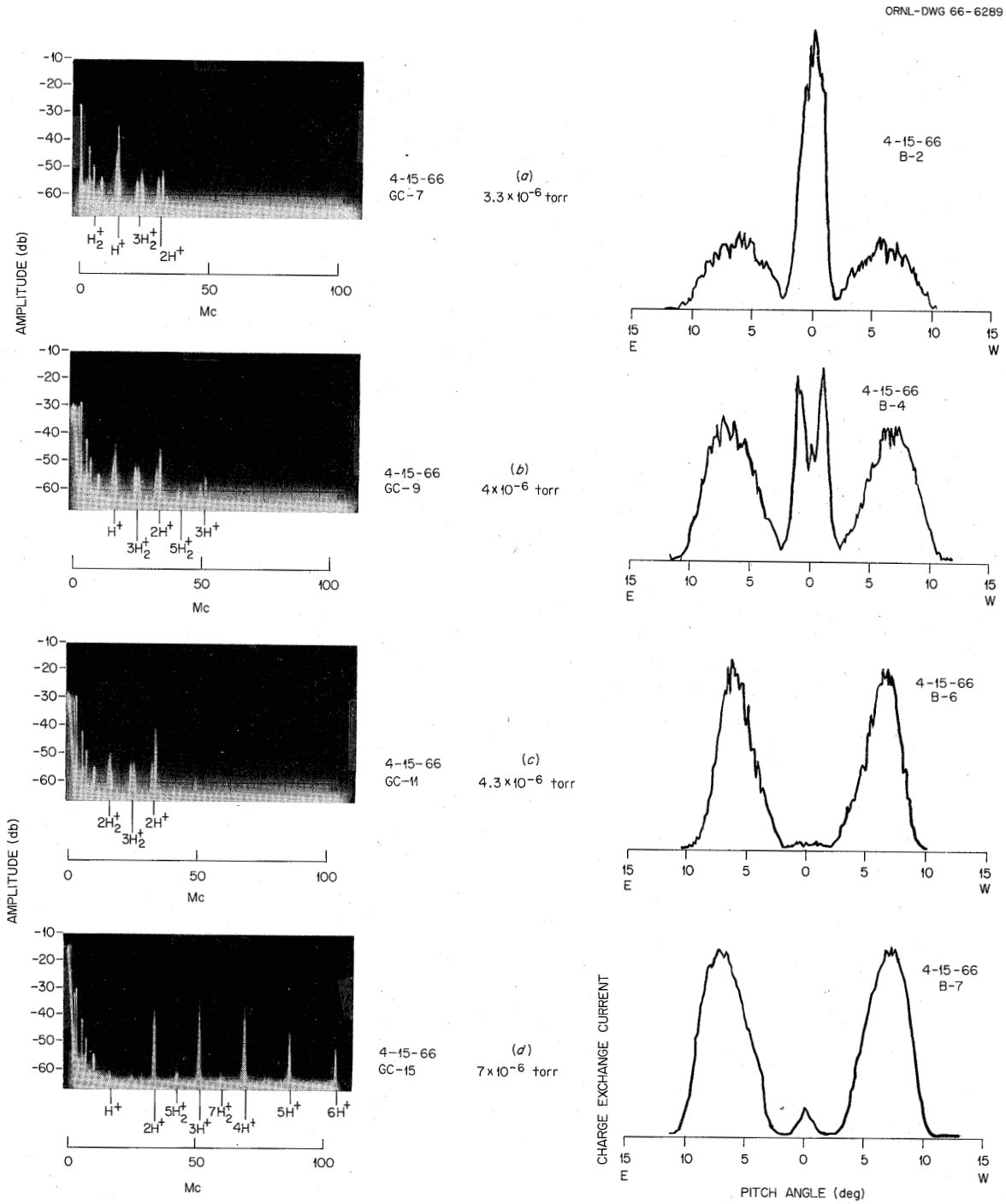

Fig. 2.7. Radio-Frequency Spectra and the Corresponding Fast-Ion Pitch-Angle Distributions for Several Modes of Plasma Behavior in DCX-2. The upper set (*a*) is for a central-peak mode seen at all pressures below 4×10^{-6} torr. The second set (*b*) corresponds to the transition with the proton fundamental vanishing intermittently and with the second harmonic strong. The third set (*c*) shows almost no proton fundamental; the peaks at ~17.4 Mc on closer examination may be identified with the H_2^+ spectrum. The second harmonic is strong, and it may or may not have the fourth and other even proton harmonics. The molecular-ion harmonics remain. The lower set (*d*) corresponds to pressures above about 6×10^{-6} torr. Note that at higher pressures the odd harmonics are suppressed.

It appears from these data that not one, but several, modes of interaction at the cyclotron frequency of the ions are taking place, and the nonlinear manifestation of these interactions can result in somewhat different pitch-angle distributions of the trapped protons. However, it should still be noted that in certain ranges of pressure the principal effect of the instability is in a change of the energy distribution of the protons. Although in particular cases direct particle losses occur, as reported below, over a wide range of operating parameters the instability serves to cause a useful energy spread and to result in interesting plasmas. The challenge will be to better understand the regimes producing the interesting plasma and, if possible, to extend these regimes to higher density.

A detailed study of some of the harmonic peaks provides some insight into the mechanism which produces the rf structure. In Fig. 2.8*a*,*b* we show in greater detail the response at the fundamental of the molecular-ion and proton cyclotron frequencies at a pressure of 3×10^{-6} torr. Note that they consist of several peaks. When a probe is inserted into the vacuum liner near the far dip, sufficiently far to stop all the molecular-ion beam, the spectrum is changed as shown in Fig. 2.8*c*,*d*.

These observations are consistent with an intuitive model of a streaming interaction. For a single beam the resonant frequencies should be expected to be shifted by the beam Doppler frequency above the cyclotron frequency. With opposing beams present a more complicated interaction occurs as a result of interactions of the same kinds of waves with the opposite beam, and so the observed frequencies are expected to be both above and below the cyclotron frequency. In this picture, if only one wavelength were amplified, sharp peaks at $\omega_{ci} \pm k_{\parallel} v_0$ (v_0 is the beam velocity) would be expected. Neglecting sheath effects the maximum

PHOTO 83875

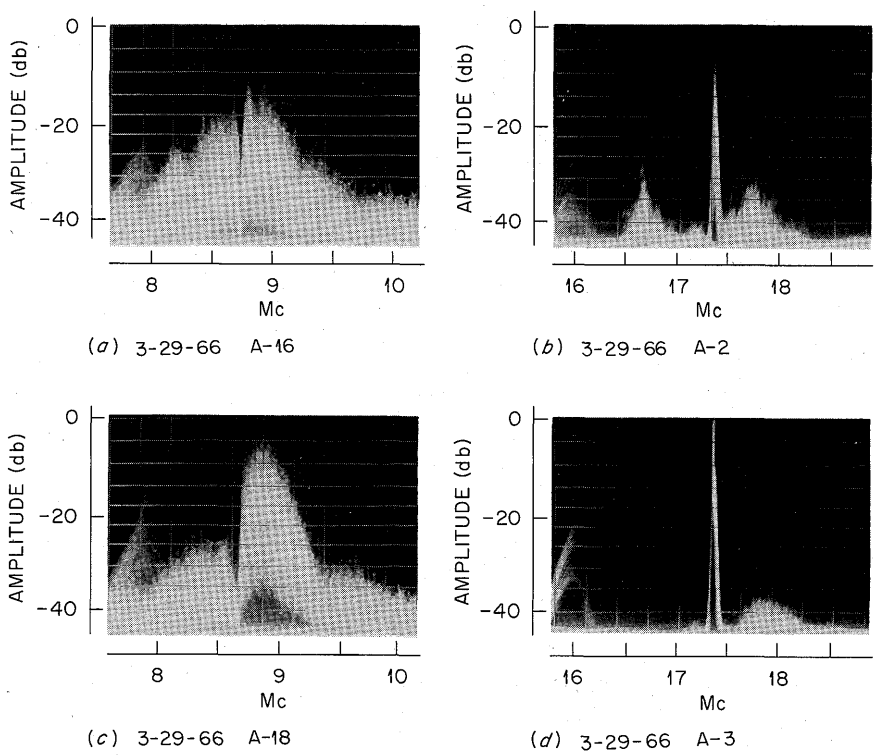

Fig. 2.8. The Molecular-Ion Fundamental (*a*) and the Proton Fundamental (*b*) Seen with a Central-Peak Gas Dissociation Plasma. When a probe is inserted into DCX-2 to stop the molecular ions after one trip from the injector to the far end, the low-frequency side of the molecular-ion peak is depressed (*c*). The lower-frequency side of the response near the proton fundamental also diminishes. The sharp dip at the center of the molecular-ion line is at exactly half the frequency of the sharp proton fundamental (*d*).

PHOTO 83876

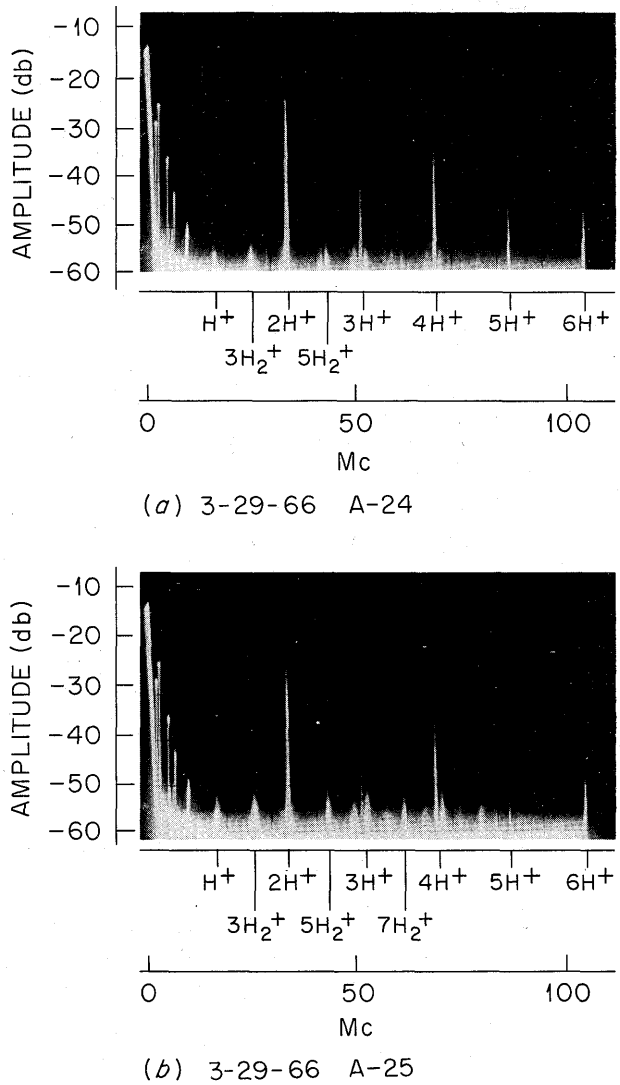

Fig. 2.9. Radio-Frequency Spectra: with the Molecular-Ion Beam Passing Both Ways in DCX-2 (*a*), and with a Probe Inserted to Prevent Reflection and Return of the Beam (*b*). Note that the molecular-ion lines seen by themselves at the odd harmonic numbers go from double to single, while the broad lines at the proton harmonics remain double.

wavelength which would be expected is $2L$, where L is the characteristic axial length of the beam. In fact, all wavelengths shorter than this may be present, and the different growth rates might be expected to select the ones seen. Thus the broad spread in the peaks is not unexpected. The wavelength corresponding to the maximum of the distribution in Fig. 2.8*b* is $\sim$50 cm.

From the observed depth of the central dip in Fig. 2.8*a* and the spectrometer bandwidth (20 kc), the minimum spacing between the side bands is $\sim$40 kc. This spacing corresponds to a wavelength of 22 m. The spacing between the mirror throats is 4 m, and the maximum distance between conducting end walls is 8 m. It may be possible to invoke sheath effects to explain the presence of the wavelengths observed. However, it is clear that a more comprehensive theoretical treatment of these observations is required. An attempt at such a treatment of streaming instabilities, including cold-plasma effects, is presented in Sect. 7.2; but the development has not yet reached the point that it may be compared with these observations.

The rf spectrum associated with proton gyrofrequencies, on occasion, shows a similar double-peak behavior which is subject to the same type of analysis. In Fig. 2.9*a* these double peaks are shown, and the effect of inserting the probe (to absorb the molecular-ion beam) on the molecular harmonics is shown in Fig. 2.9*b*. Note that the proton harmonics are still double, but the peaks associated with molecular ions are single.

2.4 ENERGY ANALYZER BEAM AND PLASMA MEASUREMENTS

We have concentrated on gas dissociation this report period partly because the diagnostics were expected to be more easily interpreted and the instability-generated plasma should be simpler to understand. With lithium-arc dissociation we had the highest H_2^+ beam breakup fraction and the highest energetic-proton density. In this mode of operation the energy analysis was difficult to interpret because of the unknown radial distribution and density of the charge-exchange centers. Thus the radial distribution of hot ions was difficult to obtain by inversion, and the absolute density was impossible to determine from energy analysis. The hydrogen arc may not produce a large nonuniform distribution of charge-exchange centers, but it does prevent experiments at low pressure. Since interesting results had been obtained previously, we returned to gas dissociation, where the charge-exchange cross sections are known for nitrogen and hydrogen and the mass spectrometer can be used to find the background gas composition.

The highly collimated scanning silicon-barrier detector (energy analyzer) has been described previously,[7] and its use in studying the energetic-proton plasma properties has been discussed in detail.[8] Of interest here is the use of the energy analyzer to measure the energetic-proton density and the spatial distribution of the H_2^+ beams. Caution is needed in interpreting the angular scans, since the total energetic neutral flux to the walls consists of dissociation and charge-exchange neutrals from the molecular-ion beam as well as the charge-exchange neutrals from the plasma of main interest. Since the beams are expected to be sharply peaked in angle, almost all the charge-exchange neutrals can be collected either by not analyzing counts at the beam angles during a parallel slit scan or by blocking these angles from the view of the detector during a perpendicular slit scan. Both methods have been used. The charge-exchange neutral spectrum will be contaminated by dissociation neutrals if the molecular-ion beam is taking part in an interaction which scatters some H_2^+ ions from their expected trajectories. Under some conditions the dissociation neutral peak associated with the returning beam has been observed to be anomalously small or wide, indicating that such an interaction is taking place. In the case where most of the injected protons are lost by charge exchange, the effect of the contamination of the spectrum will be small or readily recognized by distinct spectrum changes. However, as discussed below, in the case of large direct particle losses, the energy analysis gives results inconsistent with other measurements.

As discussed above, there are two plasma regimes with gas dissociation, one with a large central peak and small side lobes and the other with large side lobes at a smaller pitch angle and no central peak. While this distinction is apparent at low and moderate pressures, both regimes are similar (large side lobes and no central peak) at pressures above $\sim 5 \times 10^{-6}$ torr. While no large beam spreading at these pressures is evident in the central-peak-dominant regime (Fig. 2.11c), the returning beam peak is much smaller than expected in the side-lobe-dominant regime (Fig. 2.10c). However, the plasma densities calculated from the energy analyzer scans and the foil neutral detector integrals for both regimes agree to within the expected accuracy (Tables 2.1 and 2.2). At moderate pressures ($\sim 10^{-6}$ to $\sim 4 \times 10^{-6}$ torr) the two regimes are distinct, and the two calculations of the energetic-proton density again agree fairly

Table 2.1. Energetic-Proton Density Measurements in the Side-Lobe-Dominant Regime

Ion Gage Pressure (torrs)	Midplane Energetic Proton Density (cm^{-3}) from –	
	Energy Analyzer	Foil Neutral Detector Integral
1.7×10^{-7}	4.38×10^{8}	2.15×10^{7}
2.65×10^{-7}	1.01×10^{9}	2.05×10^{7}
1.1×10^{-6}	2.47×10^{8}	
2.8×10^{-6}	9.4×10^{7}	4.8×10^{7}
6.3×10^{-6}	1.32×10^{8}	8.0×10^{7}
2.1×10^{-5}	1.2×10^{8}	1.0×10^{8}
6.7×10^{-5}	8.2×10^{7}	5.5×10^{7}

Table 2.2. Energetic-Proton Density Measurements in the Central-Peak-Dominant Regime

Ion Gage Pressure (torrs)	Midplane Energetic Proton Density (cm^{-3}) from –	
	Energy Analyzer	Foil Neutral Detector Integral
2.7×10^{-7}	8.58×10^{6}	
3.95×10^{-7}	3.33×10^{6}	
1.35×10^{-6}	4.23×10^{7}	4.55×10^{7}
3.3×10^{-6}	5.97×10^{7}	4.8×10^{7}
5.2×10^{-6}	5.2×10^{7}	3.0×10^{7}
1.0×10^{-5}	4.12×10^{7}	3.15×10^{7}

[7] *Thermonuclear Div. Semiann. Progr. Rept. Oct. 31, 1963,* ORNL-3564, p. 17; and *Thermonuclear Div. Semiann. Progr. Rept. April 30, 1963,* ORNL-3472, p. 12.

[8] *Thermonuclear Div. Semiann. Progr. Repts. Oct. 31, 1965,* ORNL-3908, pp. 19–26; *Apr. 30, 1965,* ORNL-3836, pp. 27–31; *Oct. 31, 1964,* ORNL-3760, pp. 17–22; *Apr. 30, 1964,* ORNL-3652, pp. 31–33; *Oct. 31, 1963,* ORNL-3564, pp. 17–22; and *Apr. 30, 1963,* ORNL-3472, pp. 11–13.

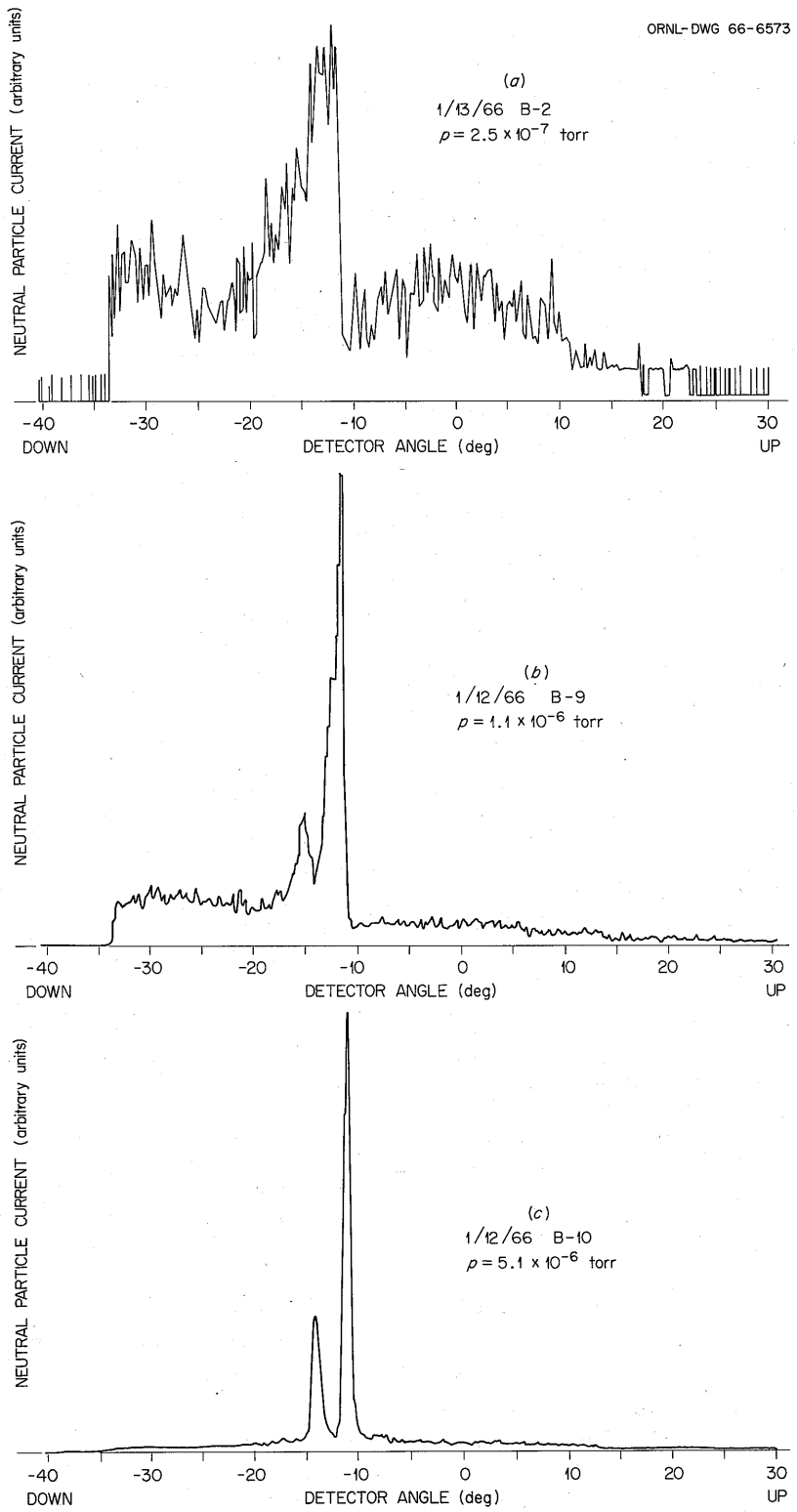

Fig. 2.10. Parallel Slit Scans of the H_2^+ Beam and the Energetic Trapped Plasma Taken 33 cm from the DCX-2 Midplane in the Side-Lobe-Dominant Regime at Pressures of (*a*) 2.5×10^{-7} Torr, (*b*) 1.1×10^{-6} Torr, and (*c*) 5.1×10^{-6} Torr. The peaks at -14.5 and -11.5° are the returning and down-going beams respectively. Large radial spreading of the molecular-ion beam is indicated by the high count rate from -33.5 to -15.5° and the small size of the returning beam peak. The sharp rise at -33.5° is due to an angular cutoff of the detector.

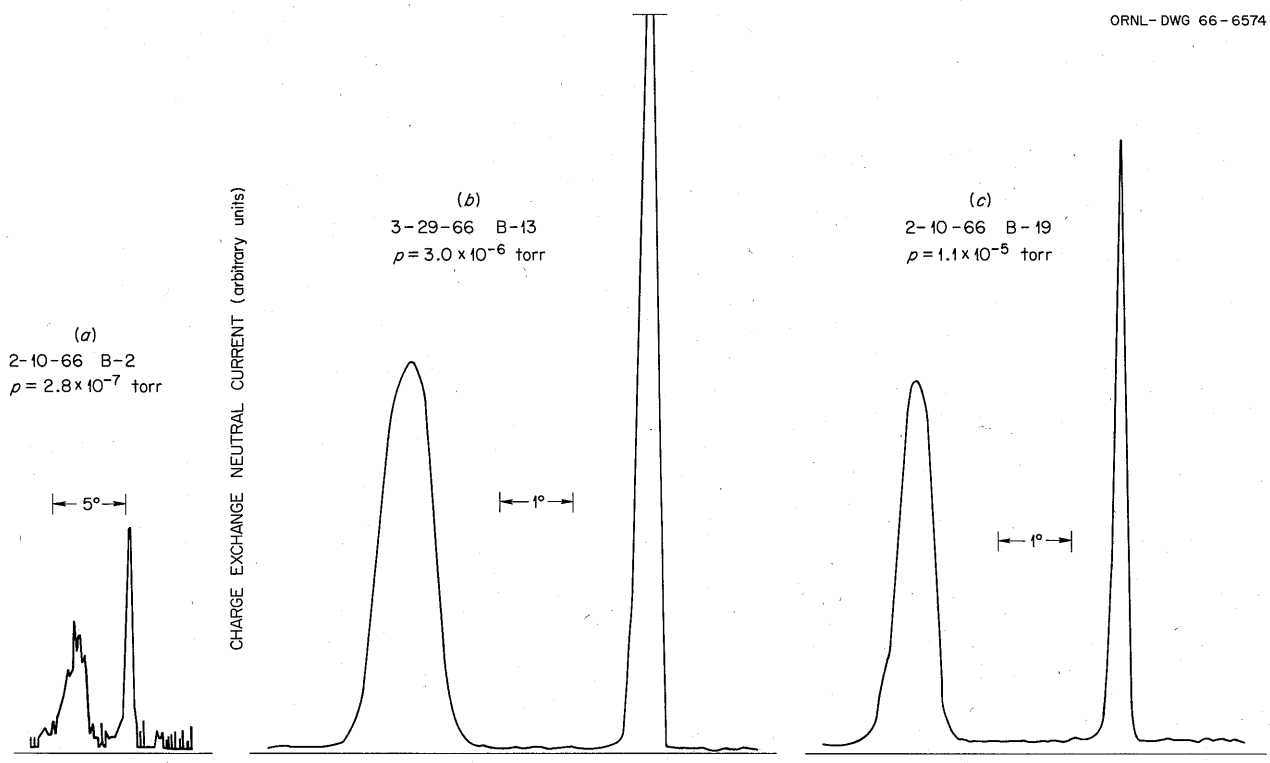

Fig. 2.11. Structure of the Beam Peaks from Parallel Slit Scans Taken 33 cm from the DCX-2 Midplane in the Central-Peak-Dominant Regime at Pressures of (*a*) 2.8×10^{-7} Torr, (*b*) 3.0×10^{-6} Torr, and (*c*) 1.1×10^{-5} Torr. In contrast with Fig. 2.10, the area under the returning beam is actually somewhat larger than that of the down-going beam peak in each scan. The angular spread of the returning beam peak may be due in part to a spread in precession angles experienced by the beam in reflecting from the far mirror.

well. The beam spreading in the side-lobe-dominant regime is now much larger (Fig. 2.10*b*), while the central-peak-dominant regime is unchanged (Fig. 2.11*b*). As reported previously,[9] in this pressure range agreement was obtained when the total current to the energy analyzers was compared with the calculated dissociation current for the plasma lacking the central peak.

For the central-peak-dominant regime at low pressures the densities calculated from the energy analyzer scans are not unreasonable (Table 2.2), and there is little evidence of large beam spreading (Fig. 2.11*a*). However, in this pressure range ($<10^{-6}$ torr) there is considerable beam spreading in the side-lobe-dominant regime (Fig. 2.10*a*). Also, the plasma densities calculated from the energy analyzer scans are 20 to 50 times those obtained from the foil neutral detector integrals, as seen in Table 2.1. Further, upon beam turnoff the current to the foil neutral detector drops by a large factor. These data indicate that at the lowest pressures only $\sim 10^{-2}$ of the initially trapped protons in these side-lobe plasmas are lost by charge exchange; the remainder presumably are lost directly to the injection duct. This large loss of energetic ions and the large spread of the molecular-ion beam may be associated. Nevertheless it appears that in most cases the energy analyzer can be used to determine proton densities consistent with other measurements so long as the charge-exchange density can be determined. However, care must still be taken to recognize contamination of the spectrum by dissociation neutrals when it occurs.

2.5 HYDROGEN-ARC EXPERIMENTS

In order to attempt to raise the density above that obtainable with gas breakup, experiments have been resumed using hydrogen-arc dissociation. The

[9] *Thermonuclear Div. Semiann. Progr. Rept. Oct. 31, 1965*, ORNL-3908, p. 26.

arc operates at approximately 200 V and 100 A in the horizontal midplane approximately 1 in. from the axis on the side opposite the injector, as in the past. At the present time the electrodes are located outside the mirror coils in the flat-field regions under the outboard booster coils. Owing to the limitation in pumping speed with the present version of titanium evaporators, the pressure in the liner region is limited to approximately 6 to 8×10^{-6} torr. The present pressure limitation does not seem to be associated with arc instabilities, since large obstacles inserted to within a few inches of the arc column do not affect the pressure in the liner. The microwave interferometer has been used to estimate the density along a chord which passes 7 in. from the axis and 8 in. from the arc. After the arc is turned off, the interference pattern shows an insignificant change in density along this chord, implying that if instabilities exist they produce only a very small electron density at large radii. The flow through the mirrors is now uninhibited by mechanical obstacles at the ends of the liner region, since the differential pump tubes in the mirror throats (venturis) have been removed.

Only preliminary experiments have been carried out so far. These experiments have surveyed parameter variations to determine optimum production of a large central-peak plasma with arc dissociation. So far, the density has been limited to $\sim 8 \times 10^8$ ions/cm^3, somewhat lower than the 2×10^9 ions/cm^3 that had been obtained in the past. The pitch-angle distribution so far obtained shows much larger side-lobe plasmas than had been seen earlier, although a prominent central peak is always present. From the experiments with gas breakup it is apparent that the large central-peak plasma results from critical adjustment of the injection location in the magnetic field. Detailed experiments are under way with arc dissociation as well to attempt to understand this phenomenon.

Insertion of an obstacle at the position of the far dip in the magnetic field to within $3\frac{1}{2}$ in. of the axis produces essentially no effect on either the trapped density, the energy distribution, or the pitch-angle distribution. Thus, it appears that in these cases all the plasma observed, both central peak and side lobes, is trapped in the central field dip.

Radio-frequency spectra with hydrogen-arc operation show characteristics similar to those at similar pressures using gas dissociation, and, as the pressure is raised slightly, the odd-even alternation of intensities reported in an earlier semiannual[6] reappears. We are above the transition pressure below which, in gas breakup, one finds a reduction of the higher harmonics and a growth of the central-peak plasma. It is not clear, of course, that a similar transition exists in the same pressure regions when the cold plasma from the hydrogen arc is present. It is apparent, however, that the characteristics of the cold plasma enter in a critical way in the relative intensities of the central-peak and side-lobe plasmas, and therefore so do pressure changes. The section which follows indicates our understandable preoccupation with improved diagnostic techniques which should enable us to better determine the cold-plasma properties.

In order to search for a lower-pressure transition which may result in a more prominent central peak, the evaporator design has been changed to evaporate larger amounts of titanium, which should enable us to obtain a significantly higher pumping speed and lower pressure.

2.6 ATTEMPT TO MEASURE COLD-PLASMA DENSITY WITH A MICROWAVE INTERFEROMETER

The cold-plasma density at high gas pressure is large enough to permit microwave interferometer measurement of density at 9 Gc. However, at the more interesting pressures, $\sim 3 \times 10^{-6}$ torr and below, the cold-plasma density is below the threshold for measurement in DCX-2. The source of the difficulty is the comparatively large antenna spacing required (linear diameter 36 in.) and the highly reflecting environment of the copper liner. The power radiated from the entrance horn reflects within the liner, and the signal entering the receiver horn after multiple reflections is not negligible with respect to the direct signal. The multiply reflected signal is easily disturbed by small shifts of probes, etc., anywhere in the liner and by changes in the dilute plasma far from the line-of-sight path.

In early measurements (1962) we reduced the amount of reflected radiation by the use of dielectric lenses spaced 22 in. apart across the plasma. With this arrangement phase shifts as small as 2° (10^9 electrons/cm^3) could be observed, since the

PHOTO 83873

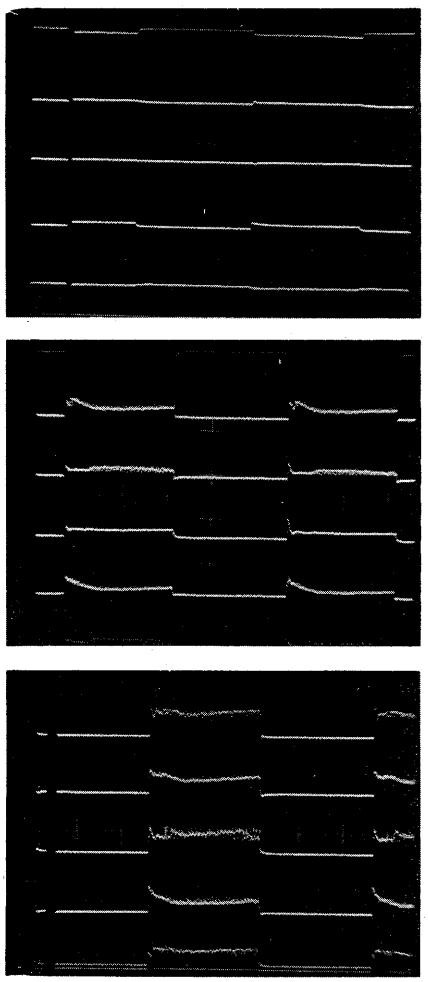

(*a*)
1-13-66
X-1
$P = 5 \times 10^{-6}$

(*b*)
1-13-66
X-4
$P = 2 \times 10^{-5}$

(*c*)
1-13-66
X-6
$P = 6.8 \times 10^{-5}$

Fig. 2.12. Interferometer Traces with the Electron Density Too Low to Be Measured (*a*), Just Above the Minimum Sure Value 2×10^{10} Electrons/cm^3 (*b*), and Well Above This Value (*c*). The horizontal axis is time, with the straight portions being the 1-sec beam-off intervals and the irregular sections the 1-sec beam-on intervals. The vertical axis represents phase shift, and the individual lines mark the successive 180° points. These points are generated by frequency shift of the oscillator and the interference of the signals reaching the detector through paths of quite different length. Since the multiply reflected signal has a longer path length than the direct signal, it passes through more phase shift and causes different effects at each successive 180° point. Thus a small change in the multiply reflected signal may cause oppositely shifted sections (*a*).

multiply reflected signal produced a maximum phase shift of 1 to 2°. Unfortunately, some of the DCX-2 plasma extended beyond 22 in. diameter, and the dielectric lenses were decomposed with a considerable rise of pressure in the tank. When the antennas are retracted to a spacing of ~33 in., the stray signal is increased to such an extent that a phase shift greater than 28° is required to assure that it represents a phase shift along the direct signal path. For a frequency of 9 Gc and an effective plasma path length of ~10 wavelengths, this phase shift corresponds to about 2×10^{10} electrons/cm^3.

The system was operated as a modified "zebra stripe" interferometer,[10] and an example of the patterns obtained below, slightly above, and well above the minimum sure phase shift are shown in Fig. 2.12. A pair of water-cooled horns that can be inserted into the weak outer fringes of the DCX-2 plasma will be prepared to study the cold-plasma density at lower pressures as a check upon the more sensitive but less accurate measurements provided by the gridded probes.

2.7 MEASUREMENTS OF THE COLD PLASMA WITH GRIDDED PROBES

Gridded probe measurements of the cold plasma have been made previously and are discussed in an earlier semiannual report.[11] A grounded first grid is used to prevent disturbance of the plasma by the probe potentials. A second grid is biased strongly positive or negative to repel ions or electrons while the collector plate obtains a repulsion curve of the remaining species as it is swept through a range of voltage.

The axial energy of the cold ions escaping from the plasma gives clear evidence of a cold-plasma body with a relatively constant internal potential joined axially with an external or streaming region which has a considerable drop of space potential under some conditions. Figure 2.13*a* is an example of a repulsion curve for ions from a gas breakup plasma at a pressure of 3×10^{-6} torr measured 20 to 30 cm axially beyond the hot-ion plasma and at a radius of 15 cm. The hot-ion plasma was exhibiting side lobes but no central peak under

[10] DCX-2 Technical Memorandum No. 121.

[11] *Thermonuclear Div. Semiann. Progr. Rept. Apr. 30, 1963*, ORNL-3472, p. 13.

PHOTO 83874

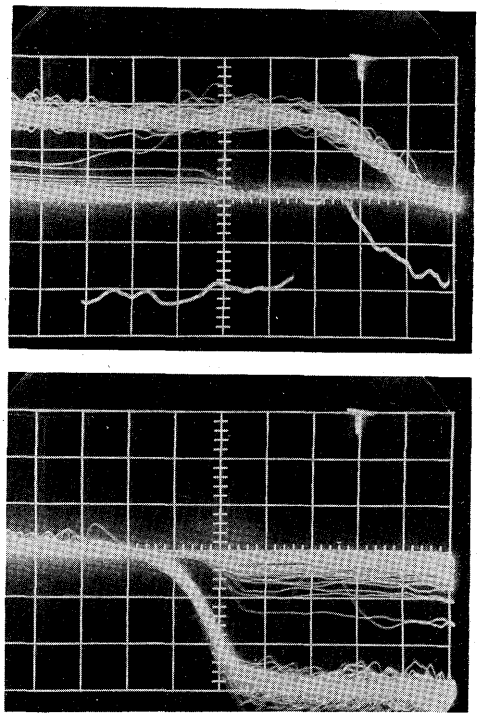

(*a*)
5-9-66
P-4

(*b*)
5-9-66
P-5

Fig. 2.13. Retarding Potential Curves for the Ions (*a*) and the Electrons (*b*) of the Cold Plasma of DCX-2 with Gas Dissociation. In *a* the second grid was biased to −850 V to prevent passage of the electrons; in *b* it was biased to +850 V to stop the ions. The horizontal scales are 170 V/division, the vertical 0.02 mA/division. The center of the graticule represents zero volts, zero current. The separated traces lying near the axis on the left side for *a* and the right side for *b* are the traces produced while the plasma decays after beam cutoff. A rough time scale can be established since the horizontal sweep is a sine wave at 60 cycles. The irregular trace at the bottom of *a* is to be ignored since it was produced by a gated step at one of the beam-off times.

these conditions. The measurement was made with a plane-faced gridded probe. The break shows a plasma potential of 400 V, and the falloff, an ion axial temperature of 170 eV. The corresponding electron curve is shown in Fig. 2.13*b*. The portion of the electron stream exceeding the plasma potential (hence reaching the probe) exhibits an axial temperature of about 107 eV. A check on the performance of the probe can be made by comparing the expected ion current with the electron current. These two currents should be equal if the temperatures and the plasma potential have been determined correctly. The ion and electron currents are, respectively,

$$i_i = n_i \left\langle v_i \right\rangle A$$

and

$$i_e = \left\langle v_e \right\rangle A\, e^{-eE_p/kT_e} ,$$

where $\langle v \rangle$ is the mean velocity, n is the particle density, A is the probe area, and T is the particle temperature.

The ratio of these currents is

$$\frac{i_e}{i_i} = \frac{n_e \left\langle v_e \right\rangle e^{-eE_p/kT_e}}{n_i \left\langle v_i \right\rangle}$$

$$= \sqrt{\frac{m_i}{m_e}} \sqrt{\frac{T_e}{T_i}}\, e^{-eE_p/kT_e} ,$$

assuming charge neutrality. Taking the observed temperatures and plasma potential, $i_e/i_i = 0.82$, in reasonable agreement with the expected value.

The curves of Fig. 2.13 show that the plasma potential diminishes to less than 20 to 30 V and the electron and cold-ion temperatures become quite low a few milliseconds after the injection beam is turned off. The density of the streaming plasma while injecting is about 1×10^7 ions/cm^3, and the density of cold ions inside the main plasma is about 8×10^7 ions/cm^3 for this particular example. The cold-plasma density thus seems to be about equal to or slightly less than that of the hot plasma. At higher gas pressures the cold-ion density increases and may become considerably higher than the hot-ion density.

Measurements with gridded probes are subject to the following errors: (1) uncertainty in grid transmission, (2) shifts in the apparent position of zero collector voltage due to plasma penetration of the grids, (3) slope shifts in the zero-current base line due to slow-ion trapping near the inner grid while measuring ions or of slow electrons while measuring electrons, (4) secondary electrons emitted from grids and collector, and (5) photoelectrons emitted from grids and collector. These errors are partly compensated by auxiliary measurements and

would not seem to be large. Nevertheless, because of inconsistencies with microwave measurements at higher densities, we do not trust the gridded probe results to better than a factor of 2 or 3.

It is generally noted that the saturation ion current and electron currents to the probe are not exactly equal. This difference could be due to attenuation of the ions whose Larmor orbits are much larger than a grid of mesh of the probe grids or to components of the ion and electron motion perpendicular to the field lines, which could cause interference by the supporting frame of the grids.

A probe having four sets of 100-mesh plane grids and four collectors was placed in the streaming plasma of DCX-2. One grid faced in the axial direction, one in the radial direction toward the axis, and the remaining two in the direction of ion rotation and its opposite. The response on all collectors except the axial one was quite small at low pressure and high plasma potential, but at higher gas pressures in the machine the cold plasma is considerably denser, the plasma potential is low, and some ion currents are found on all the collectors. Figure 2.14 shows the ion-repulsion curves observed. No electron components were found except on the axial collector. The component of ions streaming around the magnetic axis in the direction opposite to that of normal precession during mirror reflection is the only important extra

PHOTO 83973

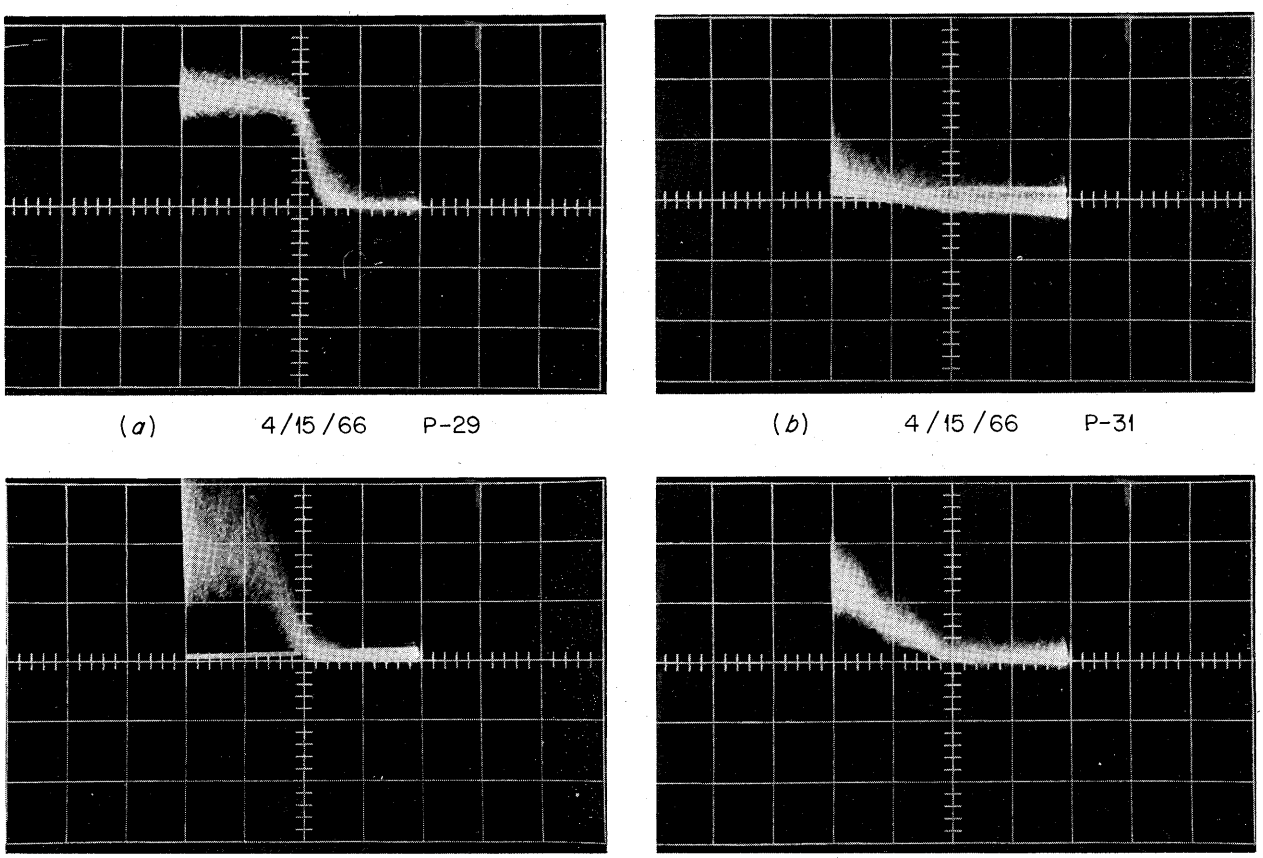

Fig. 2.14. Ion-Repulsion Curves Seen on the Four Collectors of the Four-Faced Probe. The horizontal scale on all traces is 100 V/cm. *a* is the axial facing probe, vertical scale 0.25 mA/division; *b* is the radially inward facing probe, scale 0.0125 mA/division; c is the probe facing in the direction of normal ion precession, scale 0.05 mA/division; and *d* is the probe facing in the direction opposite to the direction of normal ion precession, scale 0.0125 mA/division.

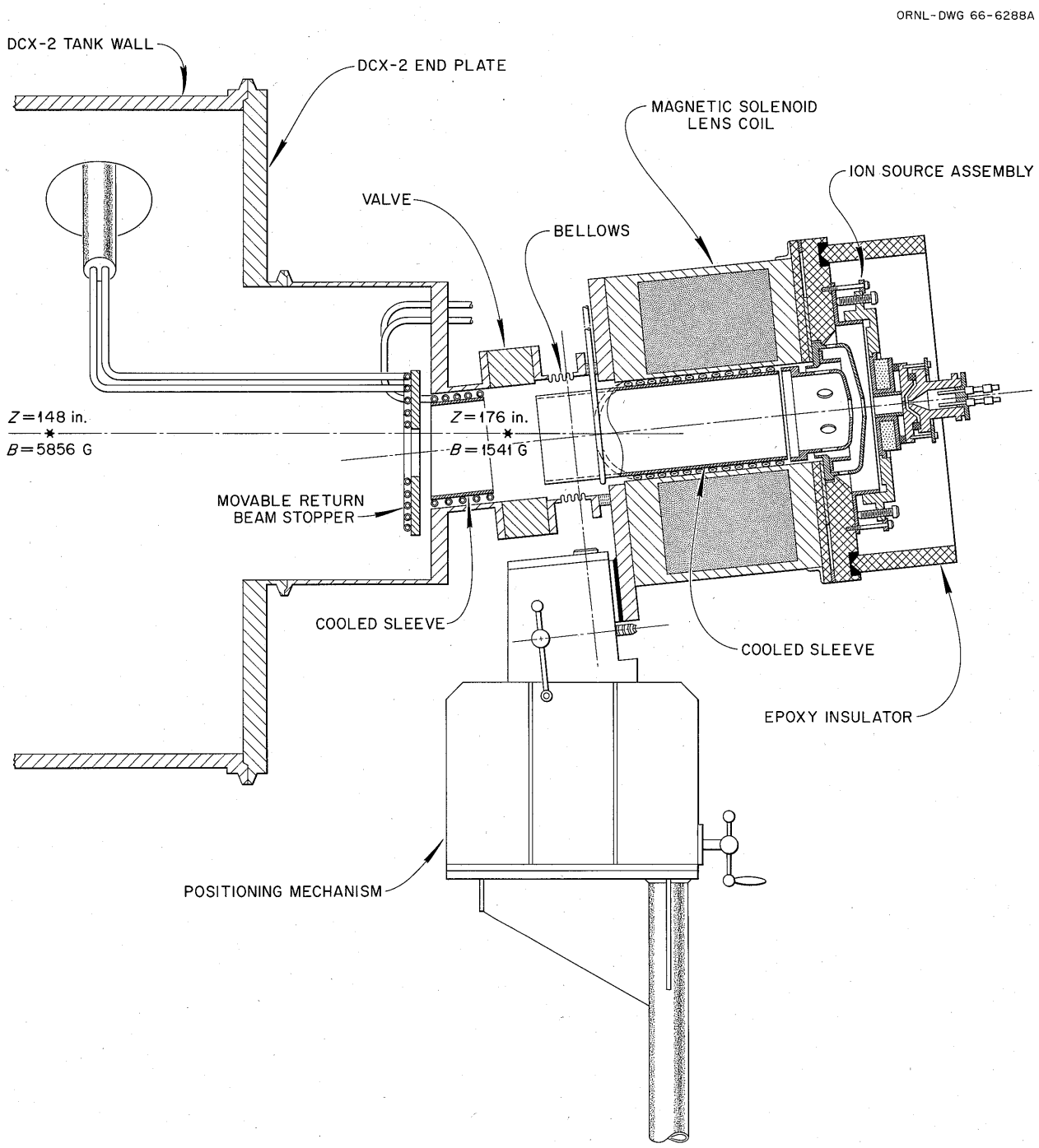

Fig. 2.15. Diagram of 100-keV Axial Beam Injector. The z distances shown are measured from the DCX-2 midplane.

component, and it constitutes less than 20% of the axial component. Since the difference in ion and electron components is usually a factor of 2, the principal cause must be the attenuation of ions by the grids.

2.8 END-INJECTION EXPERIMENTS

The interaction which builds the central-peak plasma may provide a means of trapping an injected proton beam. Protons produced outside one of the mirrors and directed in such a way that they just get through the mirror may lose enough axial energy in the central plasma region to be reflected and trapped. This beam of particles can be expected to interact with the background plasma to produce plasma waves parallel to the field at frequencies $\omega = \omega_{pe}\ (k_{\|}/k)$ and waves transverse to the field at the Doppler-shifted ion cyclotron frequency. Even in the absence of effects produced by the beam itself, its particles will be acted on by the strong rf fields produced when the usual 540-keV beam is injected.

An ion source and an acceleration system have been installed on one end plate of DCX-2 to test this method of injection (see Fig. 2.15). The injection angle can be varied in the horizontal and vertical planes about a value chosen on the basis of trajectory calculations. The calculations were used only as a rough guide in the design, however, since the effect of space charge and the presence of a large magnetic yoke in the beam focusing system were not taken into account in the calculation. According to these calculations a ray which passed through the first mirror at an angle of 6.5° with respect to the perpendicular would just be reflected at the second mirror by a 3% increase in field strength.

The initial experiments show an unexpectedly slow variation of transmission through the first mirror with injection angle. At the same time it was not possible with a 3% increase in the strength of the other mirror to reflect a significant number of particles from that mirror. Currents of more than 200 mA at 100 keV have been injected, and 92 mA was measured calorimetrically at the far end of the machine with 160 mA injected. Between 5 and 10% of this current cannot be accounted for at the ends, and some current may be trapped. The discrepancy may be in measurement, however, and in some cases at high background pressure the loss can plausibly be attributed to charge exchange. There is, however, no response from the energy analyzers or foil neutral detectors. When this beam only is present, there is weak radiation in a broad band of frequencies centered at about 50 Mc with occasional other bands at 100 and 150 Mc. Many weak peaks also are seen in the frequency range from 7 to 30 Mc. None of these peaks can positively be identified with the proton gyrofrequency or its harmonics. Initial experiments involving both the end injector and the usual 540-keV injector are inconclusive, because of the effect of uncontrolled pressure variations. Further tests with greater asymmetry in the magnetic mirror field are planned.

3. Electron-Cyclotron Heating

3.1 INJECTION OF NEUTRALS AND TRAPPING ON AN ELECTRON RESONANT ENVIRONMENTAL MEDIUM (INTEREM)

W. B Ard
M. C. Becker[1]
R. A. Dandl[1]
H. O. Eason
A. C. England
G. M. Haas
H. C. Hoy
R. L. Knight
N. H. Lazar
R. L. Livesey
O. D. Matlock
M. W. McGuffin

3.1.1 Introduction

The injected neutral-beam current has been recalibrated, and it has been found that only a maximum of 12 mA equivalent has been injected rather than the previously reported 60 mA.

The energy spectrum of the protons in INTEREM, which are trapped by gas and by the electron-cyclotron plasma (ECP), has been measured. No energy spreading has been observed.

A device to measure the transverse (Z axis) distribution of the trapped protons has been constructed. A very slight amount of spreading occurs in the presence of the ECP, but this may be due to normal scattering processes rather than an instability.

The previously observed contamination has reappeared since the cavity was cleaned. Spectral studies have shown that carbon is the main contaminant. The carbon is apparently coming from the 20-keV beam drift tube vacuum system.

3.1.2 Neutral-Beam Injection Studies

The 20-keV energetic neutral beam, described previously,[2–5] has been used for proton trapping studies in the ECP in the INTEREM facility. An error was found in the calorimetric calibration, and the previously reported[5] beam current of 60 mA equivalent is in error. Presently, a maximum of 12 mA equivalent of neutral beam has been measured on the target in the INTEREM facility.

Energy Spectra. – Recent developments[6] have made it possible to measure the energy spectra of low-energy particles with good resolution. A low-energy spectrometer was constructed to determine the spectra of the emerging charge-exchange neutrals from the ECP. To make it possible to count and analyze single particles, the spectrometer had to be moved a considerable distance from the machine. A 6-in.-diam, 19-ft-long evacuated tube was added to the south side of the INTEREM facility. The spectrometer was mounted at the end of this tube with an adjustable slit immediately preceding it.

To further reduce the counting rate in this detector, a baffle was added in the tube about 10 ft from the spectrometer. Small (0.030- to 0.050-in.-diam) holes were located in the baffle so as to view selected regions of the plasma volume. Together with another set of apertures on the cavity wall (for microwave containment) and a detent plate which could be used to select one set of apertures at a time, selected regions of the plasma could be sampled. A lead shutter arrangement was also added to the tube to reduce the x-ray flux in the detector.

The spectrometer consists of a liquid-nitrogen-cooled silicon barrier detector and an associated

---

[1] Instrumentation and Controls Division.

[2] *Thermonuclear Div. Semiann. Progr. Rept. Apr. 30, 1964*, ORNL-3652, sect. 3.1.

[3] *Thermonuclear Div. Semiann. Progr. Rept. Oct. 31, 1964*, ORNL-3760, sect. 3.1.

[4] *Thermonuclear Div. Semiann. Progr. Rept. Apr. 30, 1965*, ORNL-3836, sect. 3.1.

[5] *Thermonuclear Div. Semiann. Progr. Rept. Oct. 31, 1965*, ORNL-3908, sect. 3.1.

[6] See, for example, *Thermonuclear Div. Semiann. Progr. Rept. Oct. 31, 1965*, ORNL-3908, sect. 5.4.

field-effect transistor (FET) input preamplifier. The detector and FET preamplifier are located together in the vacuum on a liquid-nitrogen-cooled mount. Further amplification takes place in a chassis immediately outside the vacuum chamber. The signal is then taken to a Tennelec TC 200 amplifier, and then to a pulse-height analyzer.

Figure 3.1 shows a spectrum taken with hydrogen gas trapping at a central gage pressure of 3×10^{-6} torr. The horizontal scale is the energy scale. The zero is depressed in the figure. Normally, H_2^+ is accelerated to 40 keV and subsequently dissociated into two 20-keV neutrals. A small fraction of 40-keV protons are also accelerated, converted to neutrals in the drift tube, and trapped by the ECP. They charge exchange and emerge as 40-keV neutrals and are seen by the spectrometer. Similarly, some H_3^+ is accelerated to 40 keV. Some of the H_3^+ may be dissociated into 13-keV H^0, which is subsequently trapped by the ECP. Hence, 13-keV charge-exchange neutrals are also seen by the spectrometer.

From the figure it is seen that the number of 40-keV neutrals detected is approximately 1.5% of the number of 20-keV neutrals. Similarly, the number of 13-keV neutrals is approximately 10% of the 20-keV neutrals. The resolution full width at half maximum (FWHM) of the detector for 20- and 40-keV neutrals is less than 3 keV.

Figure 3.2 shows a spectrum taken under the same conditions as the previous picture, but with the ECP present and 30 kW of microwave power being fed into the cavity. The resolution of the peaks remains unchanged. Also, the relative ratios of 13-keV neutrals, 20-keV neutrals, and 40-keV neutrals are not markedly changed. The total number of particles detected during the 1-min count has increased, indicating that increased trapping has occurred. Some additional counts are also observed at higher energies, indicating the presence of x rays in this energy range. The important point is that no energy spread or shift is evident.

The two figures are for the spectrometer viewing the axis. The spectrometer can also view a region

PHOTO 83974

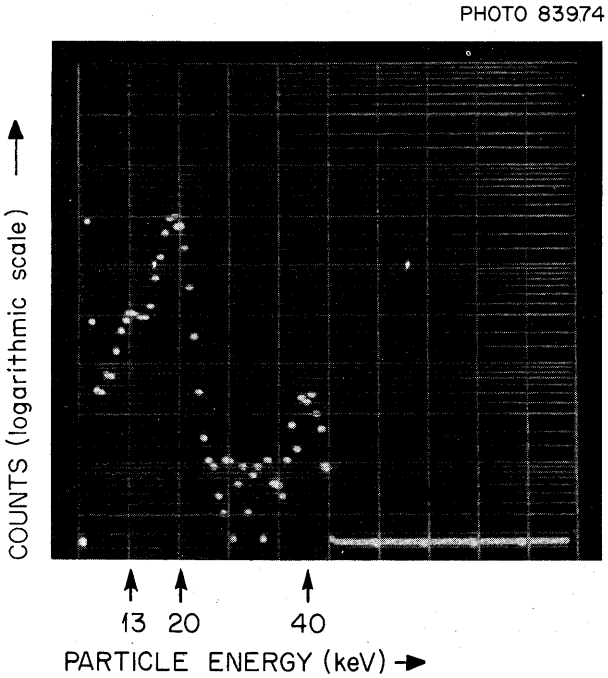

Fig. 3.1. Spectrum Taken with Hydrogen Gas Trapping. Three particle groups are seen: 13, 20, and 40 keV. The resolution is less than 3 keV FWHM. This spectrum is for the collimator aimed at the axis of the machine.

PHOTO 83975

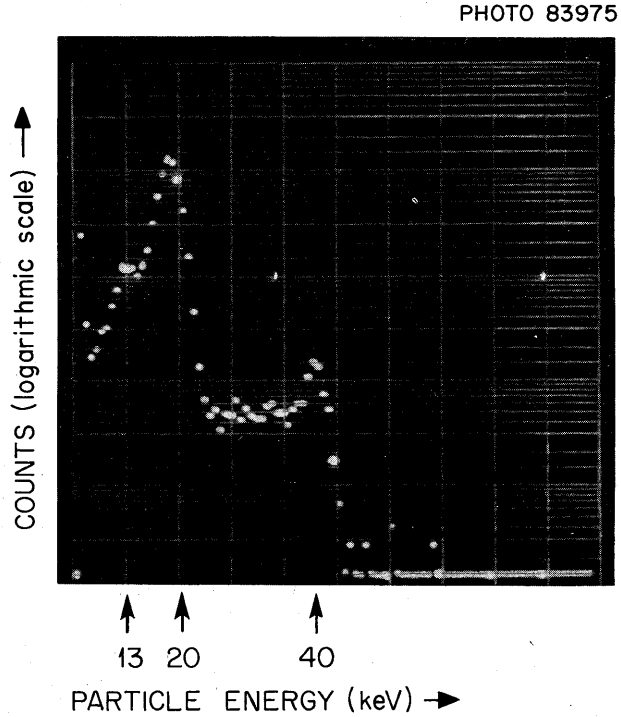

Fig. 3.2. Spectrum Taken with Trapping on an ECP (30-kW Microwave Power). The same three particle groups are detected with no observable energy spread, that is, the resolution is unchanged. The collimator is aimed at the axis of the machine.

1.5 in. above the axis, 3 in. above the axis (approximately an equilibrium orbit for 20-keV protons), and 1.5 in. east of the midplane on the axis. In all cases, the same conclusion holds except that the ratios of the peak amplitude of the three proton groups vary slightly due to the orbit size effects.

An absolute density measurement can also be made from these spectra. Since the solid angle and plasma volume are well defined by the slits, the number of particles detected by the spectrometer in a given time can be used to calculate the density in the machine. The main uncertainty is the chord length of the plasma. The calculation gives a trapped density in the presence of the ECP of $\sim 2 \times 10^7$ protons/cm^3 when the injected beam is ~ 8 mA. With gas trapping the density is about an order of magnitude lower.

3.1.3 Transverse Scans of the Trapped Proton Population

For the purpose of measuring the transverse position of the trapped protons, a movable detector was added to the top of the INTEREM facility. In order to reduce the radiation damage to the silicon barrier detector, it was mounted at the end of a 4-ft-long tube. The detector was mounted in a lead shield at the end of a long collimator. The collimator was aimed at the axis. Motion parallel to the axis of the machine was accomplished by means of sliding vacuum seals and a motor-driven linear actuator. The detector was used as a current measuring device similar to those used previously and was not capable of energy measurement. An improved (FET input) version of the previously used dc current amplifiers was used to amplify the detector output current.

Figure 3.3 shows a transverse scan made with the beam injected into the facility and trapped on hydrogen gas only (no microwave power). It is somewhat surprising that the distribution is so narrow. The beam enters the facility through a limiting aperture of 2 in. diameter located about 4 ft from the axis. Since the beam has some distance to go and can spread during its travel, it could have a transverse width of more than 2 in. (5 cm) before arriving at the axis. The collimator views a narrow region near the axis. The scan shows a narrow peaked distribution about 0.9- to 1-cm wide (full width at half maximum or FWHM) located on the midplane and a wider "talus slope" distribution with an FWHM of about 2.5 to 3 cm.

PHOTO 83976

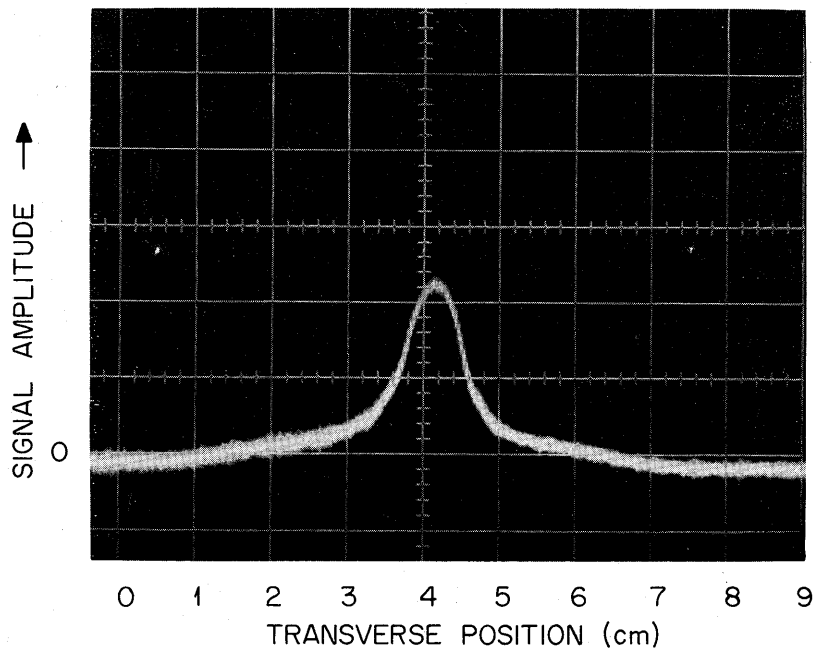

Fig. 3.3. Transverse Scan with Proton Trapping on Gas Alone (No ECP). Horizontal scale: 1 large division = 1 cm travel. The peak is on the midplane. Transverse resolution is 0.4 cm.

The measurable signal extends to no more than 5 to 6 cm along the axis, which is the size of the limiting beam aperture.

Figure 3.4 shows a transverse scan made with the beam trapped on the ECP. The measured FWHM of the peak is again 0.9 to 1 cm and the talus slope is similarly unchanged, although the beam amplitude changes with pressure and power. There is a very slight increase in the FWHM as the gas pressure is reduced, both with and without the ECP present. However, this broadening is so slight that it may be attributable to multiple scattering effects because of the increased lifetime of the trapped particles.

The proton charge-exchange decay time after beam turnoff was investigated as a function of the transverse position of the detector. No observable change was seen in the decay time regardless of the detector position.

Unfortunately, only rarely were the long tails seen on the decays in the presence of the ECP. These had been previously observed usually at higher microwave power levels than could now be obtained. Normally, the tail had an e-folding time about an order of magnitude larger than the fast component. The microwave power level capability has not increased as had been expected.

3.1.4 Vacuum Conditions

At the end of the last semiannual report period, the microwave cavity was disassembled and cleaned. This was found necessary for reasons mentioned in the last semiannual report: pump oil "varnish" had coated the interior of the microwave cavity and had produced excessive outgassing when bombarded with plasma during operation with the ECP. During operation the gage pressure would not drop below about 2×10^{-6} torr, and the light from the ECP acquired a blue-white color rather than the characteristic blue-pink hydrogen color.

After cleaning and reassembly, the facility operated satisfactorily for a period before this condition reappeared. Low-vapor-pressure Dow-Corning 705 diffusion pump oil was being used in the main pumps to prevent oil migration to the cavity walls. The base pressure was 5×10^{-8} torr, lower than it had been prior to cleaning.

PHOTO 83977

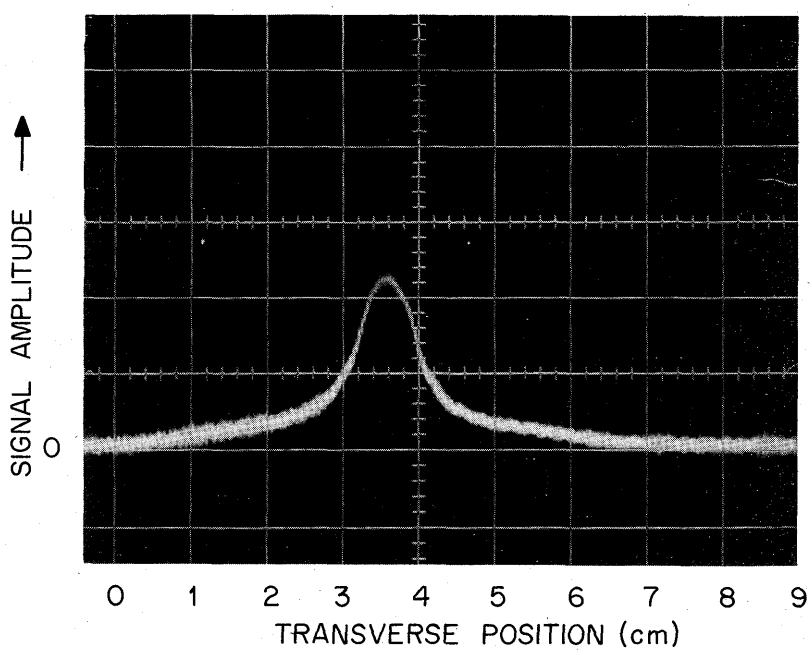

Fig. 3.4. Transverse Scan with Proton Trapping on ECP with 30-kW Microwave Power. Horizontal scale: 1 large division = 1 cm travel. The peak is on the midplane. Transverse resolution is 0.4 cm. The apparent shift in position of the peak compared to Fig. 3.3 is not real.

Spectroscopic studies showed that the outgassing condition which reappeared was not due to this diffusion pump oil since no silicon lines were found. Dow-Corning 705 pump fluid is a complex organic compound containing silicon, an element fairly easy to observe spectroscopically. Only carbon lines, copper lines, and hydrogen lines were prominent in the spectra.

It appeared that the oil causing the difficulty was streaming down the 20-keV beam drift tube into the central section of the cavity. A black oily deposit has always appeared on the beam target after even a short operating time with the beam. The above-mentioned spectroscopic studies and some additional studies with other gas feeds are discussed in more detail in Sect. 3.1.5.

3.1.5 Spectral Studies in INTEREM

J. R. McNally, Jr. A. C. England
R. A. Dandl M. W. McGuffin

We present two very preliminary spectral intensity curves as a function of microwave power in the INTEREM facility (see Figs. 3.5 and 3.6). No attempt has been made to interpret the information; however, it is possible that He^0 does not penetrate the high-power plasmas (no Franck-Condon neutrals are involved as in D_2 support gas), although self-absorption effects might cause some saturation since λ 3888 Å involves the ^3S metastable level of He^0. The presence of doubly (N^{2+}, Ar^{2+}, C^{2+}) and trebly (N^{3+}) ionized species has been recognized for the first time in an ECP. Further studies appear warranted to investigate more carefully the importance of various feed materials for features favorable to an environmental plasma containing ultrahot electrons.

Neutral copper and Cu^+ are also observed, but it is not known as yet whether these are peripheral or volume effects.

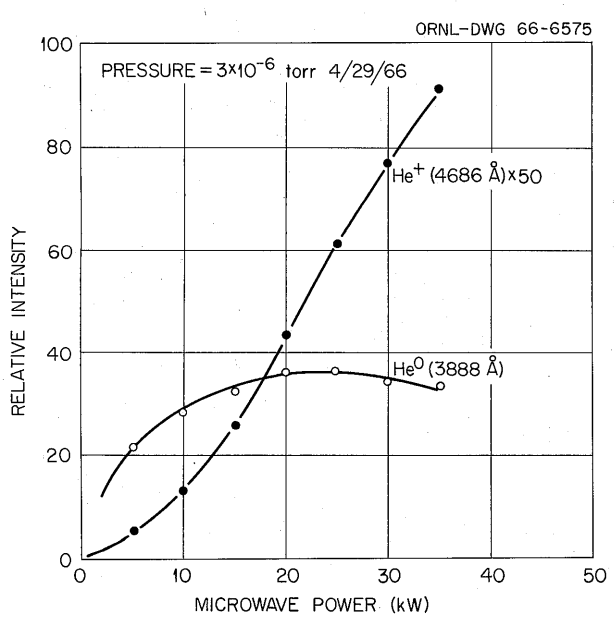

Fig. 3.5. Spectral Emission from Helium-Fed Plasma in INTEREM Facility vs Microwave Power.

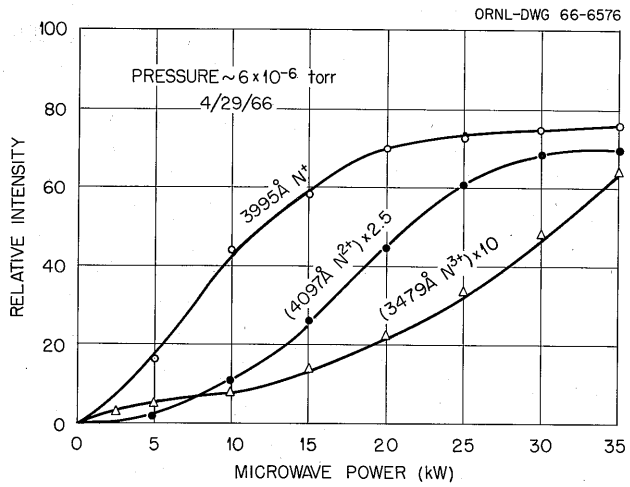

Fig. 3.6. Spectral Emission from Nitrogen-Fed Plasma in INTEREM Facility vs Microwave Power. N_2^0, N_2^+, N^0 not monitored in this series.

3.2 ELECTRON-CYCLOTRON HEATING EXPERIMENTS IN THE ELMO FACILITY

W. B. Ard A. C. England
M. C. Becker[1] G. M. Haas
R. A. Dandl[1] R. L. Livesey
H. O. Eason M. W. McGuffin

During this semiannual period the 8-mm ECP was formed in a 3.6-liter cavity constructed mostly of thin stainless steel so as to permit the faster observation of diamagnetic perturbations in the plasma. The major emphasis was an investigation which attempted to measure the density, temperature, and containment time of the warm electron component (50 to 5000 eV) responsible for ionizing

the neutral background gas. During plasma relaxation after interruption of the microwave power, this population stops pumping and disappears in the first $\frac{1}{4}$ msec, and this was the period of plasma lifetime examined.

The schematic diagram of the measuring apparatus is shown in Fig. 3.7. The loops $L3$ and $L4$ are connected series-adding, then to a summing amplifier connected also to loops $L1$ and $L2$, filtered and phased so as to minimize spurious signals from the motor generator supplying magnetic field current. The dominant frequencies removed by the filter are the commutator and shaft wobble frequencies. A pulser connected to a test loop inside the cavity was used to calibrate the flux sensitivity and measure the overall time response of the system. The 10 to 90% response time is 50 μsec and the sensitivity is 20 Mx/msec above the systematic noise on the dc channel. The dc channel was also differentiated and amplified (E_0 fast) so as to permit observation of microsecond-duration diamagnetic events associated with instabilities.

The slow plasma current probe, also shown in Fig. 3.7, was arranged to permit a radial scan of the slow plasma electron current leaving the magnetic mirror. This current profile is related to the radial distribution of the hot electrons which ionize the neutral gas influx.

Figure 3.8 shows a decay trace (after microwave power turnoff) taken with the above-mentioned diamagnetic arrangement. The middle trace is the diamagnetic signal with the positive direction corresponding to the rate of decrease of total energy in the plasma. (The upper trace is the same signal on a slower time scale.) The first excursion on the middle trace results from the mirror scatter loss combined with the neutral gas ionization cooling of those warm electrons that do most of the ionization of the neutral back-

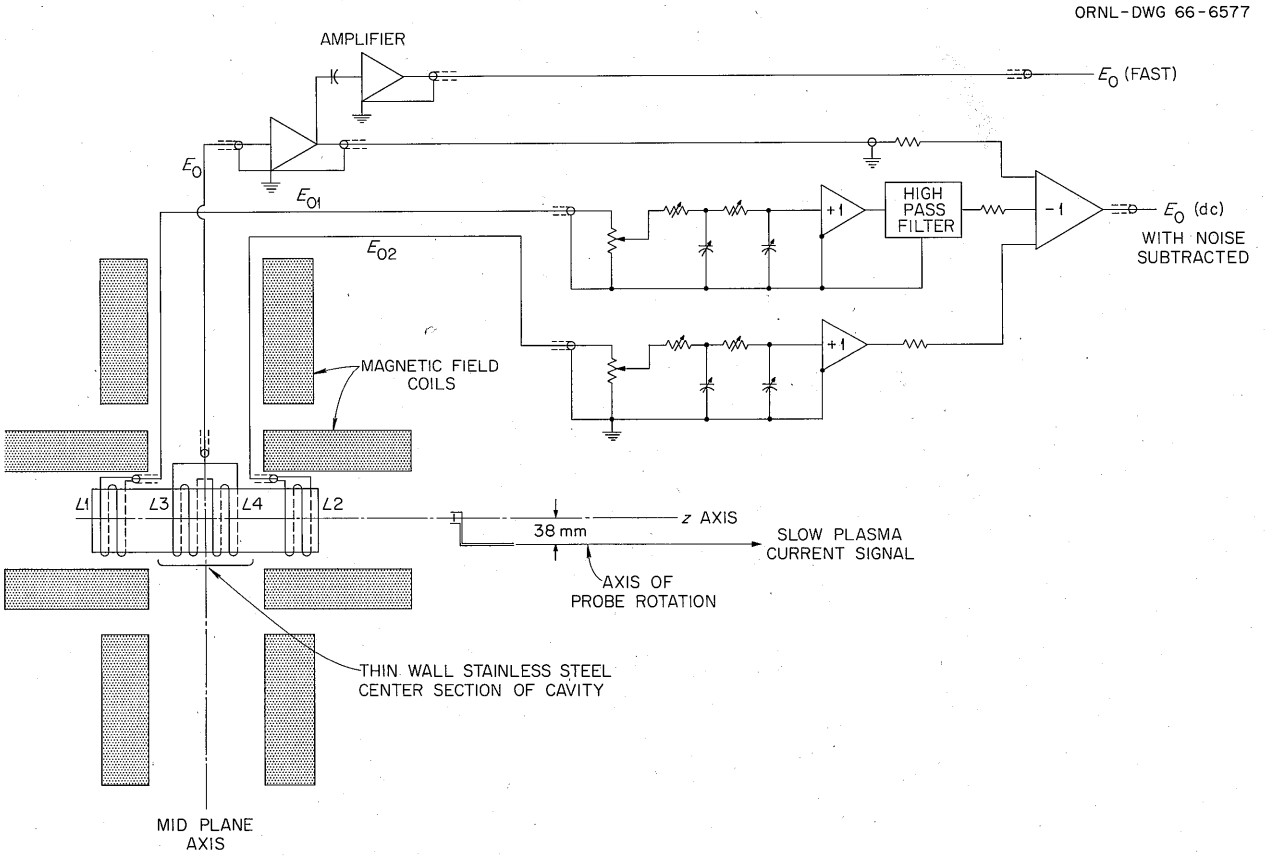

Fig. 3.7. Schematic Diagram of the ELMO Facility, Including the Diamagnetic and Plasma Current Measuring Apparatus.

PHOTO 83978

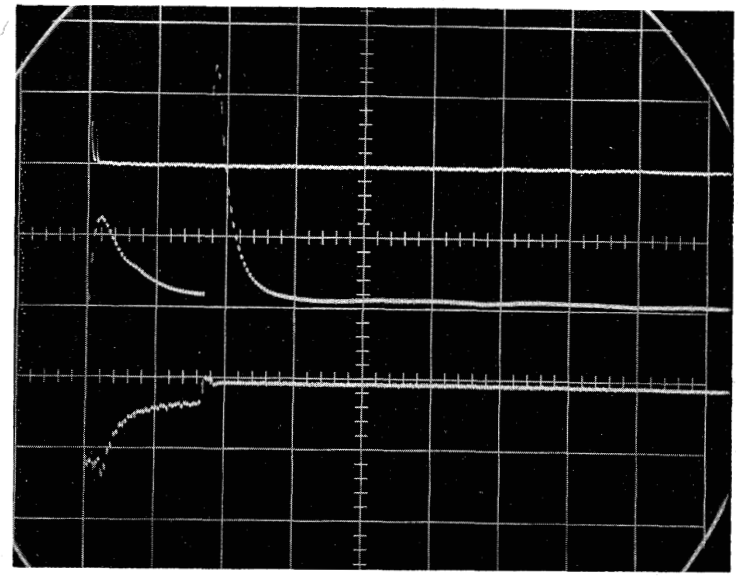

DIAMAGNETIC SIGNAL
5 msec/cm

DIAMAGNETIC SIGNAL
200 μsec/cm

END CURRENT PROBE
200 μsec/cm

END CURRENT PROBE ON AXIS, 1850 W MICROWAVE POWER BEFORE TURNOFF

Fig. 3.8. Decay of the Diamagnetic Signal and the Slow Plasma Current Signal After Power Turnoff. Note that the top and middle traces are the same signal but at different sweep speeds. This figure shows two diamagnetic events, one of which is an instability.

ground gas. The area under this pulse is a measure of the total energy of this group of electrons. The second diamagnetic event on the middle trace is due to an instability in a less dense, but higher temperature electron group.

The calculation of total energy density in the warm electron group from the total measured flux depends, of course, on the plasma size, but especially on the plasma radius when using a solenoidal approximation. The radial profile of axial slow plasma current was used to measure the warm electron plasma radius. The lower trace in Fig. 3.8 shows the decay of this current with relaxation of the warm electron plasma. The probe was positioned at $r = 0$ for this trace. The initial cold plasma current increase arises from the increase in neutral gas flux to the center of the plasma shortly after turnoff. This flux increase is due partly to the cessation of pumping of the promptly lost peripheral cold plasma (resulting in a gross pressure rise), and it is due also to a reduction in neutral shielding of the center by the more promptly lost surface of the warm electron plasma. Notice that those electrons lost in the instability (second excursion of middle trace) do not appreciably change the cold plasma current. Note also that considerably more energy is involved in this group than in the cooler group, so one can infer that those electrons lost in the instability were much hotter and less dense.

Figure 3.9 is a similar photograph except the radial position of the current probe is at $r = 2.5$ cm. One quite common occurrence illustrated on the middle trace is a third diamagnetic excursion caused by a second instability after turnoff.

Some critical features of this figure are: the prompt decay of the cold plasma current (because it is sampling the periphery of the warm electron plasma) and the appearance of flute frequencies ($\simeq$100 kc) on the current probe signal just before the hot electrons are lost (second diamagnetic excursion).

Since in this plasma stabilization against flutes is most probably due to cold plasma coupling of the hot plasma to metallic end walls, the loss of the cold plasma source (i.e., the warm, efficiently ionizing electrons) after the first 150 μsec causes the remaining hot electrons to go flute-unstable and hit the walls. Their loss results in a change

PHOTO 83979

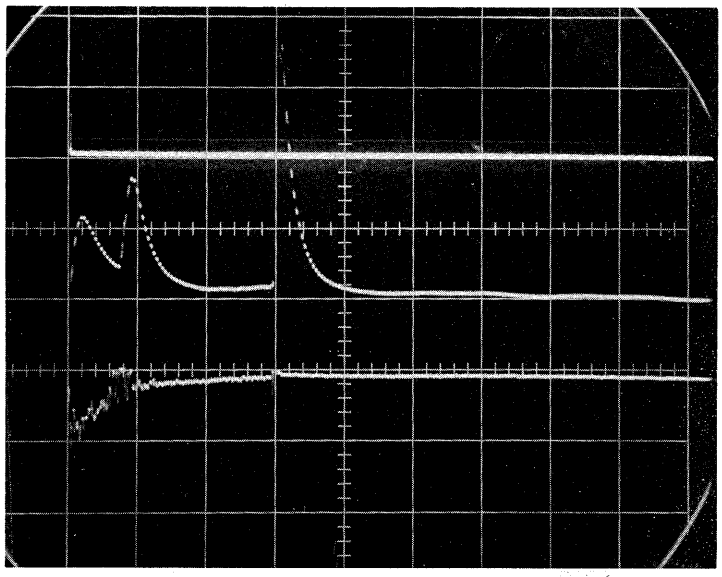

DIAMAGNETIC SIGNAL
100 msec/cm

DIAMAGNETIC SIGNAL
200 μ sec/cm

END CURRENT PROBE
200 μ sec/cm

END CURRENT PROBE OFF AXIS, 1800 W MICROWAVE POWER BEFORE TURNOFF

Fig. 3.9. Decay of the Diamagnetic Signal and the Slow Plasma Current Signal After Power Turnoff. Again, note that the top and middle traces are the same signal but at different sweep speeds. This figure shows three diamagnetic events, two of which are instabilities.

of total energy measured by the area under the second diamagnetic excursion (the first instability).

Faster sweeps show typical flute frequencies of 100 kc on the plasma current, which for fundamental modes (e.g., $m = 1$) and a 1% radial field gradient give a temperature of 7.5 keV for those electrons in the first instability. Observation of the current probe signal on a fast sweep has shown that the second instability (third diamagnetic pulse) is also flutelike. It should also be mentioned in support of the flute model that much higher frequencies with little manifestation of energy loss sometimes precede the lower frequencies resulting in the full-blown flute. Longer time diamagnetic signals show (on stable turnoff) still another more energetic group of electrons of lower density.

In Fig. 3.10 we have plotted the radial profile of the cold-plasma current, referred to the radius in the midplane of the magnetic mirror. In view of the time-decay behavior of this current at different radii, one can argue that the center of this plasma must be highly ionized. This consideration requires the density profile to be narrower than the current profile of Fig. 3.10 in order to overcompensate the reduction in neutral pressure on the axis and still exhibit a peak radial current distribution.

The peak energy density has been calculated with an estimated density profile in lieu of a more exact computer calculation. This number is 3 to 5×10^{15} eV/cm^3 in the warm electron group.

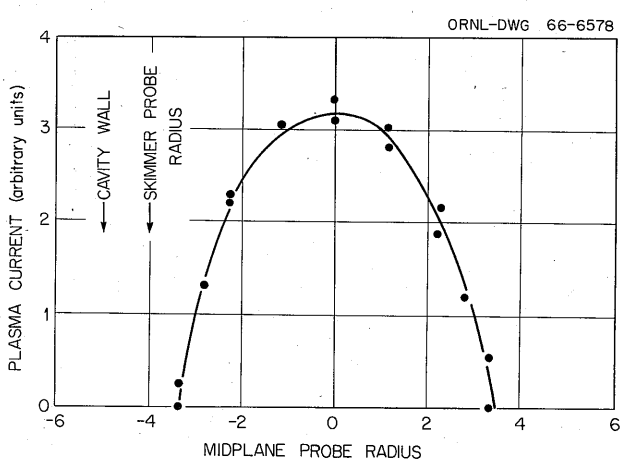

Fig. 3.10. Radial Profile of the Slow Plasma Current Referred to the Radius in the Midplane of the Magnetic Mirror.

Measurements of temperature by analysis of soft bremsstrahlung spectra (e.g., photon energy >5 keV) employed the silicon barrier layer detector and preamplifier system used in the INTEREM proton spectrometer experiment described in Sect. 3.1 of this report. The slope of the spectra indicates a temperature in the neighborhood of 2 keV, giving a peak density of 2×10^{12} particles/cm^3, in rather good agreement with the cold-plasma production rates measured. However, it should be emphasized that this slope was measured at a photon energy about five times higher than the inferred electron temperature. This situation seems unavoidable, since the noise threshold of our best silicon detector preamplifier system is about 6 keV.

3.3 FLUTE INSTABILITIES IN THE PHYSICS TEST FACILITY (PTF)

W. B. Ard
M. C. Becker[1]
R. A. Dandl[1]
H. O. Eason
A. C. England
G. M. Haas
R. L. Livesey
M. W. McGuffin
E. H. Christy, Jr.

The large radial loss of energetic electrons in the PTF plasma, under some conditions, has been reported previously.[7] This instability was at least tentatively identified as a flute. Further studies of the instability show that it is almost certainly a gradient-*B*-driven flute.

Fast x-ray detectors were used to measure the time dependence of the electron loss to the wall. In order to follow the motion of the plasma surface in space and time, two probes were inserted on the midplane of the mirror field. The probes were separated by 120° in azimuth and positioned near the surface of the plasma (see Fig. 3.11). The probes were simply copper rods. One rod was fixed in position, while the other could be moved in and out.

A collimated x-ray detector was positioned to detect the x rays emitted from each probe. The purpose of two probes was to attempt to determine the phase velocity of waves on the plasma surface. In order to make this measurement, the movable probe was positioned so that the x-ray intensities from the two probes were approximately equal during an instability. Figure 3.12 is a photograph of the output from the two detectors during an instability displayed on a dual-beam oscilloscope.

[7] *Thermonuclear Div. Semiann. Progr. Rept. Oct. 31, 1965*, ORNL-3908, sect. 3.3.

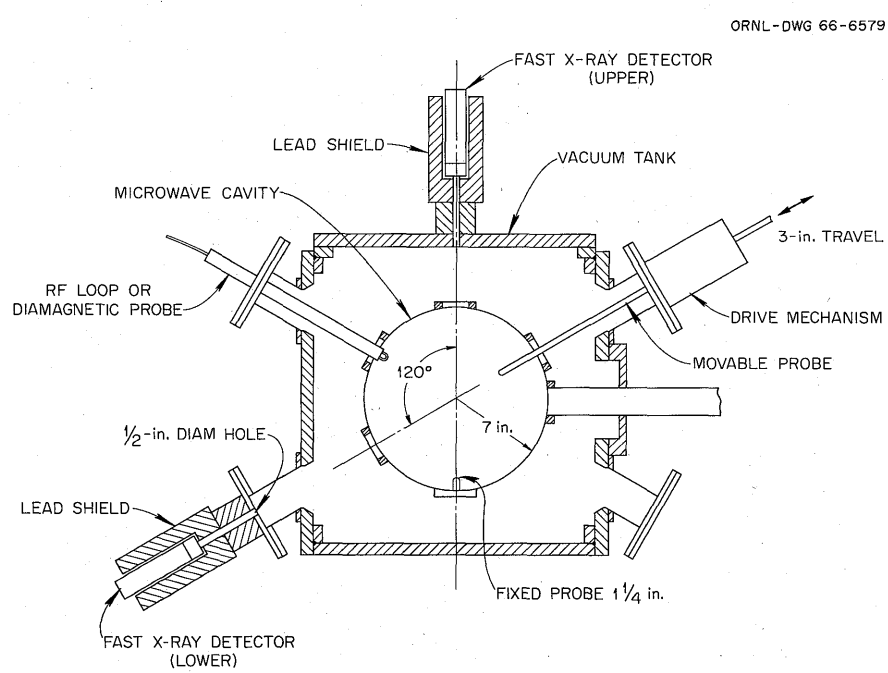

Fig. 3.11. Schematic Diagram of PTF Midplane, Showing Relative Position of Various Detectors.

The x rays from the probes are emitted in bursts separated in time by about 1.3 μsec. This same period was observed on a very large number of photographs made under a considerable range of conditions. The patterns on the two probes seem to be separated in time by about 0.9 μsec. We conclude from this that the time required for a perturbation to propagate once around the plasma surface is 2.7 μsec. This is twice the period between the bursts, which indicates that the perturbations that are observed are $m = 2$ perturbations. However, in many cases much shorter wavelength perturbations are observed (see Figs. 3.13 and 3.14). These short-wavelength perturbations generally have the $m = 2$ perturbations superimposed to a greater or less extent. Although short-wave-

PHOTO-83980

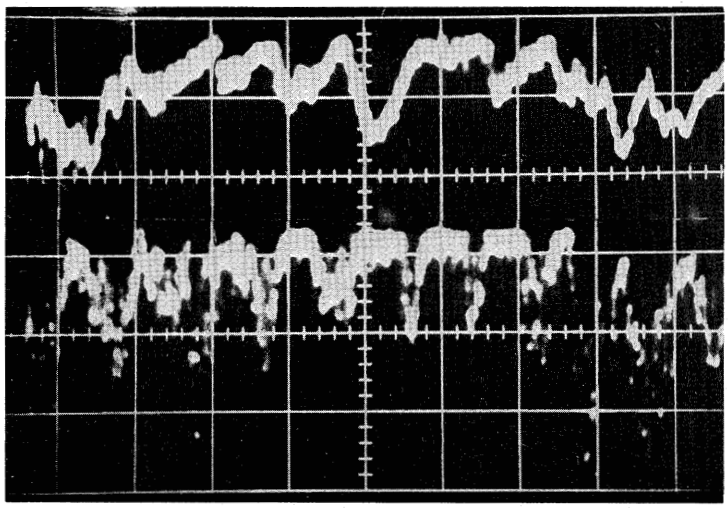

Fig. 3.12. Oscilloscope Traces of Output of X-Ray Detectors Looking at Copper Probes. The tips of the probes are the same distance from the field axis and are separated from each other 120° in azimuth. The sweep speed is 2 μsec/cm.

PHOTO 83981

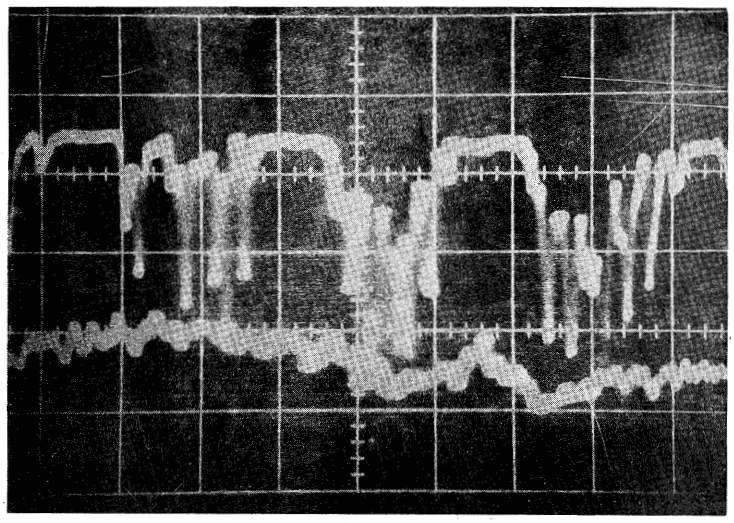

Fig. 3.13. Output of X-Ray Detectors. The upper probe is closer to the field axis than the lower. The sweep speed is 0.5 μsec/cm.

PHOTO 83982

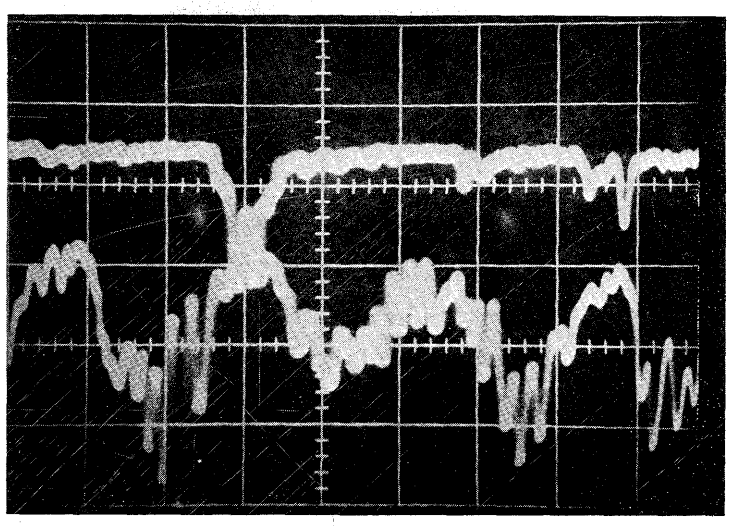

Fig. 3.14. Output of X-Ray Detectors. The lower probe is closer to the field axis than the upper. The sweep speed is 0.5 μsec/cm.

length variations are often not resolved on the x-ray output, high-frequency oscillations are always detected by a loop inserted into the cavity at the midplane. The frequencies observed on the loop in general correspond to the frequencies present in the x-ray detector outputs. This leads one to speculate that the short-wavelength perturbations are unstable, and as the distortion in the plasma surface grows, the gross shape of the surface tends toward the $m = 2$ symmetry. This is essentially in agreement with Coensgen *et al.*,[8] who frequently observe short-wavelength perturbations on the plasma surface when their "pictures" are taken before the flutes are fully developed. In fact, the output from our x-ray detectors is entirely consistent with what one would expect if the plasma were shaped like Coensgen's photographs and were rotating around the field axis.

The measured phase velocity of the flute,

$$\frac{2\pi r}{2.7 \times 10^{-6}\ \text{sec}},$$

is 2.8×10^7 cm/sec. For a hot-electron plasma, $T_e \gg T_i$, the phase velocity given by Krall[9] is very nearly the gradient-B drift velocity of the electrons. A drift velocity of 2.8×10^7 cm/sec in the PTF device would require electrons of 21-keV energy. Bremsstrahlung spectra show that a large fraction of the contained electrons in the PTF plasma have energies between 20 and 35 keV. There are roughly as many electrons with energies above 35 keV as below, but the distribution of these electrons in energy is more or less uniform up to a few hundred keV. Figure 3.15 is a plot of the density of electrons as a function of electron energy calculated from measured x-ray spectra. Due to absorption of x rays in the air path between the vacuum window and the detector, the spectra cannot be used to determine the density of electrons with energy less than about 15 keV.

A microwave interferometer was used to measure the density of the plasma streaming along the field lines. The assumption was made that the cold plasma was flowing freely from the microwave-heated region along the field lines to the ends. The interferometer was positioned so as to measure the density in the plasma streaming from an opening in the end of the microwave cavity. If the above assumption is valid, the density outside the cavity would be the same as the density just inside the cavity. The measured density was proportional to the neutral gas pressure inside the cavity. At the pressure required to make the plasma just stable, the density was about 1×10^9 electrons/cm^3 between the microwave horns. However, due to the diverging magnetic field lines, the cross-sectional area of the plasma between the

[8]F. H. Coensgen *et al.*, *Phys. Fluids* **9**, 187 (1965).
[9]N. Krall, *J. Nucl. Energy: Pt. C* **7**, 283 (1965).

horns was six times the area of the plasma column at the end of the cavity. We conclude, therefore, that the density at the cavity wall was about 6×10^9 electrons/cm^3. The density of hot electrons in the heated region was between 1 and 2×10^{11}/cm^3. This density is arrived at from either the x-ray intensity measurements or from using the measured β (≈ 0.06) and an average electron energy from the x-ray spectra.

The fact that the flutes are stabilized by a rather low density of cold plasma indicates that a dispersion relation derived by Guest and Beasley[10] for a hot-electron plasma in a PTF-like configuration is appropriate. The theory of Guest and Beasley is based on the assumption that the dominant mechanism affecting the growth of the gradient-B drift waves is the reactance of the cold plasma between the hot plasma and the conducting end walls. They predict stability when the density of the cold plasma connecting the hot plasma to the end walls is of the order of 10^{-1} times the hot-plasma density. They also find that short-wavelength modes require higher cold-plasma density for stabilization than long-wavelength modes. We are not able to show definitely that the gross particle loss to the walls is preceded by the growth of short-wavelength modes. However, the frequent presence of short-wavelength modes on the plasma surface during a flute and the detection of high-frequency oscillations by the rf loop support this conclusion.

We summarize our conclusion as follows: the microwave-heated plasma in the PTF device has an electron distribution consisting of a background of cold electrons resulting from ionization of neutral gas, a large group of contained energetic electrons bunched in energy at around 25 to 30 keV, and about an equal total number of electrons at higher energy. This plasma is unstable to perturbations that propagate azimuthally around the surface of the plasma with a phase velocity that is near the gradient-B drift velocity of the 25-keV group of electrons. The growth of these perturbations is limited by the reactance of the cold plasma connecting the contained hot plasma to the conducting end walls. When the density of this cold plasma is around 5×10^{-2} times the hot-plasma density, the growth of the perturbations is completely suppressed. The fact that very short-wavelength perturbations are not observed suggests that some other mechanism is effective in their stabilization.

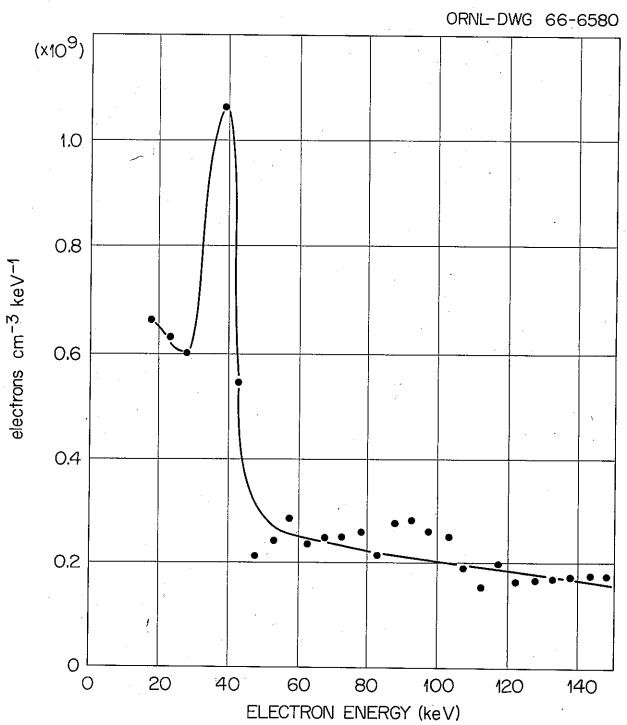

Fig. 3.15. Plot of Electron Density as a Function of Electron Energy.

[10] *Thermonuclear Div. Semiann. Progr. Rept. Oct. 31, 1965*, ORNL-3908, sect. 7.2.

4. Plasma Physics

4.1 BEAM-PLASMA INTERACTION EXPERIMENTS

I. Alexeff W. D. Jones
R. V. Neidigh

4.1.1 In Burnout IV

In previous experiments[1] we inferred that some ions in the plasma of the Burnout machines were being heated to quite high energies, several kilo-electron volts. These earlier experiments included the observation of high-energy ions escaping through openings in the circumference of a machine, neutrons emitted from D-D reactions, and Langmuir and power probe measurements. The present data appear to demonstrate spectroscopically that the ions in Burnouts IV and V have a mean kinetic energy corresponding to about 1 keV.

Spectroscopic measurements were made with a Littrow spectrograph of the light emitted by a deuterium plasma in Burnouts IV and V. Two spectrograms showing the Balmer β spectral line are shown in Fig. 4.1. Behind the bright lines is a dim, complex spectrum, the nature of which is unknown. The Balmer β line is observed to consist of a bright core plus a fuzzy envelope. We have been led to interpret this spectral line structure as follows: The bright central core is due to neutral deuterium excited directly by electron bombardment. The diffuse envelope is due to recombination radiation emitted by hot ions in the plasma that have captured electrons and have emitted radiation while still moving rapidly. If the spectral spread in the emitted recombination radiation is attributed to a temperature distribution in the ions, then preliminary calculations give an ion temperature of about 1 keV.

Several checks have been made which support our assumption that the diffuse envelope is not due to effects other than thermal spread. First, the envelope spread cannot be due to Stark, Zeeman, or collision broadening because the core line, due to the excitation of atomic hydrogen, is not broadened.

Second, the envelope cannot be due to the fogging of the photographic emulsion because of a strong overexposure of the core line. This fact is demonstrated by placing a stop in the center of the spectroscope slit, which results in the dark stripe running through the spectrograms of Fig. 4.1. We observed that the Balmer β lines do not spread appreciably vertically into the shadow cast by the stop, so that the horizontal spreading must be true spectral effect.

Third, the diffuse envelope is observed to be tilted, with respect to the central core, which would correspond to the hot ions having a component of rotation about the axis of the machine. We have shown that this assumption is apparently true by reversing the magnetic field in the machine and observing that the tilt of the envelope does indeed reverse. Thus, the tilt in the upper spectrogram of Fig. 4.1 is the opposite of the tilt in the lower spectrogram, suggesting that the tilt is due to ion rotation.

Thus, the above spectrographic work supports earlier experiments which suggest that hot ions are present in Burnouts IV and V.

In another experiment, a Fastax camera, capable of taking 4000 frames/sec, was used to observe the transition from radiation cooling (mode I) to burnout (mode II) in the Burnout IV plasma. The transition is apparently made in less than 250 μsec. The most important observation made was that all light to which the

[1] *Thermonuclear Div. Semiann. Progr. Rept. Oct. 31, 1965*, ORNL-3908, p. 52; *Thermonuclear Div. Semiann. Progr. Rept. Apr. 30, 1965*, ORNL-3836, p. 36; *Thermonuclear Div. Semiann. Progr. Rept. Oct. 31, 1964*, ORNL-3760, p. 30.

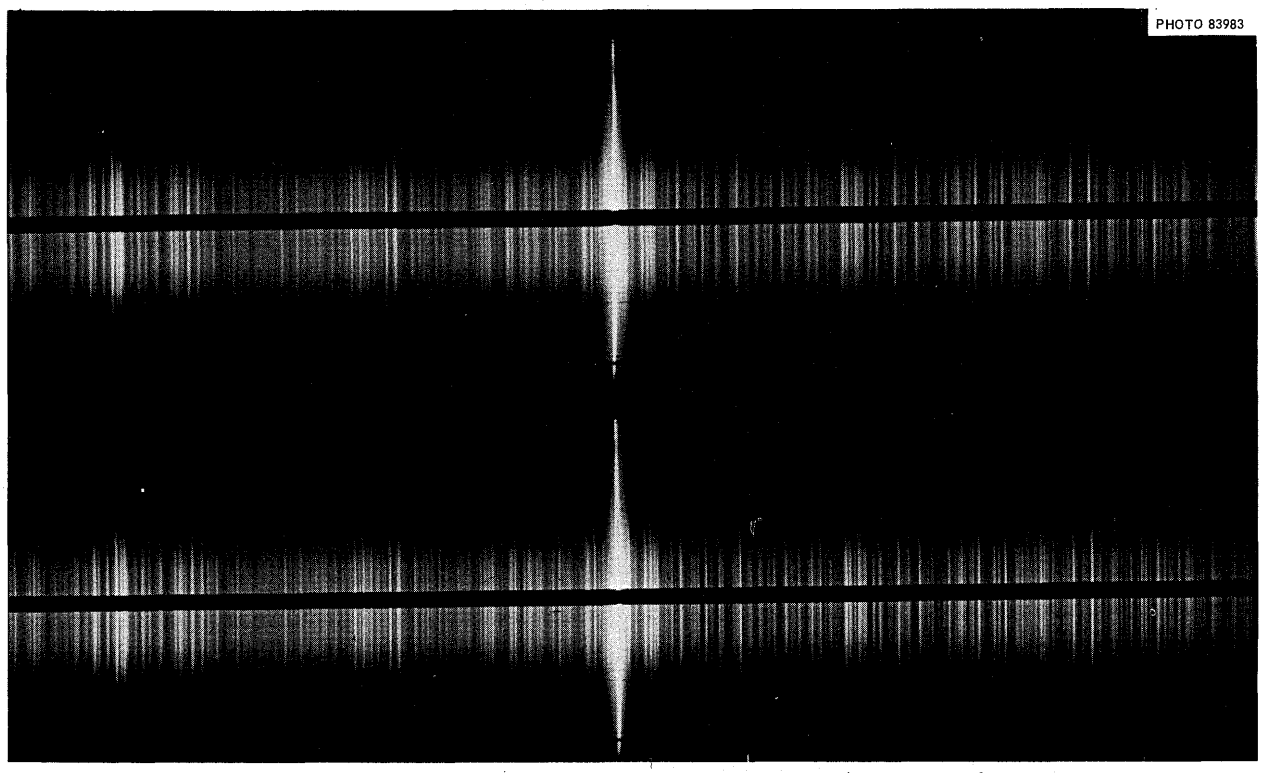

Fig. 4.1. Two Spectrograms Showing Doppler Slant and Broadening of the Balmer β Line from the Plasma of Burnout IV. In one spectrogram, the magnetic field is opposite that of the other. The center of the slit was masked, producing the dark band.

film (Kodak Royal-X Pan, High-Speed, Sp. 430M) is sensitive disappears for nearly 100 msec after the transition takes place. After this, impurity spectra, molecular spectra, and Balmer spectra increase in intensity to that seen in the spectrogram (Fig. 4.1). Note the series of photos of the plasma and the time of each after the onset of burnout in Fig. 4.2. The appearance of impurity spectra is probably due to outgassing of the liner surfaces as they are bombarded by energetic ions from the burned-out plasma. This impurity spectrum has been observed to diminish in intensity after some hours of operation and is probably symptomatic of a simple "cleanup" process.

4.1.2 In DCX-1

In the burnout experiments,[1] it has been found that the achievement of a burned-out plasma requires power densities large enough to overcome radiation cooling by the neutral gas initially present. For reasonable plasma volumes, power inputs of the order of many kilowatts are necessary. For steady-state operation with available power supplies, this requires anode-cathode potentials of several kilovolts. It has also been found that to produce plasmas of interesting densities, an initial gas pressure in the beam-plasma interaction region of at least 1 μ Hg is necessary. Since kilovolt potentials cannot be maintained at this high pressure and since the interaction region is inside the anode itself, a large pressure differential must exist in the anode-cathode and anode-anticathode regions. Or, in other words, a pumping system having a large gas-handling capability in the regions of the cathode and anticathode is required for the Oak Ridge type burnout experiments. Primarily because of the large pumping system of the DCX-1 machine, a series of burnout experiments were undertaken in this device.

Besides having a pumping system with a large gas-handling capability, the DCX-1 machine has a number of other desirable features not present in any of our regular Burnout devices. One of

PHOTO 83984

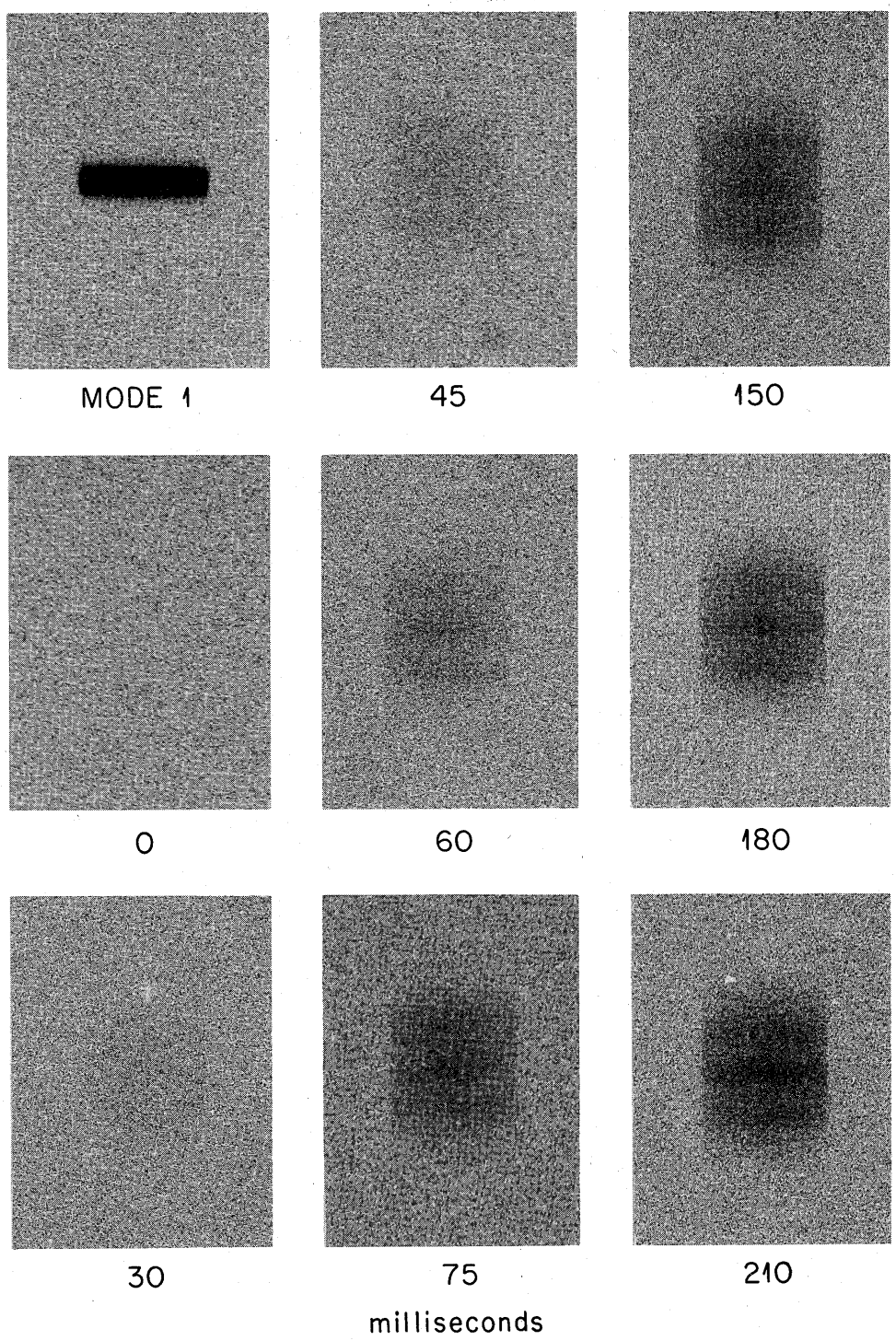

Fig. 4.2. The Mode I to Mode II Transition in Burnout IV. The first frame shows the plasma in mode I. The second is 0.2 msec later. Note the absence of light. The succeeding frames were taken at the times shown. The plasma becomes visible to the film after about 30 msec.

these is that the plasma is easily accessible for diagnostics. Another is that DCX-1 is a large machine, especially in the axial direction, thus allowing a large degree of flexibility in design and configuration of the electrode structure.

Although the burnout experiments performed in DCX-1 were beneficial, they were not as successful as had been originally expected, due to an unforeseen unfavorable combination of characteristics of the apparatus. The unfavorable combination involved the location of the pumps, the fact that pumps are made of a magnetic material, and the geometry of the vacuum wall of the machine. In particular, the small diameter of the outboard-coil spool cans relative to other DCX-1 cross-sectional dimensions proved to be a serious limitation on the size and placement of the reflecting electrodes. A further complicating feature was that the magnetic field axis does not seem to be coincident with the geometrical axis of the machine. In spite of these adverse features, however, it seems quite probable that, guided by information learned from the present experiments, a future effort, if desirable, could lead to the initially anticipated performance. More important, though, the experience gained here, at relatively little expense and effort, will be valuable in designing any future burnout machine.

The basic motivation for these experiments was that, with the superior gas-handling capability of the DCX-1 pumping system, a much greater pressure differential could be maintained, and, consequently, it should be possible to dissipate large quantities of power in the machine. With these large quantities of power it was expected that a dense plasma would be produced which would subsequently be heated by the beam-plasma interaction. Owing to the limited amount of time the machine would be available to us for burnout experiments, it was decided at the beginning to keep the diagnostic program to a minimum until there was evidence that a plasma had been produced with properties definitely superior to those which had been produced in previous experiments. Since such plasmas were not produced, the diagnostics done on the plasmas which were produced were not varied or as complete as they normally would have been. Also, because the power *density* (although not total power, which was larger than in any previous burnout experiments) was lower and consequently the plasmas less interesting, the diagnostics yielded values which in most cases are less impressive than those for previous experiments. Nevertheless, some new information was learned and some confirmation of previous measurements was obtained. Bearing in mind the limited number of measurements made, the results of the diagnostics program may be summarized as follows:

1. Ion densities, based on ion saturation currents to Langmuir probes, of at least 10^{12} cm^{-3} were present. Densities this high seemed to be present only near the axis of the machine, however, decreasing exponentially with radius with an e-folding distance of 2 to 3 cm.
2. Ion temperatures, based on spectroscopic observation of Doppler shifting of recombination radiation, of about 200 eV were found.
3. Electron temperatures, based on Langmuir probe data, in the range of 10 to 20 eV were found. These values, as well as those of the ion density, must be viewed with some reservation, of course, since the interpretation of Langmuir probe data obtained in strong magnetic fields is by no means completely unequivocal.
4. Based on x-ray measurements using a scintillation detector, no evidence for "hard" x rays (i.e., x rays capable of penetrating $\frac{3}{4}$ in. of glass) was found.
5. For the one such measurement made, the emission spectrum from the plasma was essentially "white" up to the 4-kMc upper limit of an rf probe specially designed by the DCX-2 group.

4.1.3 In Burnout V

Some preliminary results on three experiments in the Burnout V device are available. Two of the experiments observed the D-D reaction products (neutrons and tritons), and the third is an attempt to increase the ambient density in the anode by letting in a pulse of gas with a fast-acting valve.

Two neutron counters have been placed inside the vacuum chamber of Burnout V. One is near an end electrode, and the other is on the midplane of the device, both about 15 in. from the magnetic axis. In these positions, they are each partially shielded by the magnet coil and its cooling water from seeing the same neutron source. With this arrangement of counters, a test source was placed at the anticathode end and produced a neutron

flux at the end counter 13 times greater than at the counter of the midplane.

The response of these neutron counters with Burnout V in operation clearly indicates neutron sources other than at the end electrodes. The ratio of end counter response to midplane response is usually about 2/1 in operation and can be made to vary from 1.8/1 to 3.1/1 by adjustment of gas feed rate and power input. The neutron source strength in the midplane region appears to be about the same as previously reported,[1] 10^5 neutrons/sec, for comparable reaction parameters.

We thought it worthwhile at this stage of development to look for evidence of D-D reactions in the midplane plasma of Burnout V. This is not an easy diagnostic, since one would be looking for reaction products from a source where there may be as little as 10^2 reactions cm^{-3} sec^{-1}, within a region where the rate appears to be 10^5 reactions/sec and this in a background of 10^7 reactions/sec from the end electrodes. If the ion temperature is about 1 kV, as Doppler broadening seems to indicate, and the density is 10^{12} to 10^{13} cm^{-3}, as radiation and probe data imply, then using the σv calculated by J. L. Tuck and quoted in Simon's *An Introduction to Thermonuclear Research,*[2] the maximum reaction rate in the plasma could be

$$n^2\sigma v = 10^{26} \times 2 \times 10^{-22}$$
$$= 2 \times 10^4 \text{ reactions sec}^{-1} \text{ cm}^{-3} ,$$

or it might be as low as 2×10^2 reactions sec^{-1} cm^{-3}.

Due to difficulty in shielding from the intense source of fast neutrons at the end electrode, it was decided to observe one of the other reaction products. Protons, tritons, or ^3He are much less penetrating and are not subject to as much scattering as neutrons; so perhaps their origin could be determined from the geometry.

Helium-3 could not be used, since it most likely would be doubly ionized and contained in the machine by the 25-kG field in the midplane. The use of nuclear emulsions to detect protons is made very difficult, but not impossible, by the high x-ray flux present, which readily fogs the emulsion. Recourse was first made to a relatively new technique,[3] using cellulose nitrate to detect the 1-MeV tritons.

Recent publications[4] indicate that the smallest particle detected by this technique has been the deuteron, mass 2. We first tested our detection material with 5.4-MeV alpha particles from an ^{241}Am source and measured track lengths of about 8 μ (Fig. 4.3*a*). Since this was done in air, the particle energy at the detector was somewhat less than that at the source. The next step was to bombard the cellulose nitrate with 1-MeV mass 4 particles (Fig. 4.3*b*). We are grateful to C. F. Barnett, J. A. Ray, and B. N. Pinegar, who bombarded our plates with He^{2+} accelerated through 500 keV. Note that the tracks are very short, but that the direction of their origin is easily discernible. We assumed that 1-MeV tritons, mass 3, of the D-D reaction would make similar tracks in the cellulose nitrate. Several photomicrographs of the tracks made by particles from the midplane region of Burnout V are shown in Fig. 4.3*c*.

Of several exposures of the cellulose nitrate to particles emanating from the midplane region of Burnout V, one appears to indicate D-D reactions in the plasma. A schematic diagram of the experiment and of the particle track distribution is shown in Fig. 4.4. One would expect the track density to be maximum at 30 mm, since this presents the largest aperture through the two holes in the diaphragms. There is a peak near this point, but also a larger peak about 42 mm from the end of the plate. A 1-MeV triton from the axis of the machine would strike the plate at 40 mm. If one assumes that the wall yields D-D reactions uniformly, then on this plate at least there appears to have been a contribution from the plasma near the axis of the machine. Thus, this one exposure does seem to indicate that we do have reactions occurring in the volume of the plasma at the midplane. However, on other exposures made under apparently identical conditions, we have obtained no evidence of reaction products at all. We have not yet determined whether this is caused by a variation in the detector sensitivity or whether the plasma reactions are sporadic.

[2] A. Simon, *An Introduction to Thermonuclear Research,* p. 19, Pergamon, New York, 1959 [quoted from J. L. Tuck, LAMS-1640 (March 1954)].

[3] R. L. Fleischer *et al. Phys. Rev.* **133A**, 1443 (1964).

[4] R. L. Fleischer, P. B. Price, and R. M. Walker, *Science* **149**, 383 (1965).

PHOTO 83985

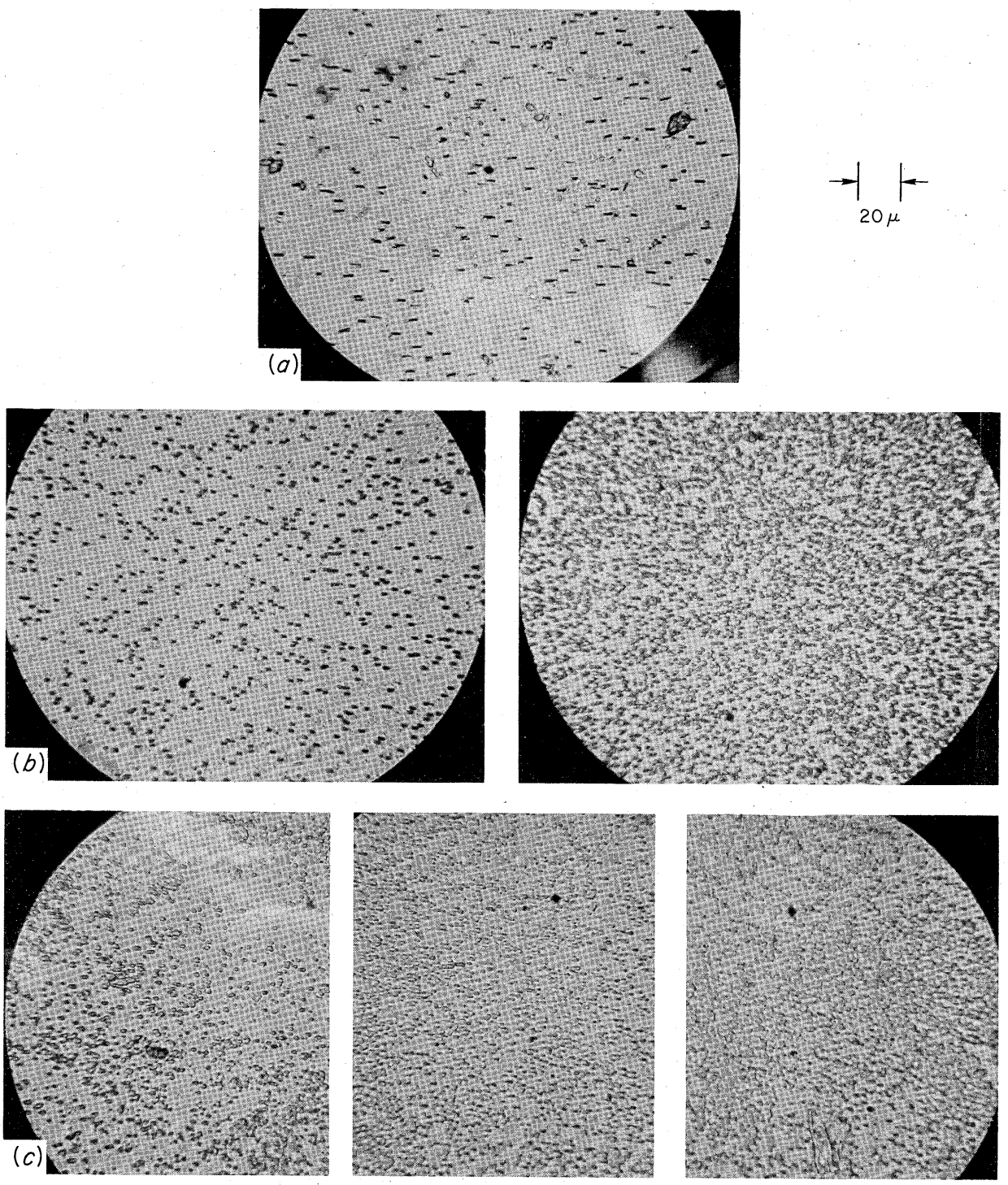

Fig. 4.3. Charged-Particle Tracks in Cellulose Nitrate. (*a*) Alpha tracks from ^{241}Am. (*b*) 1 MeV, mass 4. (*c*) Apparently tritons from midplane region of Burnout V. Note the scale, which applies to all photos. The cellulose nitrate was etched in 5 *N* NaOH for 2 h.

In order to increase the ambient pressure within the anode of a burnout device and still hold the accelerating potential of the electron beam, we have experimented with pulsing the gas to the anode region. The preliminary results are very interesting.

A technique similar to that used by Marshall[5] is shown schematically in Fig. 4.5. With the machine running normally and gas flowing into the anode region at about $\frac{1}{4}$ cm^3/sec, the pulse valve is activated, and an additional burst of gas is expelled into the anode region. Moving under thermal velocities, about 100 μsec would elapse before the gas will escape to the cathodes. As the space charge is relieved, electron current increases. Accelerating potential is maintained by the stored energy of the power-supply capacitor bank. This first experiment appears to show an additional burst of neutrons (Fig. 4.6) when the gas is pulsed.

[5] John Marshall, *Proc. U.N. Intern. Conf. Peaceful Uses At. Energy, 2d, Geneva, 1958* **31**, 341 (1959).

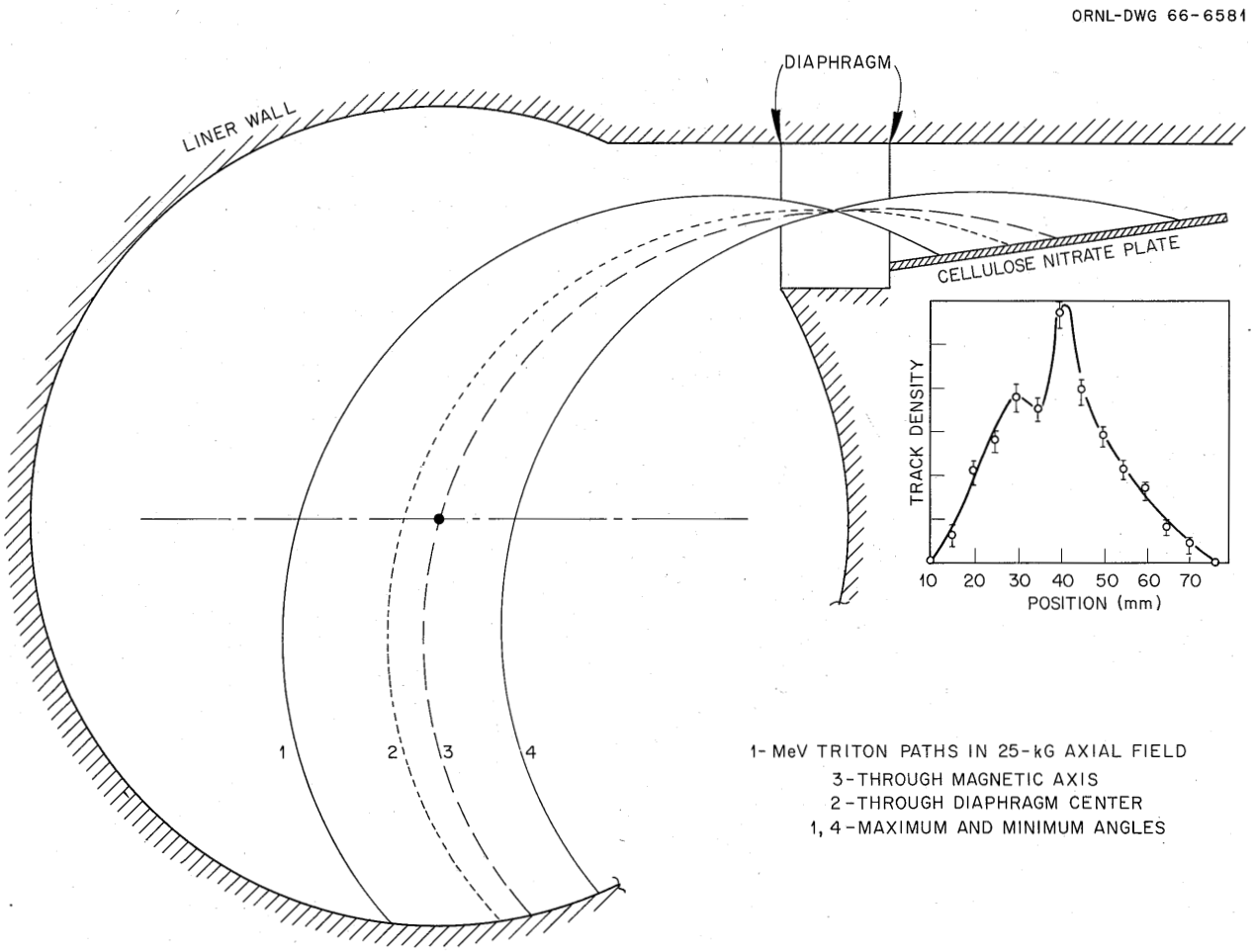

Fig. 4.4. Schematic Diagram of the Midplane Section of Burnout V, Showing the Location of the Cellulose Nitrate Plate and Possible Paths of 1-MeV Tritons. Inset, density distribution of tracks on the cellulose nitrate.

ORNL-DWG 66-6582

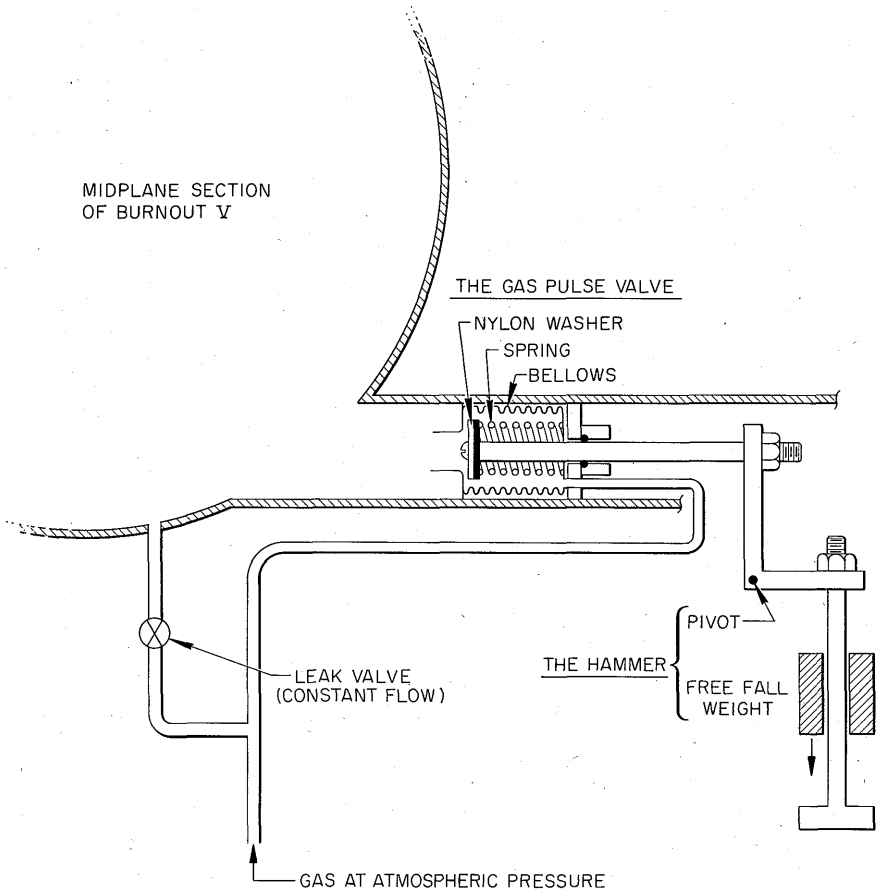

Fig. 4.5. Schematic Diagram of the Midplane Section of Burnout V, Showing the Gas Pulse Valve and Actuating Hammer.

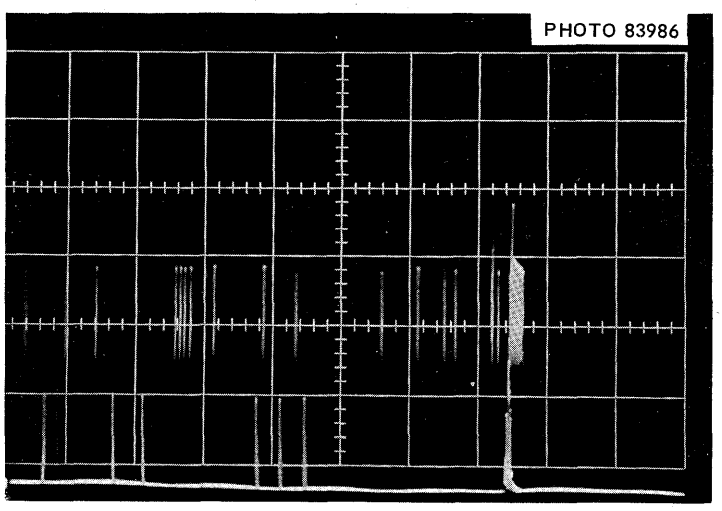

Fig. 4.6. Probable Burst of Neutrons Due to Gas Pulse. Sweep speed, 5 msec/cm. Upper trace, neutron counts from the end counter. Burst occurs at about 7.5 cm from beginning of trace. Lower trace, neutron counts from the midplane counter. Note that the midplane burst precedes the burst of the end, but the end burst is longer in duration.

4.2 BEAM-EXCITED ION-CYCLOTRON OSCILLATIONS

W. B. Ard
M. C. Becker[6]
R. A. Dandl[6]
H. O. Eason
A. C. England
G. M. Haas
R. L. Livesey
M. W. McGuffin

4.2.1 Introduction

The study of the excitation of plasma oscillations in the large-signal case requires the production of strong electric fields. The use of a modulated electron beam makes it possible to obtain large radio-frequency powers for plasma studies, and these radio-frequency fields are generated internal to the plasma. This study is being undertaken in order to investigate the possibility of supplying energy to the plasma ions.

[6]Instrumentation and Controls Division.

4.2.2 Apparatus

In order to begin the study of the interaction of a modulated electron beam with a plasma, the apparatus shown in Fig. 4.7 was constructed. The magnetic field is a 3:1 mirror field with a maximum $B_z(0,0)$ of 690 G. The electron gun consists of a filament, a modulating grid structure, and an anode. The beam hole in the gun is $\frac{3}{8}$ in. in diameter, and all elements of the gun are water cooled. The gun is capable of several hundred milliamperes at 5 kV in steady-state operation. Because the gun is operated near the temperature limit, at lower voltages the current is correspondingly less. At 2 kV the maximum current for the spacings used was about 150 mA.

Voltage for the modulator grid is supplied by a 500-W continuous-wave transmitter with a frequency range of 2 to 18 MHz. This modulator is capable of modulating a 2-kV, 150-mA beam up to 100%. The plasma is generated by the ionization of the gas by the electron beam.

ORNL-DWG 66-6583

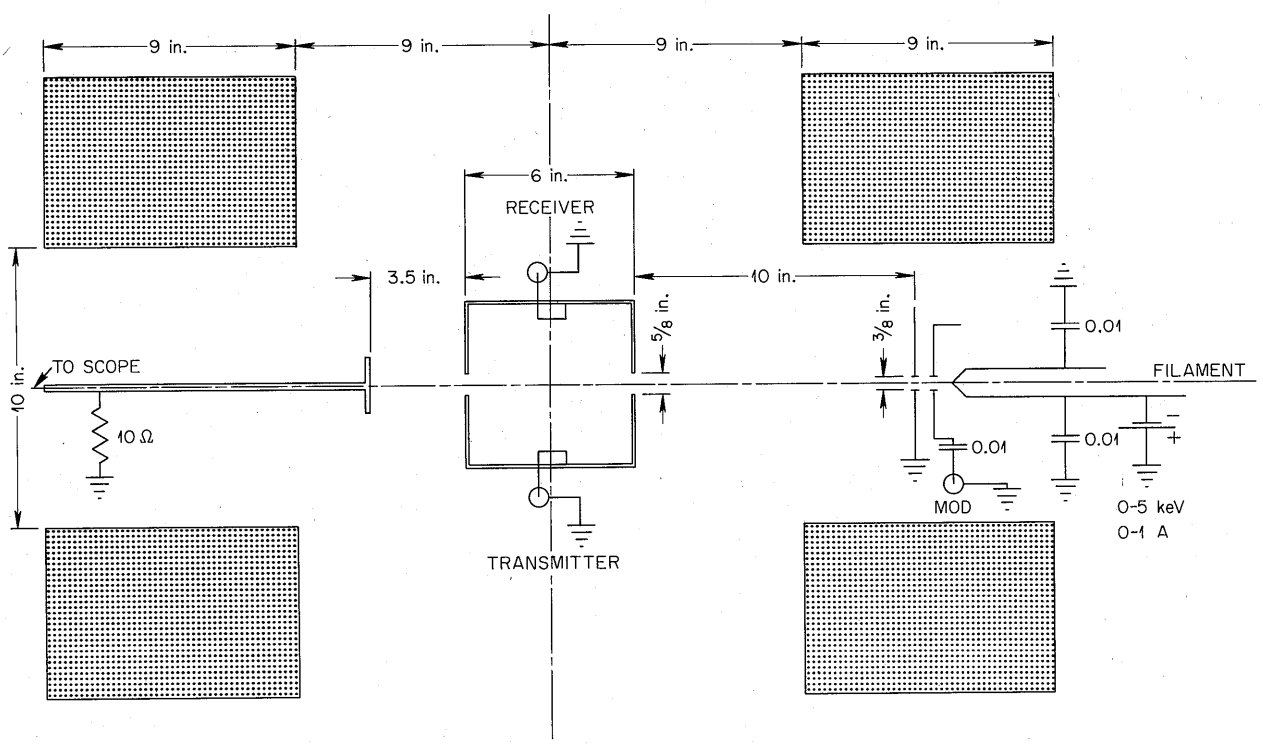

Fig. 4.7. Electron Beam Experimental Facility.

The plasma density was measured with a microwave cavity operating in the TM_{010} mode.[7] The cavity is 6 in. in diameter and 6 in. long and has $\frac{5}{8}$-in.-diam holes in each end. The TM_{010} mode frequency was 1500 MHz. For a circular beam of uniform density, the plasma density is given by

$$n_e = 6.77 \times 10^{-8} f \, \Delta f \frac{R^2}{r^2}, \qquad (1)$$

where f is the mode frequency, Δf is the frequency shift, R is the radius of the cavity, and r is the beam radius.

[7] S. C. Brown and D. J. Rose, MIT, Research Laboratory of Electronics Report RLE-230 (May 6, 1952).

The system was checked by inserting a $\frac{1}{2}$-in.-diam Plexiglas rod through the cavity and observing the frequency shift. The calculated phase shift (30 MHz) and the measured phase shift agreed.

4.2.3 Experimental Observations

Some results of applying modulation to the beam are shown in Figs. 4.8 and 4.9. These pictures represent the rf spectrum as seen in a panoramic receiver connected to an electric probe on the midplane 2 in. from the axis. Figure 4.8*a* shows the spectrum with no modulation, while Figs. 4.8*b* and 4.8*c* show the results of 30 and 100% modulation at a frequency of 3.1 MHz. At 30% modulation

PHOTO-83987

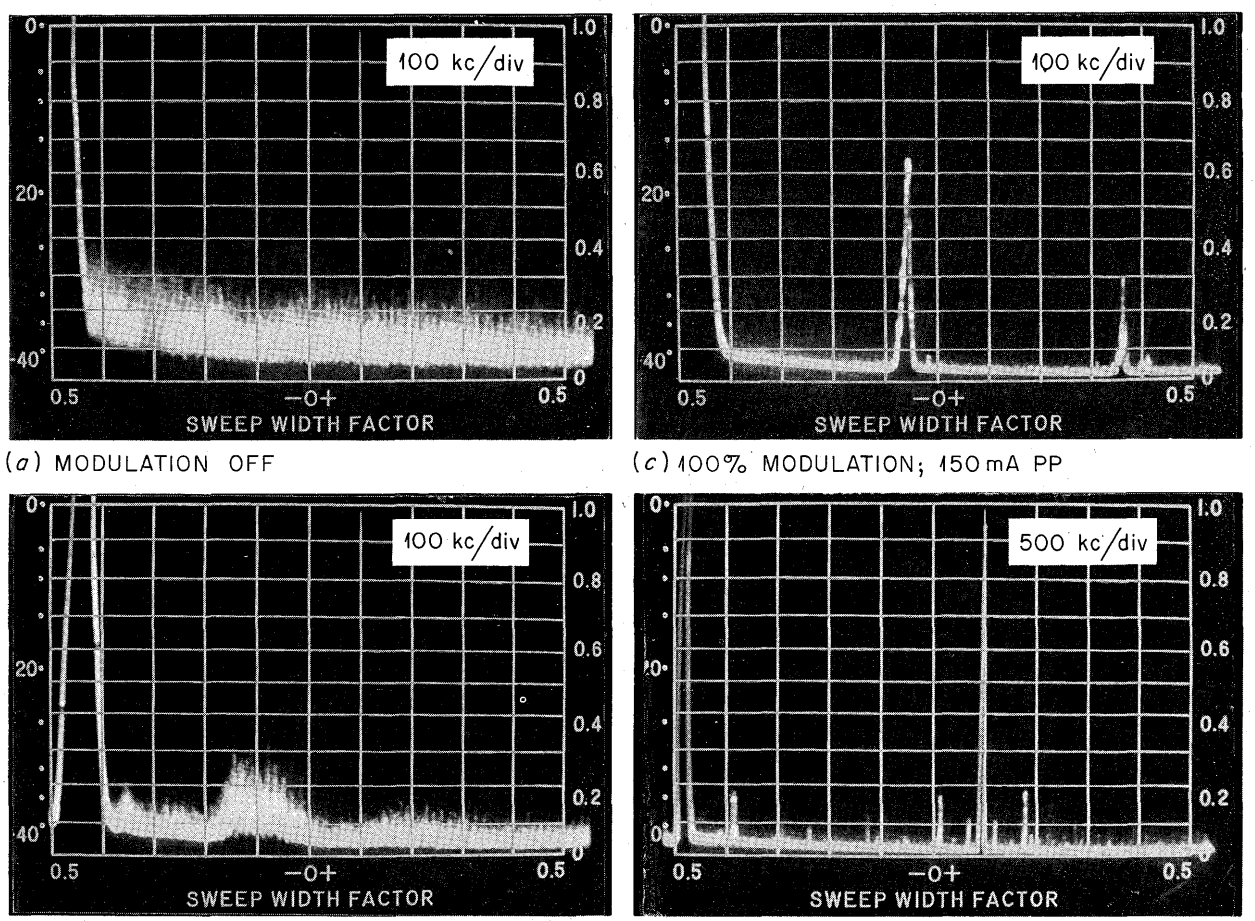

(*a*) MODULATION OFF

(*c*) 100% MODULATION; 150 mA PP

(*b*) 30% MODULATION; 50 mA PP

(*d*) 100% MODULATION

$B_z(0,0) = 415$ G
$V_B = 2000$ V

$I_{dc} = 150$ mA
$P = 2 \times 10^{-4}$ mm Hg

$f = 3.1$ Mc
HYDROGEN GAS

VERTICAL SCALE, LOGARITHMIC

MAY 3, 1966

Fig. 4.8. Low-Frequency Spectrum With and Without Modulation.

an rf band from 320 to 500 kHz is present, while at 100% modulation a sharp peak of approximately 430 kHz is present. For the magnetic field used [$B_z(0,0)$ = 415 G], the midplane ion cyclotron frequency for H_2^+ is 320 kHz, and since the system is in a 3:1 mirror field, the 430-kHz frequencies fall in the range of the ion cyclotron frequency. Thus the 430-kHz signal was identified with collective oscillation of the H_2^+ ions at their ion cyclotron frequency. In order to check this, two things were done. The shift of the signal with magnetic field was observed. This is shown in Fig. 4.9. Although the modulating frequency is different, the oscillations are produced at the same frequency as with the lower modulating frequency. As can be seen, the signal increased with magnetic field in approximately the proper proportions. No change in plasma density was observed

PHOTO 83988

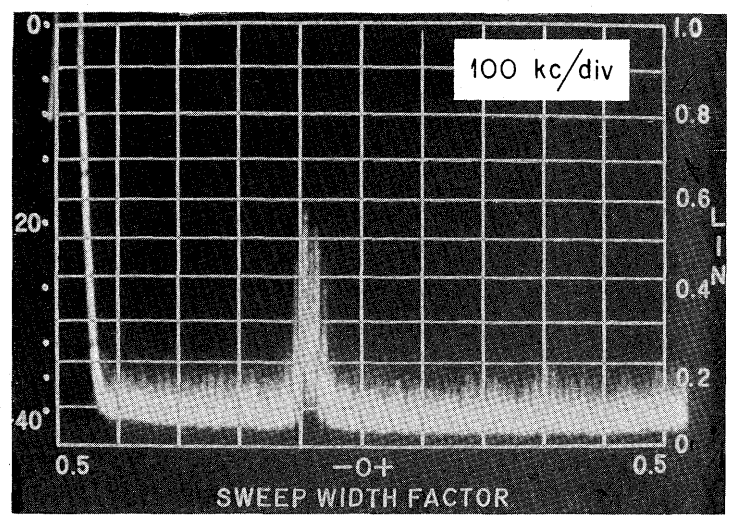

$B_z(0,0) = 368$ G

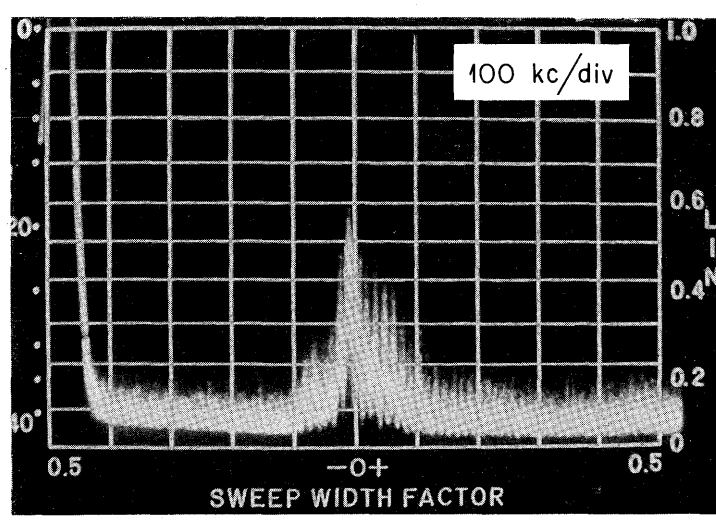

$B_z(0,0) = 485$ G

$V_B = 2000$V
$P = 2 \times 10^{-4}$ mm Hg
HYDROGEN GAS

$I_{dc} = 120$ mA
$f = 11.8$ Mc
MAY 2, 1966

Fig. 4.9. Shift in Low-Frequency Spectrum with Change in Magnetic Field.

as the magnetic field was changed. Second, the plasma was produced using helium and neon. In both cases the peaks shifted downward. Unfortunately, due to the 3:1 mirror, it is impossible to tell if the variation with field and gas type is exact, but the gross variations do support the contention that these signals are associated with collective oscillation at the ion cyclotron frequency.

For the beam and plasma conditions of Fig. 4.8, the observed shift in the cavity resonant frequency was approximately 500 kHz. It has been observed that the presence of strong modulation decreases the plasma density. For the conditions of Fig. 4.8 with the modulation off, the observed frequency shift was 2 MHz. The exact diameter of the plasma is unknown, but it appears to fill about one-half of the hole in the cavity ends. The limiting aperture at the electron gun is $\frac{3}{8}$ in., and thus the beam and plasma might be expected to have approximately this diameter. Using a plasma diameter of $\frac{3}{8}$ in. and assuming a uniform distribution, the plasma density is 1.55×10^9 cm^{-3}. For a peak beam current of 150 mA, the peak beam density would be 6.2×10^8 cm^{-3}. Thus the plasma density is in excess of the peak beam density by at least a factor of 2. In both cases there is an uncertainty due to the size and distribution of the beam and plasma. However, these results are in general agreement with those of Kornelov *et al.*,[8] who found that in the low-pressure region (less than 10^{-3} mm Hg in hydrogen) the plasma density was four times the beam density for a 4-keV, 20-mA beam. The plasma density of 1.55×10^9 cm^{-3} corresponds to an ion plasma frequency for H_2^+ of 5.6 MHz. The rf spectrum of the beam alone shows strong signals up to the fifth or sixth harmonic. Thus a fundamental of 3.1 MHz would have its first harmonic at 6.2 MHz, quite close to the measured ion plasma frequency. One might also expect that, due to density gradients and the harmonic content of the electric fields from the beam, no distinct resonant frequency for the interaction would be observable but that oscillation at the ion cyclotron frequency could be generated over a wide range of modulator frequencies.

[8]E. A. Kornelov *et al.*, *Soviet Phys. — Tech. Phys. (English Transl.)* 10(8), 1064 (February 1966).

The electric field strength of these oscillations may be estimated in a very rough fashion. If one solves Poisson's equation in the simplest case (i.e., uniform current distribution and infinitely long beam in cylindrical geometry), the electric field for the lowest mode at the surface of the beam may be written as

$$E = \frac{\rho a}{4\epsilon_0} \frac{1}{\ln b/a},$$

where ρ is the charge density, a is the beam radius, and b is the cylinder radius. For the 150-mA, 2-keV beam, with a radius of $\frac{3}{8}$ in. and $b/a \cong 10$, the electric field at the beam surface in this case is approximately 10^4 V/m. From Fig. 4.8*d*, one can then estimate the electric field strength of the collective oscillations as 1/100 of those of the beam. Thus, these signals have electric fields in the range of volts per centimeter at the surface of the beam. Insufficient information (both qualitative and quantitative) is available at present to determine the exact nature of the oscillations or the mechanism by which they are excited. However, certain additional observations have been made. The effect is strongly dependent on pressure, beam current, and the amplitude of the modulation. The effect of modulation frequency, beam voltage, and magnetic field are not quite so pronounced.

4.2.4 Conclusions

This experiment strongly suggests that the intense rf electric fields produced by a high-current modulated electron beam can indeed produce strong collective oscillations of the plasma at the ion cyclotron frequency. The mechanism by which these oscillations are excited may be due to the coupling of the beam to the plasma by virtue of the modulation at the ion plasma frequency. For the condition present in the experiment, this frequency is also equivalent to the lower hybrid frequency. Further investigation is necessary in order to clarify the exact nature of the interaction and also to study the feasibility of using this technique to increase the ion energies of the plasma.

4.3 AN ELECTRON-COLLECTING PROBE AS AN ION WAVE DETECTOR[9]

I. Alexeff W. D. Jones

The very sensitive technique for detecting ionic sound waves by having them perturb an electron-carrying sheath around a probe has now been experimentally shown to apply to cold electron-absorbing probes as well as to hot electron-emitting probes.[10] One must be careful to keep the cold probe small in size and the applied positive potential low, or oscillations or a glow discharge, respectively, develops around the probe.

The manner in which an ion wave can perturb the current from the cathode of a discharge tube has been surmised before,[11] but has never before been so clearly demonstrated as now. These observations of plasma motion affecting the emission of electrons from a hot filament or collection of electrons by a positive anode may help explain the feedback mechanism that sustains many of the low-frequency oscillations observed in discharge tubes and other plasma devices.

[9] I. Alexeff and W. D. Jones, *Phys. Letters* **20**, 269 (1966).

[10] I. Alexeff and W. D. Jones, *Thermonuclear Div. Semiann. Progr. Rept. Oct. 31, 1965*, ORNL-3908, p. 69.

4.4 PLASMA DENSITY MEASUREMENT IN A HOLLOW-CATHODE ARC BY ARC REVERSAL

I. Alexeff W. D. Jones
W. Halchin J. F. Potts

We have measured the average electron density in a magnetically supported hollow-cathode arc by reversing the applied potential and collecting and measuring the total ionic charge stored in the arc. The average density found in our typical argon arc is greater than 10^{14} electrons/cm^3. At these high densities the standard Langmuir probe and microwave techniques are quite difficult to use, while the "arc-reversal" technique is remarkably simple. A similar technique has been used in the past to measure the plasma density in a reflex discharge.[12]

Figure 4.10 shows the circuit used in reversing the cathode potential and collecting and measuring the ionic charge in the arc. Figure 4.11 is a typi-

[11] I. Alexeff and W. D. Jones, *Thermonuclear Div. Semiann. Progr. Rept. Oct. 31, 1963*, ORNL-3564, p. 55; *Compt. Rend. Conf. Intern. Phenomenes Ionisation Gaz, 6^e, Paris, 1963* **3**, 36 (1964).

[12] I. Alexeff and R. V. Neidigh, p. 141 in *Third Symposium on Engineering Aspects of Magnetohydrodynamics, University of Rochester, New York, 1962*, Gordon and Breach, New York, 1963.

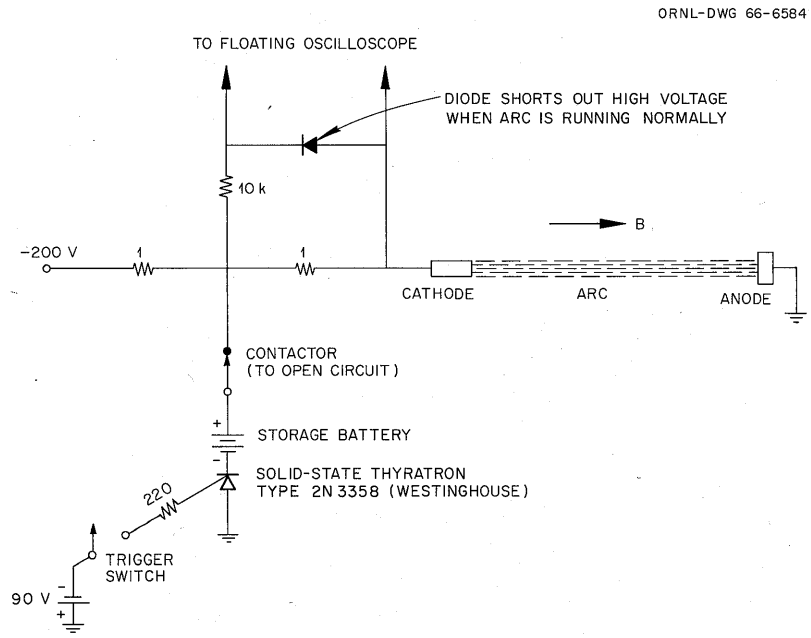

Fig. 4.10. Schematic of Arc-Reversal Experiment. The current in the normally operating arc is about 50 A.

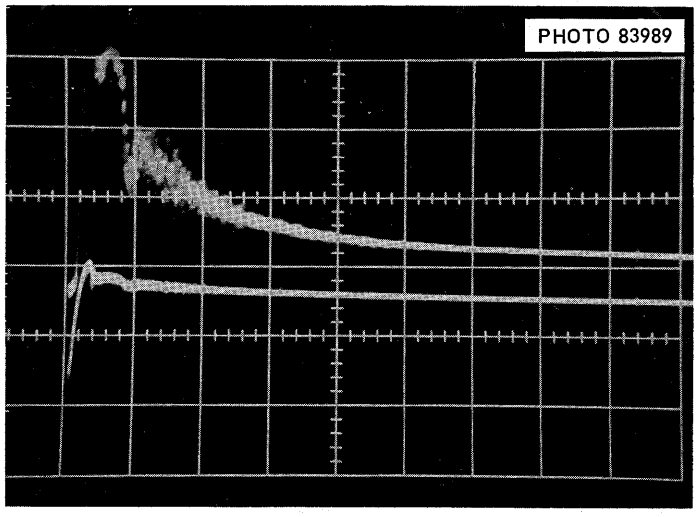

Fig. 4.11. Oscillogram of the Ion Current During Arc Decay. The upper trace represents ion current. One large square vertically corresponds to about 1 A. The horizontal scale has one large square corresponding to $\frac{1}{10}$ msec. The lower trace corresponds to arc voltage and shows that the voltage reversed in a time short compared to the ion current decay.

cal photo showing the rapid turnoff (bottom trace) of the arc voltage and the subsequent slow collection (top trace) of the ionic charge from the arc.

4.5 USE OF AN ORDINARY CAMERA AS A STREAK CAMERA

I. Alexeff W. D. Jones

We report on the use of an ordinary camera as a streak camera. With a streak camera, a one-dimensional line image of an object is plotted as a function of time. The advantage of streak cameras over ordinary cameras is that they are capable of shorter resolving times.

In a typical streak camera an objective lens images an event on a plate with a slit.[13] The slit selects a one-dimensional slice of the image, which in turn is imaged on a photographic film via a second lens system and a rotating mirror. The rotating mirror sweeps the slit image over the photographic film, resulting in a plot of the one-dimensional image as a function of time. In the present technique the entire camera is rotated, thus eliminating the rotating mirror. This is done simply by manually rotating an ordinary camera, with the shutter held open, so that the field of view passes rapidly past the event of interest. The experiment is done in a darkened room, and the object being studied is illuminated. Any camera having a shutter which can be held open can be used. However, Polaroid cameras are recommended because of the faster film generally available.

In conventional streak photography the time scale is determined by the angular speed of the rotating mirror. Here the time scale can be provided by a flashing light source of known frequency, say a neon bulb operated on 60-cycle ac current, located in the field of view of the rotating camera. The streak photograph then is supplied with a series of spots of light with known time separation, giving a built-in time calibration.

A streak camera can be used in two ways: as a chronometer and as a velocity meter. In the first case, a series of events is imaged on the slit plate, and from the time calibration, time intervals between the events can be measured. In the second case, an object moves parallel to the slit during the exposure, resulting in a sloping line on the photograph, from which the velocity can be determined. In the data shown in Fig. 4.12, both capabilities of the technique can be observed. Figure 4.12*a* is an ordinary photograph taken of a hot-cathode glow discharge. To the unaided eye, as to

[13] R. H. Huddlestone and S. L. Leonard, *Plasma Diagnostic Techniques*, sects. 2.1.2 and 2.2, Academic, New York, 1965.

an ordinary camera when using normal-length exposure times, the discharge tube appears to be rather uniformly luminous. Figure 4.12*b*, however, taken with the same camera[14] rotated in the hands as described above, shows that the discharge is striated,[15] that is, it is made up of alternate light and dark regions. Furthermore, as the figure shows, the striations are moving rapidly along the length of the discharge tube.

The striations being studied in Fig. 4.12 have the property that they move in the direction toward the cathode.[15] In this experiment the reversal of

[14]Polaroid Land camera model 110B, Polaroid Corp., 119 Windsor St., Cambridge, Mass. 02139.

[15]I. Alexeff and W. D. Jones, *Thermonuclear Div. Semiann. Progr. Rept. Apr. 30, 1964,* ORNL-3652, p. 56; *Thermonuclear Div. Semiann. Progr. Rept. Oct. 31, 1963,* ORNL-3564, p. 59.

PHOTO 83990

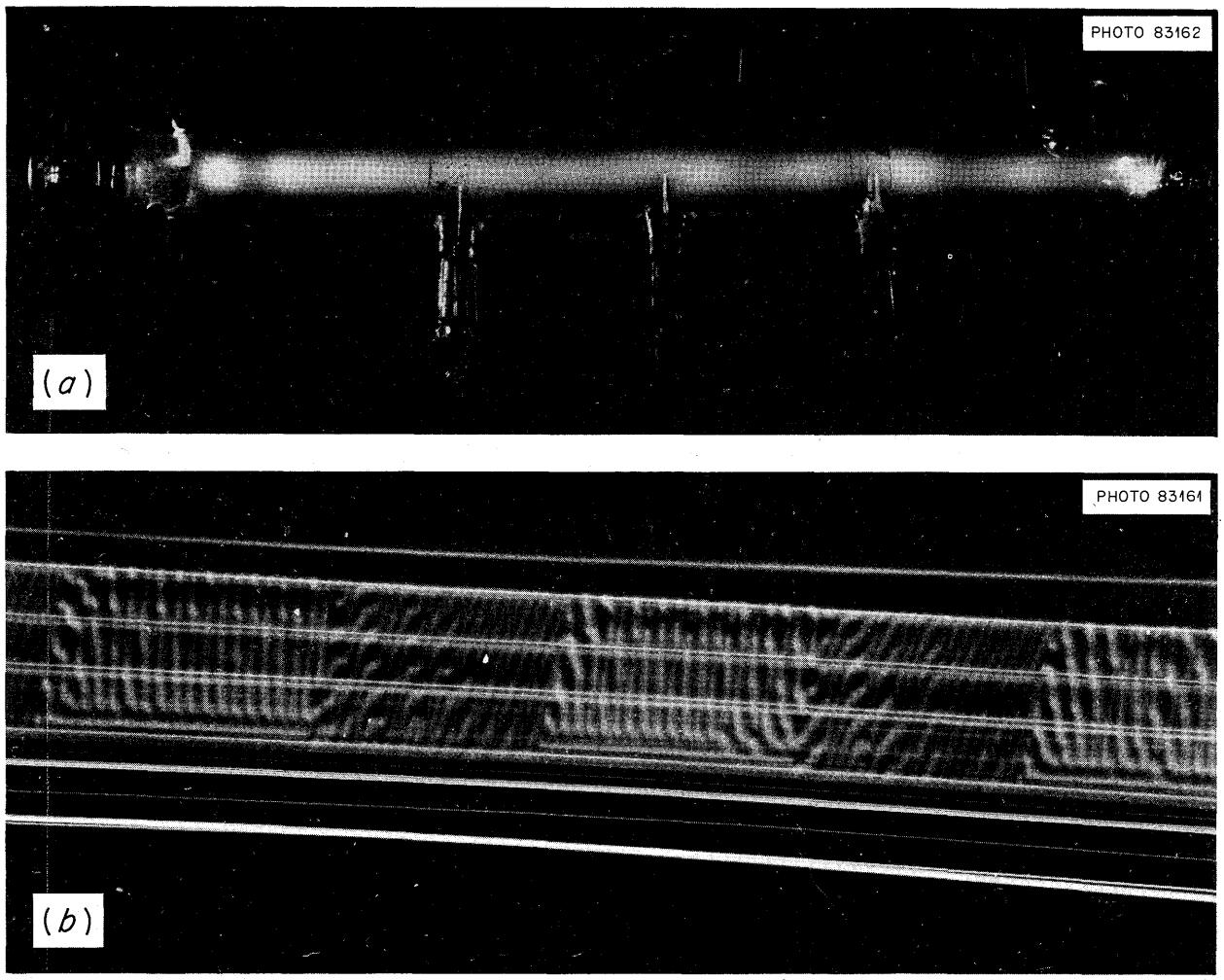

Fig. 4.12. (*a*) Photograph of a Xenon Gas Discharge, Taken with an Ordinary Camera Using a Normal-Length Exposure Time; (*b*) Streak Photograph of the Same Discharge, Taken with the Same Camera but Used in the Manner Discussed in This Report for Doing Streak Photography with an Ordinary Camera. Photograph *a* shows what appears to be a rather uniformly luminous discharge, while photograph *b*, having much greater time resolution, shows that the discharge is actually striated, with the striations moving rapidly along the length of the discharge. In *b*, time increases from top to bottom, with the nearly horizontal lines representing the moving striations. The almost vertical lines in *b* result from reflections from different parts of the discharge tube of the hot cathode sources at the ends of the tube. In *b*, the separation between the camera and the (approximately 30-cm-long) discharge was some three times greater than that in *a*, leading to the shorter image seen in *b*.

propagation direction upon interchanging the anode and cathode was studied. The discharge tube was constructed so that the anode and the cathode could be interchanged electrically 120 times each second by means of a mercury switch. Thus Fig. 4.12*b* has a built-in time calibration. As noted from the change of slope of the lines, five reversals occurred during the sweep time of the rotating camera. From the figure one can obtain some idea of the time resolution possible with this simple technique. The striations are seen to be generated approximately every 0.5 msec and have a velocity of about 10^5 cm/sec (for this particular photograph the axis of rotation of the camera was not quite parallel to the discharge axis, giving rise to an apparent asymmetry in the velocities in the opposite directions). For this particular photograph the discharge was photographed directly without a slit, since the narrow discharge tube approximated a one-dimensional image. Since the finite width of the discharge tube corresponds to a finite resolving time for the system, the resolution could be increased by placing a narrow slit against the tube parallel to the tube axis. Another way to increase resolution would be to stand back further from the event during the photographing, so that the sweep time of the field of view past the event would be shorter for the same rotational speed of the camera. To prevent the image from becoming intolerably small, one could use a telephoto lens on the camera. For Fig. 4.12*b*, the camera was located approximately 10 ft from the discharge.

4.6 A CESIUM PLASMA WITH NO SHORT-CIRCUIT EFFECTS AT THE END ELECTRODES

I. Alexeff W. Halchin

We have developed a plasma source in which cesium chloride is dissociated and the cesium ionized on a hot surface. Such thermal plasma sources have been very useful in that they produce a dense plasma, $n_e \gg 10^{10}$ cm^{-3}, that is quiescent. Our source is unique in that the hot surface is electrically nonconducting. Previously used surfaces were metallic and acted as a short circuit across the end of a magnetically supported plasma column. This short circuit made plasma instability studies difficult. The short circuit does not exist in our apparatus.

4.7 VARYING PLASMA ELECTRON TEMPERATURE IN DISCHARGE TUBES BY A SIMPLE AUXILIARY ELECTRODE

I. Alexeff W. D. Jones

We have produced a simple auxiliary electrode that, when inserted into a simple discharge tube, allows us to vary the electron temperature of rare-gas plasmas over a wide range. In general, producing large variations of the electron temperature in a discharge tube containing a given gas has not been possible. Increasing the current producing the plasma, for example, generally results in a denser plasma, but the electron temperature remains relatively constant. In our apparatus, the electron temperature is varied by an auxiliary electrode. The auxiliary electrode is essentially a hot probe[16] of quite large dimensions. When heated, this electrode becomes a strong emitter of electrons and approaches plasma potential. Under this condition of operation, the electrode rapidly absorbs energetic electrons from the plasma and replaces them with relatively cold thermionically emitted electrons. By increasing the operating temperature of the electrode, we can reduce the electron temperature from its normal value (several electron volts) to essentially the thermal temperature of the electrode (about 1/10 eV).

A schematic of the experimental apparatus is shown in Fig. 4.13. The discharge tube used is that described in our earlier ionic-sound-wave work.[17] An important feature of this apparatus is that the electrons producing most of the ionization are not plasma electrons but are high-energy electrons extracted from the hot tungsten cathode by the adjacent copper-mesh anode. Thus, varying the plasma electron temperature does not drastically change the rate of plasma production.

Two types of auxiliary electrodes have been used. The first type is a tantalum strip wrapped

[16] F. F. Chen, *Plasma Physics Diagnostics* (ed. by R. H. Huddlestone and S. L. Leonard), chap. 2, sect. 6.3, Academic, New York, 1965.

[17] I. Alexeff and W. D. Jones, *Phys. Rev. Letters* **15**, 286 (1965); I. Alexeff and W. D. Jones, *Phys. Letters* **20**, 269 (1966); W. D. Jones and I. Alexeff, *Proceedings of the VII International Conference on Ionization Phenomena in Gases, Belgrade, Yugoslavia, August 1965* (to be published).

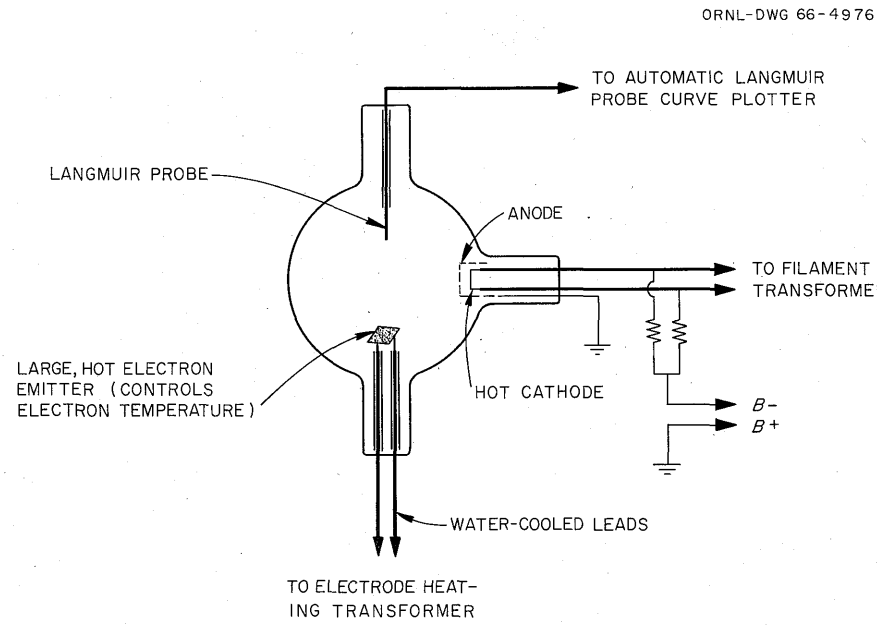

Fig. 4.13. Schematic of Apparatus. The discharge tube is a sphere about 5 liters in volume. The gas pressure used ranged from about 1 to 10 μ.

with a platinum mesh which is coated with a mixture of oxides.[18] The oxide coating emits electrons strongly at moderate temperatures. The auxiliary electrode is about 2.5 by 2.5 cm in area, is electrically floating, and is supported on water-cooled leads. The advantage of this oxide-coated auxiliary electrode is that it can lower the electron temperature to the low value of about 0.1 eV, the low operating temperature of the electrode itself. A disadvantage of this oxide-coated electrode is that it can emit a large quantity of water vapor that poisons the plasma if the electrode is not thoroughly outgassed.

A second type of auxiliary electrode is a loop containing about 15 cm of 1-mm tungsten wire. This electrode has the advantage of being essentially gas-free. However, since the electrode operates at a very high temperature, it can cool the plasma electrons to only about 0.2 eV, at best.

The temperature and density of the electrons in the plasma are monitored continuously by a Langmuir probe 0.06 cm^2 in area. The characteristic of the Langmuir probe is plotted automatically on an oscilloscope by means of a simple electronic circuit.[19] The continuous monitoring of the properties of the plasma allows us to follow rapid changes in the electron temperature as the temperature of the auxiliary electrode is varied.

Typical experimental results obtained with the above apparatus are shown in Figs. 4.14*a* and 4.14*b*. In Fig. 4.14*a*, the electron temperature in a xenon discharge varies over a range of 4 to 1 as the temperature of the auxiliary electrode is varied. In Fig. 4.14*b*, the electron temperature in a helium discharge varies over a range of 5 to 1. In our most extreme case, in helium, the electron temperature varied over a range of 43 to 1. However, at the highest electron temperature measured, approximately 11 eV, the Langmuir plot did not show a clear-cut Maxwellian distribution, and so these data are not reproduced here.

We have observed that the cooling effect of the auxiliary electrode depends on the current flow

[18] Triple Carbonate (RCA No. 33C-144), Radio Corporation of America. [A satisfactory oxide cathode may be made by mixing equal gram-molecule parts of barium and strontium carbonates, making a paste of these in distilled water, and applying it to the platinum mesh. Heat decomposes the carbonates to the appropriate oxides. (Private communication, Prof. W. H. Bennett, Physics Dept., North Carolina State University, Raleigh.)]

[19] I. Alexeff and W. D. Jones, *Thermonuclear Div. Semiann. Progr. Repts. Apr. 30, 1963*, ORNL-3472, p. 47; *Oct. 31, 1963*, ORNL-3564, p. 62. (May be obtained from Clearinghouse for Federal Scientific and Technical Information, National Bureau of Standards, U.S. Department of Commerce, Springfield, Va.)

PHOTO 83991

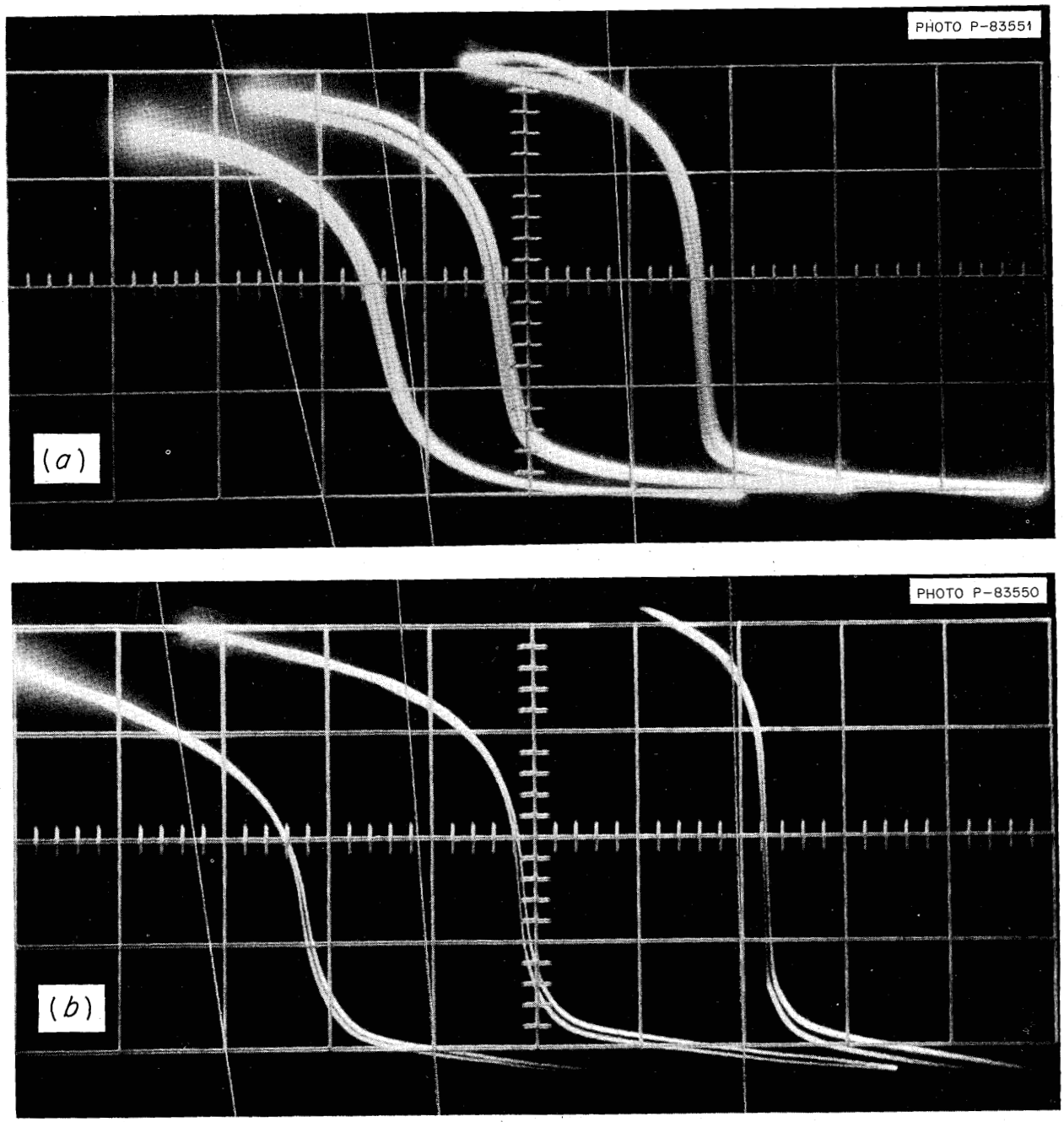

Fig. 4.14. (*a*) Langmuir Probe Plots, Showing the Electron Temperature Variation in a Xenon Plasma. Each large square horizontally represents 3.8 V applied to the probe. The vertical scale is logarithmic, with each large square corresponding to a factor of *e* in probe current. The three curves from left to right represent electron temperatures of 0.76, 0.38, and 0.19 eV respectively. The plasma density at the highest electron temperature is 1.4×10^9 cm^{-3}. An oxide-coated auxiliary electrode was used. (*b*) Langmuir Probe Plots, Showing the Electron Temperature Variation in a Helium Plasma. The coordinate scales are as described above. The two curves from left to right represent electron temperatures of 1.9 and 0.38 eV respectively. The plasma density at the highest electron temperature is 5.8×10^8 cm^{-3}. A pure tungsten auxiliary electrode was used.

through the electrode as well as on the temperature of the electrode. In Fig. 4.14*a*, the center probe curve corresponds to the electrode hot and with the heating current flowing, while the right-hand trace corresponds to the electrode hot, but no heating current – the heating current had just been turned off. The curve without the heating current corresponds to a plasma twice as cold as that with the current present. Apparently the magnetic field produced by current flowing through the electrode impedes the electron flow to and away from the electrode and thus reduces the cooling of the plasma electrons. Such a magnetic effect on electron flow has been observed before.[20] In any case, the rapid cooling of the plasma electrons in response to turning off the electrode heating current shows that the plasma cooling effect is certainly not due to evolution of gas from the electrode.

As the experimental data given above illustrate, the auxiliary electrode clearly shifts the electron temperature of the discharge tube plasma over a wide range. In addition, the electron energy distribution appears not to be distorted but to remain a Maxwellian. The experimental data also show that as the electron temperature is reduced, the electron density apparently increases. Such an increase in density may be expected, because the thermal electron pressure[21] tending to drive plasma to the wall decreases as the electron temperature is reduced, decreasing the plasma loss.

There are many possible applications of this technique for varying plasma electron temperature. For example, in radio-frequency studies near the plasma electron frequency, the damping due to the finite transit time of electrons through the rf electrode system could be varied. In our own work we have observed that the velocity of ion acoustic waves[17] decreases as the electron temperature is reduced.

It is a pleasure to acknowledge the valuable suggestions of Roy F. Stratton, Ray Davis, and Dave Weaver concerning the construction of the oxide-coated probes. We also appreciate the help of J. G. Harris and B. B. Coulter, who constructed the vacuum system and the auxiliary electrode respectively.

[20] I. Alexeff, W. D. Jones, D. Montgomery, and M. Rankin, *Proceedings of the VII International Conference on Ionization Phenomena in Gases, Belgrade, Yugoslavia, August 1965* (to be published).

[21] I. Alexeff and R. V. Neidigh, *Phys. Rev.* **127**, 1 (1962).

4.8 HOT-ELECTRON PLASMA BLANKET

4.8.1 Introduction

The blanket, or annulus, that we have produced between mirror coils by an off-axis reflex discharge is known to possess two, and possibly three, energetic-electron distributions. Improved electrode design has permitted higher power dissipation and correspondingly more dense plasmas. A promising method has been discovered which has permitted a factor of 2 increase in the axial midplane magnetic field without detrimental effect upon the performance of the discharge.

4.8.2 Arc Electrode Modifications

V. J. Meece W. L. Stirling

The gradual increases in blanket plasma density since our last report[22] are largely due to the increased power input into the primary reflex discharges. Calorimetric power measurements have shown that approximately 55% of the input power is deposited on the anticathode, which is electrically insulated. In order to dissipate the high power densities, 30 to 50 kW/cm^2, an iron shield "beam expander" has been placed around the anticathode (Fig. 4.15). The effect of this shield on confining magnetic field is shown in Fig. 8.6. The resultant beam spread is about a factor of 5 increase. We have increased power input for single-arc operation by a factor of 2, up to 40 kW. Indeterminable spurious effects still occasionally cause damage to the anticathode surface. However, operational experience allows one to recognize those conditions of operation which are the most hazardous.

4.8.3 Temperature and Density Measurements

I. Alexeff V. J. Meece
W. D. Jones W. L. Stirling

We have concerned ourselves primarily with measurements of the intermediate- and low-energy

[22] *Thermonuclear Div. Semiann. Progr. Rept. Oct. 31, 1965*, ORNL-3908, p. 62.

ORNL-DWG 66-5258A

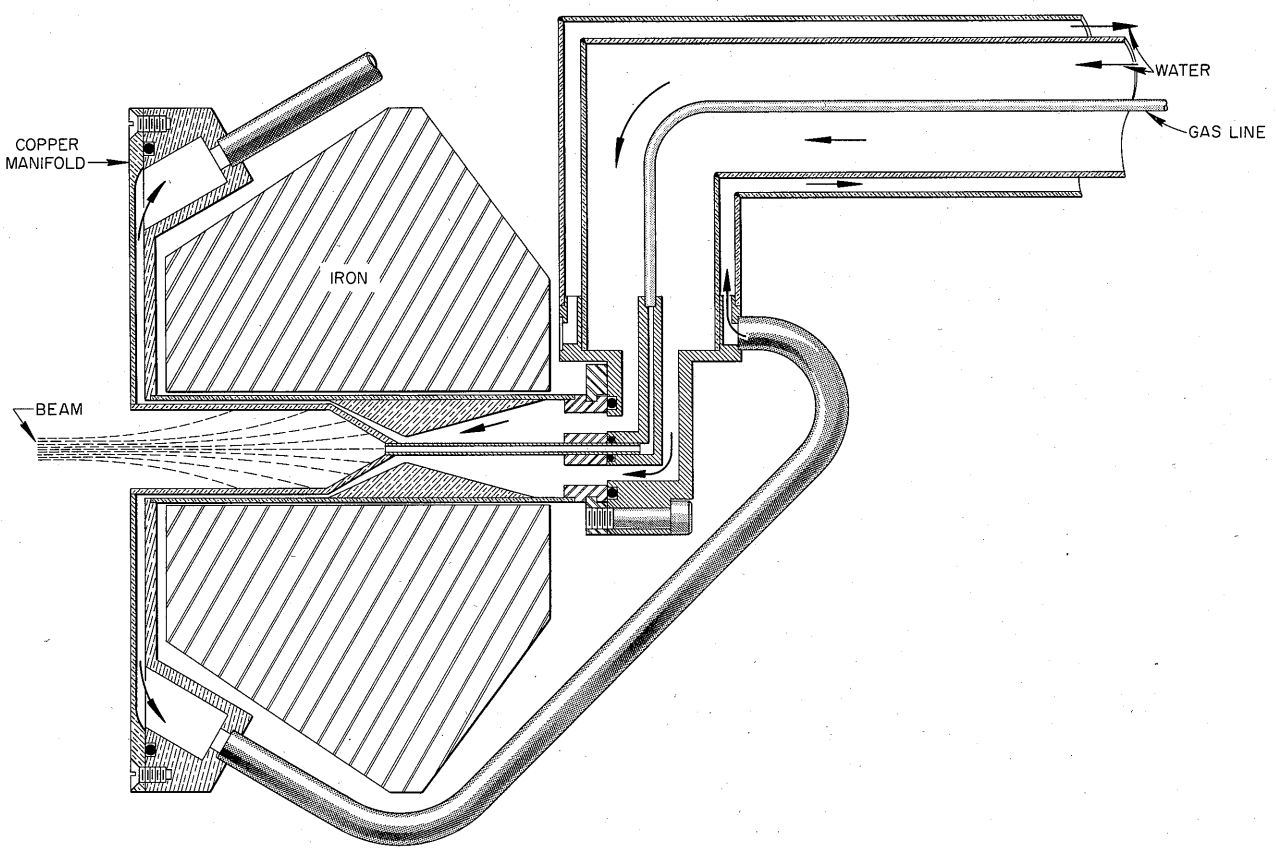

Fig. 4.15. Anticathode with Iron Beam Expander. The curvature of the magnetic field lines toward the iron spreads the power of the beam over an increased area of the internal anticathode surface.

electron distributions. We estimate from total x-ray-intensity measurements that the density of the 100-keV energy electron component is in the range of 10^9 to 10^{10} cm^{-3}, an increase by a factor between 10 and 100 since the last report.[22]

A great deal of difficulty is encountered when measuring the properties of the intermediate-energy electrons. The intermediate-energy component is defined as those electrons of energy sufficient to ionize the background gas but insufficient to produce x rays. The presence of these electrons may be easily observed by inserting a paddle into the annulus. The x-ray-producing distribution is wiped out, but the background gas is still being ionized, as evidenced by the streaming of cold plasma out the mirrors. We have measured the power delivered to the paddle, or probe, by the electrons drifting in the annulus. Since the power delivered to the probe per square centimeter is the product of the number of electrons per cubic centimeter, the energy per electron, and the average drift speed of the electrons, the density of the particles may be expressed in terms of the energy per electron, drift speed, and power to the probe. However, the drift speed in the existing magnetic field gradient is proportional to the energy of the particles. Assuming the electrons to be Maxwellian, the density is inversely proportional to the square of the energy for a given power dissipation. Thus an independent measurement of the electron drift speed, or energy, is needed to determine the electron density from the power delivered to the probe.

An attempt was made to measure the electron drift speed by perturbing the reflex discharge and looking at the resulting effect on a current probe 180° in azimuth away. The oscilloscope traces are difficult to interpret, possibly due to voltage pick-up other than that from the desired current variations. No conclusions have been reached.

We can impose only an upper and a lower limit to the temperature of the intermediate-energy electrons. An energy upper limit is determined by the fact that the electrons are non-x-ray-producing: $E_{max} \leqq 20$ keV. A lower limit can be determined from the assumption that the electron drift time for one revolution of the annulus is of the order of, or shorter than, the scattering time of the electrons out the mirrors. This assumption is reasonable, since there is negligible decay of the plasma with azimuth. This condition requires that $E_{min} \gtrsim 2$ keV.

Langmuir probe studies of the plasma annulus on the midplane indicate two electron distributions. Figure 4.16 shows a linear plot of the voltage-current characteristic. The long sloping tail at high negative voltages has been investigated out to 3 kV, but ion saturation is still not achieved. The conventional semilogarithmic plot yields an electron distribution with a mean energy of 100 eV. Extrapolation of the curve beyond −3 kV yields a value of the ion saturation current which, when subtracted from the meter reading, gives an electron current vs voltage characteristic. This characteristic shows the existence of another electron distribution with an electron temperature of 1.75 keV.

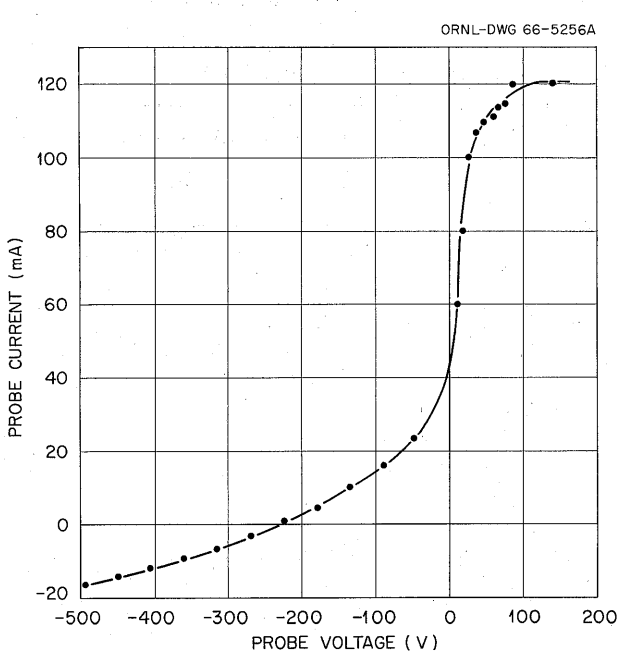

Fig. 4.16. Voltage-Current Characteristic for Probe on Midplane.

Since a 100-eV component is very short-lived, relaxation time about 20 μsec compared to about 200 μsec for a 2-keV distribution, we assume that the energy reaching the power probe is contained predominantly in an electron distribution of about 2 keV mean energy. Our power measurements then yield an electron density between 1 and 5×10^{11} cm^{-3}.

An independent determination of the electron density can be made. Knowing the gas density inside the machine and measuring the rate of flow of secondary plasma out the mirrors of the machine, one can compute the generation rate of secondary plasma inside the machine. Since σv for ionization is approximately independent of energy, the density of ionizing electrons is calculated to be about 2×10^{11} cm^{-3}. This figure falls well within the density figure of 1 to 5×10^{11} cm^{-3} determined above.

Spectroscopic studies, based on Doppler shifting of recombination radiation from the plasma, indicate little or no ion heating.

4.8.4 Diffusion of the Plasma

G. E. Guest W. L. Stirling

An attempt has been made to measure the radial diffusion of the plasma escaping from the annulus. A current probe located on the midplane was moved radially through the annulus. The azimuth of the probe was 90° from either arc and was therefore best situated to study the diffusion from the blanket and not from the discharge column itself. Unfortunately, the perturbation of the plasma by the probe increases as the probe penetration into the blanket increases. Since the drift velocity of the plasma along the magnetic field is very much higher than the azimuthal drift in the magnetic field gradient, the probe completely wipes out all plasma at a radius greater than the radius of the probe tip and all plasma at an azimuth greater than 90° (measured from the arc in the direction of ∇B drift) for the entire length of the machine.

Figure 4.17 shows a semilogarithmic plot of the probe current vs radial position from annulus center. The probe was biased to measure the ion current. The radial diffusion coefficient was calculated from that region of the curve for large radius in order to minimize the perturbing effects of the probe in the plasma.

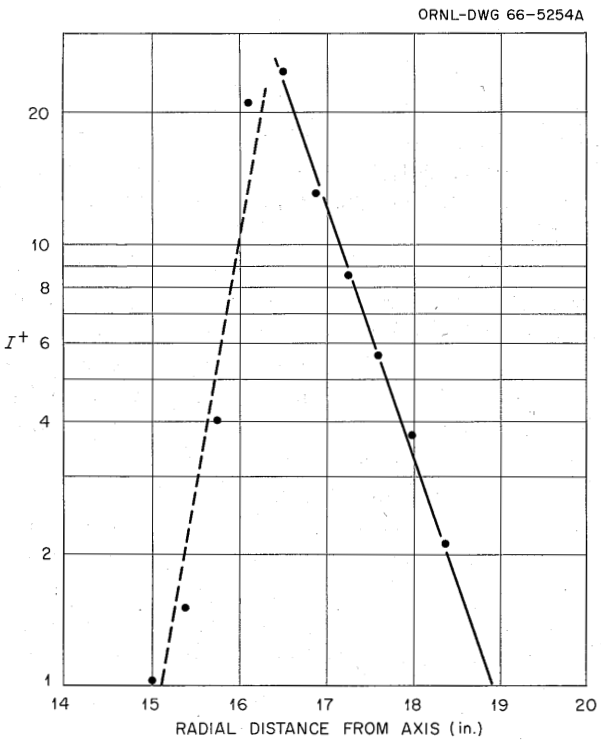

Fig. 4.17. Variation of Ion Current with Radial Distance from Magnetic Axis for Probe at Midplane.

Using the model of Simon,[23] we may infer a value of the perpendicular diffusion coefficient from the e-folding length X_0. For planar geometry, Simon showed that the density varied as exp $(-X/X_0)$; for cylindrical geometry, this becomes $r^{-1/2}$ exp $(-r/r_0)$. In the present case, the ratio of the blanket thickness ΔR to the radius of curvature R is $\Delta R/R \approx 1/5 \ll 1$; so that we shall use the planar geometry. The e-folding length X_0 and the diffusion coefficient $D_\perp$ are related by the following expression:[23]

$$D_\perp = \frac{2vX_0^2}{L},$$

where v is the ion thermal speed and L is the length of the plasma. We wish to compare the observed diffusion coefficient to the "classical" value based on binary collisions with neutral gas atoms,

$$D_\perp \text{ (classical)} = \frac{\lambda v}{3} \frac{1}{1 + \omega_c^2 \tau_{\text{coll}}^2},$$

where λ is the mean free path for scattering from neutrals, τ_{coll} is the mean free time, and ω_c is the ion gyrofrequency. For cases of interest to us, $\omega_c^2 \tau_{\text{coll}}^2 \gg 1$, and we can write

$$D_\perp \text{ (classical)} \approx \frac{2}{3} \frac{T_i}{eB} \frac{1}{\omega_c \tau_{\text{coll}}},$$

where T_i is the ion temperature and B is the magnetic field strength. Since the ion temperature is not well known experimentally, we observe that $T_i \sigma \sim 30 \times 10^{-15}$ cm^2 eV for 10 eV $\lesssim T_i \lesssim$ 100 eV, and rewrite $D_\perp$ (classical) in the form

$$D_\perp \text{ (classical)} \approx \frac{2}{3} \frac{T_i \sigma N_0 v}{eB\omega_c}$$

$$\approx \frac{(2 \times 10^{-14} \text{ cm}^2 \text{ eV}) N_0 v}{eB\omega_c},$$

where N_0 is the density of neutral atoms. Finally,

$$\frac{D_\perp \text{ (observed)}}{D_\perp \text{ (classical)}} \approx \frac{(2X_0^2/L)v}{2 \times 10^{-14} \text{ cm}^2 \text{ eV } N_0 v/eB\omega_c}$$

$$= \frac{X_0^2 eB\omega_c}{LN_0 \times 10^{-14} \text{ cm}^2 \text{ eV}}.$$

The experimental values are $X_0 \approx 2$ cm, $L \approx 150$ cm, $N_0 \approx 2 \times 10^{12}$ cm^{-3}, and $B \approx 1.5$ kG; hence

$$\frac{D_\perp \text{ (observed)}}{D_\perp \text{ (classical)}} \approx 300.$$

Since the observed rate is so much larger than the classical rate, one might compare it to the Bohm rate,

$$D_{\text{Bohm}} = \frac{10^5 T_e}{16B},$$

[23] A. Simon, *Proc. U.N. Intern. Conf. Peaceful Uses At. Energy, 2nd, Geneva 1958* **32**, 343–48 (1959).

with T_e in eV and B in kG. Thus

$$\frac{D_\perp \text{ (observed)}}{D_{\text{Bohm}}} \approx 3.2 \times 10^{-4} \frac{X_0^2 v_i B}{L T_e} \frac{\text{sec eV}}{\text{cm}^2 \text{ kG}},$$

or, if $v_i \sim 10^7$ cm/sec,

$$\frac{D_\perp \text{ (observed)}}{D_{\text{Bohm}}} \approx \frac{10^2}{T_e} \text{ eV}.$$

Since the proper value to use for T_e is in considerable doubt in this case, we shall only point out that the observed diffusion rate equals the Bohm rate for 100-eV electrons. In any event, the diffusion is much faster than the classical rate.

4.8.5 Investigation of Magnetic Field Effects

V. J. Meece W. L. Stirling

To be useful as an environmental plasma, the electron plasma blanket must be generated in magnetic fields higher than the nominal 1500 G axial midplane value now attainable. In general, the interaction will not generate the blanket at magnetic fields above 1800 G. Raising the field higher has the equivalent effect of throwing a short across the arc electrodes, causing the discharge to extinguish.

A $\frac{3}{8}$-in.-thick, 4-in.-ID iron cylinder was placed around the anode to reduce the field in the anode channel. Thus a stronger magnetic field in the machine would be necessary to bring the field value in the anode channel back up to the original operating value. With this modification, it was found that the optimum axial midplane field value rose to about 1900 to 2000 G. The magnetic field reduction in the center of the anode was about 25%. In addition, the power input has been increased to about 40 kW. These results may indicate the presence of an instability in the anode region of the type studied by Hoh[24] or Simon[25] which extinguishes or shorts out the discharge at sufficiently high magnetic fields.

Figure 4.18 shows the magnetic field present in the anode channel with a shaped $\frac{3}{4}$-in.-ID iron cylinder. The unperturbed field is also shown for comparison. The arrowheads indicate the spacing of the electrode surfaces, the anode being 5.5 in. long and the iron being 4.5 in. long. The cathode is positioned in the center of the 2:1 ratio mirror coil. With this arrangement we have successfully generated the blanket at a magnetic field of 4000 G, although operation is much more steady at 3000 to 3300 G. Under the operating conditions of Fig. 4.18, the axial midplane field is about 3100 G. The field in the center of the anode, with iron, is about 3000 G. This is about the same value of field in the anode when operating at 1500 G axial midplane field with no iron shielding about the anode. Estimates of the intermediate-energy electron density are a factor of 2 to 3 down from that obtained at 1500 G with no iron shielding. The interaction with iron shielding is not nearly so sharply tuned with magnetic field as is the case with no shielding.

Attempts to achieve a power input in the vicinity of 40 kW resulted in destruction of the anode. The inner wall of the anode melted at the location of the maximum magnetic field, point A, because of the iron end effect.

Figure 4.19 shows an anode and a field-producing coil which are now being assembled to replace the original anode and iron shield. This coil is capable of bucking out an applied magnetic field of about

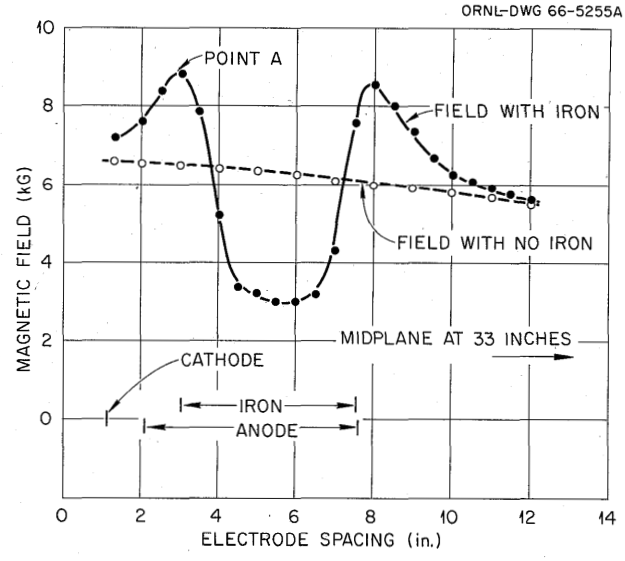

Fig. 4.18. Variation of Longitudinal Magnetic Field Intensity in Anode Channel. Axial midplane field about 3100 G.

[24] F. C. Hoh, *Phys. Fluids* **6**, 1184 (1963).

[25] A. Simon, *Phys. Fluids* **6**, 382 (1963).

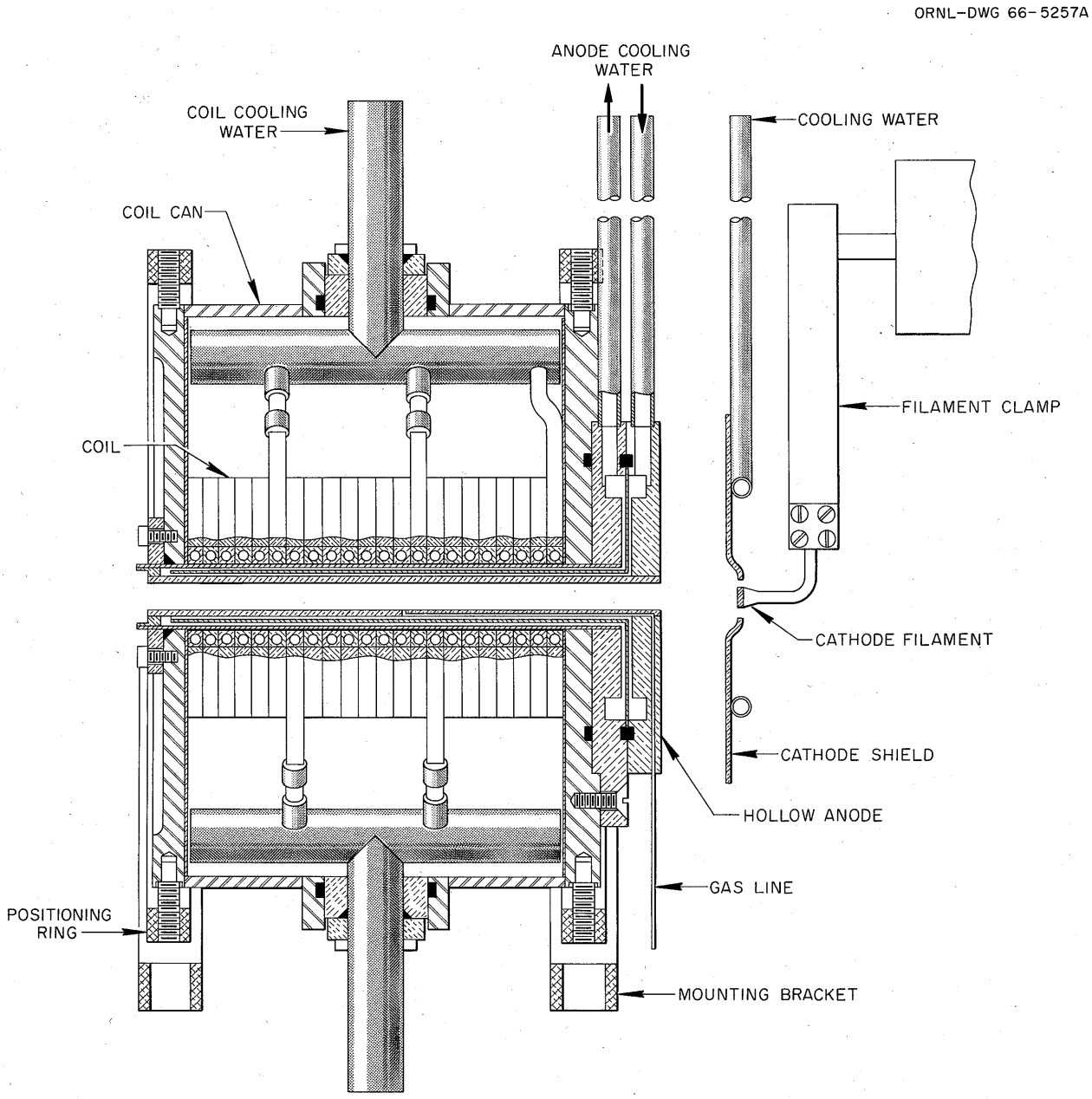

Fig. 4.19. Schematic of Anode-Cathode Assembly with Magnetic Field Bucking Coil Around Anode Channel.

18 kG, which is the maximum attainable with the present mirror configuration. It is hoped that the absence of the intense peaks caused by the iron end effects will permit further increases in power input to the discharge.

4.9 A CURVED ARC

J. F. Potts W. Halchin
P. R. Bell G. F. Leichsenring
W. K. Russell

4.9.1 Introduction

Some of us have been curious about the properties of magnetically collimated vacuum arcs in curved systems ever since the observations of peculiar burn patterns and particle deposits from curved carbon arcs in the DCX-1 experiment about 1957. More recently, concern with hydromagnetic instability of plasmas and observation of fluting in gas arcs led to questions about whether dc arcs in magnetic fields with a high degree of curvature might add to the understanding of anomalous plasma losses.

The immediate question was whether an arc could continuously run along a magnetic field possessing a high degree of curvature. Bell and Wright performed an experiment in a small apparatus,[26] in which they placed two small coils on adjacent legs of a glass pipe cross and ran a short carbon arc around a corner, giving rise to encouragement that a more refined apparatus might indeed work and provide interesting opportunities for study.

The first questions considered in the design of an apparatus to perform these curved-arc experiments concerned vacuum pumping requirements and diagnostics access – the bane of all curved plasma experimental systems. It was observed that if the system, including coils, weren't too large, placing spaced pancake coils inside a vacuum chamber would be practicable and would provide a unique freedom of access for both pumping and diagnostics. The first design effort was expended with the idea of "throwing something together." This wasn't completed when it became abundantly clear that one would want to compare equivalent straight and curved systems and provide flexibility against the possible subsequent needs of differential pumping, ultralow pressure, much diagnostics access, and completing the torus.

4.9.2 The J-Arc Facility

The facility constructed to fulfill the above objectives was so named because the discharge of initial interest resembled the letter "J." Although its design and construction involve a number of novel (to us) engineering features, such as an all-aluminum vacuum system, fully encapsulated coils,[27] smoothing by ferromagnetic shimming of magnetic field,[28] circulating hot water bakeout system, etc., the apparatus will be only briefly described here.

Figure 4.20 depicts an overall view of the J-Arc Facility. The insulated line in the foreground conducts liquid nitrogen from a remote Dewar to pump baffles. The vacuum pumping is accomplished by two independent systems, each containing a 10-in. oil diffusion pump with baffle and automatic gate valve. Because of its proximity to the plasma chamber, all vacuum components are nonmagnetic. Figure 4.21 shows the scale of the apparatus with projections of coils shown in all possible locations, with side and bottom openings illustrated. The top plate has 3-in. diagnostic ports between all toroidal coil locations. Figure 4.22 shows the eight-coil arrangement for a 22-in.-long straight arc (equal in length to a 180° bend in the curved arrangement). The multiple-pass water and electrical leads for the coil are encapsulated in epoxy and lead out past O-rings to epoxy-surface seals. Novel plastic fittings were used to connect water and electrical circuits. Figure 4.23 is a view of the under side of the tank, showing the external coil connections.

The magnet system is capable of producing a 5500-G axial field and, with the aid of existing magnetic shims (a compromise on coil internal diameter), less than 3% fluctuation in field over the central 1 in. of solenoid.

[26] C. Michelson, *Thermonuclear Proj. Semiann. Rept. July 31, 1959*, ORNL-2802, p. 55.

[27] J. F. Potts *et al.*, *Thermonuclear Div. Semiann. Progr. Rept. Apr. 30, 1965*, ORNL-3836, pp. 120–25.

[28] U. Christensen, *Princeton Plasma Physics Laboratory Annual Report for 1963*, pp. 371–73.

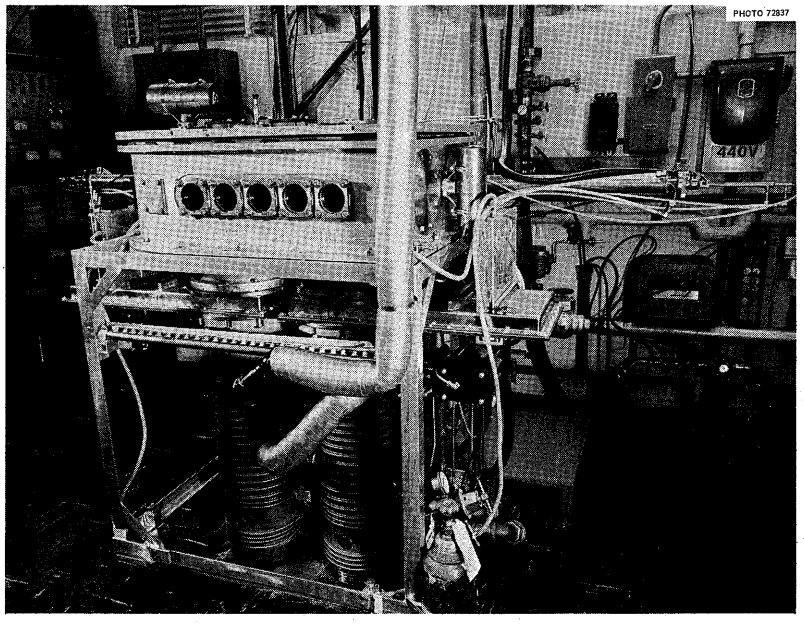

Fig. 4.20. The J-Arc Facility. Overall view.

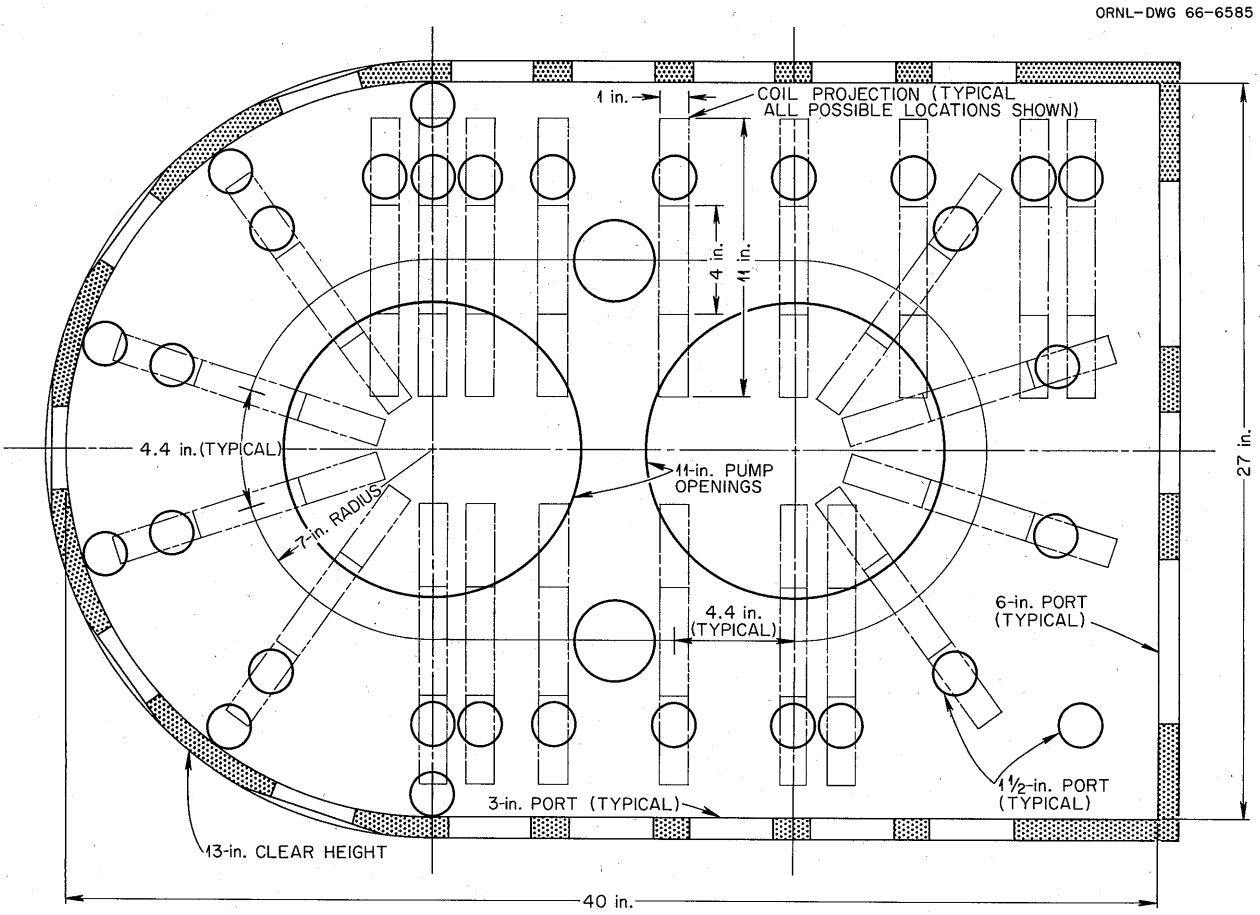

Fig. 4.21. The J-Arc Facility. Tank bottom and side layout.

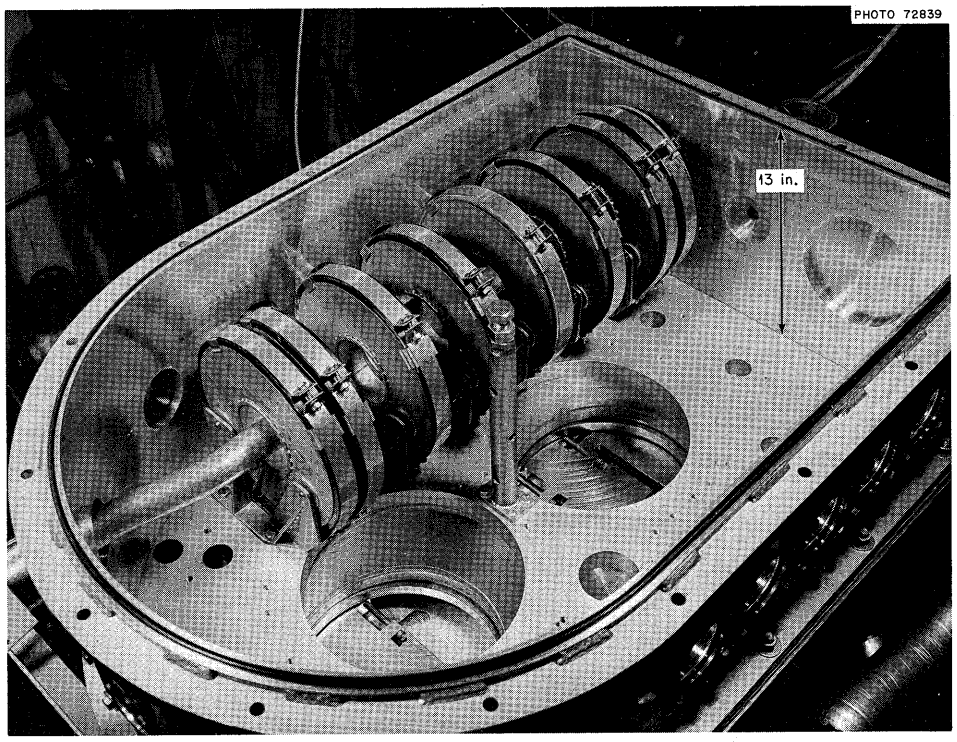

Fig. 4.22. The J-Arc Facility. Coils and electrodes arranged for 22-in.-long straight arc.

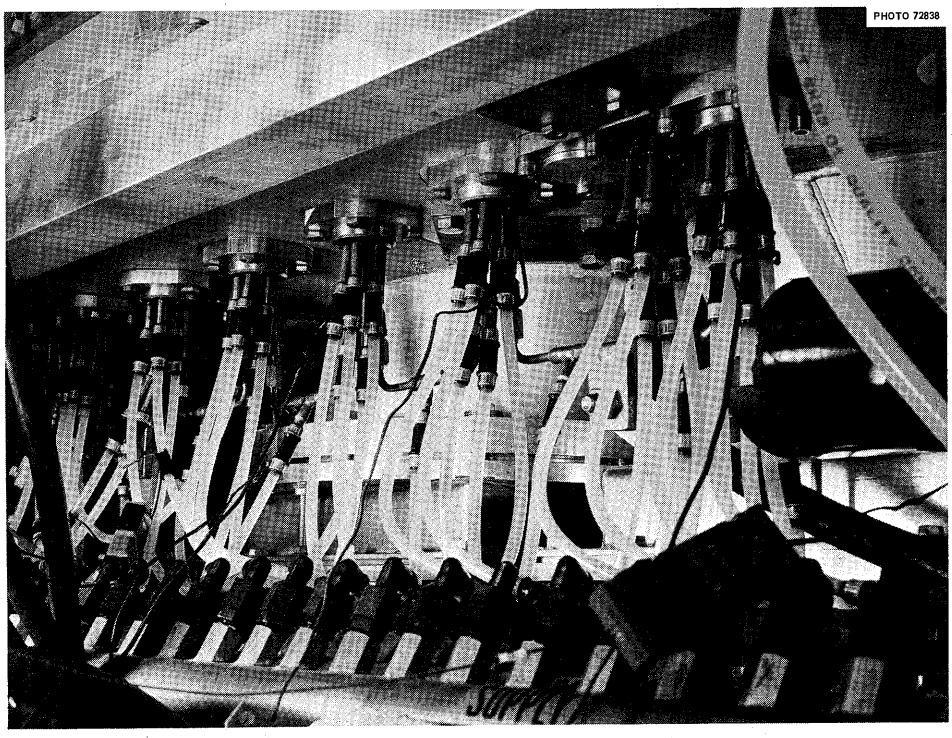

Fig. 4.23. Underside of J-Arc Facility, Showing Electrical Cooling Connections to Coils.

4.9.3 Results

To date only argon or helium arcs have been run in the facility, mainly because of the relative ease of operation of these arcs commensurate with a minimum of system contamination. The only real difficulties encountered were those associated with basic cathode design,[29] having nothing to do with the curved geometry. The arc is usually operated most stably with the cathode in an axially symmetric magnetic field environment, although successful operation has been realized with electrodes in the curved magnetic field. The system background pressure is distressingly high with stable argon-arc operation. A 22-in.-long straight arc can be made to operate at 2×10^{-5} torr background pressure with a 70-A arc current at 150 V dc and 4000 G magnetic field, whereas a 53-in.-long J-arc at similar magnetic field and current requires 200 V dc, and one realized 3×10^{-4} torr background pressure. In these cases about 0.5 std cm^3/sec of argon gas is only fed inside a $\frac{3}{4}$-in.-ID hollow water-cooled anode. The $\frac{1}{4}$-in.-OD self-heated tantalum cathode had its tip recessed $4\frac{1}{2}$ in. in an electrically isolated water-cooled sleeve of $1\frac{1}{4}$ in. inside diameter. Gas is fed into the cathode only until the cathode tip electron emission will support the arc.

Figure 4.24 shows a 53-in.-long argon J-arc in operation with a 2-in.-thick Lucite plate replacing the usual aluminum cover. This illustration makes clear that the whole system is communicating fairly directly to the pumping system and that the customary arrangement of arc or plasma pumping is missing. This can be supplied by use of appropriate baffles.

So far, the accomplishment with the facility (apart from the successful demonstration of several engineering innovations) is to show that the stable operation of dc arcs in configurations with a high degree of curvature can be obtained. The next step is, of course, to explore the details of these unique arcs.

[29] We particularly appreciate the valuable suggestions and advice generously given by J. E. Francis, Homer Terry, and Leroy Ellis.

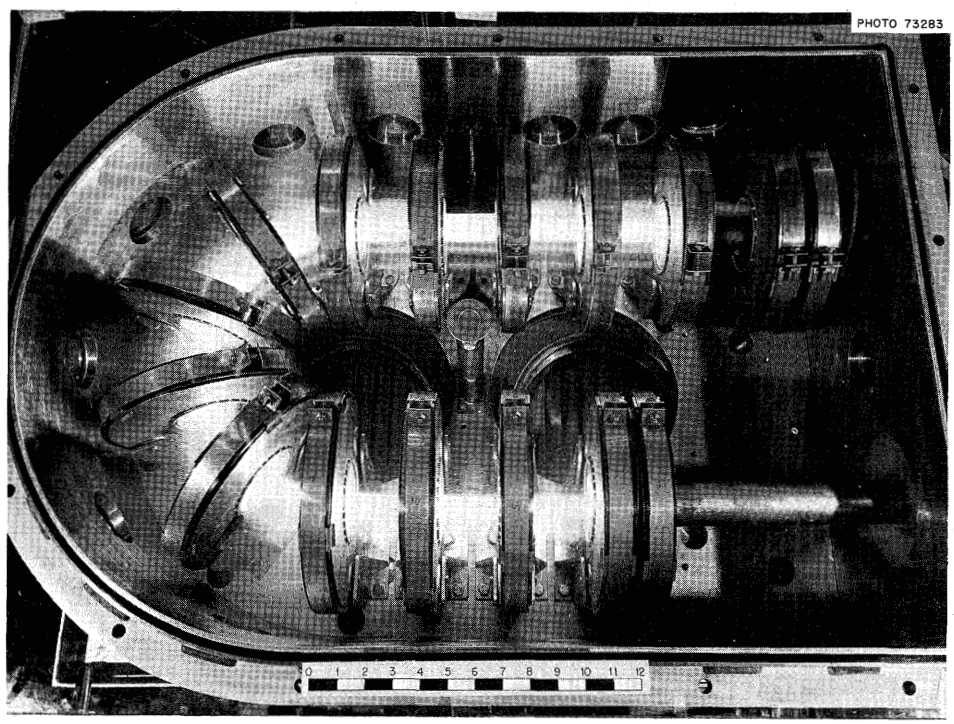

Fig. 4.24. The J-Arc Facility. 53-in.-long argon arc viewed through Plexiglas plate.

4.10 BOUNDARY WALL TREATMENT IN THE PENNING ION GAGE

D. E. Harrison[30] E. D. Shipley
O. C. Yonts

The Penning ion gage seems to offer a simple device for testing various forms of the boundary impedance network (BIN).

There are numerous types of oscillations possible in a Penning ion gage. These include plasma oscillation, cyclotron oscillations, electromagnetic wave modes of confining vacuum volume if the walls are conducting, and oscillation about the potential energy minimum due to the electric field of the anode ring. All these various modes can be coupled under proper conditions. For study it is necessary to eliminate some of the modes and coupled modes. Cavity modes can be largely eliminated by mounting the gage in a glass vacuum container. The resulting oscillations are much cleaner and more amenable to identification. The application of a modified BIN to the cathode wall further simplifies the observed oscillations. Figure 4.25 shows a diagram of a Penning or a Philips ion gage as modified for use in these experiments. The ring size and limiting geometry are always those of the Philips ion gage, which has been used so successfully for the past 20 years in the electromagnetic isotope separation plant. Oscillations can be detected by probes, antennas, or simple coupling into the external circuitry. Below 100 Mc it is immaterial which method is used. Figure 4.26 shows the electrical circuits. The flat cathode walls can be replaced by BIN walls of various types; however, only the plain and slotted stainless steel (316) walls of Fig. 4.25 are reported on here.

[30]Consultant, U.S. Naval Postgraduate School, Monterey, Calif.

ORNL-DWG 66-6586

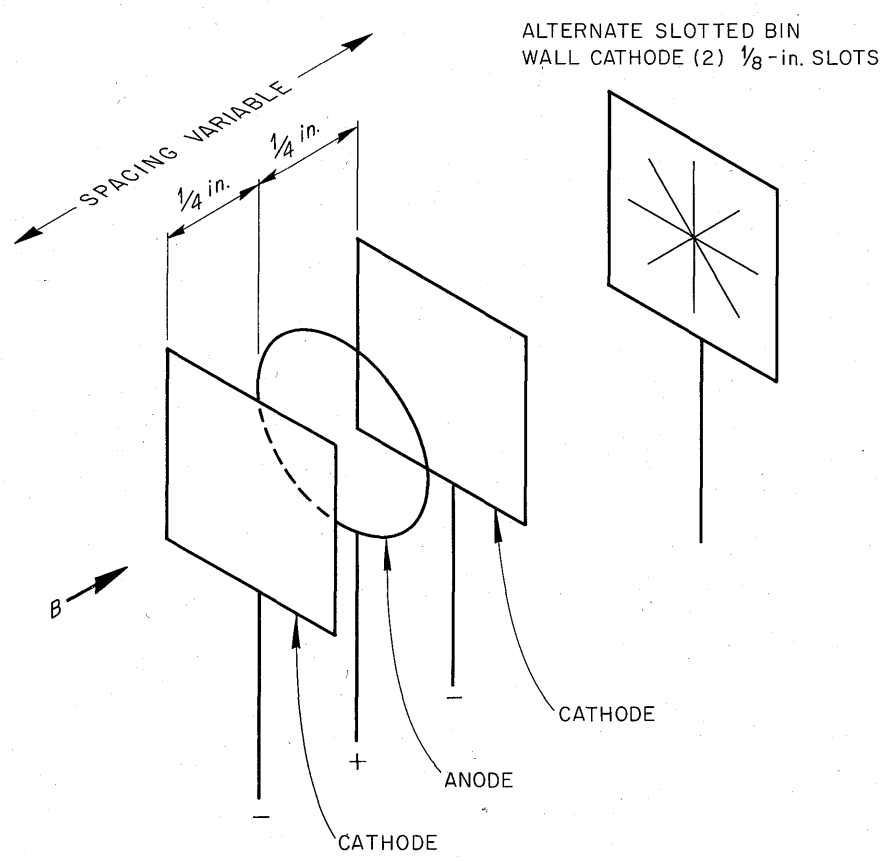

Fig. 4.25. Penning Ion Gage.

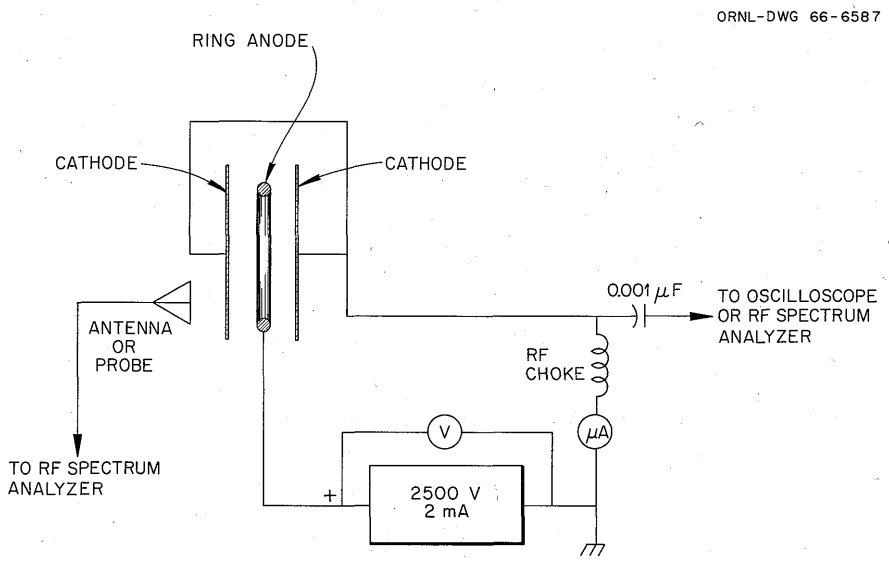

Fig. 4.26. Basic Electrical Circuit.

The following preliminary observations can be made for the Penning ion gage in a glass vacuum system:

1. Oscillations occur in pulses with a repetition rate proportional to pressure. The frequencies of the oscillations are below 300 Mc. Since the pulse time (Figs. 4.27 and 4.28) is inversely proportional to the pressure, a possibility is that the time is determined by the length of time to neutralize the space charge near the ring.
2. Oscillations in the pulses are due to electron motion of the $\mathbf{E} \times \mathbf{H}$ type. This is implied by the curve in Fig. 4.29 for a flat cathode gage, for which the frequency varies inversely with the magnetic field. Frequency measure is the center of a broad band $\approx$10 Mc wide.
3. Use of the BIN sharpens the bands so that the effects due to variation of magnetic field and electric field can be observed in greater detail. Figure 4.30 shows one curve for a slotted cathode-type BIN wall with a bandwidth $\approx$2 Mc. Figure 4.31 shows the change of rf spectrum as a pair of slotted BIN walls are rotated a few degrees with respect to one another. The bottom photo, when the slots are in alignment at the two ends of the apparatus, shows a behavior very similar to that of an ordinary flat cathode. The top photo, when slots are not in alignment, shows the emergence of a line spectrum. Dispersion in the photo is $\sim$10 Mc/cm; the center line of the photograph is 50 Mc.
4. Use of a BIN wall reduces the energy of slow ions falling out of the system, especially opposite the anode ring. Figure 4.32 shows the energy of slow ions as a function of position across the anode.
5. No frequency is observed which would correspond to electrons oscillating along the magnetic field through the potential well of the ring.

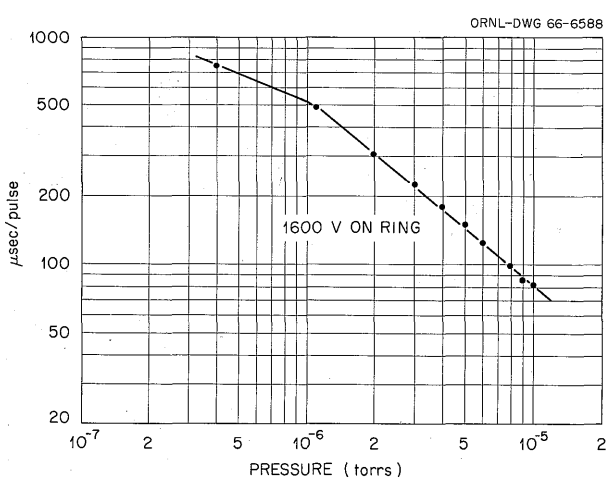

Fig. 4.27. Pulse Time vs Pressure for Penning Gage.

PHOTO 83992

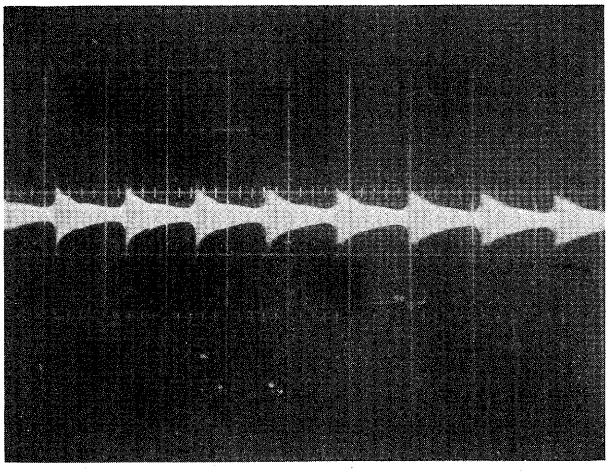

Fig. 4.28. Photograph of Pulses from Penning Ion Gage.

ORNL-DWG 66-6589

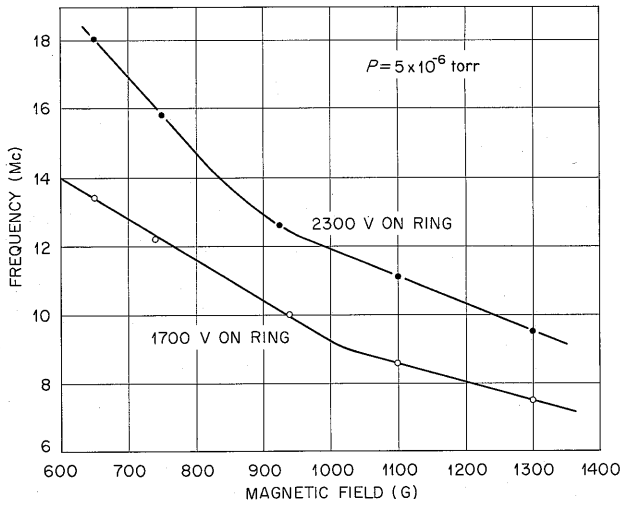

Fig. 4.29. Variation of Frequency with Magnetic Field for a Plain Flat Cathode Penning Gage.

PHOTO 83993

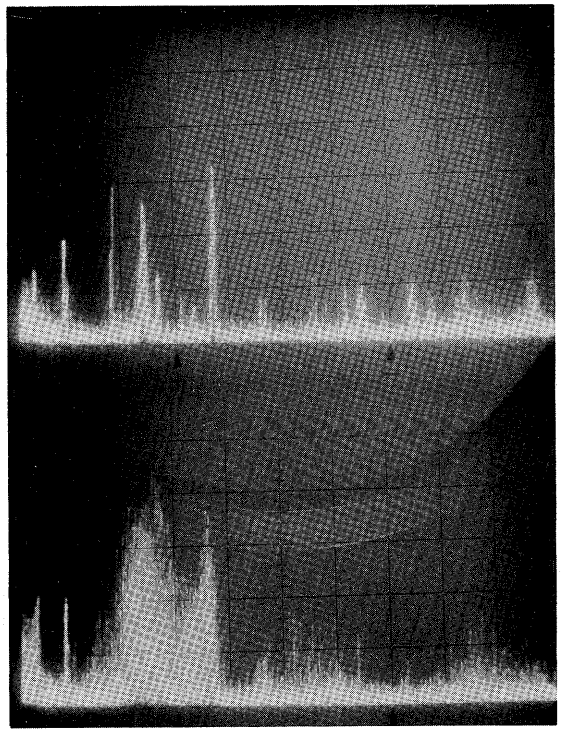

SLOTS NOT ALIGNED

SLOTS IN BINS ALIGNED

Fig. 4.30. Variation of Frequency with Magnetic Field for a Slotted Cathode (Modified BIN).

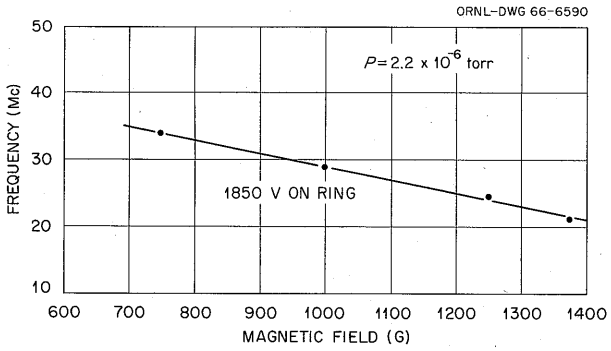

Fig. 4.31. Change in RF Spectra with BIN Rotation.

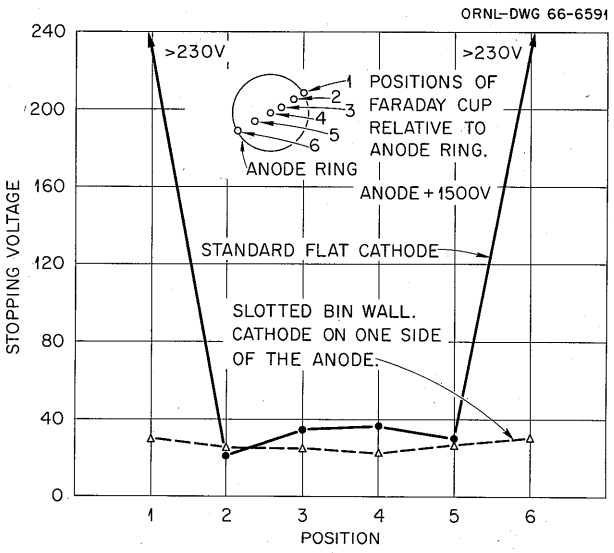

Fig. 4.32. Slow-Ion Energy as a Function of Position.

6. Oscillations of this type (item 5) can be introduced by injecting electrons from a gun. With the gun on the system center line, oscillations corresponding to electron time of flight can be introduced if an electron reflector is also placed on the center line; removal of the reflector stops the oscillation.

Future study will include frequencies below 5 Mc and above 1000 Mc.

4.11 FURTHER STUDIES OF THE EXCITATION HEATING OF IONS

J. Rand McNally, Jr. M. R. Skidmore
P. M. Jenkins

4.11.1 Introduction

During this report period we have made further studies of the very long, magnetically confined, low-pressure carbon arc and other arcs which exhibit hot ions ($T_{+\perp}$ up to 500 eV) in the presence of cold electrons ($T_{-} \sim 5$ eV).[31] This unusual dynamic equilibrium has been ascribed to a new chainlike inelastic collision process called *excitation heating*,[32] whereby (1) electrons excite the 6.5-eV metastable states of C^{2+}, (2) subsequent inelastic collisions between pairs of metastable ions result in ion heating, and (3) the cycle repeats many times. The densities of the ionic species C^{2+}, C^{2+*}, and C^{3+} have been determined by vacuum ultraviolet absorption spectroscopy, using two parallel carbon arcs 19 ft long, for various conditions. The data, though imprecise and preliminary, tend to support the excitation-heating theory.

4.11.2 General Discussion

Two standard ½-in.-diam carbon cathodes were introduced into the Long Solenoid Facility with appropriate insulators to permit separate operation from individual dc power supplies ($\gtrsim$300 A, 300 V capacity). A 6-in.-diam carbon anode served as a common anode. The 19-ft-long arcs were relatively stable at the separation distance of about 4 in. Repeat scans of individual spectral lines (see Table 4.1) indicated intensity repeatability of about 10% for either arc separately or both arcs operating simultaneously for short-term operation and excluding gross arc fluctuation. Several spectral scans were made on each line to eliminate gross fluctuation effects (as well as on the central image) using a 1-m Seya-type vacuum spectrometer.

Three sets of intensity measurements were required (see Fig. 4.33): (1) absorber arc alone (I_A),

[31] J. R. McNally, Jr., and M. R. Skidmore, *Appl. Opt.* 2, 699 (1963).

[32] J. R. McNally, Jr., *et al.*, *Appl. Opt.* 5, 187 (1966).

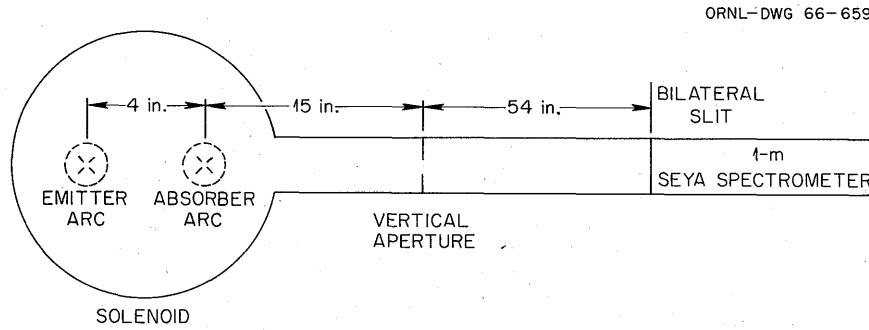

Fig. 4.33. Outline of Experimental Arrangement.

Table 4.1. Spectral Lines Used in Absorption Experiment

Wavelength (Å)	Ion Species	Transition[a]	f_{abs}	Excitation Potential of Lower Level (eV)
977	C^{2+}	$2s^2\ {}^1S_0 - 2s2p\ {}^1p_1^\circ$	1.08[b]	0.0
1175.7	C^{2+*}	$2s2p\ {}^3P_2^\circ - 2p^2\ {}^3P_2$	0.16[c]	6.5
1548	C^{3+}	${}^2S_{1/2} - {}^2P_{3/2}^\circ$	0.19[b]	0.0
2296[d]	C^{2+}	$2s2p\ {}^1P_1^\circ - 2p^2\ {}^1D_2$		12.7

[a]C. E. Moore, *Atomic Energy Levels*, NBS Circular 467 (1959).

[b]From H. Griem, *Plasma Spectroscopy*, McGraw-Hill, New York, 1964.

[c]Calculated by Bates-Damgaard method. Total population of $2p^2\ {}^3P$ levels $= 1.8 \times n({}^3P_2)$.

[d]Used as a control line for intensity normalization of I_{A+E}. Expected population <10% of ground-state population.

(2) both emitter and absorber arc (I_{A+E}), and (3) emitter arc alone (I_E). The relation between these measurements is

$$I_{A+E} = I_A + I_E e^{-k_\nu x} ,$$

where x is the effective thickness of the absorber arc (assumed 2 cm), and k_ν is the absorption coefficient,

$$k_\nu = k_0 e^{-[2(\nu - \nu_0)/\Delta\nu_D]^2 \ln 2}$$

$$\rightarrow k_0 \text{ at line peak,}$$

neglecting instrumental broadening effects. The absorption coefficient at the line peak is

$$k_0 = \frac{2\lambda^2}{\Delta\lambda_D} \sqrt{\frac{\ln 2}{\pi}} \frac{\pi e^2}{mc^2} n_i f_{abs} ,$$

where

λ = wavelength of line under study,

$\Delta\lambda_D$ = measured Doppler half-width of line,

n_i = density of ith class of absorbers populating lower level of the spectral transitions,

f_{abs} = absorption oscillator strength.

Since k_0, λ, and $\Delta\lambda_D$ are determined experimentally and f_{abs} can be calculated (see Table 4.1), the density of ions in different states can, in principle, be determined.

Preliminary estimates indicated that ion densities could probably be determined at the anode end of the arc, where the expected density and half-widths

were compatible with meaningful data reduction; however, as expected the densities at the cathode end were measured with considerable difficulty.

4.11.3 Results

Table 4.2 illustrates the preliminary results of several runs. The statistical errors were computed in terms of the reciprocal attenuation coefficients,

$$e^{k_0 x} = \frac{I_E}{I_{E+A} - I_A},$$

since the scatter was so bad in several cases as to indicate negative absorption! The uncertainty listed in the table is based on the standard deviation from the mean of the average reciprocal attenuation coefficient. The electron density is calculated by sum, assuming $n_e = 2 \Sigma n_{++} + 3n_{+++}$.

4.11.4 Discussion of Results

The following preliminary inferences can be drawn from columns 1 and 2 of Table 4.2:

1. The electron density of $\sim 10^{14}$ electrons/cm^3 confirms earlier measurements on various types of carbon arcs.
2. The total ion density is about one-tenth as high at the cathode end as at the anode end (also, $T_{+K} \sim 10T_{+A}$, so that $n_+ kT_+ \sim$ constant).
3. The density ratio, $\Sigma n_{++}/n_{+++}$, is higher at the cathode end than at the anode end. This agrees qualitatively with the greater emission ratio also observed at the cathode end, that is,

$$[I\ (977\ \text{Å})/I\ (1548\ \text{Å})]_K > [I\ (977\ \text{Å})/I\ (1548\ \text{Å})]_A;$$

however, the measurement of ion densities by absorption techniques is not as susceptible to variations in electronic excitation or other excitation processes.

4. The relative population of metastables, $n_{++*}/\Sigma n_{++}$, is lower at the cathode end than at the anode end. This agrees with the trend to be expected due to a preferential depopulation mechanism such as the excitation-heating process would provide (however, subsequent data did not confirm this trend).
5. The Saha electron temperature, based on the $\Sigma n_{++}/n_{+++}$ ratio, is about 27,000°K at the cathode end and about 28,000°K at the anode end. Thus, both electron temperatures are in reasonable agreement with the microwave diag-

Table 4.2. Ion Densities at Various Locations Along a 228 ± 2 in. Long Carbon Arc

Ion Species	Ion Density		
	40 in. from Anode (2 runs, 160 A)	186 in. from Anode (5 runs, 140–200 A)	186 in. from Anode (3 runs, 250 A)
C^{2+}	$1.3 \pm 0.1 \times 10^{13}$ ions/cm^3	$0.26^{+0.20}_{-0.22} \times 10^{13}$ ions/cm^3	$0.50^{+0.24}_{-0.27} \times 10^{13}$ ions/cm^3
C^{2+*}	$4.5 \pm 1.0 \times 10^{13}$ ions/cm^3	$0.31^{+0.23}_{-0.31} \times 10^{13}$ ions/cm^3	$2.7^{+1.4}_{-1.3} \times 10^{13}$ ions/cm^3
C^{3+}	$3.4 \pm 0.8 \times 10^{13}$ ions/cm^3	$0.16^{+0.31}_{-0.16} \times 10^{13}$ ions/cm^3	$2.0^{+0.4}_{-0.3} \times 10^{13}$ ions/cm^3
n_e (by sum)	2.2×10^{14} e/cm^3	0.16×10^{14} e/cm^3	1.2×10^{14} e/cm^3

nostic method, which gave 4 to 8 eV,[33] and the emission spectroscopic values, which range from 18,000 to 60,000°K, depending on the method of interpretation.[32]

6. An ion density of 2×10^{12} ions/cm^3 is extremely difficult to measure in an absorption path length of 2 cm for such wide spectrum lines (up to 0.7 Å) and for such small values of the oscillator strengths of λ 1175.7 Å ($f_{abs} = 0.16$) and 1548 Å ($f_{abs} = 0.19$).

Columns 2 and 3 of Table 4.2 suggest the following tentative conclusions:

1. Higher arc currents increase the total ion density in the cathode region. This seems to be in a direction to keep $n_+ kT_+ \sim$ constant, since $T_{+\perp}$ is observed to decrease with increase in current.
2. The relative population of metastables, $n_{++*}/\Sigma\, n_{++}$, increases for high arc currents. This suggests that the depopulation mechanism via ion-heating collisions is not as strongly operative and that excitation processes are therefore relatively more efficient.
3. The relative abundance of C^{3+} is higher for the higher arc currents. This would be expected to suppress the ion-heating collision rate due to fewer metastable-metastable collisions as well as due to the impurity cooling effect.
4. The Saha electron temperature is up slightly for the higher arc currents (i.e., $T_e \sim 28{,}000$ vs 27,000°K).

In summary, the hypothesis of the excitation-heating mechanism previously proposed[32,34] seems to be adequately supported by the observation of a large concentration of C^{2+} as well as metastable C^{2+*} in the carbon arc. The adjusted estimate for the required cross section in the cathode region for ion-heating collisions is increased by roughly $\Sigma\, n_i/n^* \sim 2.3$ to 5×10^{-15} cm^2 (see ref. 32, where σ was initially estimated as 2×10^{-15} cm^2 and $\Sigma\, n_i/n^*$ assumed to be 5/3).

4.11.5 Conclusions

Despite the uncertainties in the actual data, there appears to be reasonable supporting evidence for the excitation-heating mechanism previously proposed. We believe that the hypothesis of excitation heating has attained the status of a theory.

Improved measurements and data interpretation (including, e.g., corrections for instrumental broadening and more detailed correlations of parameters) would be desirable.

---

[33] W. B. Ard, Jr., *Thermonuclear Div. Semiann. Progr. Rept. Jan. 31, 1960*, ORNL-2926, p. 43.

[34] J. R. McNally, Jr., *et al.*, *Thermonuclear Div. Semiann. Progr. Rept. Oct. 31, 1965*, ORNL-3908, p. 82.

5. Atomic and Molecular Cross Sections

C. F. Barnett M. O. Krause R. A. Langley J. A. Ray

5.1 EXCITED STATES OF H, H_2, AND H_3

In previous semiannual reports we described measurements involving highly excited electronic states of H, H_2, and H_3. Excited states of H_2 were described as Rydberg states, analogous to the hydrogen atom with a single high quantum electron revolving around a stable H_2^+ core. This concept led to the prediction that H_3 would also be stable in such states and should be formed in a similar manner. Theoretical calculations have indicated that H_3 forms an antibonding, or repulsive, ground state and is therefore unstable. Owing to the difficulty in separating the collisional dissociative reactions from the electron capture collisions into the excited states, we had not been able to confirm the hypothesis that stable states exist when an excited electron is associated with a stable core. Recent measurements have confirmed the reality of these stable states of H_3.

Briefly, the apparatus consists of an accelerator and analyzing magnet to provide the required beam species. The beam passed through a hydrogen gas cell, where electron capture collisions occurred into all states. The charged component was removed from the beam, which was then passed through a parallel-plate electric field ionizer. Application of electric fields greater than 10^3 V/cm ionized the higher quantum states. These ions were then detected with a high-resolution silicon surface-barrier detector which was also used to detect the un-ionized neutral component. The ratio of ions formed by the electric field to the total number of neutral particles was then the fraction of particles in high quantum states.

In all the measurements of the H_2 excited state population an anomaly has been present. If the model of Rydberg states for molecules is correct, then the magnitude of the fraction of H_2 ionized at a given electric field should be the same as that for H. Also, the rate of increase of the fraction ionized as the electric field increased would be identical for both H_2 and H. These measurements have been repeated using better detection techniques than previously, and the results are shown in Fig. 5.1. Shown is the fraction ionized as a function of the applied electric field for equal-velocity H and H_2, which corresponds to particle energies of 40 and 80 keV. The accuracy and repeatability of the measurements are ±10%. Here again we find that both the magnitude and the slope of the yield curves are different for H and H_2. The velocity of the particles was increased to where the Born approximation should be valid and to where there should be less mixing of the internal states. These results are shown in Fig. 5.2 for 100-keV H and 200-keV H_2. The results are obviously similar to those shown in Fig. 5.1, with the data suggesting a mechanism for loss of H_2^+. If

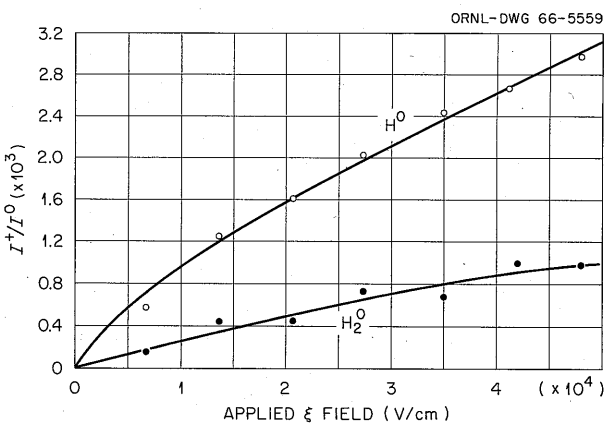

Fig. 5.1. Integral Excited-State Population of 40-keV H and 80-keV H_2 Formed by Electron Capture Collisions in Hydrogen Gas.

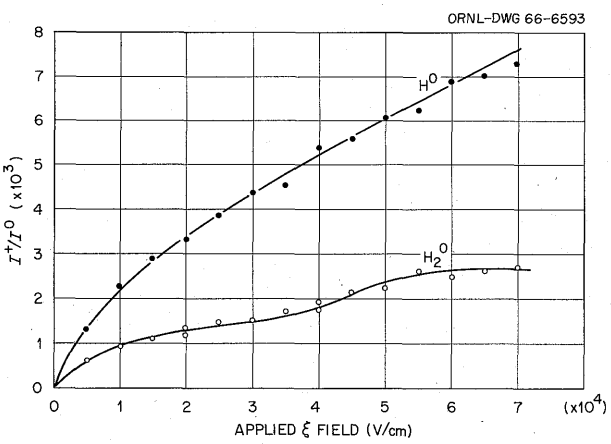

Fig. 5.2. Integral Excited-State Population of 100-keV H and 200-keV H_2 Formed by Electron Capture Collisions in Hydrogen Gas.

processes occurring in the electric field region are examined, one finds that as the H_2 entered the region of intense field the electron was immediately stripped, leaving the H_2^+ ion in indeterminate vibrational and electronic states. If these states were antibonding, or repulsive, the H_2^+ would be dissociated and thereby not detected as an H_2^+ ion. Another possibility existed if the ion was formed in a stable, electronic state but subsequently dissociated by the presence of the electric field. The magnitude of the dissociation depends upon the population of the $\nu = 17$ and $\nu = 18$ vibrational level of the H_2^+ ion when in the ground electronic state. If the H_2^+ ion formed in the electric field possesses the same vibrational level populations as the H_2^+ from the accelerator and before the electron capture collision, then the vibrational level population is approximately an order of magnitude less than that needed to account for the present discrepancy. However, we do not know if a rearrangement of the vibrational levels occurred during the electron capture process and the subsequent electric field ionization of H_2.

The magnitude of both processes, (1) ionization giving rise to antibonding levels and (2) further field ionization of H_2^+, should depend on the strength of the applied electric field. In Fig. 5.3 the difference in the fraction of H and H_2 ionized is plotted as a function of the applied electric field. This difference increases with field as expected; however, the curve fits no simple power or exponential relation, suggesting that the anomaly results from more than one process.

Experiments involving H_3 are difficult because of the many particles resulting from dissociative collisions and electron capture collisions into repulsive states, and because of our inability to experimentally distinguish between these two types of collisions. The energetic H_3 neutral particles must be detected in a background of 10^4 to 10^5 H and H_2 particles. To increase the signal-to-noise ratio in the present experiment, only the H_3^+ particles resulting from field ionization were detected. Since most of the capture collisions are into the repulsive ground level and since the H_3 signal-to-noise ratio is so small, it was necessary to normalize the data to H_2 data taken at a field of 2.8×10^4 V/cm. The results of these measurements are shown in Fig. 5.4, where the normalized fraction is plotted as a function of the electric field. Also shown for direct comparison are the same results for H_2 as are shown in Fig. 5.1. The rate of increase of the ionized fraction of H_3 approximates that of H_2, indicating that the same secondary processes occur for H_3^+ as for H_2^+. The errors associated with the H_3^+ measurements are large, ±50%. We have concluded that highly excited H_3 does exist, although these states can only qualitatively be identified with the hydrogen-atom Rydberg states.

Additional measurements have been made of the excited levels of H formed by capture collisions in H_2 gas. As a check of the present electric field ionizer geometry, we have compared the results of the excited-state population for 180-keV H with

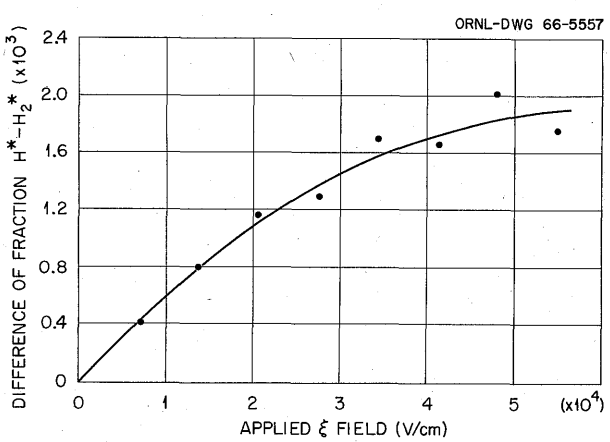

Fig. 5.3. Experimental Difference of Excited-State Population for 40-keV H and 80-keV H_2 as a Function of Electric Field Strength.

those obtained by Il'in *et al.*[1] The results are shown in Fig. 5.5, where the integral fraction is plotted as a function of the electric field. For reference, a field of approximately 4×10^4 V/cm will ionize all levels of $n \geqq 12$. A constant difference exists between the two results. The fractional discrepancy is small at higher field strengths, but at fields of $(1-2) \times 10^4$ V/cm the results differ by a factor of 2. In the present work no correction was made for the field distortion resulting from the apertures in the parallel electrode structure, since the apertures were 0.010 in. and the gap spacing was 0.030 in. If this small correction were made, the discrepancy would be slightly greater.

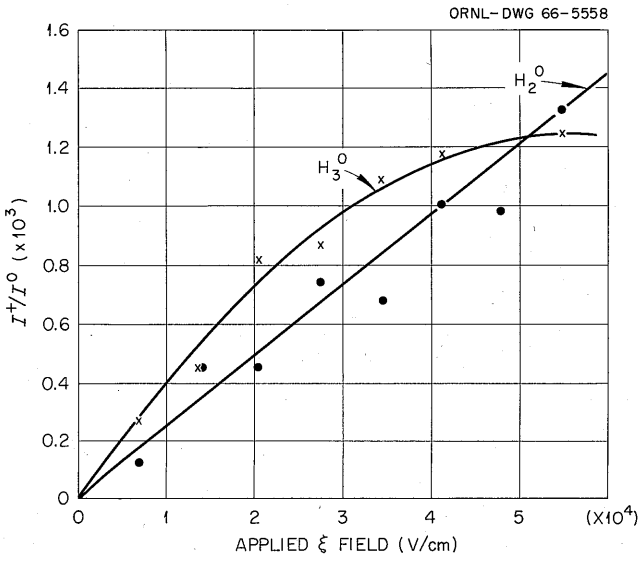

Fig. 5.4. Normalized Integral Excited-State Populatior of 120-keV H_3 Compared with 80-keV H_2.

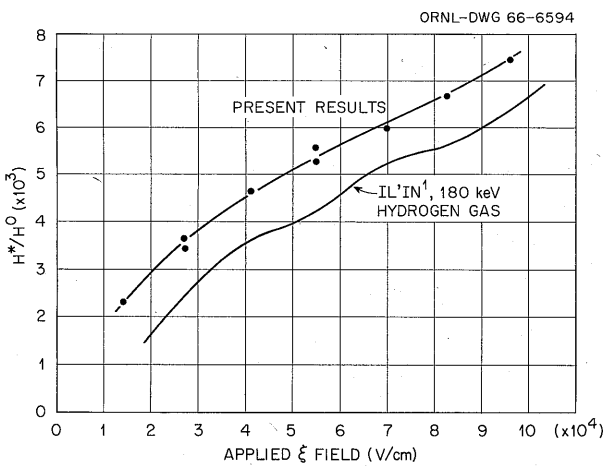

Fig. 5.5. Integral Excited-State Population for 180-keV H Formed by Electron Capture Collisions in Hydrogen Gas.

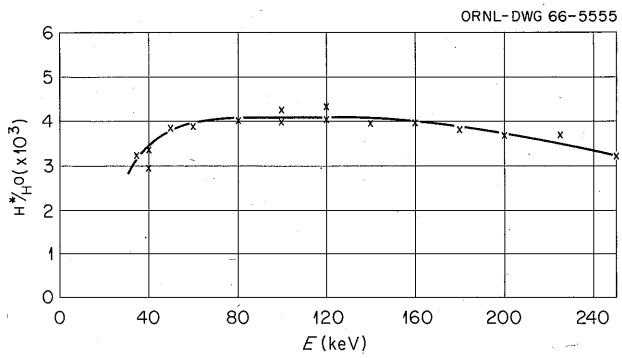

Fig. 5.6. Fraction of H Particles in States $n \geqq 12$ as a Function of Particle Energy. Hydrogen gas cell.

For velocities where the Born approximation is valid ($v > 10^8$ cm/sec), Oppenheimer[2] showed that the probability of charge exchange into high n levels was proportional to n^{-3}. Recently, many investigators have adopted the practice of extrapolating this same relationship to lower energies. To determine the range of validity of this assumption, the integral population of states $n \geqq 12$ was measured, and the results are shown in Fig. 5.6. If the n^{-3} prediction is valid, then the integral fraction should be constant, as is indeed indicated in Fig. 5.6 for energies greater than 60 keV. Below 60 keV the integral fraction decreases, indicating a steeper dependence on n than the n^{-3} dependence.

5.2 CHARGE STATES OF ATOMS FOLLOWING READJUSTMENT TO INNER-SHELL VACANCIES[3]

It was shown earlier[4] that creation of an inner-shell vacancy in an atom will, as a rule, lead to multiply charged ions following reorganization of the orbital electrons. Extent of self-ionization

---

[1] R. N. Il'in *et al.*, *Soviet Phys. JETP* **20**, 835 (1965).

[2] J. R. Oppenheimer, *Phys. Rev.* **31**, 349 (1928).

[3] In collaboration with T. A. Carlson, Chemistry Division.

[4] E. P. Cooper, *Phys. Rev.* **61**, 1 (1942); O. Kofoed-Hansen, *Phys. Rev.* **96**, 1045 (1954); A. H. Snell and F. Pleasonton, *J. Phys. Chem.* **62**, 1377 (1958).

has been studied in recent years[5] by using x rays for the initial ionization and then employing a mass spectrometer to measure abundances of the ions formed. In this systematic study we have produced initial vacancies in various atomic shells of helium, neon, argon, krypton, and, most recently, xenon and mercury. Average charges of the resulting ion charge distributions[6] are plotted in Fig. 5.7 as a function of atomic number for *K*, *L*, and *M* shells. The experimental points for the rare gases are shown at *Z* values of 2, 10, 18, 36, and 54. Also shown are calculated values for elements with atomic numbers 3 to 35 and also 86. For many of these elements the atoms do not exist in the free state but are bound in molecules or lattices. However, the family of curves shown in Fig. 5.7, which gives the average charge of the ions, is also valid for atoms in molecules or solids. These bound atoms, even when surrounded by electron donors, will attain the same or approximately the same average charge as free atoms, though only for a very short time, approximately 10^{-15} sec. The temporary creation of such strong electron sinks of atomic dimensions has several consequences. For example, in a gaseous molecule,[4,7] electrons from adjacent atoms are attracted, the electrical field is in the neighborhood of 10^{10} V/cm, and the "collection" of positive ions is driven apart by Coulomb forces (Coulombic explosion of the molecule), giving the charged fragments kinetic energies in the order of 10 eV. In the liquid or solid phase, various disorders can be expected, such as vacancy clusters, Frenkel defects, and color centers (by the Varley mechanism).

Data such as shown in Fig. 5.7 enable investigators who use ionizing radiation or projectiles to determine electron losses associated with inner-shell ionization and to evaluate subsequent effects.

5.3 MEASUREMENTS OF KINETIC ENERGIES OF H^+ AND H FOLLOWING DISSOCIATION OF H_2 BY ELECTRON IMPACT

Mechanical construction of a combined mass and energy analyzer, described in the previous report, has been completed, and the various components have been tested. Mass resolution of the mass spectrometer (of the time-of-flight type) was about 1% for a ¾-in.-diam entrance aperture. The

[5] M. O. Krause *et al.*, *Phys. Rev.* **133**, A385 (1964); T. A. Carlson and M. O. Krause, *Phys. Rev.* **137**, A1655 (1965).

[6] T. A. Carlson, E. W. Hunt, and M. O. Krause, to be published.

[7] S. Wexler and D. C. Hess, *J. Phys. Chem.* **62**, 1382 (1958); T. A. Carlson and M. White, to be published in the *Journal of Physical Chemistry*.

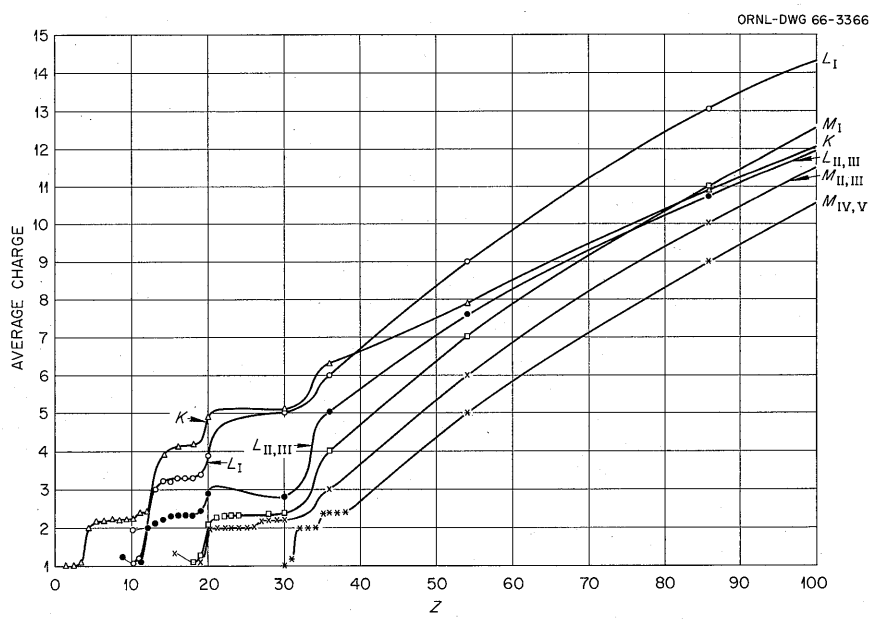

Fig. 5.7. Average Charge of Ions Produced by the Reorganization of Atoms Initially Ionized in an Inner Shell.

signal-to-noise ratio for the mass analyzer section was 10^3 at pressures of the order of 10^{-7} torr. Preliminary tests of the energy analyzer section indicated an energy resolution of about 10%. Tandem operation of the mass and energy analyzer has not been possible because of the delayed delivery of a 100-Mc scaler, an essential part of the electronic circuitry. With completion of the associated electronics, measurements of the kinetic energies of H^+ and H particles will begin in the near future.

5.4 HIGH-ENERGY CHARGE-EXCHANGE CROSS SECTIONS[8]

The electron capture (σ_{10}) and electron loss (σ_{01}) cross sections are to be measured for H^+ and H in H_2, N_2, CO, CO_2, CH_4, and H_2O in the energy range 0.25 to 2.8 MeV. These molecules, major contributors to impurities of vacuum systems, are of particular interest in the study of thermonuclear devices, such as DCX-2, due to their interaction with various constituents of the plasma and with input beams.

Protons are provided by a 3-MeV Van de Graaff and are incident on an apparatus consisting of: (1) a collision chamber to produce H, (2) a set of electrical deflection plates to remove H^+ when σ_{01} is being measured, (3) a differentially pumped collision chamber where σ_{01} and σ_{10} are measured, (4) an electrostatic analyzer to deflect H^+, and (5) two silicon surface-barrier detectors and a Faraday cup detector.

The cross sections to be measured are anticipated to be of the order of 10^{-24} cm^2;[9] therefore, it is necessary to maintain the pressure in the electrostatic analyzer sections and the detector section to less than 10^{-3} of the pressure in the collision chamber.

All components of the system have been fabricated, assembled, and pumped to a base pressure of 2.5×10^{-9} torr. First attempts to obtain data were unsuccessful owing to the failure of the machine shop to hold to specified tolerances, resulting in misalignment of the collision chamber apertures.

[8]In collaboration with L. Toburen, Health Physics Division.

[9]C. F. Barnett and H. K. Reynolds, *Phys. Rev.* **109**, 355 (1958); R. V. Pyle, *Phys. Rev.* **140**, A729 (1965).

5.5 DETECTION OF LOW-ENERGY NEUTRAL ATOMS

Modifications to both the electronic and physical geometry for silicon surface-barrier detectors have resulted in pushing the energy resolution of these detectors down to 1.8 keV. Attempts to extend the energy range below 6 to 8 keV have resulted in failure caused mainly by the signal pulses becoming embedded in the noise pulses. In addition to the noise problem, the direct transfer of momentum to the atoms of the crystal becomes an energy sink, and this energy lost in the hard collisions is not available to produce electron-hole pairs, so that the result is smaller signals. Direct transfer of momentum becomes of increasing importance in detecting particles of higher mass.

To overcome these problems, secondary electron emission from heavy-particle impact on solids has been investigated to determine its adaptability as a quantitative detector of low-energy neutral particles. Both Afrosimov and Daly[10] have constructed a detector in which the incoming particles impinge on a metallic plate, giving rise to secondary electrons which are accelerated to 20 to 40 keV. These electrons are then collected by a scintillation detector, whose pulse spectrum is a broad band above the inherent noise of the detector system. In the present series of experiments the scintillator was replaced with a high-resolution silicon surface-barrier detector, shown schematically in Fig. 5.8. The incoming neutral particles strike a copper target mounted at 30° to the beam and are then accelerated by a negative 15-kV bias

[10]N. R. Daly *et al.*, *Nucl, Instr. Methods* **36**, 226 (1965); N. R. Daly, *Rev. Sci. Instr.* **31**, 264 (1960); V. V. Afrosimov *et al.*, *Soviet Phys. – Tech. Phys. (English Transl.)* **5**, 1378 (1961).

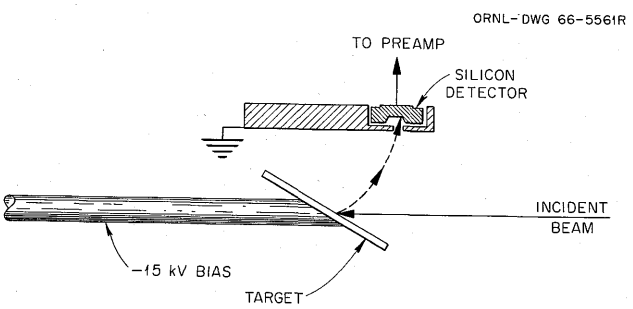

Fig. 5.8. Schematic Diagram of Secondary Emission Detector Geometry.

to the detector. Initially, the detector was replaced with a conducting glass plate coated with zinc sulfide. With the incoming beam collimated to $\frac{1}{4}$ mm and with the glass plate mounted in the detector position approximately 2 cm from the copper plate, the focus of the electrons was a 1-mm-diam visible spot. With this spot size, which was much less than the area of the 50-mm^2 detector, no additional focusing lens elements were necessary.

Typical pulse spectrum curves are plotted in Figs. 5.9 and 5.10 for 2- and 20-keV H, respec-

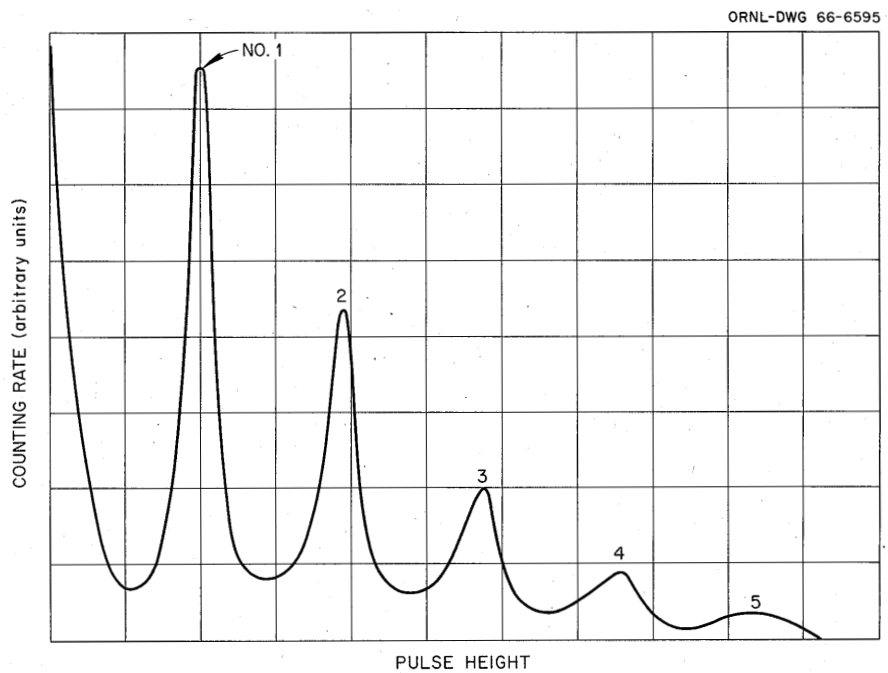

Fig. 5.9. Pulse Spectrum for 2-keV H on Copper.

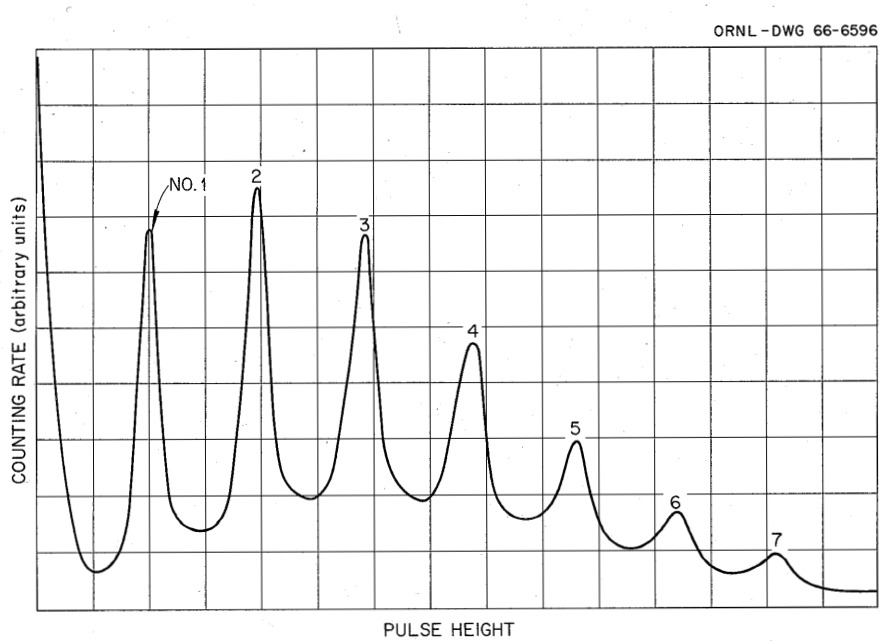

Fig. 5.10. Pulse Spectrum of 20-keV H on Copper.

tively, impinging on a "dirty" copper target. Shown is the number of counts per unit energy interval as a function of the pulse height. The most striking feature of the electron spectrum is the many peaks, or groups. As the H particles interact with the copper lattice, secondary electrons are emitted, with a certain probability that each incident particle will liberate 0, 1, 2, 3, ... electrons. The peak labeled 1 results from one electron being emitted, accelerated to 15 keV, and giving rise to a 15-keV pulse. The peak labeled 2 arises from each incident particle liberating two electrons which arrive at the silicon detector in coincidence. The electron energies add to form a 30-keV pulse. In this manner the detector will identify the number of electrons per incident particle, and from Fig. 5.10 one observes groups of up to seven electrons per H. Comparison of Figs. 5.9 and 5.10 shows that as the H energy is increased from 2 keV to 20 keV, the pulse-height spectrum shifts toward the higher peaks, implying increased secondary electron yield as the particle energy increased, which is well known. This shift of yield from copper was true throughout the H energy range of 2 to 50 keV. Similar spectra of this type have been obtained by Haussler[11] for low-voltage electron impact on Be-Cu and NaCl targets.

The most sensitive variable parameter in these measurements was the negative bias on the copper target which determined not only the electron focusing but also the efficiency of the silicon detector in counting the electrons. To determine the optimum negative bias, the counting rate of the detector was determined for a constant H beam impinging on the copper plate as the bias was varied. These results are shown in Fig. 5.11, where the counting rate saturates at −14 kV. All succeeding measurements were taken with −15 kV on the target. Excessive electrode voltages induced corona, which contributed to the background, or noise.

These observations suggest that a system such as this could be adapted as a quantitative detector of neutral particles. The sum of all the pulses was the number of H particles incident on the copper target if it is assumed that all H produce at least one electron. Further remarks on the efficiency will be made in the next section. The pulse spectrum shifted to higher pulse heights as the H energy was increased, indicating that the relative intensities of the various groups were sensitive to particle energy. The ratio of the intensities of the various groups to the intensity of the first group was determined as a function of the energy. Part of the results are plotted in Fig. 5.12 for peaks corresponding to five, six, seven, and eight electrons. A linear relationship exists for the ratios for H energies less than 30

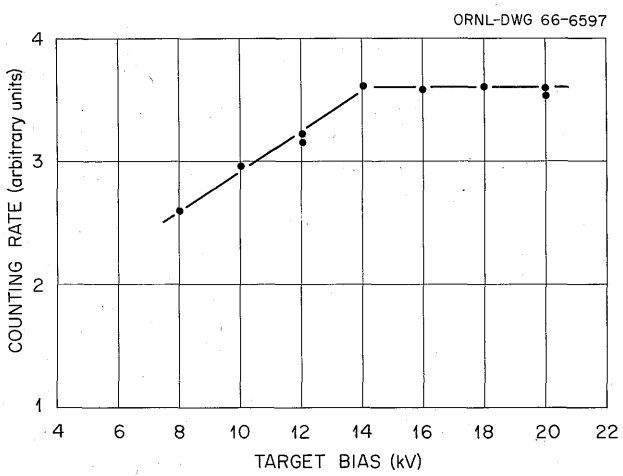

Fig. 5.11. Electron Counting Rate as a Function of Target Bias.

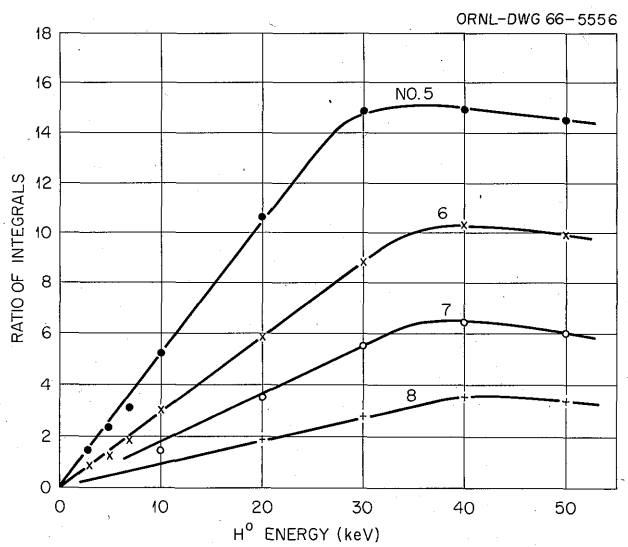

Fig. 5.12. Ratio of the Area of Electrons in Groups 5, 6, 7, and 8 to Group 1 as a Function of H Energy. H on copper with −15-kV bias.

[11] P. Haussler, *Z. Physik* **179**, 276 (1964).

to 40 keV. For groups 2 to 4, this linear relationship holds for energies of <20 keV. By determining the ratio of these groups, the average energy of the incoming H beam can be determined. To verify this statement, equal numbers of H at 4, 8, and 12 keV were allowed to strike the target. The pulse spectrum of the combined energies is shown in Fig. 5.13. Comparison of the ratio of the number of electrons in group 5 to group 1 with a previous calibrated curve gave the expected average energy of 8 keV. Comparison of group 6 to group 1 resulted in an average energy of 7.7 keV.

The advantage of such a detector is that neutral particles can be measured down to near zero energy. Disadvantages include: (1) only average energy can be determined rather than energy spectrum, (2) the absolute efficiency is unknown at the present time, and (3) small response changes of approximately 10% that occur from day to day necessitate frequent calibration. This last disadvantage is probably a surface effect and can be removed by ensuring cleaner surfaces in the vacuum system.

The system worked equally well for detecting protons. Since the target was maintained at −15 kV, the protons were accelerated this additional amount before striking the target surface, resulting in a different response for neutral and charged beams. In addition, the electric field existing between the target and detector deflected the charged beam slightly, requiring a change in target position. Use of detectors with larger areas (200 mm^2) would eliminate this problem.

The detector response for heavier particles was determined for neon atoms in the energy range 2 to 15 keV. In general, the secondary emission was higher, resulting in a shift of the pulse spectrum to a higher electron peak. No other differences were noted in the operational characteristics of the system in detecting neon.

An attempt was made to improve the detector by replacing the copper target with an Ag-Mg target removed from the first dynode of a 6292 photomultiplier. The process of dynode removal and installation was carried out under an argon atmosphere to minimize surface contamination. A typical spectrum obtained with the Ag-Mg target is shown in Fig. 5.14 for a 20-keV H beam. As expected, the secondary electron yield increased with a shift of the spectrum to higher electron groups. Groups corresponding to the emission of 12 electrons are easily resolved, and in some cases a peak corresponding to 14 electrons was found. For H energies less than 30 keV the yield from Ag-Mg was greater than that from copper. For energies greater than 30 keV the integral curves corresponding to multielectron yield decreased more in Ag-Mg than in copper, in relation to the single electron curve. This is shown in Fig. 5.15, where the ratio of the area of the five-electron to one-electron emission is plotted as a function of H energy. Above 30 keV, there exists a marked decrease in this ratio for Ag-Mg, while for copper the ratio is approaching a flat maximum. Owing to the erratic behavior for sensitive surfaces such as Ag-Mg, we have concluded that surfaces such as copper, molybdenum, or tungsten are more appropriate for use as a detector target.

Use of these techniques provides means of detailed study of the secondary emission of electrons from solids. If the assumption is made that each incident particle produces at least one secondary electron, then the secondary emission coefficient is given by

$$\gamma_i = \frac{\sum_n N_n n_e}{\sum_n N_n} = \frac{\text{total secondary electrons}}{\text{total incident ions}},$$

where N_n is the integral number of pulses in each electron group n_e. The results of integrating the various electron groups and determining the secondary emission coefficient of H on copper are shown in Fig. 5.16, where γ_i is plotted as a function of particle energy. The curve labeled γ' was obtained directly from the data. Since the copper target was mounted 30° to the incident beam, this curve must be corrected by dividing by the secant of 60° to compare with data taken at normal incidence. Making this correction results in the curve γ_c. Both Cousinie[12] and Murdock[13] have measured the secondary emission of H^+ on copper in the energy range less than 50 keV, and their results are as shown. The agreement between the three sets of measurements is within 50%. From these measurements the following conclusions can be made: (1) the detector system has a high efficiency, (2) secondary emission studies can be made in a detailed manner, (3) the departure of the H secondary emission curves from the H^+ curves at lower energies indicates the importance of differences in surface reflection and secondary emission of low-energy hydrogen ions and atoms.

---

[12] M. P. Cousinie *et al.*, *Compt. Rend.* **249**, 387 (1959).

[13] J. W. Murdock *et al.*, ISC-625 (1955).

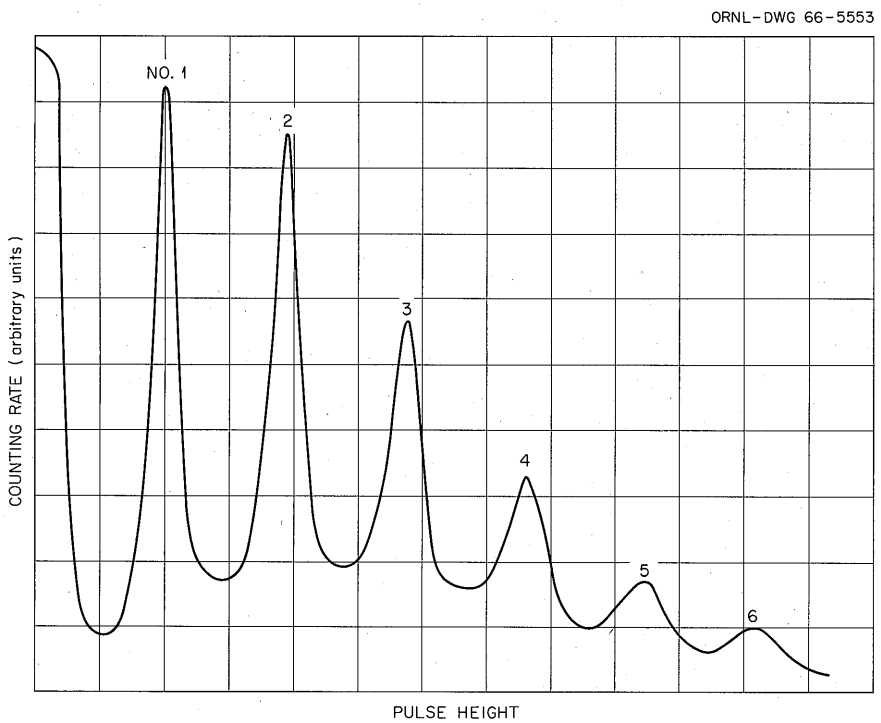

Fig. 5.13. Pulse Spectrum of 4-, 8-, and 12-keV H on Copper.

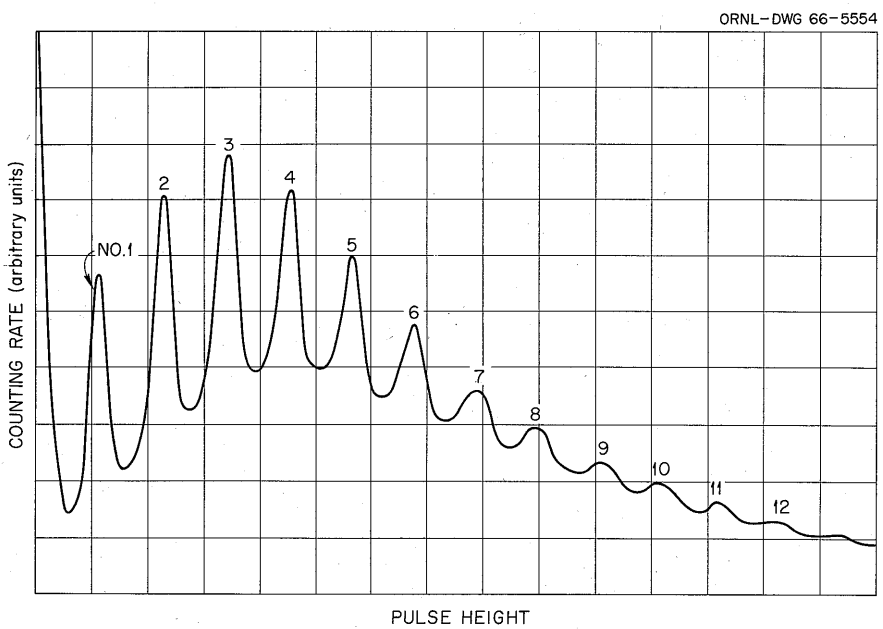

Fig. 5.14. Pulse-Height Spectrum of 20-keV H on a Silver-Magnesium Target.

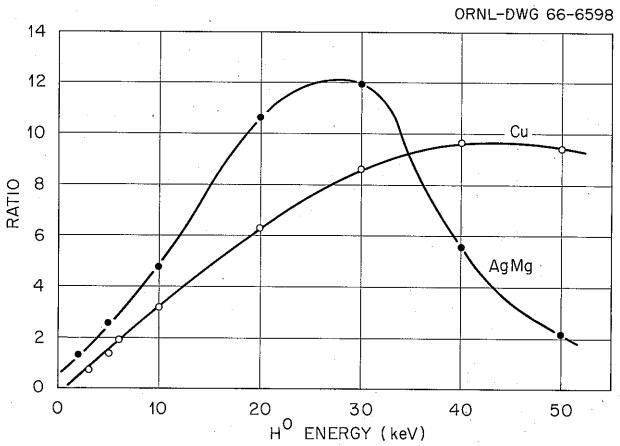

Fig. 5.15. Comparison of Areas of Electron Group 5 to Group 1 for Copper and Silver-Magnesium Targets as a Function of H Energy.

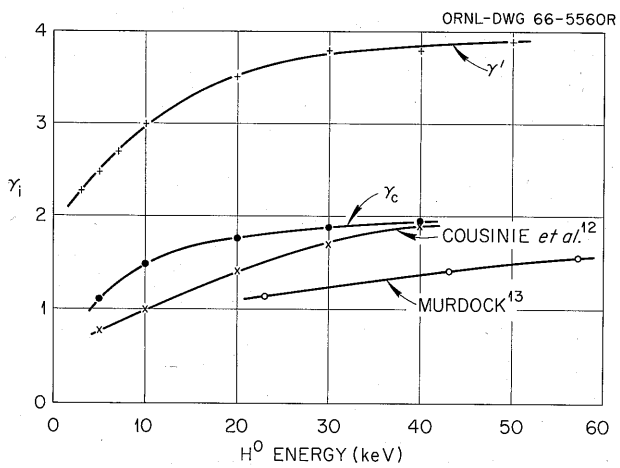

Fig. 5.16. Secondary Electron Emission Coefficient of H on Copper.

5.6 PRESSURE MEASUREMENTS FOR CONDENSABLE GASES

Extension of atomic cross-section measurements to condensable gases depends upon a suitable pressure measuring device to determine the target density in the collision chamber. Recent developments in pressure measuring apparatus have included a capacitive differential manometer sold commercially (Baratron) and calibrated in the range 0.2 to 3.0 torrs. The calibration of this gage is independent of the mass of the gas. Atomic cross-section measurements are usually made with a target density corresponding to 10^{-4} to

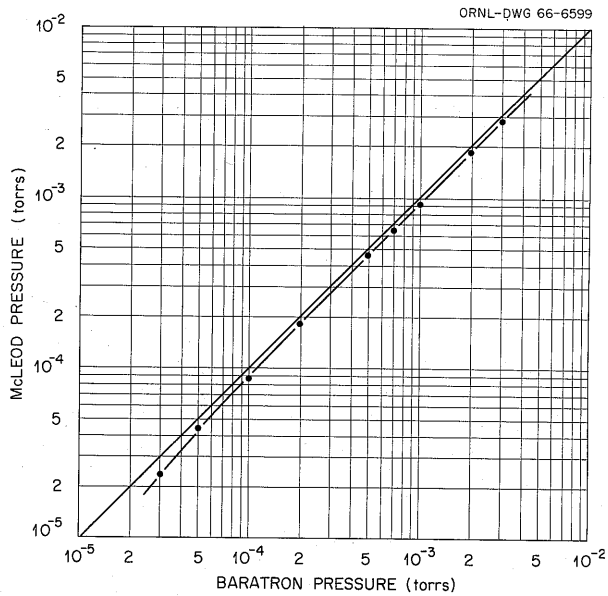

Fig. 5.17. Calibration Curve of the Baratron Pressure Gage.

10^{-2} torr. The calibration of the gages has been extended down to the 10^{-5}-torr range by using hydrogen gas and by comparing the Baratron with McLeod gages. With hydrogen gas the mercury streaming error is less than 2%. The results of the calibration are shown in Fig. 5.17, where the McLeod gage response is plotted as a function of the manometer response. Below pressures of 10^{-3} torr the Baratron gage becomes nonlinear, with the magnitude of error increasing as the pressure decreases. The source of the nonlinearity is unknown; however, the curves are repeatable over a long period of time. With this high degree of repeatability and with the small 15 to 20% correction necessary, the Baratron can be calibrated in the desired pressure range and used as a secondary standard in cross-section measurements.

5.7 THE ATOMIC AND MOLECULAR PROCESSES INFORMATION CENTER

C. F. Barnett
D. A. Griffin
M. O. Krause
R. A. Langley
J. R. McNally, Jr.
J. A. Ray

The past report period has been devoted primarily to searching current literature, preliminary evaluation of journal articles, and issuing an-

notated bibliographies. The 1964 bibliography has been printed and issued as AMPIC-3, 1964. Our most popular activity and publication, as judged from the number of requests, was the *International Directory of Workers in the Field of Atomic Collisions*. This report is continually being revised, and an enlarged version will be published in the near future. The bibliography of atomic and molecular processes for 1965 has been assembled and partially evaluated. Current references are being key punched directly on IBM cards; this eliminates many errors and decreases the time to obtain a computer-printed working bibliography from a period of two months to less than a week. This method will allow current control of bibliographical data on a month-to-month basis.

Our program for storage of information has proven to be very efficient and satisfactory. The technique of entering data from a journal paper onto many punched cards with the first card having a fixed field and subsequent trailer cards having an open field has been tested on a data base of 7000 punched cards. These tests have proven the reliability of the system, which has been adopted for our future use. Computer programs are now being written to retrieve from this data base, with main emphasis on retrieval by specifying the collision process and reactants.

Permission has been granted to publish our formal evaluation and reviews by a commercial publisher in the form of monographs. Negotiations are under way with four publishers, one of which will be selected to publish a series of monographs. The first review, "Ion-Atom Interchange Reactions," is approximately 75% completed in rough draft form. It is expected that the rough draft will be completed by June 1, 1966, with the manuscript in final form by September 1, 1966. The second review, "Ionization, Excitation and Dissociation by Heavy Particles," has been planned, with four external specialists in the field consenting to be authors. Further work is contingent upon sufficient funds to carry on these activities.

6. High-Current Ion-Beam Production and Injection

R. C. Davis G. G. Kelley
R. R. Hall O. B. Morgan
R. F. Stratton

6.1 FOUR-ELECTRODE H_2^+ SOURCE

The four-electrode version of the duoplasmatron ion source described in the last report[1] (Fig. 6.1) has been tested on the 600-kV test stand. This source operates stably at a low pressure and delivers a high percentage of H_2^+ ions (65%), even with a total hydrogen ion current of ~250 mA.[1] The 600-kV tests were made to determine the fraction of the beam from this source that could be made available for DCX-2 injection ($1\frac{5}{8}$-in.-diam × 30-in.-long duct beginning ~100 in. from the lens). Initial attempts to extract a beam from the source shown in Fig. 6.1 were unsuccessful. The beam was very divergent, with the beam impinging on the tube electrodes resulting in excessive heating and instability. This problem was pursued by making changes in the ion source and beam extraction geometry on the 600-kV test stand. Simultaneously, the 100-kV test stand was used to look at the beam from similar sources on a target located only ~20 cm from the source with no focusing. When the source shown in Fig. 6.1 was used with the 100-kV test stand, there were two beam envelopes on the target. For example, at 70 keV and 100 mA there was a $2\frac{1}{2}$-in.-diam intense beam and a 5-in.-diam dilute beam on the target at 20 cm. The latter beam is apparently the source of the ions impinging on the 600-kV accelerator tube electrodes. In these tests the ion source that produced the beam with the smallest divergence was similar to the one used in the assembly shown in Fig. 6.3 with the lens coil not energized. However, in incorporating the auxiliary coil shown in Fig. 6.3 around the anode expansion cup into the 600-kV accelerator,[2] it is necessary to redesign the electrodes for the top of the accelerator to prevent the stray field from this coil from producing electron trapping regions, causing Phillips ion gage (PIG) discharge troubles. The electrodes had been designed to prevent PIG discharges from the stray field from the magnetic

[1] *Thermonuclear Div. Semiann. Progr. Rept. Oct. 31, 1965*, ORNL-3908, p. 103.

[2] *Thermonuclear Div. Semiann. Progr. Rept. Oct. 31, 1962*, ORNL-3392, p. 50.

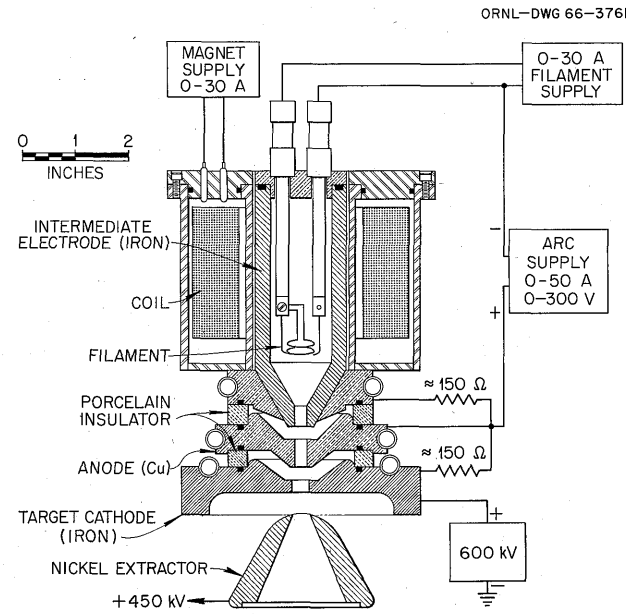

Fig. 6.1. Four-Electrode Ion Source Used for Producing Intense H_2^+ Ion Beams.

lens located at ground potential. This type of problem emphasizes the need for an accelerator design to completely eliminate electron trapping regions. Since a solution to this problem had already been achieved for a one-gap (100-kV) accelerator, it was decided to pursue the same problem for 600 kV rather than considering redesigning the present accelerator. This will be discussed in detail later in this report. From further tests on the 600-kV test stand it was found that changing the magnetic field shape in the ion source (Fig. 6.1) by making the target cathode of copper instead of iron resulted in a 97-mA 540-keV beam through the test stand injection duct from a total beam of 190 mA. This limitation seems to be in the beam brightness, since earlier analysis indicated that at least 65% of this beam is H_2^+. By coincidence this is the same current limitation found for the conventional three-electrode duoplasmatron,[3] where the limitation was the inability to produce more H_2^+ ions. More detailed studies of this beam restriction would be desirable but have been postponed while other problems are pursued.

6.2 NON-PIG SOURCE DESIGN

The system shown in Fig. 6.2, where the epoxy plate is used for up to 100-kV insulation instead of a more typical porcelain cylinder, results in

[3] *Thermonuclear Div. Semiann. Progr. Rept. Oct. 31, 1964*, ORNL-3760, pp. 64–65.

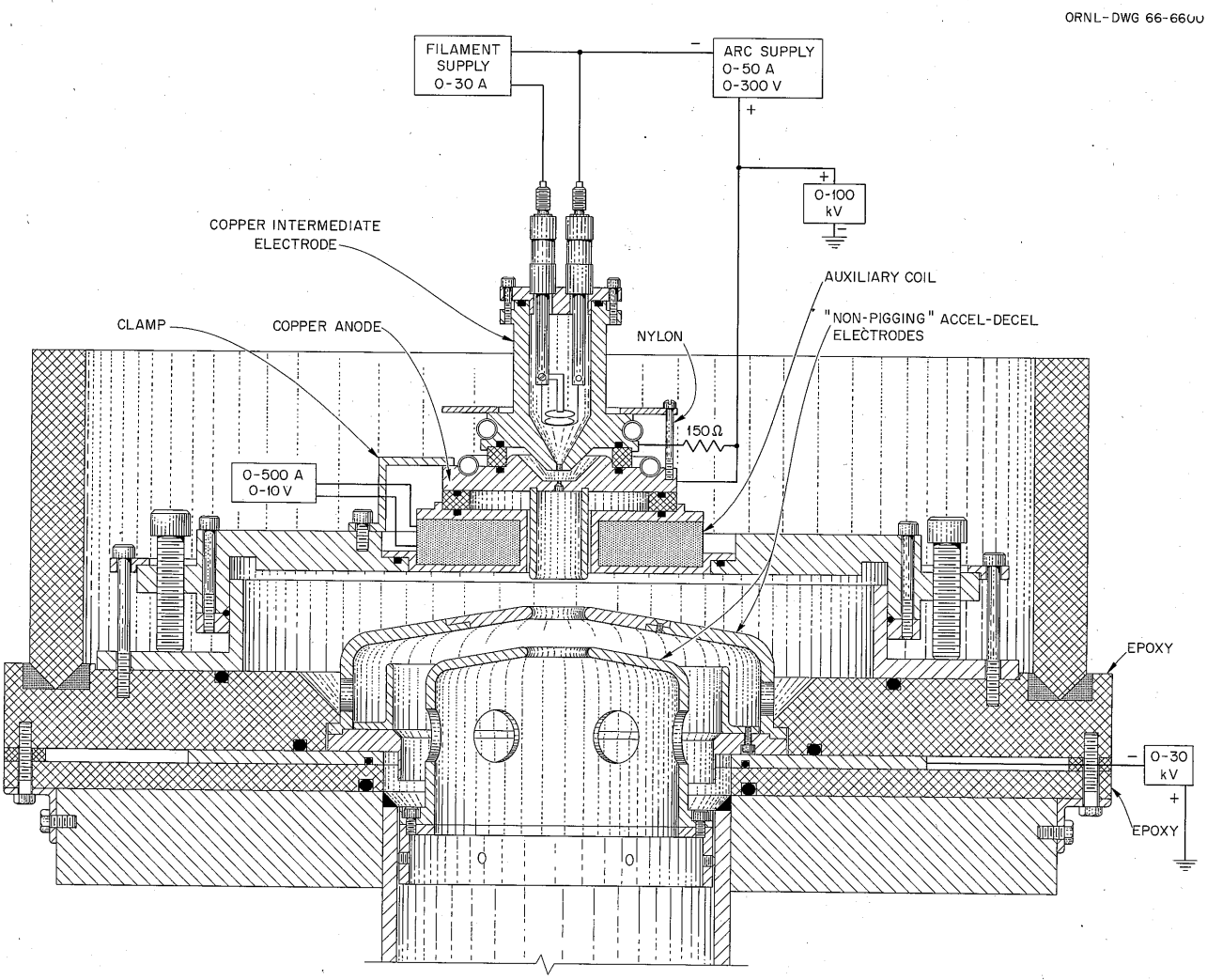

Fig. 6.2. Intense Ion Beam Assembly Designed to Prevent PIG Discharges. All-copper three-electrode H^+ ion source.

a non-PIG system for ion beams. The electric equipotential surfaces are convex, as viewed looking from positive to negative in the 0- to 100-kV acceleration region. This geometry permits a wide variation in magnetic field shape without permitting electron trapping. The system also includes a second epoxy plate that allows a negative potential to be applied to the extractor electrode. Incorporating a ground plane after this electrode results in an accel-decel electrode combination that traps electrons between these electrodes and the magnetic lens and allows space-charge neutralization in this region. The system shown in Fig. 6.2 has an all-copper three-electrode H^+ ion source and has been used for beams of 0 to 300 mA at energies of 80 to 100 keV. The system is capable of more current,[4] but in the present applications it has not been used at higher currents at this energy. A second, more compact and hopefully improved version of the non-PIG accel-decel system is shown in Fig. 6.3. The ion source shown with this system is the four-electrode H_2^+ source and will be used for producing 40-keV H_2^+ ions for injecting 20-keV neutrals into DCX-3 and probably other neutral injection applications. Either of the above ion sources or the more conventional duoplasmatron can be used on either of these systems over the entire energy range up to at least 100 keV. Figure 6.4 shows the H^+ and H_2^+ ion current from the system shown in Fig. 6.2 through a 1-in. aperture located 42 in. from the magnetic lens. The ion source shown in Fig. 6.2

[4] *Thermonuclear Div. Semiann. Progr. Rept. April 30, 1965*, ORNL-3836, pp. 74–80.

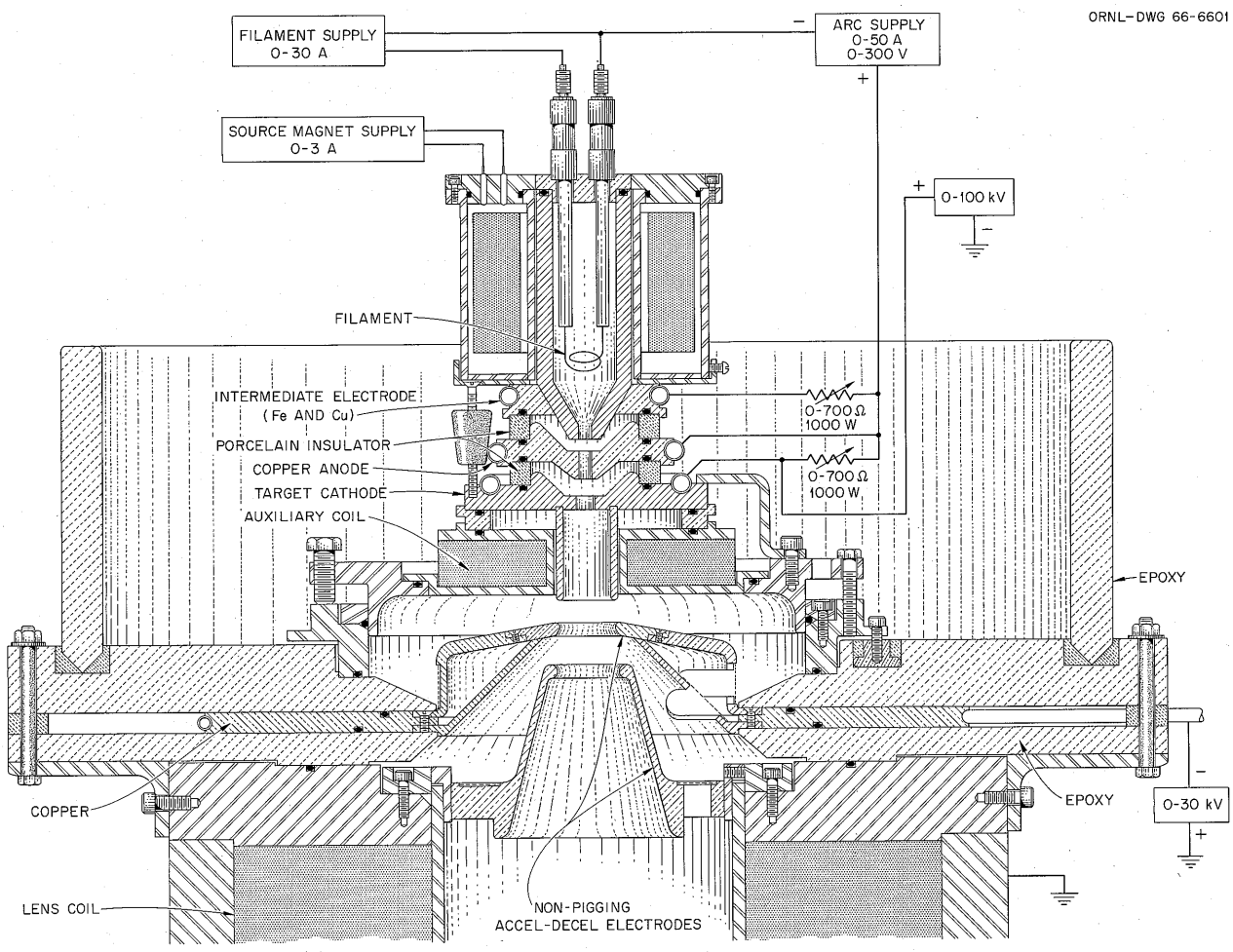

Fig. 6.3. Modified Intense Ion Beam Assembly with non-Pig Design. Four-electrode H_2^+ ion source.

was used for H^+ ions, and the source shown in Fig. 6.3 for H_2^+ ions. The numbers shown were taken from runs where various source parameters were being studied and do not necessarily indicate the maximum attainable current. Figure 6.5 indicates the variation in H_2^+ current through a $1\frac{1}{4}$-in. aperture located 92 in. from the lens after the beam passes through a 1-in. aperture located 42 in. from the lens. This is the first time this strong dependence on neutral density has been seen in a system designed to provide space-charge neutralization. Earlier studies with higher-energy beams indicated no strong dependence on neutral density in this pressure range. Attempts to provide a second source of electrons for neutralization from a thoriated tungsten filament did not appreciably affect the results shown in Fig. 6.5. This problem might not be important in the production of neutral beams, since the neutralizer can be placed close to the source and since it provides a supply of electrons for neutralization of the incoming beam. Preliminary tests with a neutral beam system show no dependence on neutral density.

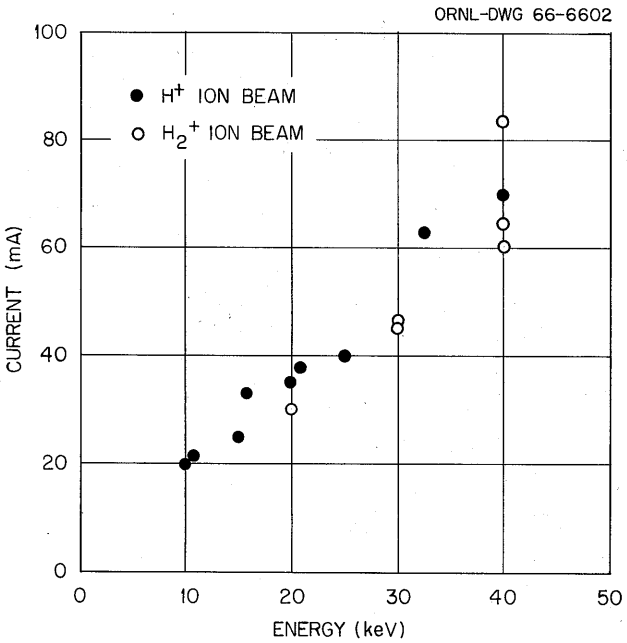

Fig. 6.4. H^+ and H_2^+ Ion Beam Current Through a 1-in. Aperture, Located 42 in. from the Magnetic Lens, as a Function of Ion Energy.

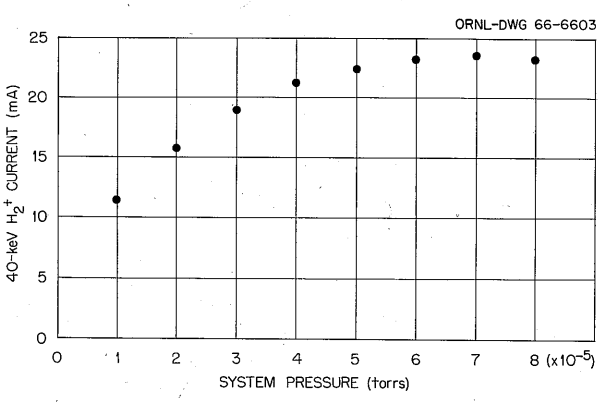

Fig. 6.5. Forty-keV H_2^+ Ion Current Through a $1\frac{1}{4}$-in. Aperture Located 92 in. from the Lens, After Passing Through a 1-in. Aperture at 42 in., as a Function of System Pressure.

Incorporation of the non-PIG ideas into a four-gap 600-kV accelerator column has resulted in a proposed design shown in Fig. 6.6. The flat epoxy insulator will have cast-in high-voltage leads and supports for the column electrodes. The electrodes will be either stainless steel or titanium and will accelerate the beam up to 600 keV in ~15 cm. Preliminary tests have been made of various proposed ideas in the system. The epoxy, Shell Epon 815 (100 parts by weight) with Versamid 140 (General Mills) hardener (40 parts by weight), has been used for several years for high-gradient 100-kV accelerator insulator applications. The vacuum surface voltage gradient of the epoxy has been tested to 135 kV across a 0.5-in. gap between two metal cylinders (the tube will have 150 kV across 1.5-in. gaps). A $2\frac{5}{8}$-in.-diam epoxy cylinder with a cast-in $\frac{1}{4}$-in.-diam copper rod has been tested by grounding the copper rod and placing the cylinder against the 150-, 300-, 450-, and 600-kV conductors of a 600-kV accelerator. This system was operated for several hours with many vacuum discharges in the accelerator but with no faults through the epoxy. The only known remaining problem is the ability to cast RG-19U cable into the epoxy for these high electric-field gradients. Test specimens always fail at the joint between the polyethylene and epoxy around the $\frac{1}{4}$-in. copper conductor of the RG-19U cable. Numerous ideas to eliminate this problem have failed, and unless a solution is found in the near future the tube will probably be built with copper conductors cast in rigid epoxy cylinders instead of the flexible RG-19U cable.

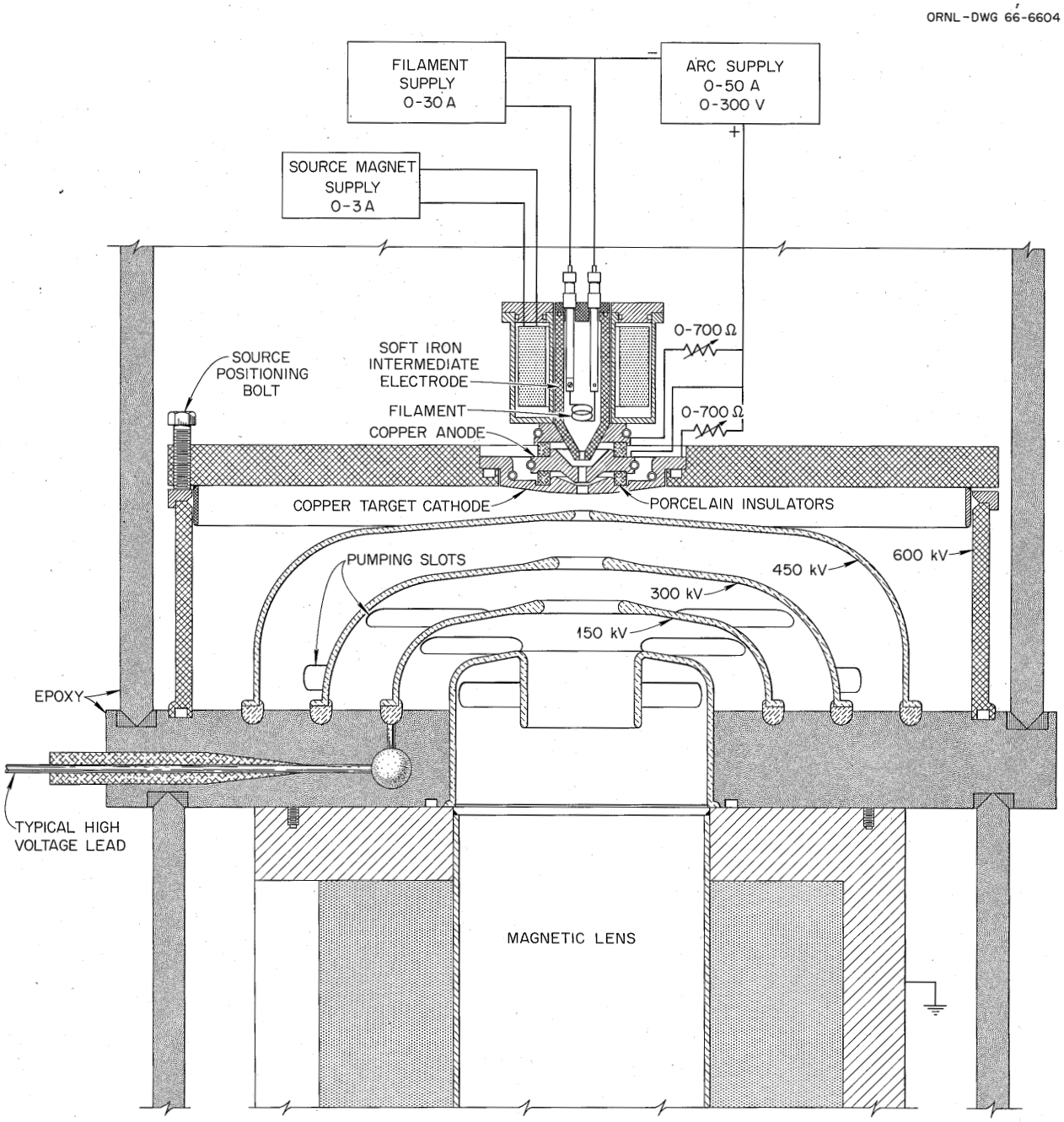

Fig. 6.6. Proposed Design of a 600-kV non-PIG Accelerator.

6.3 THE DCX-2 END INJECTOR

The DCX-2 end injector, which consists of the ion source and non-PIG accelerator shown in Fig. 6.2, has been operated at 90 keV with an H^+ ion beam of 50 to 300 mA. There have been no indications that the ion source and accelerator will not be capable of injecting a 100-kV, 500-mA H^+ beam for which they were designed. The primary problem in these preliminary tests has been the dissipation of the stored energy in the system during a vacuum discharge in the accelerator without damaging the ion source power supplies or the RG-19U cables used for the isolated 440-V, three-phase current. The energy storage is primarily in the cables, since they are quite long. The 100-kV, 50-kVA isolation transformer is located beside the 100-kV, 3.5-A power supply at a distance of 100 ft from the machine. The cables have been isolated from the terminal equipment by means of chokes, and they have been terminated in their characteristic impedance at the power supply end. In addition, thyrites and pellet-type lightning arrestors are used at the terminal to limit the voltage surge on the 440-V line. These measures appear to have been successful. The end injector has not been operated adequately to determine the feasibility of trapping a significant fraction of the ion beam. The results are discussed more fully in the DCX-2 section of this report.

6.4 INTENSE D-T NEUTRON GENERATOR

In conjunction with the Armed Forces Radiobiological Institute, Washington, D.C., the Health Physics Division, and the Edgerton Germeshausen and Grier Corporation, a 150-kV, 500-mA dc ion source and accelerator for a neutron generator have been designed, built, and tested. These tests were made with hydrogen, since adequate radiation shielding was not available for testing the final system with D^+ ions on a tritium target. The ion source used was a conventional duoplasmatron with a copper anode and a very high-source arc current (30 to 50 A). With this very dense arc the ion source delivers primarily (at least 80%) atomic ions. In a typical 4-h operation the system operates continuously except for occasional (at ~10- to 40-min intervals) vacuum discharges which result in "downtimes" of a few seconds.

6.5 NEUTRAL BEAMS

A joint effort has recently been initiated with the DCX-1 group to test various neutral-forming cells (especially metal vapors) with intense ion beams. The ion beam can be either H^+ or H_2^+ over an energy range of ~20 to 60 keV.

7. Plasma Theory and Computation

7.1 THEORETICAL INTERPRETATION OF SOME DCX-2 OBSERVATIONS

E. G. Harris[1]

7.1.1 Introduction

Some of the striking phenomena observed in DCX-2 are: (1) ion cyclotron harmonics as high as the 100th are observed; (2) under some conditions only the even multiples of the ion cyclotron frequency appear; (3) a highly anisotropic plasma with $n \sim 10^8$ cm^{-3} and $T_\perp/T_{||} \sim 10^3$ is sometimes built up and confined between shallow mirrors with a mirror ratio of about 1.001; (4) after the beam is turned off this highly anisotropic plasma is stable against the emission of ion cyclotron harmonics. We shall discuss the interpretation of these observations in the light of theoretical knowledge of linear stability theory, quasi-linear theory, mode-mode coupling, and finite plasma effects.

The equations which we shall assume describe the plasma in DCX-2 are:

$$\frac{\partial E_{\mathbf{k}}}{\partial t} = (i\omega_{\mathbf{k}} + \gamma_{\mathbf{k}})E_{\mathbf{k}} + \sum_{\mathbf{q}} M_{\mathbf{k},\mathbf{q}}\, E_{\mathbf{k}-\mathbf{q}}\, E_{\mathbf{q}}\,, \qquad (1)$$

$$\omega_{\mathbf{k}} \cong \omega_{pe}\frac{k_z}{k}\,, \qquad (2)$$

$$M_{\mathbf{k},\mathbf{q}} = \frac{e}{m}\frac{k}{2}\frac{\omega_{\mathbf{k}-\mathbf{q}}(\omega_{\mathbf{k}} + 2\omega_{\mathbf{q}})}{\omega_{pe}^2\,\omega_{\mathbf{q}}}\,, \qquad (3)$$

$$\gamma_{\mathbf{k}} = \frac{\pi}{2}\left(\omega_{pe}\frac{k_z}{k}\right)\sum\frac{\omega_p^2}{k^2}\sum_{n=-\infty}^{+\infty}\int d^3v\, J_n^2\left(\frac{k_\perp v_\perp}{\omega_c}\right) \times\left(\frac{n\omega_c}{v_\perp}\frac{\partial f}{\partial v_\perp} + k_z\frac{\partial f}{\partial v_z}\right) \times\delta\left(\omega_{pe}\frac{k_z}{k} - k_z v_z - n\omega_c\right)\,, \qquad (4)$$

$$\frac{\partial f}{\partial t} = \frac{\pi\omega_p^2 k_z}{M_k^3}\sum_{n=-\infty}^{+\infty}\sum_{\mathbf{k}}\frac{|E_{\mathbf{k}}|^2}{8\pi}\left(\frac{n\omega_c}{v_\perp}\frac{\partial}{\partial v_\perp} + k_z\frac{\partial}{\partial v_z}\right) \times\left[J_n^3\left(\frac{k_\perp v_\perp}{\omega_c}\right)\left(\frac{n\omega_c}{v_\perp}\frac{\partial f}{\partial v_\perp} + k_z\frac{\partial f}{\partial v_z}\right) \times\delta\left(\omega_{pe}\frac{k_z}{k} - k_z v_z - n\omega_c\right)\right]\,. \qquad (5)$$

This assumes that the waves are essentially electrostatic waves in a cold plasma; hence Eq. (2). The hot ions emit and absorb waves, so they contribute to $\gamma_{\mathbf{k}}$ but do not appreciably change $\omega_{\mathbf{k}}$. It is conceptually helpful to view this emission and absorption quantum mechanically.

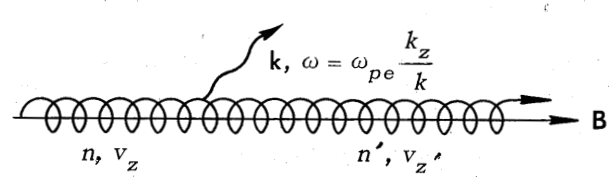

The energy of an ion is

$$E = \hbar\omega_{ci}\left(n + \frac{1}{2}\right) + \frac{M}{2}v_z^2\,. \qquad (6)$$

[1]Consultant, the University of Tennessee.

Conservation of momentum and energy gives

$$M v_z = M v_z' + \hbar k_z ,$$

$$\hbar \omega_{ci} \left(n + \frac{1}{2}\right) + \frac{M}{2} v_z^2 = \hbar \omega_{ci} \left(n' + \frac{1}{2}\right) + \frac{M}{2} v_z'^2 + \hbar \omega_{pe} \frac{k_z}{k} , \quad (7)$$

from which

$$(n - n') \omega_{ci} + \frac{M}{2\hbar} \left[v_z^2 - \left(v_z - \frac{\hbar}{M} k_z \right)^2 \right] - \omega_{pe} \frac{k_z}{k} = 0 . \quad (8)$$

In the classical limit $\hbar \to 0$ we obtain

$$(n - n') \omega_{ci} + k_z v_z - \omega_{pe} \frac{k_z}{k} = 0 . \quad (9)$$

This is just the argument of the δ function which occurs in Eqs. (4) and (5).

One can do a quantum mechanical calculation and obtain Eqs. (4) and (5) in the classical limit. It is clear from such a calculation that $\gamma_{\mathbf{k}}$ is proportional to the difference between the number of ions which emit and the number which absorb plasmons of wave vector $\mathbf{k}$. With each emission or absorption the velocity of a particle changes. Equation (5) describes the resulting change in $f(\mathbf{v})$. If we let $N_{\mathbf{k}}$ be the number of plasmons with wave vector $\mathbf{k}$, then

$$\frac{dN_{\mathbf{k}}}{dt} = \dot{N}_{\mathbf{k}} = 2\gamma_{\mathbf{k}} N_{\mathbf{k}} . \quad (10)$$

This is stimulated emission and absorption. A spontaneous emission term could be added to Eq. (10), but it is generally negligible.

The last terms in Eq. (1) are the wave-wave coupling terms. They are often neglected in discussing instabilities. However, in DCX-2 and similar experiments they are not negligible. They describe the process indicated by the diagram (Fig. 7.1) and its inverse. Conservation of momentum and energy of the plasmons gives

$$\mathbf{k}_1 + \mathbf{k}_2 = \mathbf{k}_3 , \quad (11)$$

$$\omega_1 + \omega_2 = \omega_3 . \quad (12)$$

ORNL-DWG 66-6605

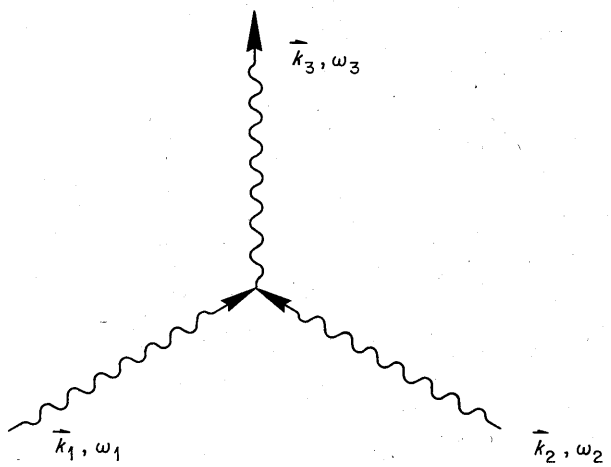

Fig. 7.1. Addition of Wave Vectors in Wave-Wave Coupling.

The coupling constant $M_{\mathbf{k},\mathbf{q}}$ has been calculated by Aamodt and Drummond.[2] We have specialized their result to a cold plasma and assumed that Eq. (12) is satisfied to obtain our Eq. (3).

7.1.2 Application of the Equations to DCX-2

We can conclude from Eq. (2) that if the nth harmonic of ω_{ci} is observed, then

$$\omega_{pe} > n \omega_{ci} . \quad (13)$$

This is a lower limit on the density. For instance, the 100th harmonic of ω_{ci} has been observed; from this

$$n > 3 \times 10^{10} \text{ cm}^{-3} . \quad (14)$$

It has been shown for the two-temperature Maxwellian that

$$\frac{T_{\parallel}}{T_{\perp}} < \frac{1}{2n} \quad (15)$$

for $\gamma_{\mathbf{k}}$ to be positive when $n\omega_{ci} \cong \omega_{pe} k_z/k$. Such a high degree of anisotropy would be difficult to

[2] R. E. Aamodt and W. E. Drummond, *Phys. Fluids* **1**, 1816 (1964); *Phys. Fluids* **8**, 171 (1965).

establish and maintain when $n \cong 100$. This suggests that the higher harmonics are excited through the wave-wave coupling terms in Eq. (1). We have estimated the importance of these terms by assuming

$$\omega_{\mathbf{q}} = \omega_{\mathbf{k}-\mathbf{q}} = \omega_{ci} , \tag{16}$$

$$\omega_{\mathbf{k}} = 2\omega_{ci} , \tag{17}$$

$$\omega_{pe} = 100\omega_{ci} . \tag{18}$$

Also, we assumed that the amplitudes of $E_{\mathbf{q}}$ and $E_{\mathbf{k}-\mathbf{q}}$ were fixed at 1.0 V/cm. We then ask for the time required for $E_{\mathbf{k}}$ to grow to the same amplitude as $E_{\mathbf{q}}$ and $E_{\mathbf{k}-\mathbf{q}}$. For k we assumed $2\pi/50$ cm^{-1}. The result is

$$\tau = \left[\frac{e}{m} \frac{\omega_{ci}\,(2\omega_{ci} + 2\omega_{ci})}{(100\,\omega_{ci})^2\,\omega_{ci}} \frac{k}{2} |E_{\mathbf{q}}| \right]^{-1} \tag{19}$$

$\cong 2 \times 10^{-3}$ sec in DCX-2. This is a rather short period of time. It must be concluded that wave-wave coupling is important.

Let us suppose that $\gamma_{\mathbf{k}}$ is positive for $\omega = \omega_{ci}$ and perhaps the first few harmonics. Then ions feed energy into waves of frequency ω_{ci}, $2\omega_{ci}$, etc. This energy is fed into still higher harmonics by wave-wave coupling. Ultimately, harmonics up to the limit given by Eq. (13) are excited. If $\gamma_{\mathbf{k}}$ is negative for these higher harmonics, one would expect a rapid decline of amplitude with harmonic number. What is observed is a rather slow decline. However, the effect of absorbing energy at these higher harmonics is to equalize the number of ions which emit and absorb, thus causing $\gamma_{\mathbf{k}} \to 0$ at values of $\mathbf{k}$ corresponding to these harmonics. This is the physical content of Eq. (5).

By Eq. (2) the values of $\mathbf{k}$ corresponding to a frequency $n\omega_{ci}$ lie on a cone in k space with apex angle θ given by

$$\cos\theta = \frac{k_z}{k} = \frac{n\omega_{ci}}{\omega_{pe}} . \tag{20}$$

The relations Eqs. (11) and (12) can be illustrated as in Fig. 7.2. One easily convinces oneself that Eqs. (11) and (12) can be satisfied.

Now suppose that $\gamma_{\mathbf{k}}$ was negative for ω_{ci}, positive for $2\omega_{ci}$, and negative for the higher harmonics. (The damping of the fundamental might be caused by the "warm" background plasma – a possibility which we shall examine later.) Now wave-wave coupling gives

$$2\omega_{ci} + 2\omega_{ci} = 4\omega_{ci} , \tag{21}$$

$$2\omega_{ci} + 4\omega_{ci} = 6\omega_{ci} , \text{ etc.} \tag{22}$$

That is, energy is fed into the *even* harmonics but not the odd. This has been observed.

We can also imagine situations in which $\gamma_{\mathbf{k}}$ is negative for ω_{ci} and $2\omega_{ci}$, positive for $3\omega_{ci}$, and negative for all higher harmonics. Then the only harmonics which would be excited would be $3\omega_{ci}$, $6\omega_{ci}$, $9\omega_{ci}$, etc. This too has been observed.

If one were ever to observe the odd harmonics alone, then this theory would have to be abandoned. Fortunately for the theory this has never been observed.

7.1.3 Damping Due to Warm Plasma

If $\gamma_{\mathbf{k}}$ is plotted vs ω for a two-temperature Maxwellian distribution of very anisotropic hot ions and a greater density of warm isotropic plasma, one gets a picture like Fig. 7.3. The solid curves in Fig. 7.3

ORNL-DWG 66-6606

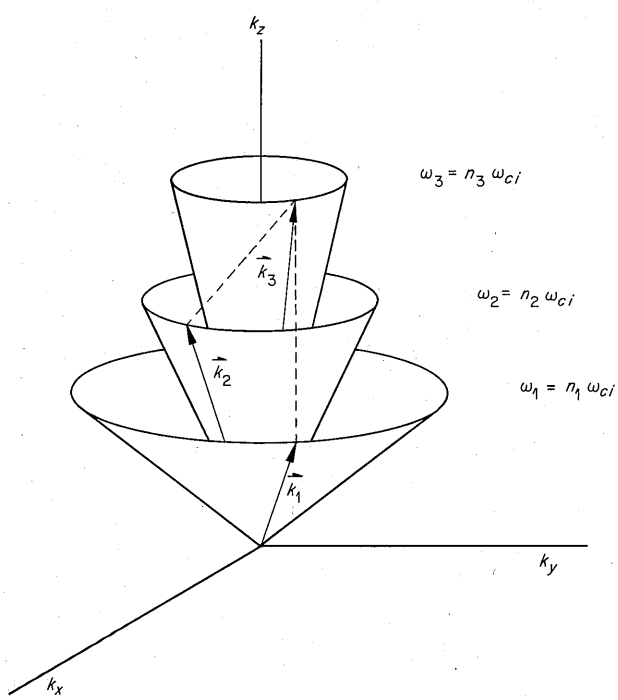

Fig. 7.2. Coupling of Wave Vectors at Harmonics of the Ion Cyclotron Frequency.

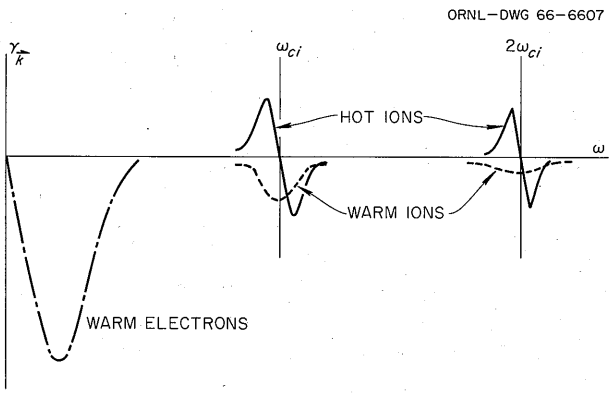

Fig. 7.3. Contribution of Hot Ions and Warm Plasma to γ_k.

are the contribution of the hot ions. They come from the $\partial f/\partial v_z$ term in Eq. (5). The dashed curve is contributed by the $n = 0$ term for the warm-electron term in Eq. (5). The dotted curves are contributed by the warm ions. The amplitudes of the warm-ion contributions drop off more rapidly with n than does the hot-ion contribution. One can conceive of situations in which the warm plasma damps the fundamental but leaves an instability at $2\omega_{ci}$.

7.1.4 Statistical Mechanics of the Waves

One would like to calculate the distribution of energy among the harmonics of ω_{ci}. It would seem to be very difficult to do this directly from Eqs. (1) to (5). However, because there are so many modes which exchange energy with one another, there is reason to hope that a statistical treatment would work.

Let us assume that all the waves in the plasma are in equilibrium at temperature T (in energy units). We would assign an energy T to each wave. Since there are $d^3k/(2\pi)^3$ waves per unit volume with $\mathbf{k}$ in d^3k, we can write

$$U = T \int \frac{d^3k}{(2\pi)^3} \tag{23}$$

for the energy density of the waves in the plasma. Now waves with very large k_z would be damped by Landau damping; so we will cut the integral off at $k_z = k_z(\max)$. Now

$$k_z = k \cos\theta , \tag{24}$$

so

$$k_{\max} = \frac{k_z(\max)}{\cos\theta} , \tag{25}$$

and

$$U = \frac{T}{(2\pi)^3} \int_0^{2\pi} d\phi \int_0^{\pi} \sin\theta \, d\theta \times \int_0^{k_z(\max)/\cos\theta} k^2 \, dk = \frac{T\, k_z^3(\max)}{(2\pi)^2} \times \int_0^{\pi} \frac{\sin\theta \, d\theta}{\cos^3\theta} . \tag{26}$$

Changing variables from θ to ω, where

$$\omega = \omega_{pe} \frac{k_z}{k} = \omega_{pe} \cos\theta , \tag{27}$$

gives

$$U = \frac{T\, k_z^3(\max)\, \omega_{pe}^2}{(2\pi)^2} \, 2 \int_{\omega_{pe}}^{0} \frac{d\omega}{\omega^3} = \int u(\omega)\, d\omega , \tag{28}$$

where $u(\omega)$ is the spectral energy density. It is proportional to ω^{-3}. Now in DCX-2 not all of the waves are in equilibrium, but only those with frequencies $\omega = n\omega_{ci}$. This is analogous to an incandescent gas which is optically thick at the emission lines of the atoms of the gas but not in between. The intensity of the emission lines is the blackbody limit. Similarly, here we expect the intensities of the cyclotron harmonics to be

$$u(\omega = n\omega_{ci}) \sim n^{-3} .$$

This means that

$$E(\omega = n\omega_{ci}) \sim \sqrt{u(\omega = n\omega_{ci})} \sim \frac{1}{n^{3/2}} , \tag{29}$$

$$E_z = E \cos\theta = E \frac{\omega}{\omega_{pe}} , \tag{30}$$

so

$$E_z(\omega = n\omega_{ci}) \sim \frac{1}{n^{1/2}}, \tag{31}$$

and

$$E_\perp(\omega = n\omega_{ci}) \sim \frac{1}{n^{3/2}} \sqrt{1 - n^2 \frac{\omega_{ci}^2}{\omega_{pe}^2}}. \tag{32}$$

What is measured experimentally is $E_\perp$ near the walls. It is difficult to relate this to the fields in the interior of the plasma, where these equations might be expected to apply. For this reason and also because of the crudity of the above argument, it is not surprising that the experimental data are in poor agreement with the $n^{-3/2}$ behavior predicted.

7.2 SOME IMPLICATIONS OF THE STABILITY OF THE ENERGETIC PLASMA IN DCX-2

G. E. Guest R. A. Dory

Recent experiments (Sect. 2) performed in the DCX-2 facility have shown that after beam turnoff there exists a stable plasma with a highly anisotropic "loss-cone" distribution of ion speeds. This is an apparent contradiction to theoretical stability criteria. Stated very crudely, these criteria predict that waves at harmonics of the ion gyrofrequency, $\omega = n\omega_{ci}$, with $n \lesssim (2T)^{-1}$, $T \equiv T_{\parallel i}/T_{\perp i}$, may be unstable if the electron density is sufficiently great, $\omega_{pe} \gtrsim n\omega_{ci}$, and if electron Landau damping is sufficiently weak, $n\omega_{ci} \gtrsim 3k_\parallel v_{\parallel e}$. In the present note we shall summarize the theoretical basis for these criteria and present results of calculations using parameters chosen to represent the DCX-2 plasma. The conclusion that theory predicts unstable growth of the first few harmonics in DCX-2 suggests that one must give more theoretical attention to the details of the growth and to the reflection and absorption processes which may occur at the axial boundaries of the plasma.

Consider a plasma having the following properties: it is (1) infinite and homogeneous in space, (2) situated in a uniform static magnetic field, and (3) made up of a group of energetic ions distributed in speeds according to $f(v_\perp^2, v_\parallel) \propto v_\perp^2 \exp(-v_\perp^2/\alpha_\perp^2 - v_\parallel^2/\alpha_\parallel^2)$ immersed in a much colder group of Maxwellian electrons. The techniques necessary to analyze the electrostatic stability properties of such a configuration have been described in detail elsewhere,[3] and we shall only review the results here.

There are important technical limitations on the analysis: it is numerically expedient to consider waves of given perpendicular wavelength (as contained in the parameter $\lambda \equiv k_\perp^2 \bar{\rho}_i^2/2$) in order to solve the dispersion relation for a given plasma configuration described by the parameters $\Theta \equiv T_{\parallel e}/T_{\parallel i}$ and $T \equiv T_{\parallel i}/T_{\perp i}$. Representative results of the marginal stability analysis are shown in Fig. 7.4 for $\lambda = 1$, $\Theta = 0.05$, and $T = 10^{-3}$. Notice the following feature of this diagram. If one specifies the ratio of plasma density and magnetic field strength in the form ω_{pe}/ω_{ci}, then the variables $z_p \equiv \omega_{pe}/(k\alpha_{\parallel i})$ and $z_c \equiv \omega_{ci}/(k_\parallel \alpha_{\parallel i})$ are no longer independent, but must satisfy the relation:

$$\left(\frac{\omega_{pe}}{\omega_{ci}}\right)^2 \frac{1}{z_p^2} = \frac{1}{z_c^2} + 2\lambda T, \tag{1}$$

that is, $k^2 = k_\perp^2 + k_\parallel^2$. It is the intersection of the lines given by Eq. (1) with the unstable zones shown in the diagram that determines the stability criterion. Thus, to find the minimum density required to support a given unstable wave, one may evaluate ω_{pe}/ω_{ci} using Eq. (1) and points (z_p, z_c) in an unstable zone. For example, using Fig. 7.4 and similar diagrams for other values of λ, we find the threshold data plotted in Fig. 7.5. The data suggest that in a plasma with the properties mentioned above and with $\omega_{pe}/\omega_{ci} \gtrsim 5$, the first five harmonics of the ion gyrofrequency may be generated spontaneously. Since no such spontaneous generation is observed in DCX-2, we must ask in what details our model of the DCX-2 plasma is inaccurate and attempt to gage the effects on our stability criteria of the inaccuracies.

The most obvious discrepancy between the model and its physical counterpart is the spatial inhomogeneity and finite size of the DCX-2 plasma. An immediate consequence of the finite size is that the wavelengths of the plasma fluctuations are limited. A reasonable estimate is that wavelengths should be less than twice the dimension of the plasma. Accordingly, we require $k_\parallel L \gtrsim \pi$ or $z_c \lesssim \omega_{ci} L/(\pi \bar{v}_{\parallel i})$. Notice that if $z_{c(\max)} \approx \omega_{ci} L/(\pi \bar{v}_{\parallel i})$ is less than $3\,\bar{v}_{\parallel e}/(n\,\bar{v}_{\parallel i})$, strong Landau

[3] G. E. Guest and R. A. Dory, *Phys. Fluids* **8**, 1853 (1965).

damping will stabilize the modes in question (this explains why the unstable zones in the z_c-z_p plane do not extend to the origin). As a first example, in DCX-1,

$$z_c(\max) \cong 1 \ll 3\bar{v}_{\parallel e}/(n\bar{v}_{\parallel i}) \cong 10/n \ .$$

By contrast, in the "central-peak" plasma in DCX-2,

$$z_c(\max) \cong 200 \gg 3\ \bar{v}_{\parallel e}/(n\bar{v}_{\parallel i}) \cong 30/n \ .$$

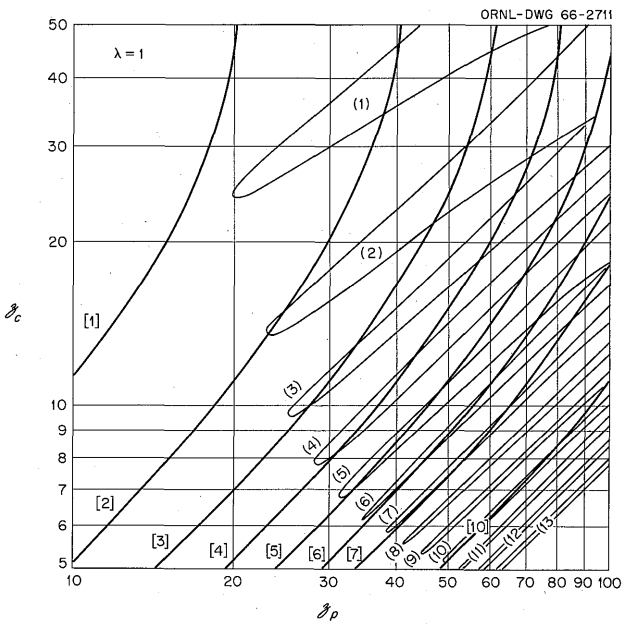

Fig. 7.4. Unstable Zones in the z_c–z_p Plane, Showing Several Lines of Constant ω_{pe}/ω_{ci} for the Following Parameters: $\Theta = 0.05$, $T = 10^{-3}$, and $\lambda = 1$.

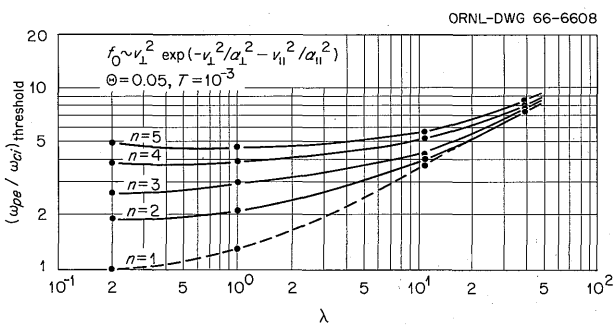

Fig. 7.5. Predicted Threshold Density as a Function of Perpendicular Wavelength ($\lambda = k_\perp^2\rho_i^2/2$) for the First Five Harmonics of the Ion Gyrofrequency in the Central-Peak Plasma.

Thus, although one would expect the observed[4] stability of the DCX-1 plasma after beam turnoff on the grounds that geometrically permissible wavelengths will suffer strong Landau damping, the corresponding arguments do not apply to the DCX-2 central-peak plasma.

Now the finite radial extent of the plasma leads to an analogous restriction on transverse wavelengths and therefore to a lower bound on the parameter λ. If this minimum value is much larger than unity, the data of Fig. 7.5 show that this restriction can lead to a significant increase in the predicted threshold density. To deduce an appropriate value for λ (min), we observe that the fluctuating potential must vanish at some finite radius R, which may be the radius of the plasma column or, at most, the inner radius of the vacuum liner. Since the radial eigenfunctions of the potential are Bessel functions, $J_n(k_\perp r)$, we may require $k_\perp R \gtrsim j_{nl}$, where j_{nl} is the first zero of the nth order Bessel function: $j_{nl} = 3.832, 5.136, 6.380, \ldots$ for $n = 1, 2, 3, \ldots$. Then $\lambda\ (\min) \approx j_{n1}^2\ (\bar{\rho}_i/R)^2$. In DCX-2, for $n = 1$, $\lambda\ (\min) \approx 2$, so that $(\omega_{pe}/\omega_{ci})_{\text{threshold}} \approx 1.65$, and again one expects instability.

Quite apart from these questions of finite size effects, one must consider the possible role of the group of cold ions which exists along with the energetic ions and cold electrons in the actual plasma. At frequencies near the first harmonic of the cold-ion gyrofrequency, these cold ions can contribute an additional damping which, although generally small, could have an observable effect on the density threshold. Using the marginal stability analysis and including a cold-ion population of ten times the hot-ion density, we have found that the central-peak plasma is still expected to be unstable. This conclusion is unchanged when the "cold" ions are given a temperature of 50 eV, as estimated for the experiment.

At this time the resolution to the conflict between existing theory and the DCX-2 observations seems likely to lie in a more detailed analysis of the characteristics of the growing waves. In particular, if these waves are convectively unstable, as suggested by Rosenbluth and Post for the high-density loss-cone modes,[5] then it is necessary to know the spatial growth rate and the reflection or

[4] J. L. Dunlap *et al.*, *Phys. Fluids* **9**, 199 (1966).

[5] M. N. Rosenbluth and R. F. Post, *Phys. Fluids* **8**, 547 (1965).

absorption properties at the axial density gradients in the plasma if one is to be able to predict the circumstances under which the waves will grow to observable amplitudes. An intensive program has been initiated to develop suitable analytical techniques for implementing the known criteria for distinguishing convective and absolute instabilities. Progress in this area is described in Sect. 7.3.

7.3 PROPAGATION PROPERTIES OF UNSTABLE WAVES

C. O. Beasley, Jr. R. A. Dory

7.3.1 Introduction

The observations of Sect. 7.2 suggest that detailed knowledge of the propagation characteristics of unstable waves may lead to a significant change in theoretically predicted instability thresholds. Our earlier work in linear plasma stability analysis has attempted only to identify regions (in a suitable plasma parameter space) in which complex solutions of the dispersion relation, $\omega(k) = \mathrm{Re}\ \omega + i\ \mathrm{Im}\ \omega$, with $\mathrm{Im}\ \omega > 0$, are obtained for real values of the propagation vector **k**. The apparent inadequacy of this procedure when compared with experiment requires that one determine whether the waves are convectively or absolutely unstable[6] and, if convective, with what spatial growth rate.

A number of authors have described criteria for distinguishing between absolute and convective instabilities,[7] and the broad features of the problem are well known. However, numerical implementation of the criteria encounters difficulties, and some work remains before we can treat realistic dispersion relations describing plasmas of interest in the controlled fusion program.

The application of generally accepted criteria for distinguishing absolute from convective waves as derived, for example, by Bers and Briggs,[8] requires that one consider the dispersion relation to be a mapping of the complex ω (angular frequency) plane onto the complex k (wave number in a specified direction) plane. It is then necessary to examine the topology of the image curves (in the complex k plane) of certain lines in the ω plane. Complications arise because solutions $k(\omega)$ are multiple-valued, even in simple cases such as the one-dimensional two-stream plasma with no magnetic field.

Our efforts to date have been directed toward the development of computer codes necessary to carry out the mappings mentioned above for dispersion relations relevant to the experimental thermonuclear program at ORNL. As a first step, we have constructed codes which operate on a given dispersion relation to obtain a graph of real ω–real k solutions (Brillouin plot) as functions of the parameters which specify the plasma configuration. These plots lead to a rapid identification of regions of real ω–real k at which instabilities may be expected for suitable sets of plasma parameters. A second code has been devised which can solve the dispersion relation for complex k and construct curves of constant Re ω (or of constant Im ω) in the k plane. Since an appreciable amount of computational time is involved in the analysis, present efforts center on devising an optimum approach to the topological search. The results should include the classification of the instability and the spatial or temporal growth rates as functions of the system parameters.

7.3.2 Real ω–Real k Solutions of Dispersion Relations: Wave Plots

The first step is to locate possible unstable regions of parameter space. We write the dispersion relation in a form $f(\omega,k) = \omega_{ci}^2/\omega_{pi}^2$. Then for a complete set of plasma parameters one may evaluate the quantity $f(\omega,k)$ at each point in the

[6] In a convecting instability, the center of a disturbance (wave packet) propagates through the system faster than the outer limits of the disturbance spread away from the center. At a fixed point in space, the disturbance eventually dies down and only by observing from a moving coordinate system can one see the exponential growth of the instability. In an absolute instability, the distance spreads faster than its center moves. At any fixed point in space, the disturbance will eventually grow exponentially in time.

[7] See for example: O. Buneman in *Plasma Physics* (ed. by J. E. Drummond), McGraw-Hill, New York, 1961; P. A. Sturrock, *Phys. Rev.* **112**, 1488 (1958); H. Derfler, unpublished; R. J. Briggs, *Electron-Stream Interaction with Plasmas*, Massachusetts Institute of Technology Press, Cambridge, 1964; P. Rolland, *Phys. Rev.* **140**, B776 (1965); and K. B. Dysthe, University of Bergen (Norway) Dept. of Applied Mathematics Report No. 8, 1966 (unpublished).

[8] A. Bers and R. J. Briggs, as reported in Briggs's book. (See ref. 7.)

ω-k plane and connect those points corresponding to specified values of $\omega_{ci}^2/\omega_{pi}^2$. These lines of constant density form a generalized Brillouin diagram (which we shall call a "wave plot") in that they give the phase and group velocities of the electrostatic waves which will propagate in a plasma having the assigned parameters. Such wave plots, illustrated schematically in Fig. 7.6, may easily be examined for evidence of instability bands, indicated by the disappearance of pairs of real ω solutions for some values of real k. For example, in Fig. 7.6, where the densities $N_1 < N_2 < N_3 < N_4$, there exists an instability whose density threshold lies between N_2 and N_3. In some cases it is possible to identify the character of the instability from this diagram alone, using criteria of the sort described by Briggs[8] (the mode in Fig. 7.6 is an absolute instability according to these criteria). However, in many cases the wave plots do not allow unambiguous identification of the wave type; and in no cases do they give information on

ORNL-DWG 66-6609

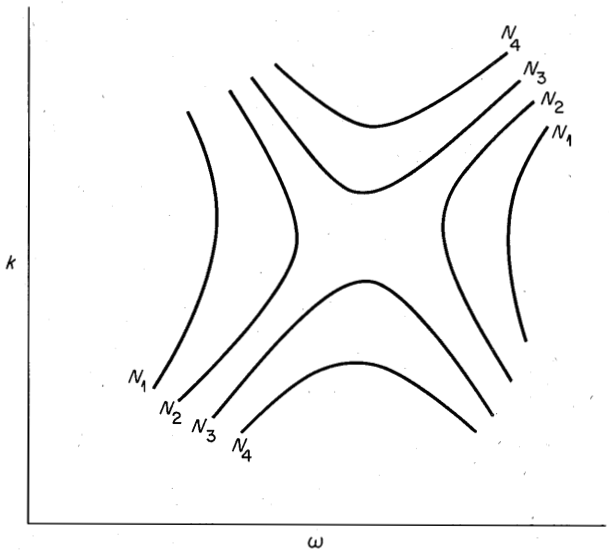

Fig. 7.6. Wave Plot (Schematic) for an Absolute Instability.

ORNL-DWG 66-6610

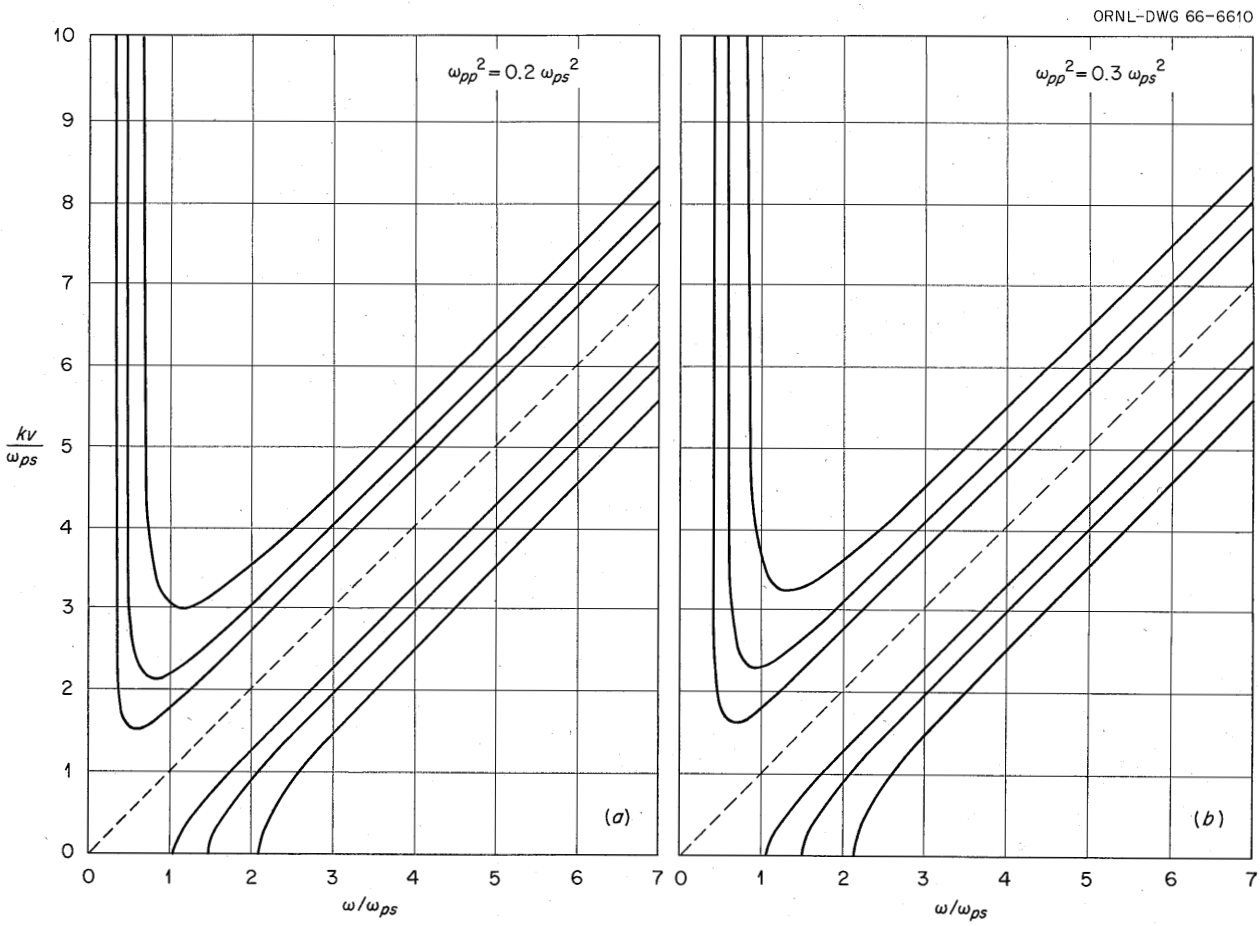

Fig. 7.7. Wave Plot for a Three-Stream Plasma: (*a*) Absolutely Unstable Case, and (*b*) Convectively Unstable Case.

growth rates, etc. To illustrate this ambiguity, we consider the dispersion relation

$$D(\omega,k) = 1 - \frac{\omega_{ps}^2}{(\omega - kv)^2} - \frac{\omega_{pa}^2}{(\omega + kv)^2} - \frac{\omega_{pp}^2}{\omega^2} = 0 \quad (2)$$

for two cold counterstreams through a stationary cold plasma. As Briggs[8] has shown, for $\omega_{pp}^2 > 0.25\ \omega_{ps}^2$ the instability supported by this plasma is convective, while for $\omega_{pp}^2 < 0.25\ \omega_{ps}^2$ it is absolute. Yet wave plots for the two cases, shown in Figs. 7.7*a* and 7.7*b*, show no obvious distinguishing characteristics.

7.3.3 Determination of Complex Roots of Dispersion Relations

In order to determine the properties of unstable waves, it is necessary to carry out the mapping lines of constant ω_i (or of constant ω_r) in the complex k plane as described above. Dispersion relations for energetic plasmas generally involve the transcendental Bessel functions and the "plasma dispersion function"[9] which complicate this mapping. We shall outline the analysis given by Bers and Briggs[8] and describe a computer routine for finding the complex roots $\omega(k_r + ik_i)$, where k_r and k_i are the real and imaginary parts of k, of an arbitrary dispersion relation $D(\omega,k) = 0$.

If for some real k there exist solutions $\omega = \omega_r + i\omega_i$ with $\omega_i > 0$ (we assume $e^{-i\omega t}$ time dependence for the wave), the plasma supports growing waves. Whether these waves correspond to convective or absolute instabilities may be determined by constructing contours in the complex k plane of lines of constant ω_r for values of ω_r in the unstable band of frequencies. For a convective instability, these constant-ω_r contours have the form illustrated in Fig. 7.8*a*; corresponding contours for an absolute instability are shown in Fig. 7.8*b*. The distinction between the two cases may be described as follows: If the ω_r contours cross the real k axis an odd number of times, an instability exists. If a pair of ω_r contours cross so that a saddle point is seen, the instability is absolute, provided that one branch of the saddle-point contour crosses the real k axis an odd number of times and the other branch crosses an even number of times.

Now if the dispersion relation is analytic in a region of interest, the Cauchy-Riemann conditions guarantee that the curves of constant ω_i will be

[9] B. D. Fried and S. D. Conte, *The Plasma Dispersion Function*, Academic, New York, 1961.

ORNL—DWG 66-6611

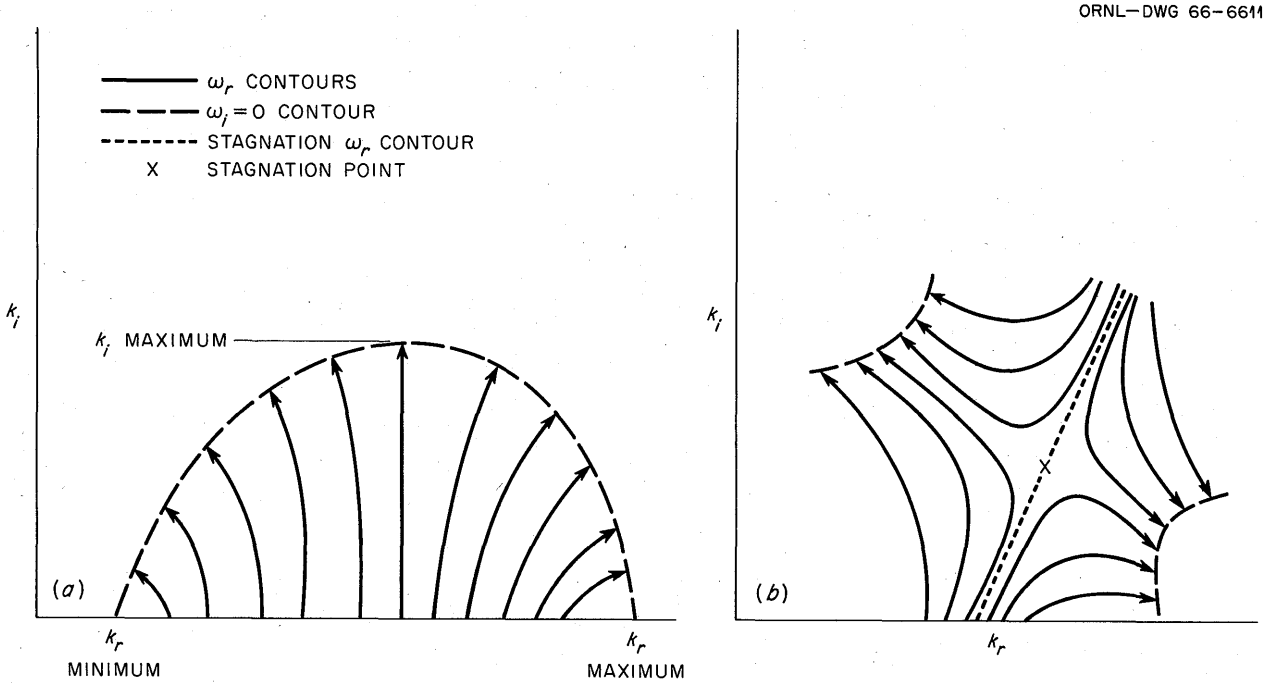

Fig. 7.8. Complex k-Plane ω_r Contours for (*a*) a Convective Instability and (*b*) an Absolute Instability.

orthogonal to the constant ω_r curves, as shown in Figs. 7.9*a* and 7.9*b*. Under these conditions one may use either set of curves to study the wave properties. From the curves one may read off the unstable frequencies and wavelengths, the growth rates, and, for convective instabilities, the growth lengths.

To determine complex $\omega = x + iy$ solutions to a dispersion relation $f(\omega,k) = |D(\omega,k)| = 0$ on a grid in the complex k plane, we use a modification of Newton's iterative method. Since $f \geqq 0$, a parabolic approximation about a solution is in order; if (x,y) are initial guesses, the next approximation is $(x + \delta x,\ y + \delta y)$, where

$$\delta x = -\,[\mathrm{sign}(f_x)]\sqrt{\frac{f}{f_{xx}\left(1 + \frac{f_{xx}}{f_{yy}}\frac{f_x^2}{f_x^2}\right)}}\,,$$

$$\delta y = -\,[\mathrm{sign}(f_y)]\sqrt{\frac{f}{f_{yy}\left(1 + \frac{f_{yy}}{f_{xx}}\frac{f_x^2}{f_y^2}\right)}}\,,$$

where

$$f_x = 2\ \mathrm{Re}\ [D(\omega,k)\cdot D'^{*}\ (\omega,k)]\ ,$$
$$f_y = 2\ \mathrm{Im}\ [D(\omega,k)\cdot D'^{*}\ (\omega,k)]\ ,$$
$$f_{xx} = |D'|^2 + \mathrm{Re}\ [D^{*}(\omega,k)\cdot D''\ (\omega,k)]\ ,$$
$$f_{yy} = |D'|^2 - \mathrm{Re}\ [D^{*}(\omega,k)\cdot D''\ (\omega,k)]\ ,$$

and

$$D' = \frac{\partial D}{\partial \omega}\ ,\ D'' = \frac{\partial D'}{\partial \omega}\ .$$

The correction is iterated until $\delta x^2 + \delta y^2$ is deemed small enough. Initial guesses are obtained from solutions found earlier at nearby values of k. Near branch points in the k plane, this choice of initial guess can lead to skipping from one Riemann sheet to another. This case is signaled by negative f_{xx} or f_{yy}. Deciding which sheet to take involves a choice which normally should be made by the user of the code. A choice is made somewhat arbitrarily – by the code; if wrong, the mistake is easily seen in the output data.

Several test programs using one-dimensional zero-temperature, multistream dispersion relations have been run, and samples of three cases are displayed in Figs. 7.10*a*, *b*, and *c*. They correspond to a

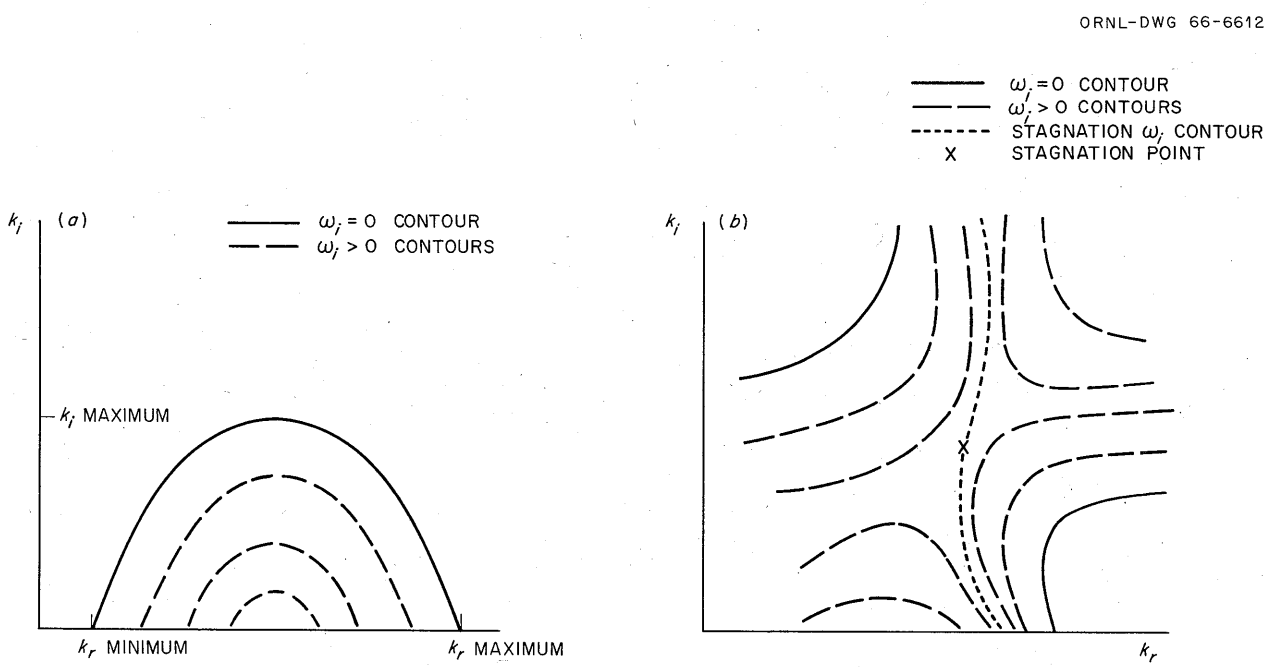

Fig. 7.9. Complex k-Plane ω_i Contours for (*a*) a Convective Instability and (*b*) an Absolute Instability.

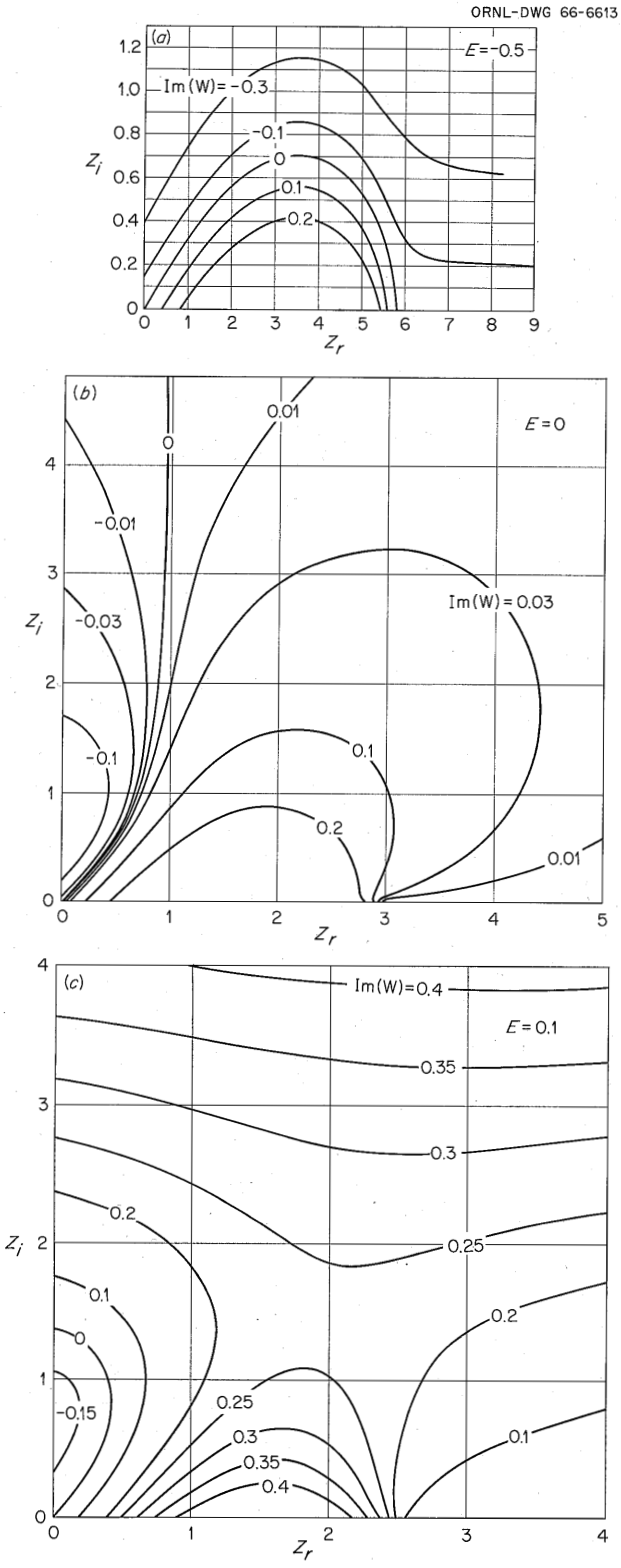

Fig. 7.10. Im(W) Contours for the Dispersion Relation $D(W,z) = 1 - (W - z)^{-2} - (W + Ez)^{-2} = 0$, Showing a Convective Instability (*a*), a Marginal Case (*b*), and (*c*) an Absolute Instability.

two-stream plasma, described by the following dispersion relation:

$$D(W,z) = 1 - (W-z)^{-2} - (W + Ez)^{-2} = 0 ,$$

where

$$W \equiv \omega/\omega_p,\ z \equiv kv_2/\omega_p,\ E \equiv -v_1/v_2 .$$

For $E < 0$, the instability is convective; for $E > 0$, the instability is absolute; for $E = 0$, the instability is marginally convective.

The program is currently being used in the analysis of two models based on the DCX-2 steady-state and "central-peak" configurations.

7.4 RELATIVISTIC INSTABILITY IN HOT-ION PLASMAS

R. A. Dory

Speck and Bers[10] have discussed an electrostatic instability of a uniform relativistic electron plasma whose distribution function is not monotonically decreasing in velocity component perpendicular to the uniform magnetic field. Since hot-ion plasmas in magnetic-mirror devices have nonmonotonic distributions because of ion loss through the mirrors, the analogous instability has been analyzed for relevance to the fusion program. First considerations which might be expected to stabilize a fusion plasma are found to be either ineffective or inapplicable. Among these are the smallness of the relativistic corrections for fusion plasmas, the possibility of Landau damping and cyclotron damping, violation of necessary instability conditions for density and wavelength, and the possible failure of the electrostatic approximation because the ratio of wave phase velocity to light speed is not vanishingly small. However, it is found that by providing a smooth energy spread for the hot ions, one can obtain stability. The amount of spread required is less than that currently regarded as necessary for controlling other microinstabilities,[11] so that no trouble should arise from this relativistic one. A detailed report of these results will be made in the near future.

---

[10] C. Speck and A. Bers, in Quarterly Progress Reports No. 79 and 80, Massachusetts Institute of Technology, Research Laboratory of Electronics, 1965 (unpublished).

[11] R. A. Dory, G. E. Guest, and E. G. Harris, *Phys. Rev. Letters* **14**, 131 (1965).

7.5 STABILITY OF DCX-1 TOWARD DRIFT-CYCLOTRON INSTABILITY AT LOW DENSITY

R. A. Dory

Stability boundaries have been calculated numerically for Harris' formulation[12] of the effect of nonzero electron temperature on the Burt-Harris[13] modes. The only extension involved in the present work is to values of $\Theta = T_e/T_i$ = electron/ion temperature ratio not given in ref. 12.

The motivation lies in the assessment given by Postma *et al.*[14] of the degree to which DCX-1 is susceptible to the drift-cyclotron[15] instability at very low densities.

The range of interest is $\omega_{pe} \lesssim \omega_{ci}$, in which case the instability requires considerable $k_{||}$ (wave vector component parallel to the external field). The results of ref. 15 for mild density gradient are then in agreement with those of ref. 13 for sharp gradient. In view of this agreement, we used the method of ref. 12 to analyze the effect of nonzero Θ. Since ref. 12 did not consider values of Θ in the range (10^{-3} to 10^{-2}) appropriate to DCX-1, we have extended the calculations.

The procedure and the notation used here were given by Harris,[12] and we need only present the results. These take the form of stability boundaries in the plane U_c vs U_p, where $U_c = (m/M)^{1/2}\, l\omega_{ci}/k_{||}v_{Ti}$ and $U_p = (m/M)^{1/2}\, \omega_{pe}/k_{||}v_{Ti}$, with m/M = electron/ion mass ratio, l = harmonic number, ω_{ci} = ion gyrofrequency, and v_{Ti} = ion thermal speed. Such boundaries are shown in Fig. 7.11, for $\Theta \doteq 10^{-1}$, 10^{-2}, and 10^{-3}.

The low-density ($\omega_{pe} \lesssim \omega_{ci}$) stable regime of interest here lies above and to the left of the unstable areas. Bounds independent of $k_{||}$ may be read from the graph as: $\omega_{pe}/\omega_{ci} \lesssim 0.579$, 0.753, and 0.699 for $\Theta \doteq 10^{-1}$, 10^{-2}, and 10^{-3}, sufficient for stability.

[12]E. G. Harris, Culham Report R-32 (1963).

[13]P. Burt and E. G. Harris, *Phys. Fluids* **4**, 1412 (1961).

[14]H. Postma *et al.*, *Phys. Rev. Letters* **16**, 265 (1966).

[15]A. B. Mikhailovski, *Nucl. Fusion* **5**, 125 (1965).

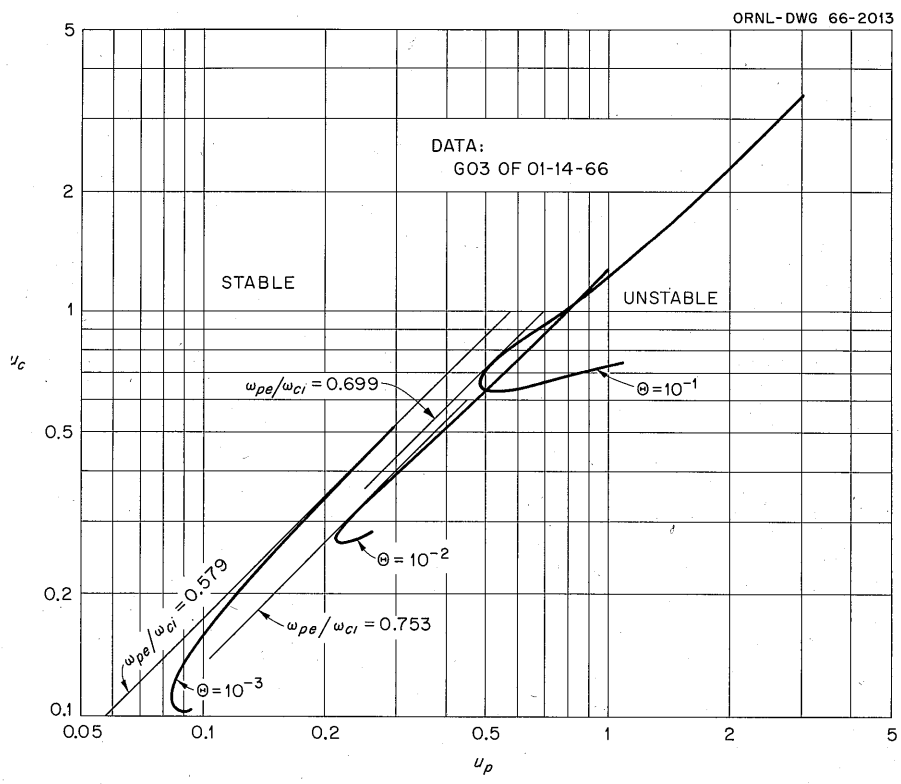

Fig. 7.11. Stability Boundaries in the U_c vs U_p Plane for $\Theta = 10^{-1}$, 10^{-2}, and 10^{-3}.

These sufficient conditions proved inadequate for ruling DCX-1 stable toward this instability at the lowest observed unstable density (another candidate, the negative mass instability, was regarded as a more likely contender). However, at the lowest densities, the relative shift $(\omega - \omega_{ci})/\omega_{ci}$ in the frequency of the unstable oscillation was experimentally very small ($\lesssim$0.1%), while the same number for the Harris[12] calculation was typically many percent. To provide a measure of this, we present in Fig. 7.12 the traces in the plane ω_{pe}/ω_{ci} vs $(\omega - \omega_{ci})/\omega_{ci}$ corresponding to those shown in Fig. 7.11. Different points on one curve correspond to different values for $k_{\parallel} v_{Ti}$. The area below the curves is stable.

For our purposes it is not necessary to know which point corresponds to what value $k_{\parallel} v_{Ti}$, since the curves for Θ typical of DCX-1 avoid the interesting point where DCX-1 is unstable. This allows us to conclude that the DCX-1 instability has properties incompatible with the drift-cyclotron or Burt-Harris modes.

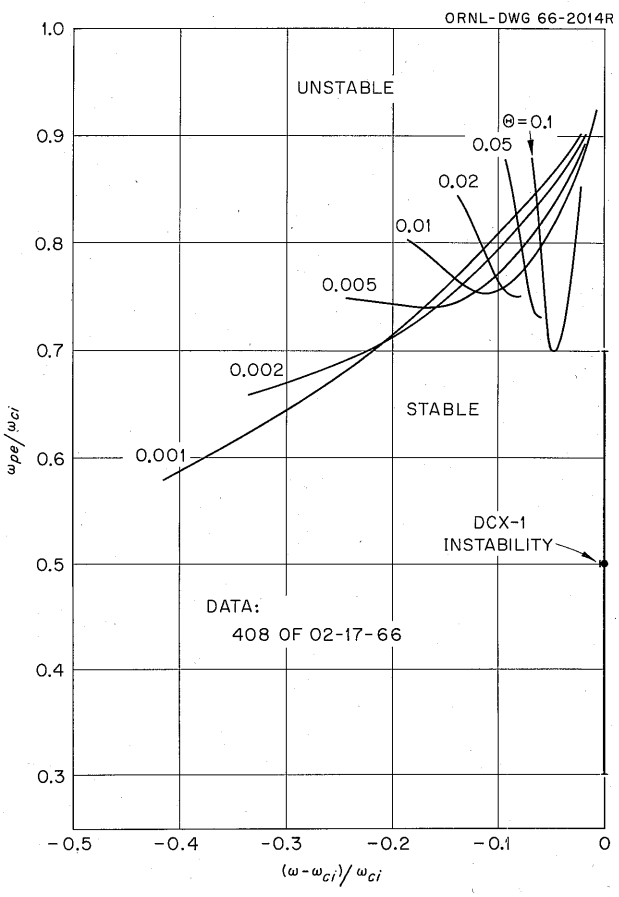

Fig. 7.12. Threshold Value of ω_{pe}/ω_{ci} as a Function of Relative Frequency Shift for Several Values of Θ. The DCX-1 instability is at a point (note error bars) well removed from the unstable zones.

A FORTRAN code exists for performing the calculations.

Discussions with T. K. Fowler, J. L. Dunlap, and G. E. Guest allowed these useful conclusions to be reached and are gratefully acknowledged.

7.6 COLD-PLASMA EFFECTS IN FINITE LENGTH PLASMAS

G. E. Guest C. O. Beasley, Jr.

Cold-plasma stabilization of flute instabilities has been studied for a variety of plasma configurations representative of experiments in which flute modes have been observed. A detailed description of the calculations and comparisons with related experiments has been accepted for publication in *Physics of Fluids*, and an abstract of this paper is included here.

Criteria are derived for the relative cold-plasma density necessary to stabilize the gradient B drift waves in finite-length energetic plasmas separated from grounded conducting end plates by a cold plasma. For a dense $(\omega_{pi}^2 \gg \omega_{ci}^2)$ hot plasma in which the precession frequency of the hot species is very much less than the ion gyrofrequency, we find

$$(N_{\text{cold}}/N_{\text{hot}})\,(\text{critical}) \sim 2l^2 \frac{\omega_g}{\omega_{ci}} \frac{L_h L_c}{2R_p^2} \frac{m}{M},$$

where ω_g is the precession frequency, L_h and L_c are the lengths of the hot- and cold-plasma regions, R_p is the plasma radius, and we have assumed $k_{\perp} = l/R_p$. Stability diagrams are given for the case, sometimes encountered in hot-electron plasmas, in which a low harmonic of the electron precession frequency approaches the ion gyrofrequency and also for the case of low-density hot-ion plasmas. Tentative comparisons are made with thresholds observed in different experiments.

7.7 PARAMETRIC EXCITATION OF TRANSVERSE WAVES IN A PLASMA[16]

David Montgomery[17]

It is shown that an externally imposed, oscillating electric field excites transverse electromagnetic waves propagating perpendicularly to it, in a cold plasma. The mechanism is closely related to the parametric excitation of longitudinal plasma oscillations recently predicted by Aliev and Silin.[18] The problem provides an application of nonsecular perturbation methods, when the equations of motion are expanded in powers of the external electric field. Arbitrarily small perturbations which arise spontaneously in the plasma are amplified by the action of the electric field for a certain range of the driving frequency. The growth rate of the oscillations is calculated.

7.8 STUDIES FOR DCX-3

C. E. Parker

Because of increased local interest in neutral injection into an open-ended minimum B configuration, the design of a mirror-quadrupole system was undertaken. To help with the task several computer programs are being used. The function of each will be described briefly.

The choice of the "best" mirror coil is not easy, since an infinite number of pairs exist. Therefore a simple code was written to display the pertinent data in a convenient form. Preliminary experience had shown that tabulated values were more useful than sets of curves. The nomenclature for the mirror coil arrangement is shown in Fig. 7.13 and defined below.

$$\alpha = \frac{a_2}{a_1} \qquad \beta = \frac{b}{a_1} \qquad \sigma = \frac{s}{a_1}$$

v = volume factor $[2\pi(\alpha^2 - 1)\beta]$

$B1$ = field of one coil alone (gauss)

BO = field of pair at center of system (gauss)

BM = field of pair at center of one coil (gauss)

MR = mirror ratio ($\cong BM/BO$)

$B_z^*(r)$ = normalized midplane field

$p(r)$ = parabolic coefficient ($B_z^* = 1 - p\rho^2$, where $\rho = r/a_1$)

For arbitrary arrays of α, β, and σ the above data were calculated and tabulated in a compact form. The field strengths are given assuming an inside radius of 1 cm and a current density of 1 A/cm^2. Using this absolute reference the coil radius or current density can be scaled easily.

Some calculations of Lorentz trapping have also been done using a code written by Riviere at Culham. Although the original version had the dimensions of the Phoenix IA system built into it, the code has been modified to input the system dimensions. After this modification, some calculations for the DCX-1 Mg vapor experiments were done. Also the original version calculated only midplane trajectories using a parabolic field shape. This is being generalized to an arbitrary trajectory with an arbitrary magnetic field.

The last problem is the calculation of the drift precessional surfaces to determine limiting conditions for adiabatic containment using another code obtained from Culham. Since it was part of their unique "library" system, many changes were necessary before it could be used here. The code is now being tested.

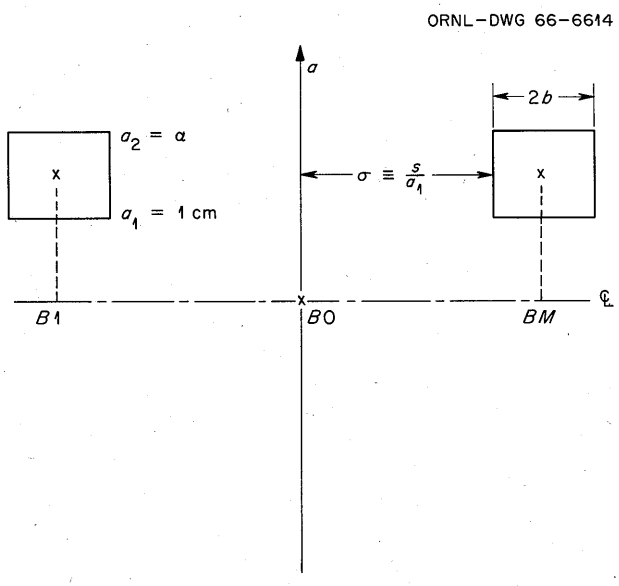

Fig. 7.13. Schematic Mirror Coil Arrangement, Showing Nomenclature of Fundamental Geometrical Parameters.

[16]Accepted for publication in *Physics of Fluids*.

[17]Consultant, Department of Physics and Astronomy, University of Iowa, Iowa City.

[18]Yu. M. Aliev and V. P. Silin, *Soviet Phys. JETP* 21, 601 (1965); V. P. Silin, *Soviet Phys. JETP* 21, 1127 (1965).

8. Magnetics and Superconductivity

8.1 NEW COMPACT TABLE FOR MAGNETIC-COIL CALCULATIONS

M. W. Garrett[1]

When designing a magnet coil, it is important to know the maximum field to which any portion of the wire may be subjected. In the case of a coil of rectangular cross section with uniform current density, the maximum field B_{max} always occurs at the midpoint of the inner cylindrical surface, that is, at point P of Fig. 8.1, whereas the design value B_0 is that at the center, O, of the system.

Some time ago Parker[2] constructed a set of curves from which the field ratio $K \equiv B_{max}/B_0$ could be read, for a wide range of ratios of the coil parameters α, β. These curves have been used to advantage in a number of laboratories; however, a new four-page table with over 4000 entries is now ready for distribution.[3] This table offers greater convenience and precision than a graphical presentation and over a wider range; α may vary from 1.02 to 10, and β from 0.05 to 10. The table permits linear interpolation to 1 part in 1000 or better; although to make this possible it was found expedient to replace K by its reciprocal B_0/B_{max} as the tabular argument. This function shows less extreme nonlinearity than K, and its value is always less than 1.0.

The table was computed with the aid of several subroutines from the previously described zonal harmonic computer package.[4] Two minor difficulties were overcome. In the early columns of the table, where β is small, as α increases the coil approximates more and more closely to an ideal disk coil or plane annular current sheet.

Such extreme shapes had not been encountered previously in using these machine codes, and it was found necessary to subdivide some of the coils. The program employs Gaussian quadrature for integration in radial depth. As may be seen

[1]Consultant, Swarthmore College.

[2]Carl Parker, ORNL-LR-DWG 58827.

[3]M. W. Garrett, *Table of the Ratio* B_0/B_{max} *for Magnet Coils with Rectangular Cross Section and Uniform Current Density*, ORNL-3972 (to be published).

[4]M. W. Garrett, *An Elliptic Integral Computer Package for Magnetic Fields, Forces, and Mutual Inductances of Axisymmetric Systems*, ORNL-3575 (1965). For the mathematical theory, see M. W. Garrett, *J. Appl. Phys.* 34, 2567–73 (1963).

ORNL-DWG 66-6531

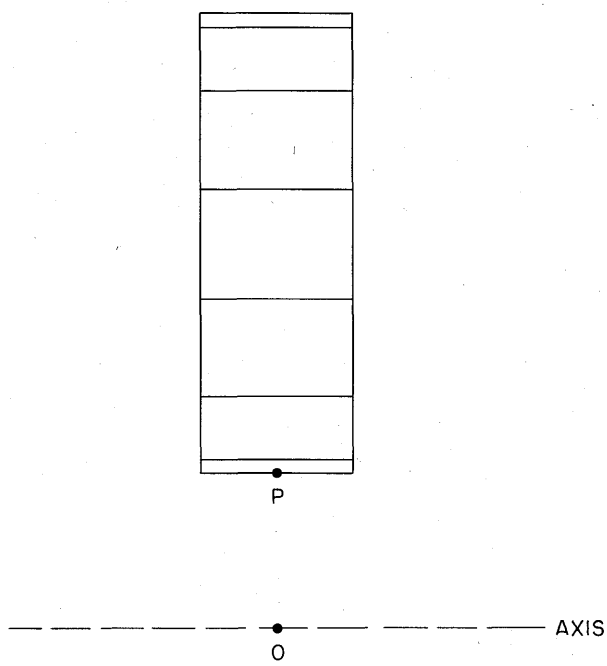

Fig. 8.1. Axial Section of Coil with Aspect Ratio 6, Showing Fictitious Gaussian Solenoids.

in Fig. 8.1, this means that the cylindrical current distribution is replaced by a set of n fictitious ideal solenoids, where n is the order of the Gaussian quadrature formula. Relying on symmetry, the field B_z at any point in the midplane is computed as twice the sum of n elliptic integral expressions. These consider in effect that the field arises from n circular singularities or "source rings" where the fictitious cylindrical sheets intersect at the end plane. The figure represents the correct placement of the solenoids for the case $n = 6$. The coil shown has an aspect ratio of 6 [defined as $(\alpha - 1)/\beta$], which is the narrowest shape that was handled in the final program without subdividing the coil. One sees intuitively that the polar angle of the innermost source, as viewed from an origin at P, must not be too large. In fact, discrepancies as large as 7 or 8% were found when the ratio $(\alpha - 1)/\beta$ was of the order of 100. They were reduced to less than 1/10000 by partitioning the very narrow coils at a depth 6β and if necessary again at 24β, while the order n was raised to 12 for the first page of the tables.

The second difficulty arose from the extreme nonlinearity of the function $1/K$ (K, as noted, would be worse) and the wish to construct a short table for linear interpolation. The maximum second-order error in linear interpolation is $\frac{1}{16}$ of the sum of the two adjacent central second differences. Initially, the table was set up by guess, with the intervals increasing in several arbitrary steps. As the values were computed, second differences were calculated along both rows and columns, divided by the functions, and multiplied by 12,500. The integral parts of these differences were printed in two separate auxiliary tables, from which the trend of variation could be seen at a glance. The intervals were adjusted in successive trials until the sum of adjacent values did not exceed 100. This ensures the validity of linear interpolation to 1 part in 1000. In the final table the interval increases by a factor of 100 in the rows and by a factor of 50 in the columns.

The table was computed in 7 min on the IBM 7090.

8.2 RIBBON COIL DEVELOPMENT

J. N. Luton, Jr.

The previous progress report[5] contained a description of a new type of ribbon coil being developed for experiments requiring small magnet coils of high current densities. The coil winding is a spiral composed of a pair of interleaved ribbons whose width is equal to the length of the coil. One ribbon is an insulator; the other, grooved on one side, is the conductor. The coolant flows through the grooves, parallel to the axis of the coil.

Ribbon coil 2 of the cited report has since been modified, mounted in the magnet laboratory, and tested with one of the large motor-generator power supplies. Current I, voltage V, flux density B, and other parameters were monitored, and the edges of the conductor were visually observed through the transparent end plates. The first indications of coil malfunction were breaks in the B vs I and V vs I curves at $I = 4660$ A. The damage to the coil was permanent in that a 1-in.-long dark spot appeared on the ribbon edge, and the value of B/I never regained its original value. Arcing was first observed through the binoculars at 4850 A. However, the coil remained stable and gave reproducible values of B and V from $I = 0$ to 5200 A. The second and third shorts occurred at 5200 and 5500 A, and by the latter level the arcing visible in the end headers had become quite general and almost continuous. The current was then set at 6500 A, and turn-to-turn shorting continued until the voltage had dropped from 80 to 30 v, at which time the test was terminated when the coil arc passed through the coil case. The damaged coil is shown in Fig. 8.2. The important point is that violent failure did not occur until the current was pushed 40% beyond the level at which malfunction was observed.

The underlying cause of the failure is not known. Assuming an isolated water groove plugged by dirt or covered by the radial supports across the coil ends, the estimated hot-spot temperature at 4600 A is 200°C, vs 150°C for a region without a flow obstruction. Although a temperature of

[5] *Thermonuclear Div. Semiann. Progr. Rept. Oct. 31, 1965*, ORNL-3908, pp. 125–28.

200°C would appear dangerous for Mylar, it is not clear from an examination of the wreckage that the shorts did in fact tend to originate under the spokes. Neither do the data of the lower part of Table 8.1 indicate that an inherent limit was reached, and it seems probable that there existed one or more constructional flaws which limited the performance of the coil. First, one could suspect the edges of the conductor ribbon. Owing to the lack of additional flat material, a previously grooved conductor was sheared to width and then dressed with a file. Arcing might have been initiated by unremoved burrs or other imperfections on the edge of the conductor. Future conductors will be cut to width, then rolled, and, if necessary, electropolished. Another likely

Fig. 8.2. Downstream Face of Ribbon Coil No. 2, Showing Three Holes Through the Winding, One of Two Holes Through the Case, Melted and Burned Mylar Insulation, Copper Sputtered by the Arcs, and Outlines of the Eight Lucite Spokes Which Were Against the Winding During Operation.

Table 8.1. Conditions of Second Ribbon Coil[a] at First Indications of Malfunction

Total current, A	4600
Maximum current density in the copper, A/in.^{2}	314,000
Minimum current density in the copper, A/in.^{2}	212,000
Overall current density in the winding, A/in.^{2}	195,000
Coil voltage, V	72
Power, kW	330
Water flow, gpm	110
Water velocity, fps	36
Pressure drop between water headers, psi	22
Total pressure drop, psi	150
Surface cooling rate, W/in.^{2}	6000
Calculated central field, kG	55
Inlet water temperature, °C	27
Mean copper temperature, °C	128
Maximum turn voltage, V	3.1
Radial pressure on the insulation, psi	$\leq$360
Tensile stress in the copper, psi	$\leq$18,700

[a]For coil parameters, see *Thermonuclear Div. Semiann. Progr. Rept. Oct. 31, 1965*, ORNL-3908, p. 129, Table 8.2.

cause is the possible plugging of thermally adjacent water passages. The coil had been run about 65 h over a period of several weeks on two different water supplies, neither of which was filtered just upstream of the coil. After 55 h of operation at about 1000 A and about 3 h at up to 4000 A, visual inspection showed that obstructions of various sorts blocked more than 10% of the cross section of 123 grooves out of a total of 1950. Light could not be seen through three isolated grooves. A third possibility is that conductive dirt entered the winding during manufacture of the coil and was pushed through the insulation as the forces and temperatures increased.

A system which should lead to a resolution of the preceding questions, and perhaps to higher coil performance, has been fabricated and is being assembled. The coil itself, Fig. 8.3, is wound on a mandril which serves both as an electric and hydraulic terminal. The water flow path, as well as one of the "wagon wheels" which transmit axial forces, is shown in Fig. 8.4. The arrangement shown fits into a copper cylinder which acts as the outer electrical terminal and also directs the water flow to the route shown.

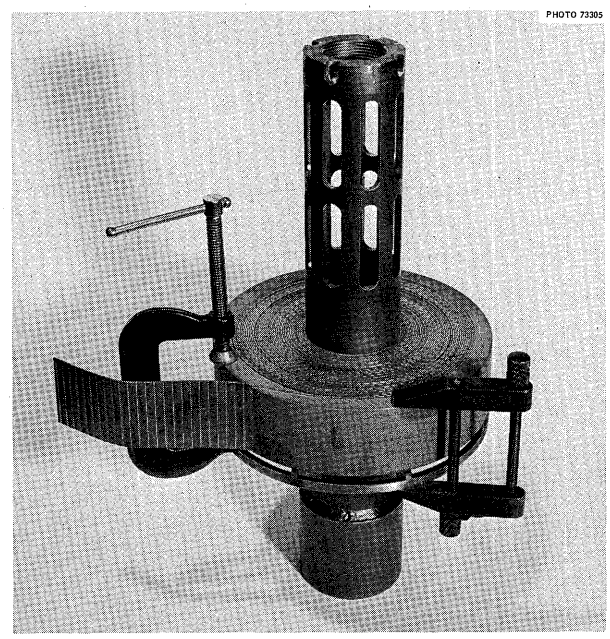

Fig. 8.3. Winding and Mandril of Ribbon Coil No. 3, Top View.

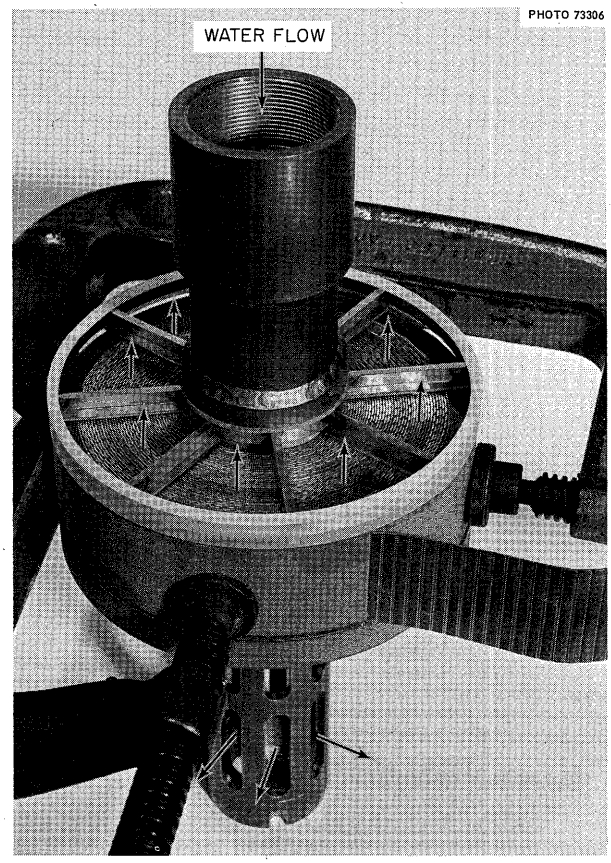

Fig. 8.4. Winding and Mandril of Ribbon Coil No. 3, Bottom View.

This subassembly then screws into the permanent case, automatically making the electric and hydraulic connections. It is expected that all parts of the assembly except the ribbons and the Micarta filler ring will be undamaged and reusable and that one coil can be tested while another is being wound on the second mandril. The entire assembly is mounted in the bore of a 60-kG coil in the magnet laboratory, with the coil axes coincident but with their midplanes separated so that it will be possible to produce axial magnetic forces. Separate generators will be available for the coils. It will thus be possible to vary the magnetic forces on the test coil while its current and temperatures are held constant, and to see the separate influence of power and force on coil failure.

Directing the cooling water through a 20-μ filter should ensure that foreign particles cannot degrade the coil. The filter has sufficient capacity to supply a coil of at least 400 in. ribbon length and will make possible the testing of several insulations within the same coil. Since with clean water the life of the coil will likely be limited by the deterioration of the insulation, fairly long endurance tests will be part of the insulation selection process, and the simultaneous testing of insulations will give considerably quicker results than sequential testing.

In some possible applications of ribbon coils, the size of the water headers at the ends of the coil will be restricted. However, if the header volume is reduced excessively the flow through the coil may become nonuniform and cause premature failure. Therefore the coil holder described above was designed so that different rotationally symmetric header configurations can be tested. The internal shape and size of the headers may be modified by adding various filler disks to the arrangement of Fig. 8.3 as the coil is being installed. If the disks are of lucite, visual observation of the coil ends can be maintained during operation.

8.3 VERSATILE, LARGE-VOLUME COIL ARRANGEMENT ("D COILS")

J. N. Luton, Jr.

The field characteristics of a large-volume magnet system with great versatility have been described previously.[6] The construction of the coils has since been completed, and the system has been installed in the magnet laboratory. Figure 8.5 shows the assembly with its protective shield removed. The axis of the coil pair is vertical, and the axial separation of the coils is maintained at 1.5 in. by a Micarta spacer plate. One of the six rectangular access ports through this plate may be seen in the center of the photograph. Cooling water and electrical power are fed through the floor, thus moving most of the header piping and electrical bus beneath the laboratory. The two power leads lie just to the left of the rightmost water header, surrounded by nylon water tubes. Just to the left of the longer electrical lead, one can see the line of bolted joints which electrically connect the pancakes. This joining method differs from the previous practice of using silver-soldered joints, and it allows the use of a relatively simple procedure for disassembling the coil. This might be useful for making future changes in the coil configuration and is especially desirable in case a damaged pancake must be replaced. The massive end plates ($2\frac{1}{8}$ in. thick), stay bolts, and center sleeve are required to restrain the axially repulsive forces generated in cusp operation. The metal ring at the top of the photograph is the flange of the center sleeve; the lower end of the sleeve screws into the bottom plate. Strain gages are mounted on the inner surfaces of the end plates, at various points on the center sleeve and its top flange, and on the six stay bolts. The bolts with their gages have been calibrated in a tensile machine, and, during the tightening of the bolts and sleeve, the strain gages are being used to determine the axial forces. This direct method should give a more accurate and symmetrical preloading than could be obtained by tightening to a given torque.

The safety tests which must precede routine operation have been commenced, but not completed. The current has been raised to 8500 A, or 92% of the design value and 85% of the value to be reached during the test. The field strength was 58 kG, as predicted. When the mirror tests are completed, the assembly will be energized and tested as a cusp pair.

[6] *Thermonuclear Div. Semiann. Progr. Rept. Oct. 31, 1965*, ORNL-3908, pp. 118–24.

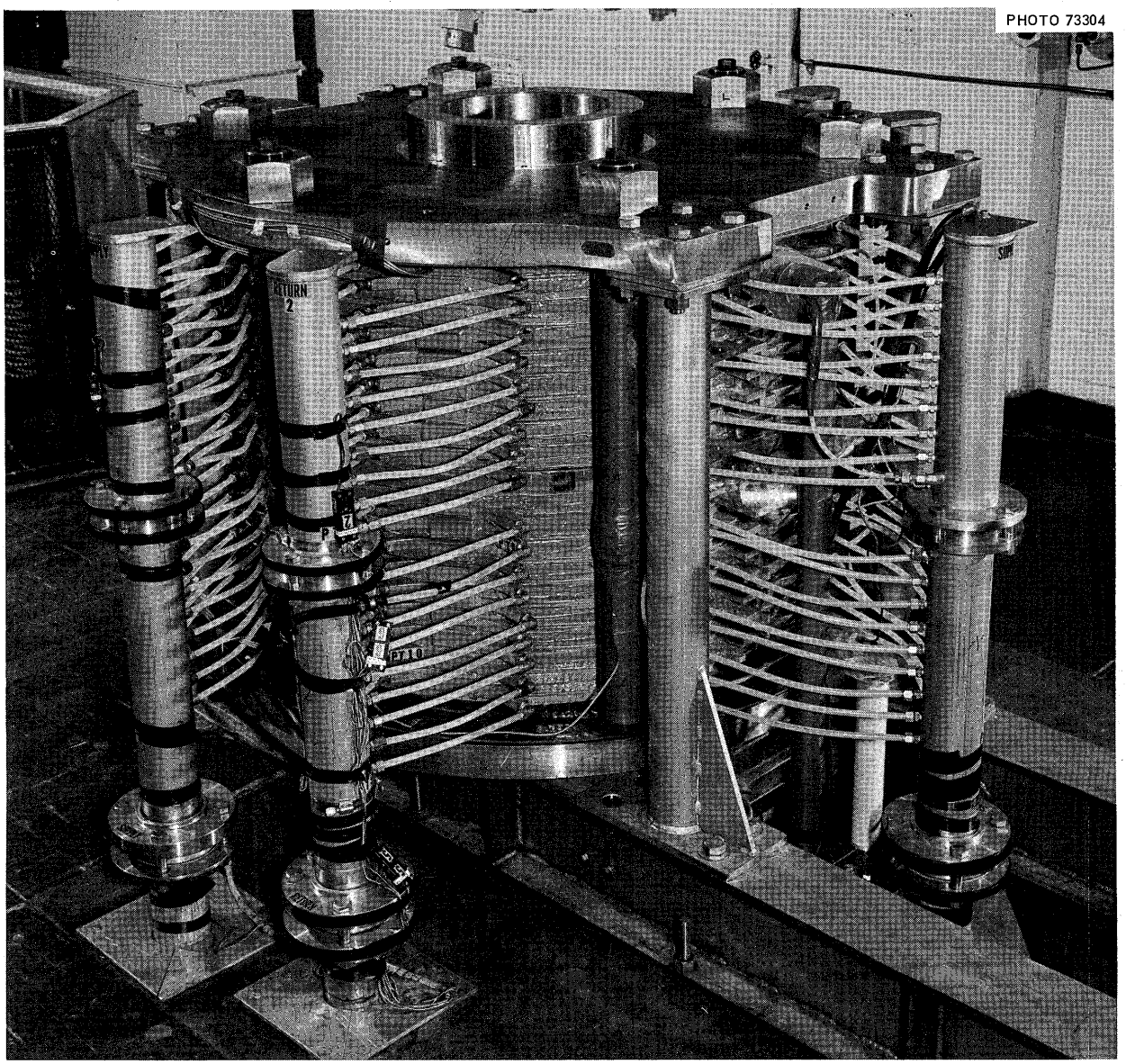

Fig. 8.5. D Coil Assembly.

8.4 FERROMAGNETIC FLUX TUBE SPREADERS

J. N. Luton, Jr. W. L. Stirling
O. M. Thomas[7]

It is sometimes desirable to locally expand the cross section of a magnetic flux tube, for example, to reduce, in the region of the target, the power density of a longitudinally directed electron beam. The required reduction in flux density B may be achieved either by means of an opposing magnet coil or by an iron shielding member. If both methods are suitable for a particular case, the method using iron is likely to be put in operation more quickly and to prove more convenient and economical than a specially constructed coil. A previous report[8] explains briefly the performance of such a ferromagnetic beam spreader for use at the pole piece of one of the gaps in the

[7]Plant and Equipment Division.

[8]*Thermonuclear Div. Semiann. Progr. Rept. Apr. 30, 1963*, ORNL-3472, p. 44.

Beta Tank Facility. The present note describes in some detail work on two new flux spreaders which were to be used in the air-cored Beam Plasma Facility.

The purpose of the first of these flux spreaders was to decrease the beam power density at the anticathode[9] and thereby allow the use of larger beam currents without damaging effects. A $\frac{3}{8}$-in. mild steel plate was cut into annuli of various sizes so that they could be stacked to form different solids of revolution. The anticathode was replaced with a mount to hold the plates in any desired number and sequence, and a field probe was arranged to measure the flux density along the axis of the stack. A starting stack compatible with the available space inside the machine was selected by intuition, and disks were removed, added, or replaced after successive field measurements. In this systematic way, the satisfactory solution shown in the upper half of Fig. 8.6 was obtained. Curve 1 is the boundary of an electron beam of $\frac{1}{4}$ in. diameter before introduction of the flux spreader. It is assumed that each beam follows a flux tube and that the flux density is approximately uniform in each cross section. The latter assumption, which is partially justified by the earlier off-axis measurements in the Beta Tank spreader, makes the procedure much less laborious.

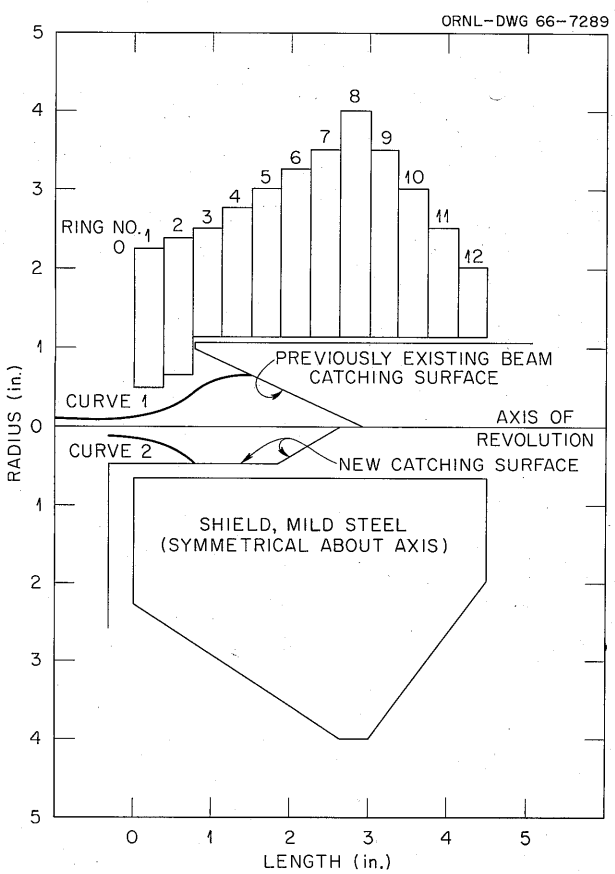

Fig. 8.6. Flux Spreaders for Anticathode of the Beam-Plasma Facility.

The following comments can be made about the results of changing the configuration of the upper half of Fig. 8.6. Adding an annulus of smaller inner diameter in position 0 reduces the flux density appreciably but moves the minimum point so far axially that the beam would be too close to the edges of the iron. In addition, the smaller hole would have increased the alignment problems present in normal operation of the machine. Adding iron at the outer diameters of positions 8 to 12 tended to saturate the iron in positions 4 and 5, as indicated by contraction of the flux tube in that region. Removing all iron beyond a diameter of $5\frac{1}{4}$ in. had little influence on the axial field until about position 4; beyond this position the field tended to rise rather than continuing to drop. Removal of iron from the inner surface of annuli 1 and 2 degraded the performance greatly in regions 1 to 3 but had little effect on the shielding ratios ultimately reached farther from the face. There was, therefore, little objection to changing the shape of the lower half of Fig. 8.6 when for other reasons the latter configuration became advantageous. As can be seen in curve 2, making the shield solid and adding iron to the bore more than compensated for the iron removed near the face.

The second spreader was to permit proper operation of the anode channel[10] with higher midplane fields. Figure 8.7 shows a cross-sectional view of the selected shield; Fig. 8.8 shows the axial fields with and without the shield. The ends of the shield were terminated conically rather than abruptly in order to avoid excessive saturation in the midregions of the shield and the resultant irregularities shown in the dotted curve of Fig. 8.8. The field at the end of the iron, point *A*, proved, in operation, still to be excessive. There is not room for a longer shield, and

[9]See sect. 4.7 of this report.

[10]See sect. 4.7.4 of this report.

ORNL-DWG 66-6615

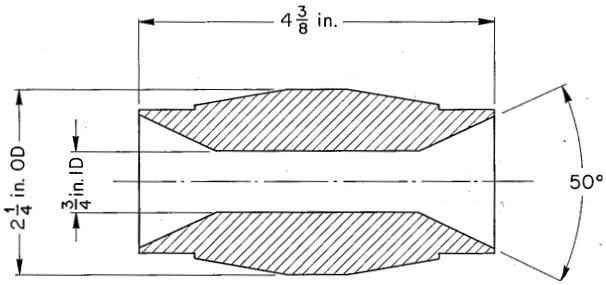

Fig. 8.7. Iron Shield Used to Reduce Field in Anode Channel.

ORNL-DWG 66-6616

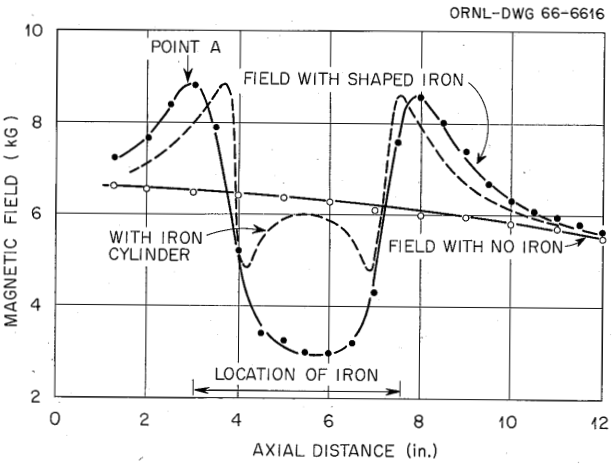

Fig. 8.8. Variation of Longitudinal Magnetic Field Intensity in Anode Channel; Axial Midplane Field About 3250 G.

there is now a desire to independently control the magnitude of the field in the anode; therefore, the shield is being replaced with a bucking coil.

8.5 FIRST SCALE-UP OF THE IRON-CORE ELECTROMAGNET PRODUCING A MAGNETIC WELL WITH NON-ZERO MINIMUM

I. Alexeff W. Halchin W. D. Jones

A minimum-*B* iron-core magnet has been built, as shown in Figs. 8.9 and 8.10. With a field of 3 kG at the center, measurements show that this magnet has a minimum-*B* field with a ratio in the worst, radial, direction of 1.2 to 1.

One-half-inch-thick Armco iron plate laminations were used for the pole pieces. The Armco iron

ORNL-DWG 66-6617

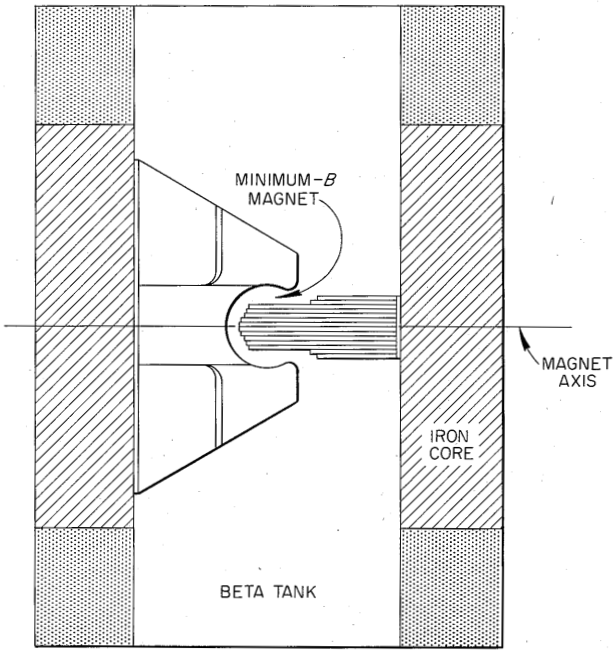

Fig. 8.9. Arrangement of Minimum-*B* Magnet in Beta Tank Facility.

PHOTO 73288

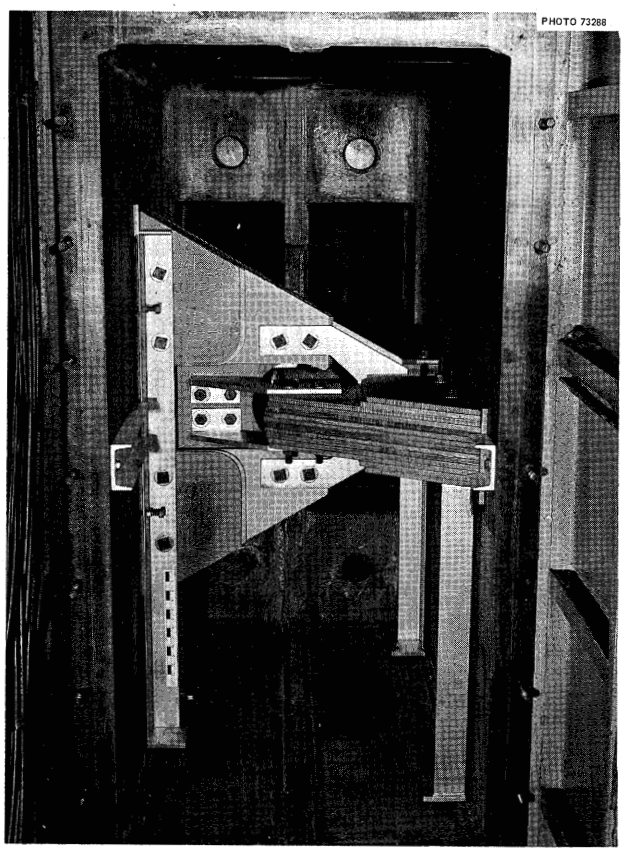

Fig. 8.10. Minimum-*B* Magnet in Beta Tank.

in the finished minimum-*B* magnet weighs 1900 lb. The center cavity is 10 in. in diameter and has a spherical shape. The iron magnet is 32 in. overall axially through the pole pieces. Power for the magnet is supplied by the Beta Tank Facility. Arrangement of the facility and magnet is as shown in Fig. 8.11. The maximum coil power of the Beta Tank Facility is 2000 A at 30 V.

Field measurements for one quadrant of the 10-in. sphere are shown in Tables 8.2–8.7. Meas-

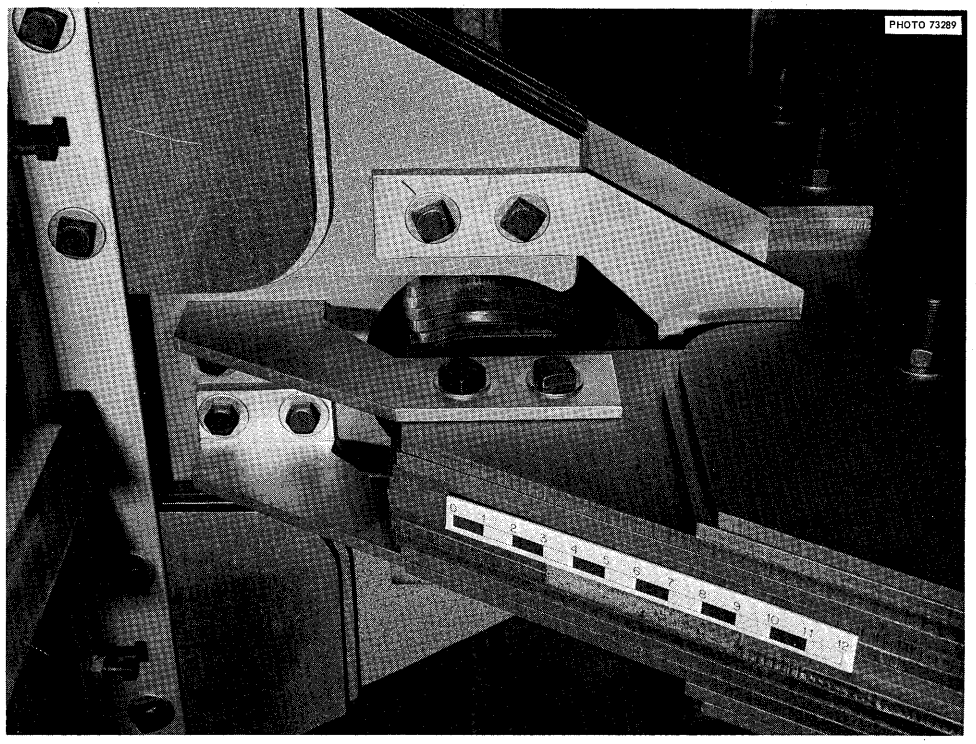

Fig. 8.11. Minimum-*B* Magnet. The center spherical opening is 10 in. in diameter.

Table 8.2. Field Measurements (kG) Taken at the Central Horizontal Plane

Radial (in.)	Axial (in.)									
	0	½	1	1½	2	2½	3	3½	4	4½
0	3	3	3.15	3.3	3.6	4	4.35	4.6	4.75	4.35
½	3	3.05	3.15	3.35	3.65	3.95	4.3	4.6	4.75	4.35
1	2.85	3	3.15	3.3	3.7	4.0	4.35	4.65	4.75	4.25
1½	3.15	3.2	3.25	3.35	3.7	4.0	4.35	4.5	4.7	
2	3.15	3.35	3.25	3.55	3.65	3.8	4.55	4.7	4.65	
2½	3.45	3.45	3.55	3.8	4.0	4.35	4.65	4.8	4.4	
3	3.55	3.65	3.8	3.9	4.1	4.5	4.5	4.2		
3½	3.6	3.65	3.6	3.95	4.2	4.4	4.55			
4	3.6	3.65	3.65	3.9	4.1	4.15				
4½	3.15	3.2	3.0	3.35						

Table 8.3. Field Measurements (kG) Taken at the Horizontal Plane ½ in. Above Center

Radial (in.)	Axial (in.)									
	0	½	1	1½	2	2½	3	3½	4	4½
0	3	3.05	3.15	3.35	3.6	3.95	4.35	4.7	4.95	4.6
½	3	3.05	3.2	3.4	3.65	3.95	4.4	4.7	4.75	4.55
1	3.1	3.1	3.2	3.45	3.75	4.0	4.4	4.75	4.8	4.4
1½	3.05	3.2	3.4	3.55	3.85	4.15	4.5	4.8	4.85	
2	3.4	3.45	3.5	3.7	4.0	4.35	4.7	5.0	4.85	
2½	3.3	3.45	3.55	3.8	4.15	4.4	4.9	5.15	5.0	
3	3.2	3.45	3.25	3.5	3.95	4.5	4.85	5.15		
3½	3.4	3.35	3.5	3.65	4.35	4.6	4.95			
4	3.6	3.55	3.65	3.95	4.20	4.55				
4½	3.2	3.2	3.1	3.5						

Table 8.4. Field Measurements (kG) Taken at the Horizontal Plane 1½ in. Above Center

Radial (in.)	Axial (in.)									
	0	½	1	1½	2	2½	3	3½	4	4½
0	2.7		3.35		3.45		5.2		6.5	8.7
½										
1	3.4		3.6		4.3		5.2		6.75	8.5
1½										
2	3.4		3.8		4.4		5.6	6.35		
2½										
3	4.2		4.3		4.9		6.3	8.69		
3½										
4	4.3		4.4		5.35	6.8				
4½	4.2		3.95							

Table 8.5. Field Measurements (kG) Taken at the Horizontal Plane $2\frac{1}{2}$ in. Above Center

Radial (in.)	Axial (in.)									
	0	$\frac{1}{2}$	1	$1\frac{1}{2}$	2	$2\frac{1}{2}$	3	$3\frac{1}{2}$	4	$4\frac{1}{2}$
0	3.6		4.1		4.8		6.45		7.4	6.8
$\frac{1}{2}$										
1	3.75		4.25		5.15		6.7		6.25	6.85
$1\frac{1}{2}$										
2	4.2		4.5		4.8		6.8	6.5	6.8	
$2\frac{1}{2}$										
3	5.2		5.3		5.8		6.75	6.8		
$3\frac{1}{2}$										
4	6.65		6.4		6.3	6.3				
$4\frac{1}{2}$	9.0		8.15	7.6						

Table 8.6. Field Measurements (kG) Taken at the Horizontal Plane $3\frac{1}{2}$ in. Above Center

Radial (in.)	Axial (in.)									
	0	$\frac{1}{2}$	1	$1\frac{1}{2}$	2	$2\frac{1}{2}$	3	$3\frac{1}{2}$	4	$4\frac{1}{2}$
0	3.75		4.3		5.8		8.75		8.25	6.9
$\frac{1}{2}$										
1	3.9		4.4		6.25		9.0		8.2	6.9
$1\frac{1}{2}$										
2	4.75		5.4		7.5		9.9	9.2	7.45	
$2\frac{1}{2}$										
3	3.85		6.3		7.8		8.7	7.4		
$3\frac{1}{2}$										
4	6.3		6.15		6.4	6.75				
$4\frac{1}{2}$	6.2		6.0	6.15						

Table 8.7. Field Measurements (kG) Taken at the Horizontal Plane $4\frac{1}{2}$ in. Above Center

Radial (in.)	Axial (in.)									
	0	$\frac{1}{2}$	1	$1\frac{1}{2}$	2	$2\frac{1}{2}$	3	$3\frac{1}{2}$	4	$4\frac{1}{2}$
0	2.8		3.2		5.0		11		10	7.75
$\frac{1}{2}$										
1	3.15		3.7		5.3		10		8.85	7.7
$1\frac{1}{2}$										
2									8	
$2\frac{1}{2}$										
3	8.3		8.6		9.3		8.8	8.2		
$3\frac{1}{2}$										
4	5.45		5.6		6.3	6.4				
$4\frac{1}{2}$	5.1		5.35	5.45						

urements were taken in parallel horizontal planes, starting at the center of the sphere.

At the time of this writing, the iron is being rearranged to obtain higher flux values at the pole piece centers and to obtain a more uniform distribution of the field at the outer extremes of the spherical configuration.

An earlier report by Alexeff[11] contains a discussion and shows a small experimental model of an iron-core electromagnet.

8.6 SOME SURFACE CURRENT PHENOMENA IN HARD SUPERCONDUCTORS

H. A. Ullmaier W. F. Gauster

8.6.1 Introduction

Recently, a number of theoretical[12–18] and experimental[19–22] publications appeared which deal with hysteresis effects in type II superconductors due to induced currents in a thin surface sheath. There are also measurements with very small ac fields.[23–26] They can be explained by the existence of currents in a thin surface layer which remains superconducting up to a field $H_{c3} > H_{c2}$. Here we report measurements of the limits of changes in the external field where the bulk flux density distribution $B(r)$ of a hard superconductor remained unchanged. We show that these limits are dependent on the external field and the surface condition of the samples, but are independent of the bulk flux distribution, which implies that the observed results are surface effects.

[11] *Thermonuclear Div. Semiann. Progr. Rept. Oct. 31, 1965*, ORNL-3908, p. 128.

[12] H. J. Fink, *Phys. Rev. Letters* **14**, 853 (1965).

[13] H. J. Fink, *Phys. Rev. Letters* **14**, 309 (1965).

[14] H. J. Fink, *Phys. Letters* **19**, 369 (1965).

[15] H. J. Fink, *Phys. Letters* **20**, 356 (1966).

[16] J. G. Park, *Phys. Rev. Letters* **15**, 352 (1965).

[17] A. Rothwarf, *Bull. Am. Phys. Soc.* **10**, 505 (1965).

[18] C. P. Bean and J. D. Livingston, *Phys. Rev. Letters* **12**, 219 (1964).

[19] M. Cardona, J. Gittleman, and B. Rosenblum, *Phys. Letters* **17**, 92 (1965).

[20] P. S. Swartz and H. R. Hart, *Phys. Rev.* **137**, A818 (1965).

[21] A. S. Joseph and W. J. Tomasch, *Phys. Rev. Letters* **12**, 219 (1964).

[22] R. W. DeBlois and W. DeSorbo, *Phys. Rev. Letters* **12**, 499 (1964).

[23] M. Strongin and E. Maxwell, *Phys. Letters* **6**, 49 (1963).

[24] M. Strongin *et al.*, *Phys. Rev. Letters* **12**, 442 (1964).

[25] D. J. Sandiford and D. G. Schweitzer, *Phys. Letters* **13**, 98 (1964).

[26] A. Paskin *et al.*, *Phys. Letters* **19**, 277 (1965).

8.6.2 Experimental Arrangement

We investigated cases with $H_{ext} > H_0$ in which changes of the external field did not influence the distribution $B(r)$ of the bulk flux density. The term H_0 is the external field where the superconductor enters the mixed state ($H_0 \approx H_{c1}$). We used cylindrical samples in longitudinal external fields H_{ext}, which were raised and lowered with sweep rates between 10 and 500 Oe/sec. In this range the results were independent of the sweep rate. Pickup coils were used to detect changes of the bulk flux density distribution $B(r)$. As long as $B(r)$ and therefore the total flux ϕ are not influenced by the change of the external field, no voltage signal appears. The sensitivity of the pickup coil arrangement (Fig. 8.12) is not sufficient to show changes of the surface currents.

The samples are listed in Table 8.8. Pickup coils of several hundred turns were wound directly around the center portion of the specimens. By means of bifilar heater windings it was possible to heat the samples above the critical temperatures. The bath temperature was 4.2°K. The external field was produced by a superconducting magnet with a 3.6-cm bore and 7.6 cm in length. Since the magnet is not much longer than the samples, the field at the rounded sample ends is only about 80% of the center field. Owing to the reduced field strength of the sample ends, end effects are less than they would have been in more homogeneous external fields.

8.6.3 Three Different Types of Experiments

The first kind of experiment (type 1) was carried out as follows: After cooling the sample in zero field, the external field H_{ext} was raised to a series of values H_1 (Fig. 8.13). In each case when H_{ext} was then decreased below H_1, no voltage appeared across the pickup coil until a certain external field H_2 was reached; that is, in the range $H_1 \geqq H_{ext} \geqq H_2$ the total flux [and also the bulk flux density distribution $B(r)$] was not influenced by a change in H_{ext}. Series of H_1 values with the correlated H_2 values are represented in Fig. 8.14. It is convenient to plot the differences $\Delta H = H_1 - H_2$ vs the H_1 values.

The sensitivity of the measurements with the equipment shown in Fig. 8.12 can be estimated as follows: We assume that the bulk flux density near the surface $B(a)$ starts to decrease with an

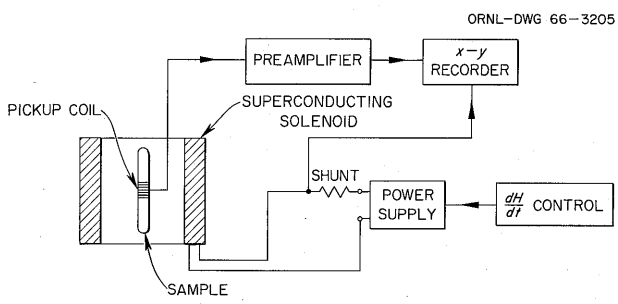

Fig. 8.12. Experimental Arrangement.

Table 8.8. List of Samples

Sample No.	Material	Length (cm)	Diameter (cm)	Surface Treatment
1	Pb–43% In, cold worked	4.3	0.60	Machined
1*a*	Pb–43% In, cold worked	4.3	0.60	Chemically polished
2	Nb–25% Zr, cold worked and annealed at 1250°C (4 h)	4.6	0.68	Machined
2*a*	Nb–25% Zr, cold worked and annealed at 1250°C (4 h)	4.6	0.68	Machined and silver plated (30 μ)
3	Nb–25% Zr, cold worked	4.6	0.63	Mechanically polished
3*a*	Nb–25% Zr, cold worked	4.6	0.63	Mechanically polished and silver plated (30 μ)

approximately constant rate $dB(a)/dt$ as soon as the external field is decreased below H_2 (a is the sample radius). If we consider a certain critical bulk current density $J_c(a)$ near the surface, the voltage generated in the pickup coil with N turns is (in mks units)

$$e = \frac{\pi a N}{\mu_0 J_c(a)} \left[\frac{dB(a)}{dt}\right]^2 t \,. \qquad (1)$$

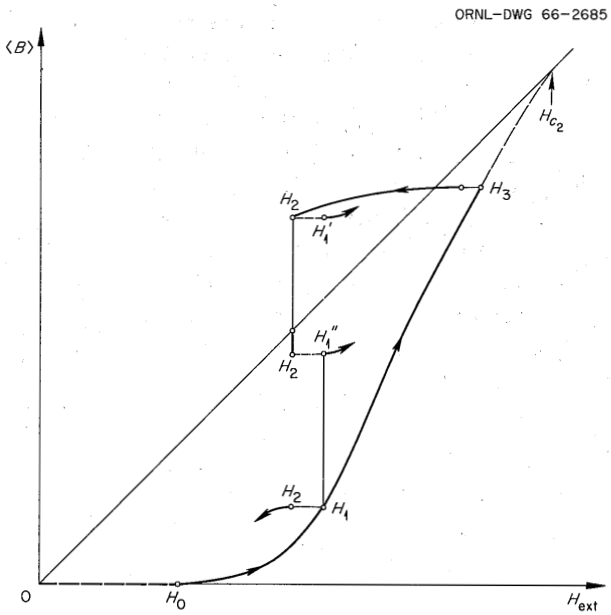

Fig. 8.13 $\langle B \rangle$ vs H_{ext} Diagram Illustrating the Performance of Experiments Type 1, 2, and 3.

On the x-y recorder with preamplifier, a voltage of 2×10^{-8} V could be easily detected. With $a = 0.3$ cm, $N = 300$, $J_c = 10^5$ A/cm^2, and $dB(a)/dt =$ 50 Oe/sec, after 0.35 sec the voltage reaches 2×10^{-8} V. During this time $B(a)$ decreased by 17.5 G. This is a pessimistically estimated value for the sensitivity of our experimental arrangement.

The type 2 experiment was as follows (Fig. 8.13): After cooling the sample in zero field, H_{ext} was first raised to a value H_3 and then lowered to H_2 (which was chosen to be one of the H_2 values of the type 1 experiment). The experiment showed that H_{ext} could be raised to a value H_1' without occurrence of a pickup voltage, that is, without changing $B(r)$. The resulting correlated $(H_1' - H_2)$, H_1' pairs of values are plotted in Fig. 8.14.

The type 3 experiments were performed in the following way: The sample was cooled in a field H_2 (which was one of the H_2 values of the type 1 experiment). The partial expulsion of

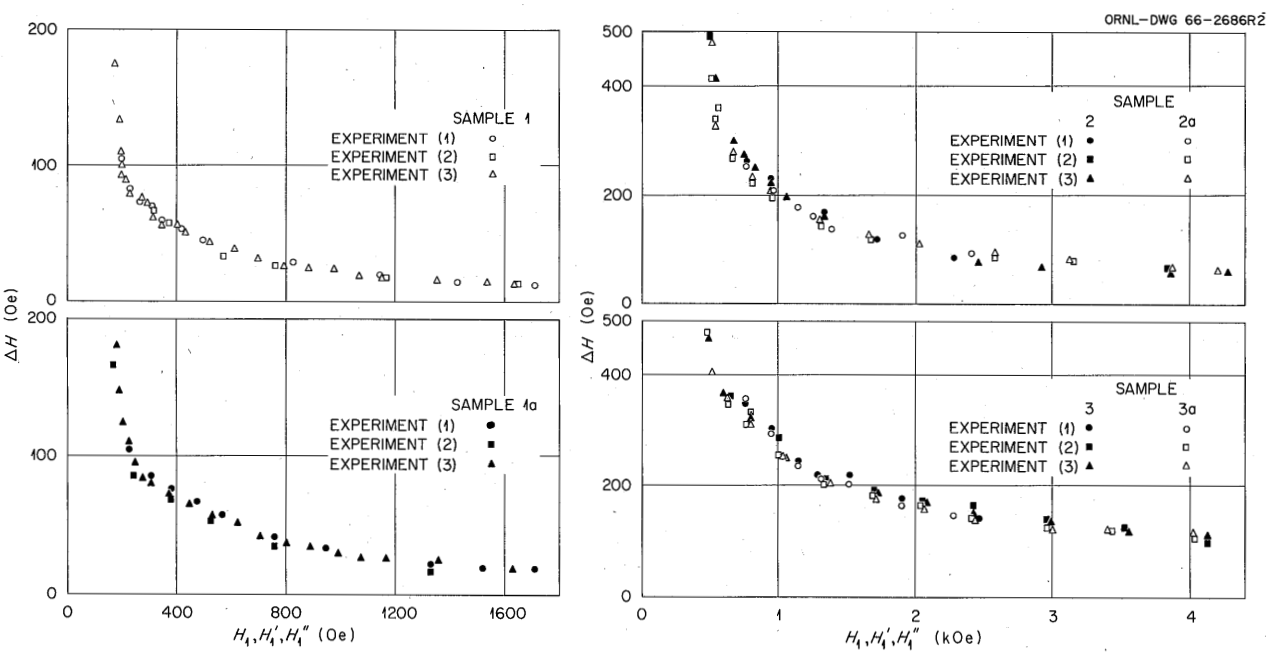

Fig. 8.14. Experimental Dependence of $\Delta H = H_1 - H_2$ as a Function of H_1 Values, for Six Different Samples in the Three Different Types of Experiments Described in the Text.

flux during the cooling-down process[27,28] produced a voltage pulse which was disregarded. After reaching thermal equilibrium, H_{ext} could be raised to a value H_1'' until a new signal across the pickup coil appeared [which indicated a change of $B(r)$]. The pairs of values $(H_1'' - H_2)$, H_1'' are plotted in Fig. 8.14.

8.6.4 Discussion

Figure 8.14 shows that the differences $H_1' - H_2$ and $H_1'' - H_2$ are almost equal to $\Delta H = H_1 - H_2$, that is, $H_1 \approx H_1' \approx H_1''$. It is of interest that in these three cases the bulk flux density distributions are very different. For a type 1 experiment Fig. 8.15*a* shows schematically the shape of $B(r)$, which does not change in the range $H_2 \leqq H_{ext} \leqq H_1$. In Fig. 8.15*b* and *c*, $B(r)$ is represented for a type 2 and a type 3 experiment respectively. These $B(r)$ distributions can be obtained by measurements with microprobes which scan the field in the gap of a hard superconductor cylinder in a longitudinal field.[29–31] In many cases the shape of $B(r)$ can be approximated using Kim's model for the dependence of the critical current density on the flux density. Kim's model does not consider the difference between H_{ext} and $B(a)$. Also, the diagrams obtained by the scanning technique do not show directly these boundary field differences because of the influence of the gap.[32] However, a refined microprobe measurement technique might lead to the desired data.

Our experiments provide only information about the external field zones $\Delta H = H_1 - H_2 \approx H_1' - H_2 \approx H_1'' - H_2$ in which the respective $B(r)$ distributions are not influenced by changes of H_{ext}. Since the value of ΔH is independent of the bulk properties of a sample, we can assume that currents in a thin surface layer induced by the changing external fields shield the bulk of the material until a certain "critical"[33] current is reached. This means that, for example, at H_1, reached by increasing the field, the bulk flux density near the surface is $B(a)$ instead of $B_r(H_1)$ (see Fig. 8.15*a*). The term $B_r(H_1)$ would be the flux density given by the reversible $B(H)$ GLAG correlation for ideal type II superconductors. The difference $B_r(H_1) - B(a)$ is due to an induced diamagnetic

[27] G. Meyer, *Phys. Letters* **7**, 93 (1963).

[28] S. H. Goedemoed *et al.*, *Phys. Letters* **3**, 250 (1963).

[29] H. T. Coffey, *Bull. Am. Phys. Soc.* **10**, 60 (1965).

[30] W. F. Gauster, K. R. Efferson, and J. E. Simpkins, to be published.

[31] H. E. Cline, R. M. Rose, and J. Wulff, *J. Appl. Phys.* **37**, 1 (1966).

[32] H. Koppe, to be published.

[33] This "critical" current should not be confounded with the critical current density J_c for the bulk of the material which is given by the pinning forces due to defects.

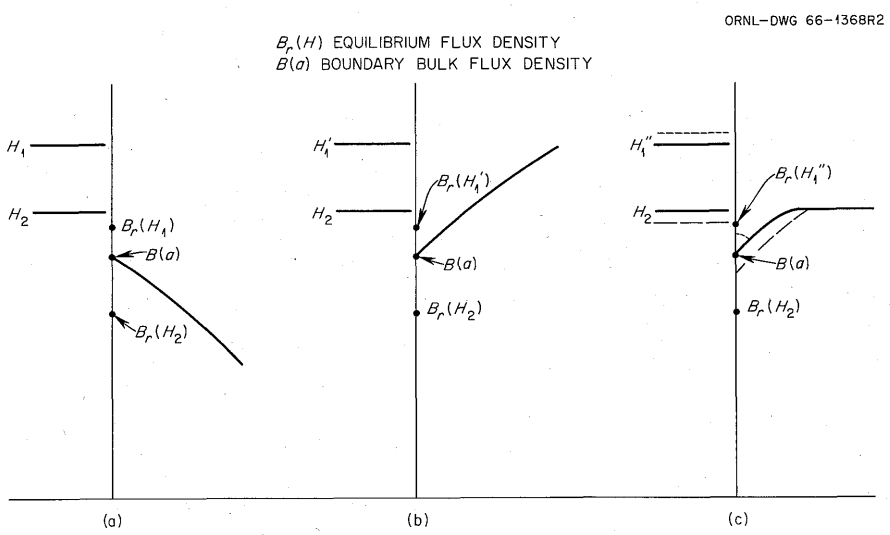

Fig. 8.15. External Fields and Bulk Flux Density Distributions in Experiments *a*, *b*, and *c*.

surface current I_d. By decreasing the external field, I_d becomes smaller and smaller, and finally a paramagnetic current I_p is induced. The external field difference ΔH obtained from our experiments is then given by

$$\Delta H = I_d + I_p \,, \qquad (2)$$

where I_p and I_d equal current per unit length. A similar consideration holds for the two other cases (Fig. 8.15*b* and *c*). A detailed theoretical investigation of these surface currents was first made by Fink,[12–15] who also used this concept to explain the results of Cardona *et al.*[19] The latter measurements yield a ΔH vs H_{ext} relation similar to ours but was obtained by a different experimental technique (microwave power losses).

Fink's calculation has been extended by Park,[16] who predicts an asymmetry of I_d and I_p. An alternative mechanism of surface shielding has been proposed by Rothwarf.[17] A numerical comparison of values calculated from both theories with our results shows that the experimental values have the same order of magnitude but are about a factor of 1.5 to 4 too small. This discrepancy could be due to surface irregularities at which an actual field higher than the external field is produced. This assumption is compatible with the fact that ΔH increases with better surface conditions (see Fig. 8.14).

The fact that the external field can be changed within finite limits $\Delta H = H_1 - H_2$ without influencing the bulk flux is of great importance for the evaluation of measurements using ac fields of large amplitudes and low frequencies (critical current density measurements with Bean's[34] method, ac losses in hard superconductors, etc.).

We gratefully acknowledge discussions with G. D. Cody, H. R. Hart, H. Koppe, and S. T. Sekula.

8.7 INFLUENCE OF SURFACE CURRENTS ON AC LOSSES IN HARD SUPERCONDUCTORS

H. A. Ullmaier

Recent measurements by Heinzel[35] on magnetic hysteresis losses in high-field superconductors were compared (by Voigt[36]) with Bean's theory.[34] He found good agreement at high field strength, whereas at low fields there are deviations up to 70%. It will be shown that these discrepancies are due to surface currents.

Experiments by Cardona *et al.*[37] and by Ullmaier and Gauster[38] showed that in type II superconductors, surface currents can be induced which shield the bulk of the superconductor against changes in the external field within certain limits. Figure 8.16 shows such field changes schematically in a $\phi - H_{ext}$ diagram (ϕ is the bulk magnetic flux). Field changes within the shaded region ΔH in Fig. 8.16 do not influence ϕ. The field difference ΔH depends on the material, on the shape and condition of the surface, and on the external field. A typical relation between ΔH and H_{ext} is shown in Fig. 8.17. Theories about surface currents which cause the field difference ΔH have been developed by Fink,[39,40] Park,[41] and Rothwarf.[42]

The following derivation of the ac losses in hard superconductors is valid under some simpli-

[34] C. P. Bean, *Rev. Mod. Phys.* **36**, 36 (1964).

[35] I. W. Heinzel, *Phys. Letters* **20**, 260 (1966).

[36] H. Voigt, *Phys. Letters* **20**, 262 (1966).

[37] M. Cardona, J. Gittleman, and B. Rosenblum, *Phys. Letters* **17**, 92 (1965).

[38] H. A. Ullmaier and W. F. Gauster, to be published.

[39] H. J. Fink, *Phys. Rev. Letters* **14**, 853 (1965).

[40] H. J. Fink, *Phys. Letters* **19**, 364 (1965).

[41] J. G. Park, *Phys. Rev. Letters* **15**, 352 (1965).

[42] A. Rothwarf, *Bull. Am. Phys. Soc.* **10**, 505 (1965).

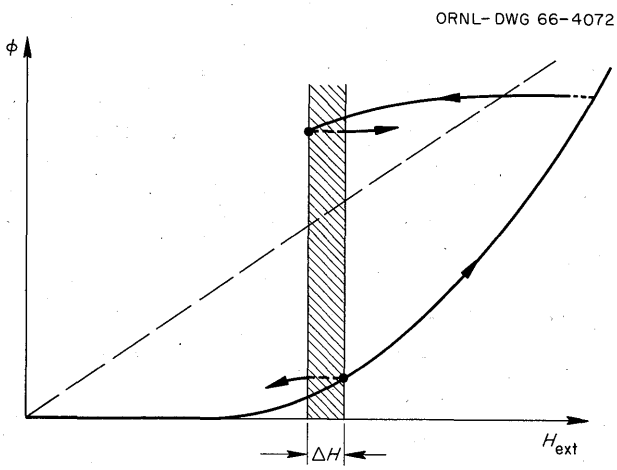

Fig. 8.16. External Field Change Zones ΔH of Unchanged Bulk Flux ϕ.

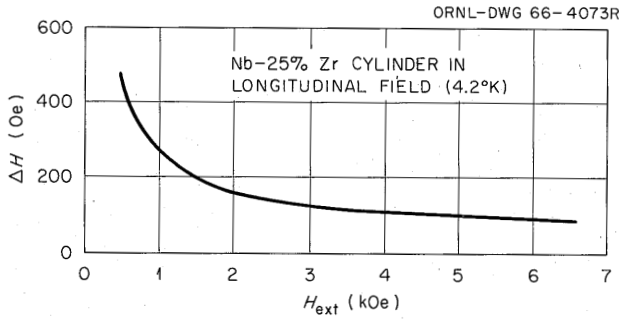

Fig. 8.17. External Field Range ΔH of Unchanged Bulk Flux ϕ as a Function of the External Field.

fying assumptions: (1) The critical current density J_c is constant in the range of twice the ac field amplitude h_0, (2) J_c is independent of the velocity of the vortex lines, and (3) the temperature increase ΔT due to the ac losses is negligibly small. Assumption 1 is fulfilled for $H_{ext} \gg H_{c1}$ (H_{c1} being the lower critical field), while the second assumption is valid for low frequencies. A rough calculation of ΔT shows that for $h_0 = 1$ kOe, $J_c = 10^9$ A/m^2, and a frequency $f = 300$ Hz, $\Delta T < 0.1$°K.[43] Figure 8.18 shows the field distribution in a cylinder exposed to a steady external field H_{ext} with a superimposed ac field with an amplitude h_0. Because of a partial shielding effect on the surface currents, the field difference effective for the motion of flux lines is $2\bar{h}_0 = 2h_0 - \Delta H$ instead of $2h_0$. This equation is approximately valid for $H_{ext} \gg H_{c1}$. During an increase or decrease of the external field, flux lines move in the radial direction. In this motion the flux lines have to overcome the pinning forces. The force per unit length of a flux line is given by $f_p = \phi_0 (H/r)$ (ϕ_0 being the flux quantum). During a displacement dr of dN flux lines, an energy per unit volume of

$$dw = dN\, \phi_0 \frac{\partial H}{\partial r} \frac{dr}{2\pi r\, dr}$$

$$\sim dN\, \phi_0 \frac{\partial B}{\partial r} \frac{1}{2\pi r \mu_0} = \frac{d\phi\, J_c}{2\pi r} \qquad (1)$$

is dissipated. The term $d\phi$ is the magnetic flux which crosses the area $2\pi r\, dr$, and $\mu_0 J_c = \partial B/\partial r$ is the critical current density, which is not too different from $\partial H/\partial r$ for $H \gg H_{c1}$.

[43] M. D. Reeber, *J. Appl. Phys.* 34, 481 (1963).

The flux change at r is

$$d\phi(r) = \mu_0 h\, (a - R + r)\, 2\pi r \quad (\text{for } R - r \ll R)\ , \qquad (2)$$

together with

$$\frac{\bar{h}_0}{a} = \frac{h}{a - R + r} = J_c\ . \qquad (3)$$

The dissipated energy per unit area of the cylinder surface is given by

$$w = \int_{R-a}^{R} \mu_0\, J_c^2\, (a - R + r)^2\, dr = \frac{\mu_0 (2\bar{h}_0)^3}{24\, J_c}\ . \qquad (4)$$

During an ac cycle the field changes from zero to $2\bar{h}_0 = 2h_0 - \Delta H$ and again to zero. Therefore the losses per cycle are (in Wsec/m^2):

$$W = \frac{\mu_0 (2h_0 - \Delta H)^3}{12\, J_c}\ . \qquad (5)$$

For $\Delta H = 0$, Eq. (5) is identical with Bean's formula.

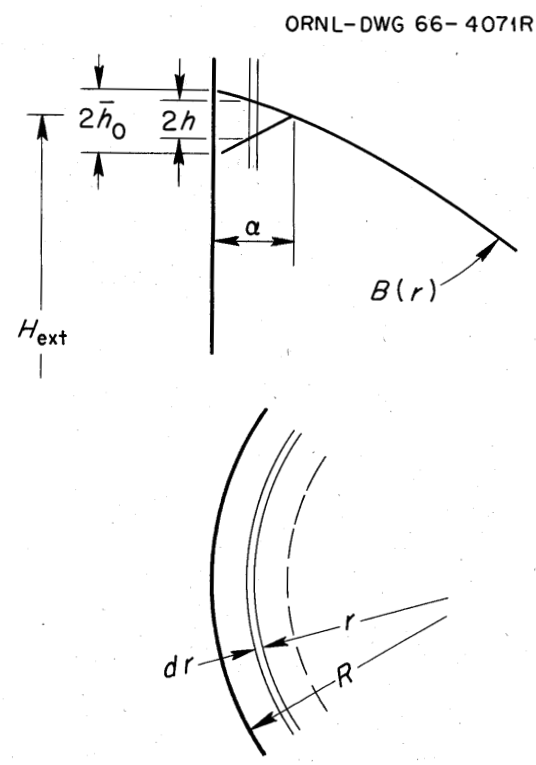

Fig. 8.18. Bulk Flux Distributions Due to a Stationary External Field and a Superimposed AC Field.

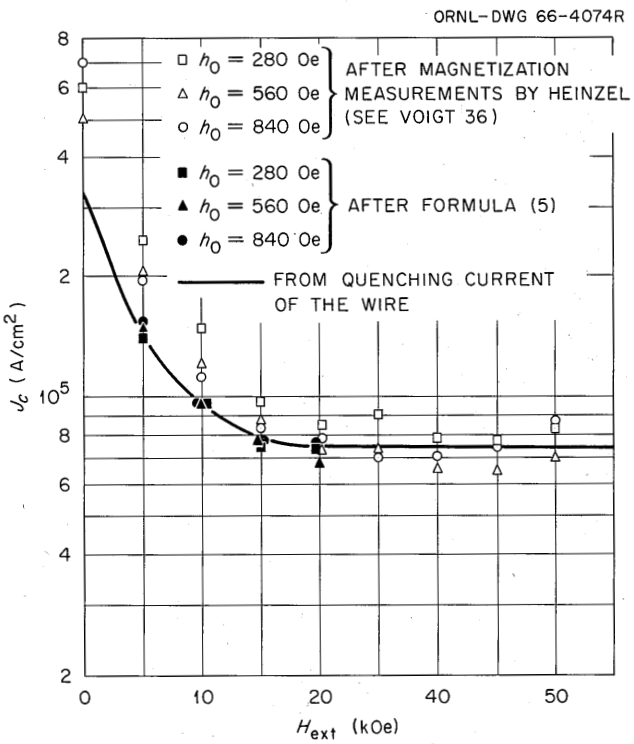

Fig. 8.19. Evaluation of the Critical Current Density, After Voigt, Compared with Results Obtained with Eq. (5).

Figure 8.19 is essentially a repetition of Fig. 2 in ref. 36 and shows that also at small field strengths the measured values of the critical current density agree well with those calculated using Eq. (5). For very small values of H_{ext} the previously mentioned assumptions are not valid, because one has to consider the difference between H_{ext} and B and the dependence of ΔH on H_{ext}. We will report this at another time.

The author is indebted to W. F. Gauster for many suggestions and interesting discussions.

8.8 SUPERCONDUCTIVITY RESEARCH DIRECTED TOWARD THE DEVELOPMENT OF LARGE SUPERCONDUCTING MAGNET SYSTEMS

W. F. Gauster J. L. Horton
K. R. Efferson J. E. Simpkins, Jr.

As mentioned in the previous progress report, work on superconductivity in this Division is sponsored by the Thermonuclear Branch of the AEC and by the George C. Marshall Space Flight Center of NASA.[44] The goal of our efforts is the development of large superconducting magnet systems (e.g., mirror coils and Ioffe bars for thermonuclear research, and active proton shielding for space vehicles). A direct engineering approach at large scale, as is being pursued at several places, based primarily on the extrapolation of results obtained with smaller coils of similar shape, is expensive and time consuming. In accordance with various other laboratories, our experimental and theoretical work is primarily directed toward a better understanding of those physical properties of high-field superconductors which are relevant to the performance of large superconducting magnet systems. In this way, we hope to promote efficiently the engineering development of these large magnet systems, and, as a "by-product," interesting details of the general physics of high-field superconductors can be clarified (see, e.g., Sects. 5 and 6 of this report).

The part of our work on superconductivity which is mainly NASA sponsored is currently described in detail in our reports[45] prepared for the George C. Marshall Space Flight Center under Government order No. H-76798. In order to avoid duplication, we restrict ourselves here to the following résumé of this kind of work done during the last semiannual period:

1. In order to elucidate the prequenching performance of "stabilized" conductors, calculations were made for "ideal compound conductors," that is, conductors consisting of a superconductor in a perfect superconducting state and a nonsuperconducting "stabilizer," considering a transitional resistivity between the superconducting and the nonsuperconducting parts. Simple straightforward one-dimensional calculations for these ideal compound conductors and a new two-dimensional potential theoretical solution for stabilizers in ribbon form are shown here. Furthermore, it is discussed for conditions under which the one-dimensional calculation yields sufficiently accurate results.

---

[44] *Thermonuclear Div. Semiann. Progr. Rept. Oct. 31, 1965*, ORNL-3908, p. 132.

[45] W. F. Gauster *et al.*, *Experimental Simulation of Large, High Field, Superconducting Magnet Operation*, ORNL-TM-1398 (Jan. 26, 1966); W. F. Gauster *et al.*, *Experimental Simulation of Large, High Field, Superconducting Magnet Operation*, ORNL-TM-1514 (June 1966).

2. The phenomenon of flux-flow voltage in hard superconductors is relevant to the performance of stabilized superconductors. Experiments with bare and copper-clad Nb–25% Zr wire (0.0005 in. in radial copper thickness) were made.
3. Unexpected and very interesting results are being obtained by experiments on the "post-quenching state" of high-field superconducting wires. These experiments are being performed with great care, and it is hoped that some final results can be reported in the near future.
4. We continued our experiments with short samples of a compound conductor which consists of a 0.005-in. Nb–25% Zr wire with copper cladding (0.0005 in. in radial thickness) which is indium-soldered on a copper ribbon $\frac{3}{8}$ in. wide and and 0.005 in. thick. We used a new type of sample holder and a new arrangement of voltage contacts. The external field was provided by our 2B magnet coil set with $6\frac{1}{2}$ in. inside diameter, which allows the generation of magnetic fields up to 85 kG, that is, higher than the critical field strength of Nb–25% Zr.
5. We tried to replace the "stabilizing" copper ribbon by electroplating an additional copper layer on the 0.0005-in. cladding of the 0.005-in. wire. For technological reasons only an additional radial copper thickness of 0.005 in. gave reproducible results.
6. Measurements of the magnetic resistance of different copper conductors were made at 4.2°K. Wires, ribbons, and tubes (as used for the center parts of the joints) were investigated, and the tests showed very different resistivities, depending on purity and cold work. Additional tests were made in order to determine the influence of an indium coating on the resistance of the copper conductors.

9. Vacuum Studies

R. A. Strehlow[1] D. M. Richardson[1]

9.1 MASS SPECTROMETRY DEVELOPMENT

9.1.1 Introduction

The primary purpose of a mass spectrometer on the DCX-2 experiment is to qualitatively assess the vacuum systems conditions. An abnormally long pumpdown time may be caused by air or water leaks, which can be distinguished by using a spectrometer, and the quality of various gases as delivered to the vacuum system can be established. Use of mass spectrometric data to provide more useful diagnostic information requires a consideration of several factors, such as significance of organic mass peaks in mass spectra obtained on unbaked systems, the effect of gage tubulation on the pressure reading of a spectrometer or ion gage, the scan speed and response times of the spectrometer, and the cracking patterns of various gases. These have been examined and are discussed below in the order listed.

9.1.2 Organic Peaks

Although the dominant DCX-2 impurity is water vapor, the presence of organic peaks (characteristically hydrocarbons) in the mass spectra leads to the desire to determine whether or not these peaks should be considered in deriving an analysis of the gas composition from mass spectrometric data.

The significance of organic peaks (e.g., 15, 29, 41, 57) has been questionable in mass spectra. Since ion gages do respond disproportionately to the environment of the gage, a study using a mass spectrometer similar to that used on DCX-2 was conducted on a separate vacuum system to determine the extent of bias present in the instrument when operated in a similar vacuum system.

Mass spectra on DCX-2 presented somewhat conflicting evidence:

1. There was generally a decay in organic peak heights for an hour after turning on the filament, which indicates a thermal effect local to the spectrometer ion source.
2. Operation of the DCX-2 experiment with deuterium was observed to yield a profusion of deuterated organic masses which could mean an unexpectedly large contamination level in DCX-2 or an instrumental vagary.
3. Normal operation of DCX-2 at slow repetition rates resulted in variation of numerous organic peaks as well as a large hydrogen fluctuation, again indicating a synthesis of volatile hydrocarbons in the experimental volume.
4. Apparent changes in the sensitivity of the DCX-2 mass spectrometer relative to an ion gage could best be interpreted as a small contamination level in the machine, leaving water as the dominant impurity.

The questions to be answered were, simply: (1) To what extent do the organic peaks reflect disproportionately the environment of the spectrometer ion source? (2) Would elevated temperature operation minimize this effect? (3) Would addition of hydrogen or deuterium result in spectra similar to those found in DCX-2? For the study, the spectrometer (a Veeco model GA-3) was installed on a system containing a nude ion gage, an enveloped ion gage, and a liquid-nitrogen trap. Elastomer gaskets were used, along with lubricated gate valves. The 10-in. diffusion pump was operated with Dow-Corning 705 oil. The spectrometer was mounted on a water-cooled flange and a 12-in. length of $2\frac{1}{2}$-in. pipe, the temperature of which

[1]Reactor Chemistry Division.

could be varied by heaters. The spectrometer envelope was wrapped with tape heaters so that it could be heated to temperatures up to 350°C. The mass spectra initially obtained showed the presence of hydrocarbons, which were attributed to the valve lubricant. It was found that addition of hydrogen through a palladium leak to the vacuum system resulted in an increase in the organic peaks. On addition of deuterium a profusion of deuterated species resulted. Warming of the envelope and tubulation resulted in large increases in the organic level. An Arrhenius plot of two organic peaks (43 and 15) had slopes corresponding to about 20 ± 2 kcal/mole, about the heat of vaporization of the valve lubricant. After operation of the spectrometer and tubulation at 125°C for 40 h the organic peaks had decayed by about a factor of 10. Addition of hydrogen at that time led to an increase of organic peaks which was (except for methane) also less by a factor of about 10. These data are shown in Table 9.1. (The spectrometer was operated at reduced ionizing current during these experiments.)

The decay of mass 15 after stopping the hydrogen flow was followed, and the time constants were determined. Before the ion source was heated, the measured constant was 2.5 sec and afterward was about 3.8 sec. In both cases the system time constant was 2.2 sec for hydrogen. The decay of mass 41 was followed initially and found to have a time constant of about 2.5 sec also. This shows that hydrogen reactions were responsible for the organic peak fluctuation. (Some methane was introduced along with air from the hydrogen manifold as an impurity.) The decrease of ion-source organic contribution during this protracted heating

Table 9.1. Use of Elevated Temperatures to Minimize Ion-Source Contamination

(ion currents in units of 10^{-13} A)

Mass	Before Heating of Spectrometer		After 40 h at 125°C	
Change	Base	With H_2 Leak	Base	With H_2 Leak
2	28	650	20	780
12	1.1	3.8	Nil	0.3
13	0.6	3.5	Nil	0.4
14	2.3	12	0.2	3.8
15	4.5	28	0.3	3.5
16	2.1	7	0.3	3.2
17	4.1	12	2.5	7.5
18	14.0	40	8.0	24
26	1.0	6	Nil	1.5
27	4.1	25	0.4	2.5
28	5.1	46	2.5	33
29	4.2	22	0.5	2.5
30	Nil	1.5	Nil	Nil
32	0.4	3.1	0.2	2.4
41	4.5	12	0.4	1.2
57	1.5	2.4	0.2	0.3
Ion gage pressure, torrs	2.0×10^{-7}	4×10^{-5}	1.6×10^{-7}	4×10^{-5}

was about a factor of 9 during the first 40 h (based on total observed organic peak height at a hydrogen pressure of 4×10^{-5} torr). An additional 24 h showed another factor of 2 improvement, as determined by this test.

The conclusions drawn from this study are:

1. The organic peaks and perhaps the water peaks are abnormally high due to spectrometer interaction.
2. Continuous operation of the spectrometer at an elevated temperature decreases these contributions to the mass spectrum.
3. Spectrometer generation of organic peaks in the presence of hydrogen or deuterium is an adequate explanation of the anomalous appearance of these peaks in the DCX-2 data.

Air was occasionally admitted to the system during these studies, followed by hydrogen. Large water peaks generally appeared. Repeating this process with deuterium resulted in the attractive mass spectrum in Table 9.2, which decayed rapidly. An oxidation of the ion-source element surfaces followed by reaction with thermally dissociated deuterium to form D_2O and some deuteromethane seems to be a reasonable explanation of these results. Decay times were not measured.

9.1.3 Effect of Gage Tubulation on Pressure Readings

The algebraic differences between nude and enveloped gage readings are particularly large in unbaked systems. The variability of the gage discrepancy and its magnitude indicated that diffusion pump oil to which nude gages respond is not its sole cause. Studies of nude and normally tubulated gages were conducted in which the temperature of the tubulation was found to be of primary importance even during a mild bake of an elastomer-free system. In the elastomer sealed system used for the mass spectrometer tests, a nude gage and an enveloped gage were operated without trapping the diffusion pump. The normal behavior of the gages under these conditions is shown in the first column of Table 9.3. Nude gages typically read high. Cooling the nude gage manifold to about $-15°C$ yielded the pressure readings shown in the second column of Table 9.3. Cooling the grid and filament leads of the nude gage resulted in no appreciable change from the normal readings, demonstrating that gas evolution from the nude gage manifold was the dominant contributor, not only to the nude gage reading, but also to the enveloped gage ion current. The nude gage, of course, is not free of an envelope. In the case of the gages normally used in this laboratory, the gage fits into a steel shell 5 cm in diameter and 7 cm long, with a conductance (distributed) of about 80 liters/sec compared with the 6 to 8 liters/sec of the normal enveloped gage. Consideration of a distributed uniform outgassing load in a pipe or tube l centimeters long pumped only at one end leads to the approximate expression

$$P_d \doteq q\pi r \left[\frac{1}{S}(r + 2l) + \frac{d}{u}(r + 2l - d)\right] ,$$

where P_d is the pressure d centimeters from the pumped end, q is the outgassing load in torr-liters sec^{-1} cm^{-2}, r is the tube radius, u is the conductance per unit length ($= 8rS_0/3$), and S_0 is the orifice speed at the pumped end. An estimate of q

Table 9.2. Effect of Adding D_2 to System with $p = 4.4 \times 10^{-6}$ torr

(units of 10^{-13} A)

m/e	Before Air Leak I^+	After 40-min Air Leak at 5×10^{-6} torr I^+
20	12	400
19	10	135
18	100	225
17	32	30
16	40	120
15	20	15

Table 9.3. Nude and Enveloped Gage Pressure Readings (torrs)

Gage	Normal Condition	Cold Nude Gage Manifold
Nude	3×10^{-6}	5×10^{-8}
Enveloped	1.8×10^{-7}	9×10^{-8}

at the nude gage manifold temperature of about 50°C was made of about 1×10^{-6} torr-liter sec^{-1} cm^{-2} (a reasonable value) for the study reported here. The gas load was found to be water with some hydrogen, the usual for unbaked steel at low temperatures. Warming of the usual tubulation of an enveloped gage was indeed found to be a significant process leading to a pressure rise during long degassing periods for this type of gage.

The tubulation outgassing therefore appears to be significant in leading to erroneously high values of either normally tubulated or nude gages. An important part of the discrepancy between nude and normally enveloped gages is the temperature of the tubulation.

9.1.4 Scan Speed and Response Times

The GA-3 mass spectrometer used in these studies has a scan speed of about 8 min. The motor-driven resistive control of the high-voltage supply was modified to allow a scan to be made in 25 sec. The electrometer with a response time of about a second was replaced with a Keithley model 417 picoammeter, which with a partially filtered output (to eliminate most of the 60-cycle ion-source contribution) was found to yield good results. These were improved for the high-mass region by tapering the voltage control resistor. The high-mass peaks were then separated, and the time between the adjacent low-mass peaks was decreased. Attenuation of the mass peaks to m/e = 70 during a scan was less than 8%, compared with the steady-state values. With this modified control and readout a study was made of pressure pips, as described below. Since the sensitivity of this spectrometer is about 0.1 $torr^{-1}$ and an emission current of 1 mA is usually employed, the ion current for a partial pressure equivalent to 10^{-9} torr is 10^{-13} A. Without employing an electron multiplier, shorter scan times do not appear feasible for the GA-3.

9.1.5 Sensitivity and Cracking Patterns

The sensitivity of this spectrometer is quite dependent upon filament placement, but is generally about 0.1 to 0.2 $torr^{-1}$. This may be compared with that of an ionization gage, 10 $torr^{-1}$. Observation of electron impact and ion impact patterns on the spectrometer source elements indicates that about one-fourth of the electrons enter the ionizing volume and perhaps about 90% of the extracted ions hit the image plate of the source assembly. The electron path length is about half that of the ion gage. It has been possible to operate with an emission current of up to 3 mA dependably. Resolution of 100 to 125 ($M/\Delta M$ definition) is normal for all masses. The ion slit is 0.005 in. wide and could probably be increased by a factor of 2 with little impairment of the resolution at $m/e \leq 40$. Cracking patterns for common gases obtained with this spectrometer (150 eV electron energy) are shown in Table 9.4. The differences between the patterns observed and those reported by the manufacturer are probably due to electron energy differences. Modification of the filament potential was made to allow operation at 75 V. The patterns for methane, carbon monoxide, and nitrogen then were in agreement. Variation from one instrument to another may be large, and in-place calibration would be needed for precise analysis.

Relative sensitivities supplied by the manufacturer are shown in Table 9.5 for various gases.

9.1.6 Conclusion

Interpretation of mass spectra on the DCX-2 system (or any unbaked vacuum system) should be made with care, since the organic peaks present in the spectra are predominantly due to the immediate environment of the ion source. Heating of the spectrometer envelope and adjacent surfaces should be employed to obtain spectra more closely related to the gases present in the volume. Earlier work showed methane as the principal organic product of electron bombardment of hydrocarbon-contaminated surfaces. Acetylene (with no principal peak of m/e greater than 26) and methane were the only organic compounds observed unambiguously during DCX-2 operation. Other organic compounds may be generally assumed to be instrumental vagaries.

Tubulation effects on ion gages and mass spectrometers, particularly in unbaked systems, must be carefully considered before interpretation of ion current readings at or near the base pressure. A normally tubulated ion gage can yield pressure readings which have little relationship to the volume gas density.

The scan time of the existing spectrometer system can be decreased by about a factor of 20 to

Table 9.4. Cracking Patterns for the Veeco GA-3 Mass Spectrometer (Relative to the Principal Peak)

Gas	m/e	Experimental Values	Manufacturer's Values
CO_2	44	100	100
	28	41	36
	22	6	5.1
	16		18.1
	12		10.4
CO	29	1.1	
	28	100	100
	16	1.1	0.4
	14	3.4	1.4
	12	2.7	2.6
N_2	28	100	100
	14	18	11.2
O_2	32	100[a]	
	16	40	
H_2O	19 (HDO^+ + H_3O^+)		0.1
	18		100
	17		27
	16		5.5
CH_4	16	94	100
	15	100	89
	14		12
	13		5.5
C_2H_6	30		20.2
	29		19.1
	28		100
	27		33
	26		23.4
	15		8.3
Argon	40	100	100
	38	0.2	
	36	1.5	
	20	60	38.5
	$13\frac{1}{3}$	4.8	
D_2	4	100	
	2	3.5	
Helium	4		100
	2		0.9

[a]Oxygen is especially subject to instrumental contributions.

Table 9.5. Relative Sensitivities of the Veeco GA-3 Mass Spectrometer for Various Gases at the Indicated m/e

Gas	Sensitivity	m/e
N_2	1.0	28
Ar	0.90	40
CO	1.0	28
CO_2	0.61	44
Ne	0.64	22 + 20
CH_4	1.29	16
He	0.38	4

30 sec by use of an appropriate electrometer. Faster scans at pressures of 10^{-8} torr will require the use of an electron multiplier.

9.2 OBSERVATION OF PRESSURE PIPS IN VACUUM SYSTEMS

Five distinct types of pressure pips (sudden periodic fluctuations in a pressure reading) have been distinguished in the experimental vacuum systems of the chemistry group. These are characterized in Table 9.6. Helium applied to the Viton sealed pump flange appeared with the pips to the extent of about 5% after $\frac{1}{2}$ h. Since one may estimate the permeation of water vapor to be about 100 times that of hydrogen[2] or helium, the preponderance of water could be related to a permeation of water through the elastomer or to the outgassing of the flanges. The observed hydrogen pipping described in column 4 of Table 9.6 was superposed on a steady system pressure of 6×10^{-7} torr and an average outgassing rate of 3×10^{-7} torr-liter sec^{-1} cm^{-2} at 125°C. These pips disappeared after cooling the system to 30°C and were replaced by air pips, as shown in column 5 of the table. The origin of these pips appears related therefore to the gasketed surfaces, although the factors determining their frequency and magnitude are still unknown. The presence or absence of oil is not a necessary factor in the generation of pips nor is an elastomer necessarily required.

[2]A. E. Symonds, Jr., *Evaluation of Plastic Films for Protective Suiting*, DP-528 (November 1960).

Table 9.6. Classes and Characterization of Pips

Characteristic	Viton O-Ring, Pump Flange	Viton O-Ring, Dry	Aluminum-Wire Gasket, Unbaked	Aluminum-Gasketed Steel System	Aluminum-Gasketed Steel System
Temperature	Room	Room	Room	Elevated (125°)	After cooling to room temperature
Torr-liters/pip	2×10^{-5}	$(1-12) \times 10^{-6}$	$\sim 2-6 \times 10^{-6}$	4×10^{-6}	$(6-8) \times 10^{-7}$
Pip composition	95% H_2O, 5% H_2 + CO	50% Air, 50% H_2O	Air	H_2	Air
Pip frequency	Two every 2 to 3 min, varying with flange temperature; 12-in. O-ring	Erratic	Erratic, about every 40 sec	About 1/sec	About every 4 sec
Rise time	>80 sec^{-1} using nude gage				
Fall time		System time constant			

10. Sputtering of Copper, Molybdenum, 304 Stainless Steel, and Tungsten by Deuterium Ions

O. C. Yonts J. P. Wood H. L. Huff[1]

Some sputtering has been done with D_2^+ ions. Copper was sputtered with D^+ and D_2^+ ions to check new equipment which we hope will enable us to attain 80 to 100 keV energy. Table 10.1 gives results of sputtering measurements for this report period.

[1]Y-12.

Table 10.1. Sputtering of Various Materials by Deuterium Ions

Ion	Energy (keV)	Target	Sputtering Ratio	Remarks
D^+	40	Copper	0.020	Previous value, 0.025[a]
D^+	50	Copper	0.013	
D_2^+	40	Copper	0.054	For copper at 20 keV, 0.035
D^+	50	Molybdenum	0.122	*b*
D_2^+	50	Molybdenum	0.180	*b*
D_2^+	29	Molybdenum	0.016	*b*
D_2^+	40	304 stainless steel	0.0084	
D_2^+	28	Tungsten	0.0089	

[a]O. C. Yonts, C. E. Normand, and D. E. Harrison, *J. Appl. Phys.* **31**, 447 (1960).

[b]If there is an error here we have not found it. The sputtering ratio at 29 keV is consistent with all the measurements. Those at 50 keV are extremely high for D^+ or D_2^+ ions on any material. Some new phenomena may be contributing to the sputtering ratio in this energy region.

11. Design and Engineering: Notes

11.1 COAXIAL ELECTRIC FIELD PROBES CONSTRUCTED WITH PYROLYTIC BORON NITRIDE AS THE INSULATION MATERIAL

W. J. Leonard[1] J. F. Potts
R. L. Heestand

The use of pyrolytic boron nitride as an insulation material in an electrostatic probe seems to have some advantages over other ceramics because of its relatively high electrical resistance over a larger temperature range, its favorable thermal conductivity, and its dielectric constant.[2] Electrostatic probes with a variety of geometries would be useful in the measurement of plasma properties; however, in this investigation, where the feasibility of constructing a probe with a rather unusual insulator is being evaluated, geometry was maintained as simple as possible. The types produced were limited to simple cylindrical probes of single inner metal wire coated with ceramic and to a shielded probe with a metal sheath on the exterior of the insulation.

Initially, attempts were made to deposit boron nitride on a tungsten wire pyrolytically at high temperatures, using BCl_3 and NH_3 as the pyrolyzed gas. The control aspects of such a process are quite critical, and details will not be discussed other than to state that stoichiometric boron nitride was successfully deposited on tungsten wires (0.005 to 0.010 in. in diameter) in thicknesses from 0.001 to 0.030 in. However, the anisotropy of the deposited boron nitride resulted in residual strain conditions that invariably resulted in cracking within 1 hr to several days after completion of the probe.

By use of the above pyrolytic deposition process, boron nitride tubing was produced using platinum-base alloy wire in which creep could be induced at the reaction temperature after obtaining the desired boron nitride thickness; this creep decreased the wire diameter and allowed removal of the platinum alloy, leaving a sound boron nitride tube. This boron nitride tube was then gas plated with tungsten on the exterior, resulting in a dense tungsten layer 0.001 to 0.002 in. thick. Figure 11.1

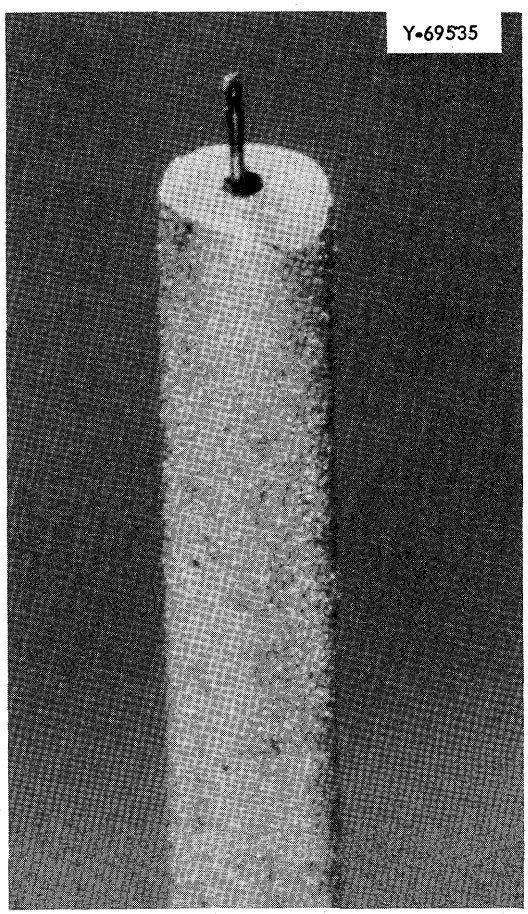

Fig. 11.1. Tungsten-Coated Pyrolytic Boron Nitride Tube with Inserted Tungsten Wire.

[1]Metals and Ceramics Division.

[2]W. J. Leonard and J. F. Potts, *Thermonuclear Div. Semiann. Progr. Rept. Apr. 30, 1965*, ORNL-3836, pp. 127–28.

is a macro photograph of one end of such a tube, approximately 4 in. long, 0.030 in. in outside diameter, 0.0055 in. in inside diameter, with a 0.005-in.-diam tungsten center wire inserted.

The results of this investigation to date indicate that sheathed probes using tungsten conductors and pyrolytic boron nitride insulators can be made small and rugged enough to be of great potential value as diagnostic probes in hot-plasma environments with probe temperatures up to 3000°K. It now remains to integrate this 2- to 4-in. "tip" with a matched coaxial probe extension with sufficient cooling.

11.2 FAILURES OF OFHC COPPER TUBING IN DCX-1 SERVICE

W. J. Leonard[1]

Failures (leaks to vacuum) in the copper tubing used to circulate high-temperature steam in the high-vacuum portion of the initial DCX machine resulted in an intensive investigation of this problem.[3] The superheated steam used was at 400°C (nominal) and was circulated through $^3/_8$-in.-diam, 0.035-in.-wall copper tubing brazed to the copper liner. The mode of failure was found to be an intergranular type of attack in the copper tubing walls, producing pinhole defects. As a result of these investigations, it was recommended that a change to 0.065-in.-wall copper tubing be made and that brazing filler metal be restricted to a copper-silver-tin alloy (type RTSN).

Since that time major modifications in the system have been made. Two parallel superheated steam liners were jacketed on an inner and outer copper liner contained within the austenitic steel containment vessel, resulting in three distinct sections within the vessel: (1) the volume between the containment vessel inner wall and outer copper liner (designated "barrier") surface, (2) the volume between the barrier and the inner copper liner, and (3) the volume of the inner liner. The tubing presently used is $^1/_2$-in.-diam, 0.065-in. wall, OFHC copper, brazed to the stainless steel steam inlet using a socket joint and RTSN filler and brazed to the copper liner using a tube on jacket fillet braze with RTSN filler. The temperature of the superheated steam at the stainless steel inlet is 600°C (approximately), at which point the flow divides into the two copper tubing systems. During operation of the DCX-1 from 1963 to 1965, numerous tube failures have occurred. The tubes alternately carry superheated steam and liquid nitrogen during the bakeout and operation stages, respectively, yielding vacuums in the range of 10^{-9} torr. During experiments, cooling water is circulated through the tubing to maintain the liner temperatures at a safe value.

It has been established by numerous comparative metallographic examinations of failed sections of tubing removed from the machine and control samples which received no steam service that the steam-heating portion of the cycle is apparently responsible for the defects produced in the copper tubing.

It has been further established that for failures observed in the oxygen-free copper, which are due to intergranular corrosion of the copper tube wall, a definite sequence of metallurgical events is necessary. First, the copper must react with oxygen to form a copper–copper oxide eutectic, which must diffuse through the wall via grain boundary paths. Second, a subsequent reducing condition must exist, in which hydrogen reacts with the grain boundary producing very high pressure in these locations, resulting in grain boundary ruptures. The ruptures grow into microfissures with continuing reaction, eventually having a continuous grain boundary fissure path through the wall. Figure 11.2 is a photomicrograph at a failed section of DCX-1 tubing. The section is taken normal to the tube axis through the wall thickness. The fine black constituent in the grain boundaries is copper–copper oxide eutectic, while the coarser black intergranular lines on the inside wall appear to be microfissures.

Since the failure path through a wall at a defect location is not expected to be normal to the axis, a metallographic section taken normal to the tube axis in this location may cut through the defect path. Thus, most sections taken at a tube leak location, such as shown in Fig. 11.2, show only a portion of the actual leak path.

Failures at the copper–stainless-steel brazed joint at the steam inlet have been much more numerous than those in copper tubing beyond this position. Investigation has indicated that the

[3]R. E. Clausing, private communication.

braze filler metal is unstable in contact with copper at these operating temperatures. A liquid phase can form at the braze-metal–copper interface and diffuse into the copper wall. It is not necessary that a liquid phase be present for diffusion of the braze-metal constituent metals into the copper wall. Figure 11.3 is a photomicrograph of a copper joint brazed with RTSN filler metal, showing the resultant diffusion under 600°C service. This intergranular diffusion of braze filler adds to the corrosive effect of intergranular attack of copper by the steam, thus making a braze joint more subject to failure under present DCX-1 operating conditions.

To summarize, the present conditions of velocity, pressure, temperature, and available oxygen

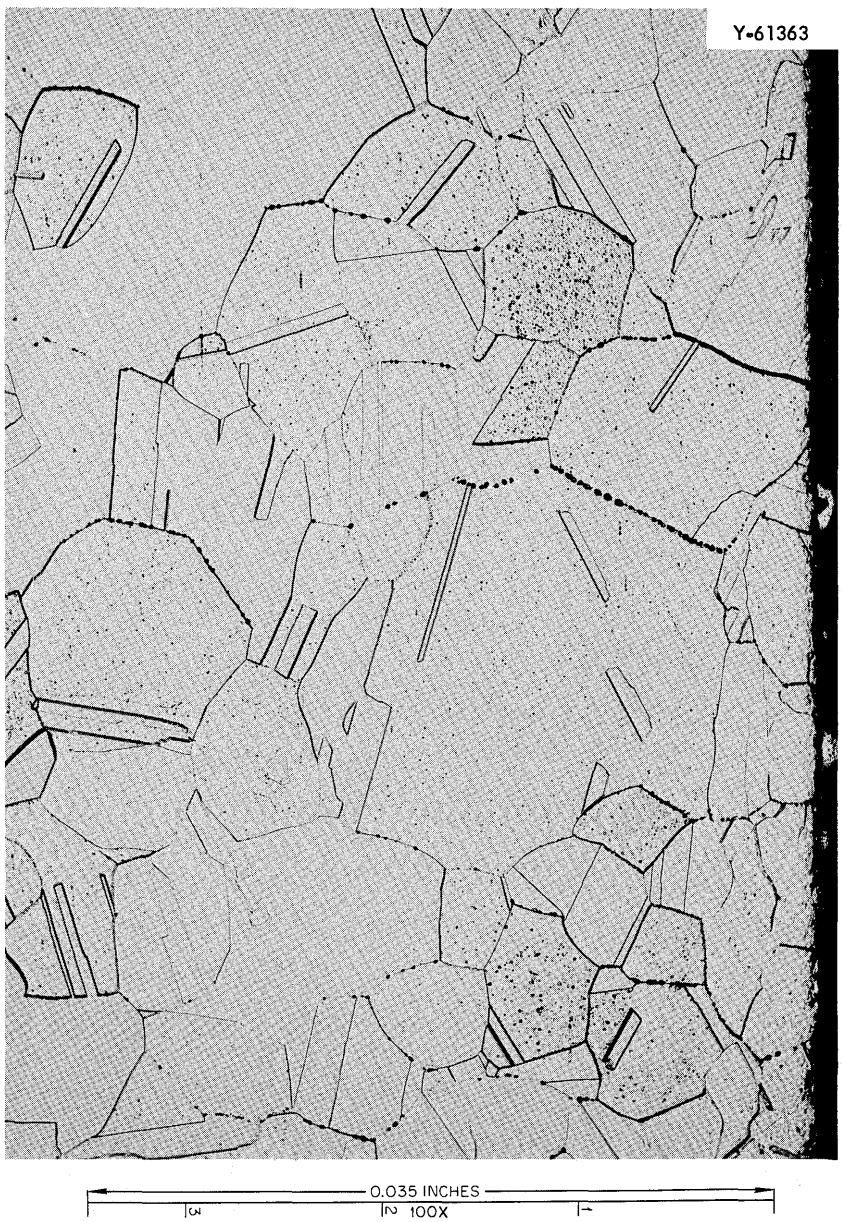

Fig. 11.2. Photomicrograph of OF Copper Tube Wall in Section Taken in Pinhole Failure Area. (Etchant: 80% NH_4OH, 20% H_2O_2.)

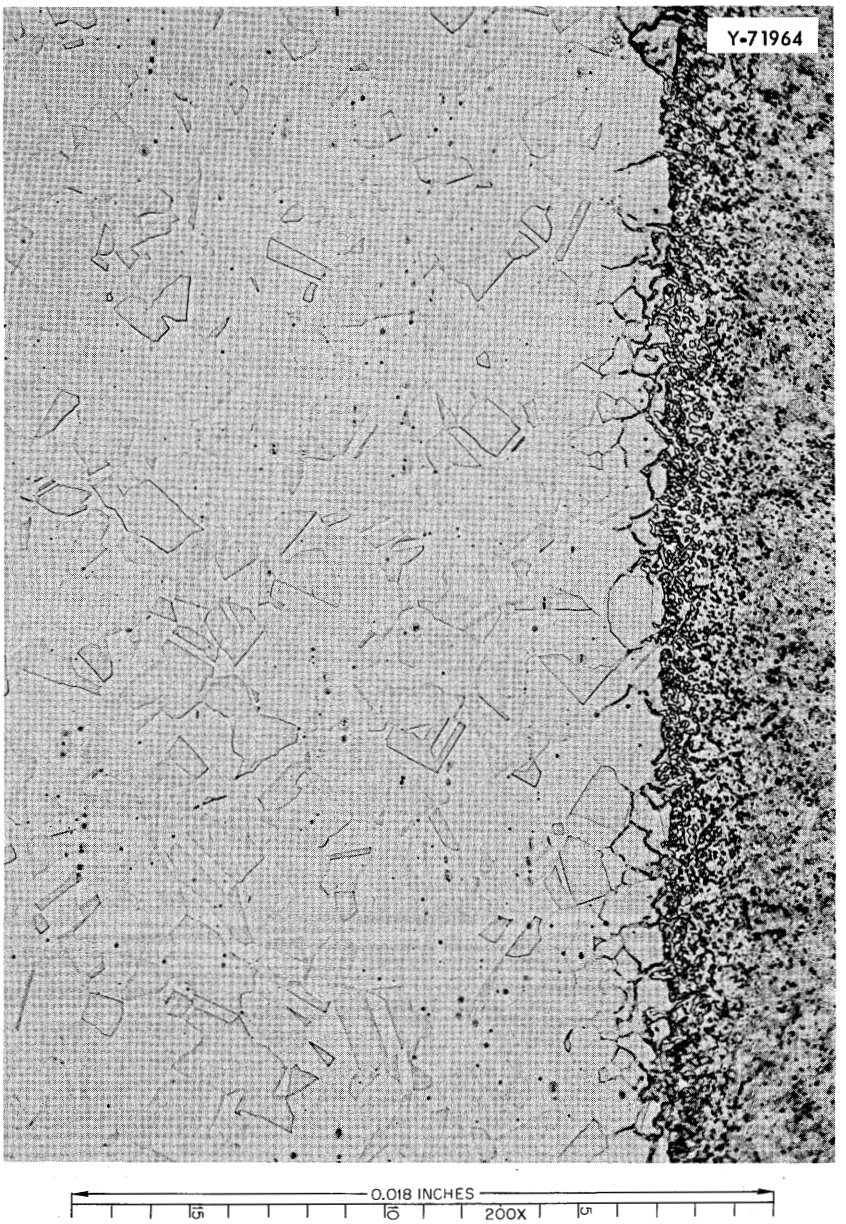

Fig. 11.3. Photomicrograph at Brazed Copper Joint, Showing Intergranular Diffusion of Brazing Alloy into Copper Wall. (Etchant: 80% NH_4OH, 20% H_2O_2.)

and hydrogen concentration of the steam circulated within the oxygen-free copper tubing are severe enough to induce a corrosion effect which results in a much shorter service life than would have been expected with OF copper.

11.3 CAST CROSSOVERS

H. L. Watts W. J. Leonard[1]

Air-core electromagnets for the Division usually consist of square or rectangular seamless copper tubing with a circular, elliptical, or oval hole, wound and assembled to form a single entity.

As the conductors are wound into "pancakes," usually three to eight "in hand" depending on the coil size, current density, etc., there must be a crossover point between layers at the ID or base of the "pancake" for each conductor.[4] If the number "in hand" is large and the ID of the coil relatively small, the problem of sufficient space to make these crossovers by bending or forming the conductors becomes more difficult, if not impossible, and other means must be devised to accomplish the job. In two recent coil designs, a crossover section was designed separate from the conductors. It was machined from a wrought section of copper to the proper configuration, and the conductors were attached to each end by brazing, thus making one continuous water and electrical path.

The machining and inspection of these crossover sections turned out to be more expensive than was first anticipated, due to the accuracy necessary to maintain the integrity of the parts so as to preclude the possibility of a coil failure.

A solution to this problem was sought that would ensure a crossover of high integrity that would be simple and inexpensive to construct. A design was generated which would consist simply of a tube as the core, with cast copper being the exterior portion of the crossover. Figure 11.4 is a sketch of a proposed crossover connection.

A metallurgical evaluation was made of various tubing materials which could withstand the casting process, provide an intimate bond to the cast copper, and possess the physical and electrical properties desired. Tubes of austenitic stainless steel, nickel, molybdenum–0.5% Ti alloy, columbium–1% Zr alloy, and K-Monel were evaluated by casting copper on these tubes in a simple sand casting. A metallographic examination of the cast-metal–tube bond was made. The interface between cast copper and stainless steel had an oxide barrier. The nickel-copper interface showed a partial oxide barrier but possessed a metallurgical bond at most of the interface. Both combinations showed some oxides and voids in the cast copper metal adjacent to the bond. The two refractory metal alloys exhibited an intimate bond. The

[4]J. N. Luton, Jr., *Thermonuclear Div. Semiann. Progr. Rept. Oct. 31, 1963*, ORNL-3564, pp. 121–25.

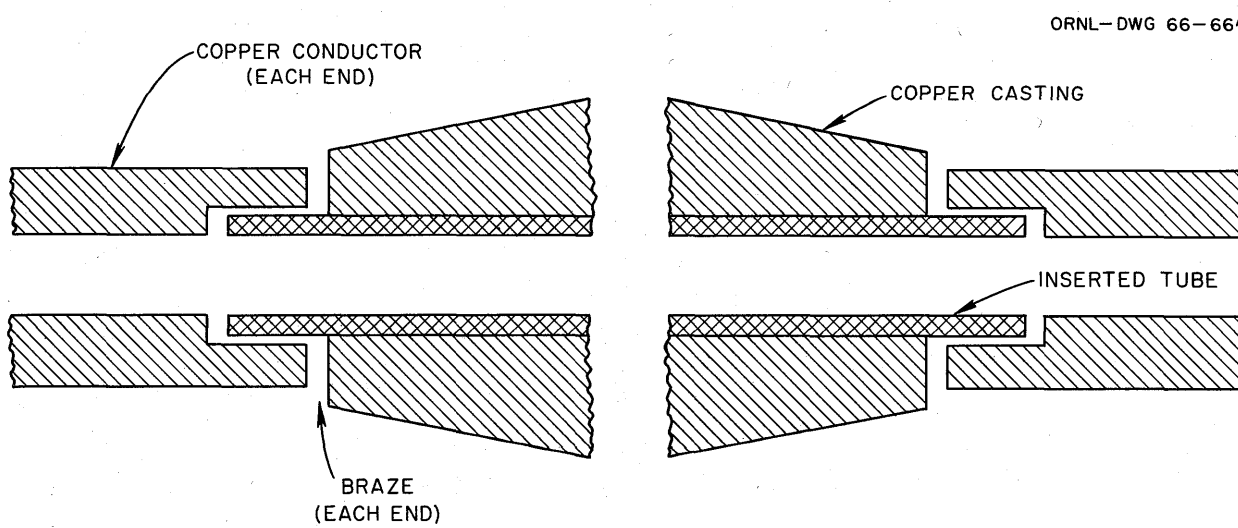

Fig. 11.4. Tentative Design for Cast Electromagnet Crossover.

molybdenum alloy had a slight oxide film at some positions, while a film was completely absent in the columbium alloy. No diffusion of copper into either refractory metal was apparent. The K-Monel–copper interface contained oxides at some positions, but along most of the length a metal-to-metal contact existed. A diffusion of the constituent metals (nickel, copper, and aluminum) appeared to occur across the interface. Figure 11.5 is a photomicrograph showing this interface. The diffusion bond is less than 0.0005 in. wide.

Since a metal is desired that matches as closely as possible the nonmagnetic properties, the heat conductivity, and the electrical conductivity of copper, nickel and stainless steel were summarily eliminated. Of the remaining metals, columbium alloy and K-Monel appear to be the best candidates, and K-Monel appears to be the best practical

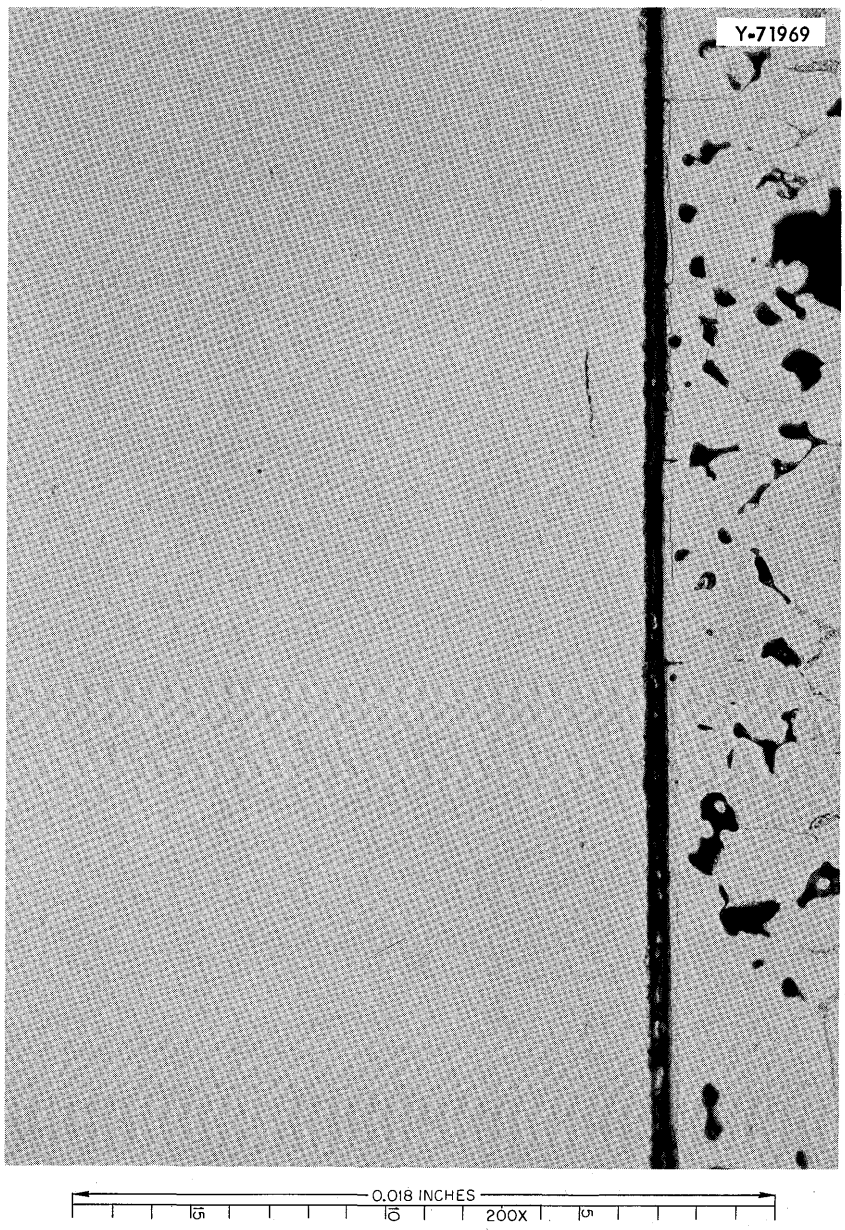

Fig. 11.5. Photomicrograph of Interface Between K-Monel Tubing and Cast Copper. (Etchant: 80% NH_4OH, 20% H_2O_2.)

choice. By previously providing a high-quality surface finish (8 to 12 rms roughness) on the tube, it is felt that a bond possessing the necessary heat and electrical conductivity can be attained in this composite crossover design.

Further development work is proceeding on the casting technique to assure dense, high-quality copper cast metal. Samples have been and are being cast typical of existing designs.

11.4 GENERAL WELDING, BRAZE-WELDING, AND BRAZING DEVELOPMENTS FOR CTR EQUIPMENT

W. J. Leonard[1]

During the past year much developmental work has been done in the field of brazing and welding to acquire the necessary data to prepare formal specifications for use in specific applications for the Division.

A welding investigation was made using oxygen-free copper from $\frac{1}{8}$ to 2 in. thick. The shielded gas arc (Heliarc) welding process was used. Many welds were made using copper plate and pipe according to the rules and requirements of American Society of Mechanical Engineers, Boiler and Pressure Vessel Code, Section VIII, for Unfired Pressure Vessels. The investigation included the proper determination of all welding parameters, joint geometry, heat treatment, etc. Weld quality was evaluated by mechanical testing, nondestructive testing (liquid penetrant and radiographic examination), and weld sectioning for metallographic examination. A formal procedure for use in welding OF copper in applications of the Division was prepared.[5]

An investigation of Heliarc braze-welding techniques for joining OF copper and various stainless steel, high nickel alloys, and copper alloys in dissimilar metal joints has been pursued. Materials include OF copper, copper-nickel alloy (70 copper, 30 nickel), Monel (70% Ni, 30% Cu), and austenitic stainless steel (type 304L). Three braze metals have been used: SilFos (Cu, 15% Ag, 4% P), BT (72% Ag, 28% Cu), and RTSN (60% Ag, 30% Cu, 10% Sn).

A braze weld differs from a braze in that the geometry of the deposited metal is similar to a weld and does not depend on nor use capillary forces to attain the desired geometry. The similarities are that the filler metal only is molten during the fabrication process.

The joints investigated all are a combination of a tube to vessel wall, a design that is used in numerous locations in equipment used in CTR experiments. Three types of joints are of primary interest: tube to header, nozzle, and tube on jacket. The primary function of such a joint is heat transfer from tube to wall or vice versa, with the joint strength as always being an important consideration. Figure 11.6 is a photograph of a jacketed braze weld design in which the tubing is joined to a plate. The samples are copper-nickel tubes, the base metal being OF copper on the left and type 304 stainless steel on the right. The welding parameters are quite critical in that tube wall thickness is maintained at the minimum possible value; thus danger of burn-through of the tube wall during fabrication is an ever present problem.

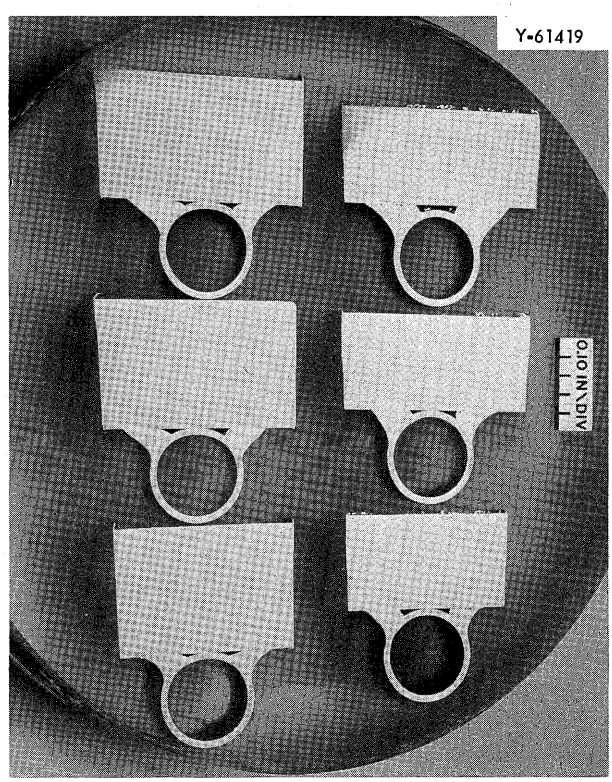

Fig. 11.6. Cross Section of Jacketed Copper-Nickel Tubing ($\frac{1}{2}$ in. in diameter, 0.045-in. wall) Brazed to OF Copper and Austenitic Stainless Steel (Type 304), Left and Right Respectively.

[5]ORNL Welding Procedure Specification Gas Tungsten Arc Welding of Copper, PS 55.

A tube-to-header joint, in which a tube enters a vessel wall and continues on, or a nozzle joint, in which a tube terminates at the outside wall surface with an internal passage continuing into the vessel, functions primarily as a connection rather than as a heat transfer point. Since, for metallurgical reasons, copper is not weldable to the other alloys used, a braze weld is used in lieu of a welded joint in such locations. As in jacketed joints, but to a lesser degree, burn-through of tubing walls must be avoided in fabrication. This requires special joint design and close control of braze-welding parameters.

The ultimate aim of such an investigation as this is to obtain the ultimate material and joint design combination which will perform at the highest possible operational temperature and heat load and maintain integrity for a reasonable period.

Oxyacetylene torch brazing and Heliarc brazing are used on multitudes of miscellaneous projects as well as distinct projects on much of the Thermonuclear Division equipment fabrication. Since by the complexity alone, attempting to cover all such fabrication by a particular specification is non-feasible, if not impossible, an attempt has been made to ensure some measure of quality in equipment fabrication by other means.

Generalized plant specifications for oxyacetylene brazing of copper exist, which include the procedure and contain operator qualification provisions. However, qualifying all personnel who might likely braze some Division equipment to such a specification would prove costly and appears to be impractical from every consideration. Therefore, it was decided to make up a simple specification for determining the level of skill of prospective brazing personnel. Specifications were prepared[6,7] requiring the operator to produce braze specimens, performed under design conditions and end quality requirements consistent with design needs. These qualification specifications satisfactorily separate personnel who possess adequate skill to satisfactorily braze on the equipment encountered in our applications from those who do not. This program is a continuing operation in cooperation with the Y-12 Research Services Department of the Y-12 Maintenance Division located in Building 9201-2.

[6]Specifications for Qualification Procedure for Oxyacetylene Brazing of Copper, TD-SP.61, Rev. 0.

[7]Specification for Qualification Procedure for Inert Gas Tungsten Arc Brazing of Copper, TD-SP.60, Rev. 0.

11.5 HELIARC BRAZING OF COPPER BUS TUBING USED IN GAS ARC FACILITY AND ELMO ELECTROMAGNETS

W. J. Leonard[1] H. L. Watts

Over several years, developmental use of the inert-gas tungsten arc (TIG) process was pursued to satisfactorily braze the external connectors to the terminal hollow magnet conductor. This was required because the oxyacetylene brazing provided an inadequate heating rate to prevent burning of nearby insulation. An apparently satisfactory procedure was developed using TIG brazing, and coils were produced in the shop that met all quality inspection requirements.

However, it was extremely difficult to satisfactorily produce this joint.[8] In fact, no welding personnel consistently produce satisfactory on-the-job joints. Therefore, several mockup joints were made in the shop by a skilled operator. These joints tested absolutely leak-tight. The joints were sectioned transversely at the termination of the two hollow conductors in the connector block. The conductors are inserted in the bottom of the block for a distance of approximately 0.185 in. During fabrication, the braze metal was introduced in a lengthwise position where the conductors entered the connector, and flowed into the gap between the outside tube surfaces to the termination of the conductors.

Although various fabricated joints may test satisfactory, it was determined by metallographic examination of sections that quite different heat inputs were used in making the joints and the amount of porosity present in the braze metal varied greatly from joint to joint in apparently satisfactory joints. One joint, in which braze metal was visually observed to flow the entire gap length (0.185 in.) during fabrication, showed one tube wall to have been completely melted away for about a 60° distance on the inner passage circumference. At a position of 0.140 in. along the gap length from the tube entrance, this same joint showed no burning of the wall of either tube. At the tube entrance position, there was evidenced considerable prior melting of the tube surfaces and of the lower connector wall cross section. These sections maintained their geometry and integrity on

[8]W. J. Leonard *et al.*, *Thermonuclear Div. Semiann. Progr. Rept. Apr. 30, 1965*, ORNL-3836, p. 128.

solidification. On the other extreme, a joint which on visual observation during brazing did not have a detectable flow of braze filler metal to the top of the gap showed on examination of sections that the base metal was not in a molten condition during any phase of the brazing (as required by the brazing specification). At a position of 0.140 in. above the tube's entrance, the gap showed about 100% void. This joint had satisfactory braze metal penetration to a depth of approximately 0.40 in. Another joint in which braze metal was visually observed at the top of the gap showed that in the transverse section at 0.140 in. above the tube entrance there was approximately 75% porosity. Figure 11.7 shows this section. At the top of the gap there was approximately 80% porosity; at 0.060-in. position, 20% porosity; and at 0.040-in. position, very little porosity. The copper base metal at the bottom of the joint showed evidence of being just at the liquidus temperature.

We believe that, with the present design and limitations of the TIG brazing process, this latter braze joint illustrates the optimum quality obtainable. This therefore indicates the need for reappraisal of these joints for future magnet design, balanced against mechanical and electrical integrity requirements of the particular equipment.

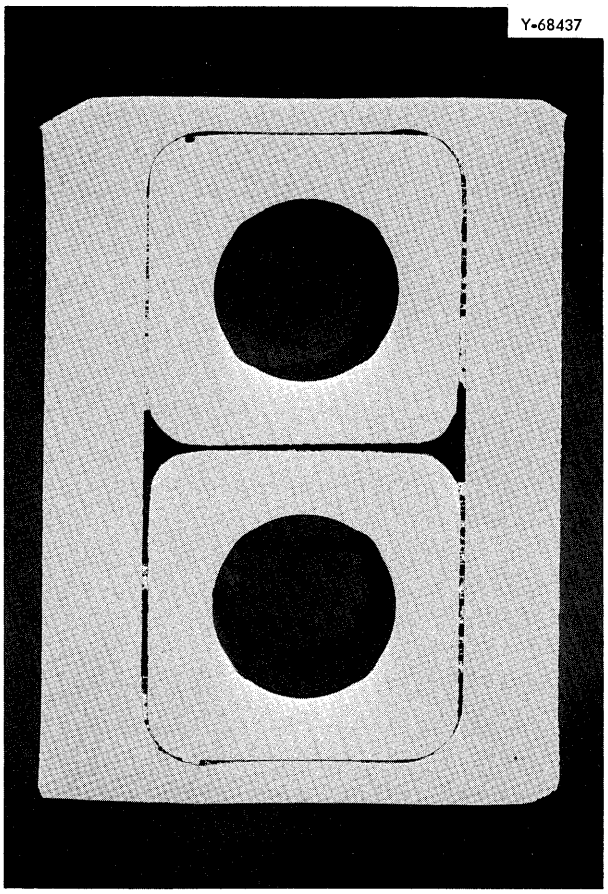

Fig. 11.7. Transverse Cross Section of Magnet Coil-Connector Brazed Joint at a Lengthwise Position 0.140 in. from Tube Entrance.

12. Design and Engineering: Service Report

J. F. Potts, Jr.

The activities of the Engineering Services Group are generally reported incidentally with those of the research groups of the Division. The Group executes or coordinates engineering design, shop fabrication, building operations, and maintenance for the Division.

Design activities for this reporting period are summarized as follows:

Jobs on hand 11-1-65 on which work had not started	4
New jobs received	136
Total jobs	140
Jobs completed	129
Jobs in progress	6
Backlog of jobs 4-30-66	5
Total drawings completed for period (does not include drawings for slides, reports, etc.)	205

Shop fabrication for this reporting period is summarized as follows:

Machine shops	
Completed jobs requiring 16 man-hours or less	205
Completed jobs requiring 17 to 1200 man-hours	108
Completed jobs of miscellaneous character (in plating, carpenter, electrical, glass, lead, etc., shops)	82
Average manpower per week (Machine Shop)	11.6
Average manpower per week (miscellaneous)	2
Number of jobs in progress	32
Electromagnet fabrication	
Completed jobs	8
Number of jobs in progress	2
Completed jobs by outside contractors (Paducah)	2
Average manpower per week	5

The tapering off of the design and construction activities during this period due to the absence of large new facilities or substantial modification of existing facilities is reflected in the above summary and in the fact that two people have been released from engineering and drafting forces respectively.

There has been much-needed cleaning and renovation, and a preventive maintenance and testing program for the large motor-generators (20 MW total) has been established. One 8400-hp motor has been reconditioned during this interval. The whole program will require around 5000 man-hours to put the machines in good working condition. However, with adequate attention to periodic measures, a program of 800 man-hours/year average is expected to maintain these and the two new (10 MW additional) sets in good working condition for several years, assuming a biannual cleaning and painting program and adequate maintenance of cooling air conditions, commutation, and oiling.

Publications, ORNL Reports, Papers, and Traveling Lecture Program

Open Literature

Author(s)	Title of Article	Journal (or Book)
I. Alexeff	Iron-Core Electromagnet Producing a Magnetic Well with Nonzero Minimum for Plasma Confinement	*J. Appl. Phys.* **37**, 2182 (1966)
I. Alexeff and W. D. Jones	Electron-Emitting and Electron Collecting Probes as Ion Wave Detectors	*Phys. Letters* **20**, 269 (1966)
W. B. Ard, R. A. Dandl, and R. F. Stetson[1]	Research Note: "Use of Silicon Solar Cells as Detectors of Energetic Electrons from Plasmas"	*Rev. Sci. Instr.* **37**, 380 (1966)
P. R. Bell, R. L. Brown, and J. S. Culver	DCX-2 Beam Injection Duct	Pp. 146–51 in *Proc. Engineering Problems of Controlled Thermonuclear Research Symp., Livermore, Calif., May 1965,* CONF-650512
E. H. Christy, Jr.[2]	Plasma Impedance Measuring Technique	*Rev. Sci. Instr.* **36**, 1659 (1965)
J. S. Culver	The DCX-2 Scanning Energy Spectrometer	Pp. 123–27 in *Proc. Engineering Problems of Controlled Thermonuclear Research Symp., Livermore, Calif., May 1965,* CONF-650512
S. M. DeCamp	Operating and Repair Experiences on DCX-2 Coils	Pp. 173–76 in *Proc. Engineering Problems of Controlled Thermonuclear Research Symp., Livermore, Calif., May 1965,* CONF-650512

[1]Research Participant, 1965, Florida Atlantic University.
[2]ORINS Graduate Student.

J. L. Dunlap, G. R. Haste, H. Postma, L. H. Reber,[3] and C. E. Nielsen[4]	Microinstability Limitations of the DCX-1 Energetic Plasma	*Phys. Fluids* **9**, 199 (1966)
R. S. Edwards	The Production of "Excited State" H_2^+ for Lorentz Dissociation in DCX-1	Pp. 27–30 in *Proc. Engineering Problems of Controlled Thermonuclear Research Symp., Livermore, Calif., May 1965*, CONF-650512
T. K. Fowler[5] and M. Rankin	Fusion Energy Balance in Mirror Machines	*J. Nucl. Energy: Pt. C* **8**, 121 (1966)
C. C. Harris, Jack K. Goodrich[6] Rebecca Hill,[6] and H. L. Stone[7]	Clinical Applications of Low-Energy High Transmission Collimators	*J. Nucl. Med.* **6**, 409 (1965)
Manfred O. Krause	Determination of *L* Binding Energies of Krypton by the Photoelectron Method	*Phys. Rev.* **140**, A1845 (1965)
J. N. Luton, Jr.	Some Problems in the Design of an Eighth-Order, Power-Optimized Solenoid	Pp. 138–41 in *Proc. Engineering Problems of Controlled Thermonuclear Research Symp., Livermore, Calif., May 1965*, CONF-650512
O. D. Matlock	A New, Versatile Vacuum Quick-Seal and Vacuum Lock	Pp. 18–19 in *Proc. Engineering Problems of Controlled Thermonuclear Research Symp., Livermore, Calif., May 1965*, CONF-650512
J. R. McNally, Jr., M. R. Skidmore, P. M. Jenkins, and J. E. Francis, Jr.	On the Possibility of Excitation-Heating of Ions to High Temperature	*Appl. Opt.* **5**, 187 (1966)
H. Postma, J. L. Dunlap, R. A. Dory, G. R. Haste, and R. A. Young[8]	Observation of Negative Mass Instability in an Energetic Proton Plasma	*Phys. Rev. Letters* **16**, 265 (1966)
J. A. Ray and C. F. Barnett	An Unconventional Ultra-High Vacuum Facility	Pp. 7–9 in *Proc. Engineering Problems of Controlled Thermonuclear Research Symp., Livermore, Calif., May 1965*, CONF-650512

[3]Deceased.
[4]Consultant, Ohio State University.
[5]General Atomic, San Diego, Calif.
[6]University of Mississippi Medical Center.
[7]U.S. Air Force School of Aerospace Medicine, Brooks Air Force Base, Texas.
[8]Summer Participant, 1965, University of Chicago.

Y. Shima	Photon Splitting in a Nuclear Electric Field	*Phys. Rev.* **142**, 944 (1966)
Y. Shima and T. K. Fowler[5]	Flute Instabilities at Ion Gyrofrequency	*Phys. Fluids* **8**, 2245 (1965)
W. L. Stirling, R. V. Neidigh, I. Alexeff, and V. J. Meece	Development of a Hot-Electron Plasma Blanket	*J. Nucl. Energy: Pt. C* **8**, 157 (1966)
E. R. Wells	The Production of 10^{-9} Torr Within a Large Plasma Container (DCX-1)	Pp. 1–6 in *Proc. Engineering Problems of Controlled Thermonuclear Research Symp., Livermore, Calif., May 1965*, CONF-650512
W. L. Wright	Dissipation of Heat from Large-Scale CTR Apparatus at ORNL	Pp. 177–81 in *Proc. Engineering Problems of Controlled Thermonuclear Research Symp., Livermore, Calif., May 1965*, CONF-650512

ORNL Reports

Author(s)	Title	Number	Date
C. F. Barnett, D. A. Griffin, M. O. Krause, J. A. Ray, J. W. Hooper,[1] D. W. Martin,[1] and E. W. McDaniel[1]	Bibliography of Atomic and Molecular Processes for 1964	ORNL-AMPIC-3	February 1966
W. F. Gauster, D. L. Coffey, K. R. Efferson, H. W. Koppe, J. N. Luton, and J. E. Simpkins	Experimental Simulation of Large, High-Field Superconducting Magnet Operation	ORNL-TM-1398	January 1966
A. H. Snell *et al.*	Thermonuclear Division Semiannual Progress Report for Period Ending Oct. 31, 1965	ORNL-3908	March 1966

[1]Consultants, Georgia Institute of Technology.

PAPERS PRESENTED AT SCIENTIFIC AND TECHNICAL MEETINGS

American Physical Society, Division of Plasma Physics, San Francisco, California, November 8–11, 1965

I. Alexeff, "A Simple Thermal Instability in Discharge Tubes – A Possible Cause of Moving Striations."

C. F. Barnett and J. A. Ray, "Production of Energy-Dispersed Beams of Neutral Hydrogen Atoms."

R. A. Dandl, W. B. Ard, and R. F. Stetson,[1] "Observation of a Mirror-Like Instability in a Hot Electron Plasma."

R. A. Dory, "Negative-Mass Microinstability Theory for the DCX-1 Plasma."

J. L. Dunlap, G. R. Haste, H. Postma, and R. A. Young,[2] "Thresholds and Growth Rates for the DCX-1 Instability."

A. C. England, R. A. Dandl, H. O. Eason, H. C. Hoy, N. H. Lazar, and O. D. Matlock, "Neutral Atom Injection into an Electron-Cyclotron Plasma."

G. E. Guest and C. O. Beasley, Jr., "Cold Plasma Stabilization of Drift Waves in Hot-Electron Plasmas."

G. M. Haas, R. A. Dandl, W. B. Ard, M. C. Becker, H. O. Eason, and A. C. England, "Energetic Electron Distribution in 8-mm Electron Cyclotron Plasma."

E. G. Harris,[3] "Wave-Vector Space Instabilities."

G. G. Kelley, R. C. Davis, R. R. Hall, O. B. Morgan, and R. F. Stratton, "High-Intensity Ion Beams."

R. V. Neidigh, I. Alexeff, and W. F. Peed, "Neutron Source Strengths in Burnout V."

C. E. Nielsen,[4] "Negative-Mass Behavior in Extended Distributions of Ions."

H. Postma, J. L. Dunlap, and G. R. Haste, "The Use of Energy Spread to Suppress a Microinstability in the DCX-1 Plasma."

W. L. Stirling, R. V. Neidigh, I. Alexeff, and V. J. Meece, "A Hot-Electron Plasma Blanket."

O. C. Yonts and E. D. Shipley, "Electron Oscillations in the Calutron Ion Beam."

Symposium on Special Problems of the Physics and Application of Hard Superconductors, Bavarian Academy of Sciences, Munich, Germany, November 17, 1965

W. F. Gauster, "Research on Hard Superconductors and Development Work on Superconducting Magnets at the Oak Ridge National Laboratory."

11th Annual Conference on Magnetization and Magnetic Materials, San Francisco, California, November 16–19, 1965

W. F. Gauster and H. A. Ullmaier, "Field Distribution in a Hard Superconductor with Adiabatic Field Charge."

Tennessee Academy of Science, Oak Ridge, Tennessee, December 10–11, 1965

J. Rand McNally, Jr., "Excitation-Heating of Ions to High Temperature."

---

[1]Research Participant, Florida Atlantic University.

[2]Summer Participant, University of Chicago.

[3]Consultant, The University of Tennessee.

[4]Consultant, Ohio State University.

Symposium on Computers and Scanning, New Orleans, Louisiana, December 16–17, 1965

C. C. Harris, "Quantification of Scan Records."

American Physical Society, Washington, D.C., April 25–28, 1966

Manfred O. Krause, Thomas A. Carlson,[5] and Robert K. Dismukes,[6] "Energy Spectrum of Shake-Off Electrons from the *L* Shell of Neon Accompanying *K* Photoionization."

American Physical Society, New York, New York, January 26–29, 1966

J. A. Ray, C. F. Barnett, and J. B. Ayers,[7] "Response of Silicon Surface Barrier Detectors to Low Energy Ions."

Annual Sherwood Theory Meeting, San Diego, California, April 21–22, 1966

R. A. Dory and G. E. Guest, "Theoretical Interpretation of Some DCX-2 Observations. II."

G. E. Guest and C. O. Beasley, Jr., "Cold Plasma Effects in Finite Length Plasmas."

E. G. Harris,[3] "Theoretical Interpretation of Some DCX-2 Observations. I."

---

[5]Physics Division.
[6]AEC Health Physics Fellow.
[7]ORTEC.

TRAVELING LECTURE PROGRAM

The Traveling Lecture Program is conducted in cooperation with Oak Ridge Associated Universities, Inc., as a part of the AEC's program of disseminating scientific and technical information to universities, particularly those in the South. Lectures delivered by ORNL personnel present unclassified atomic energy information to university undergraduate and graduate students and members of the faculty. The principal objectives of the program are to stimulate interest in atomic energy and related research in the university departments and assist the teaching staff in expanding the scope of instruction offered under their regular curricula. Listed below are names of members of the Thermonuclear Division staff who participated in the Traveling Lecture Program during this report period.

P. R. Bell	"High-Energy Plasma Experiment, DCX-2," Georgia Institute of Technology, Atlanta, Mar. 2, 1966
P. R. Bell	"High-Energy Plasma Experiment, DCX-2," The University of Texas and the Laboratories for Electronics and Related Science Research, Austin, Nov. 19, 1965.
P. R. Bell	"High-Energy Plasma Experiment, DCX-2," Howard College, Birmingham, Ala., Dec. 16, 1965.
R. A. Dory	"Progress Toward Power from Thermonuclear Fusion," Jacksonville University, Jacksonville, Fla., Nov. 19, 1965.
W. F. Gauster	"Research in High Field Superconductors (A)," Texas A and M University, College Station, Feb. 17, 1966.
W. F. Gauster	"Research in High Field Superconductors," The University of Texas Laboratories for Electronics and Related Science Research, Austin, Feb. 18, 1966.

G. E. Guest	"Thermonuclear Fusion Research at Oak Ridge National Laboratory," University of Alabama, University, Jan. 6, 1966.
G. E. Guest	"Plasma Stability Theory and Controlled Fusion," Southern Illinois University, Carbondale, Jan. 28, 1966.
G. E. Guest	"Thermonuclear Fusion Research at Oak Ridge National Laboratory," University of Virginia, Charlottesville, Mar. 3, 1966.
G. E. Guest	"Thermonuclear Fusion Research at Oak Ridge National Laboratory," Roanoke College, Salem, Va., Mar. 4, 1966.
G. E. Guest	"Thermonuclear Fusion Research at Oak Ridge National Laboratory," Western Maryland College, Westminster, Mar. 7, 1966.
G. E. Guest	"Thermonuclear Fusion Research at Oak Ridge National Laboratory," North Texas State University, Denton, Apr. 13, 1966.
G. E. Guest	"Plasma Stability Theory and Controlled Fusion," Louisiana State University, Baton Rouge, Apr. 14, 1966.
G. E. Guest	"Plasma Stability Theory and Controlled Fusion," University of Mississippi, University, Apr. 15, 1966.
N. H. Lazar	"General Progress in the Controlled Thermonuclear Energy Program (G)," Muskingum College, New Concord, Ohio, Apr. 13, 1966.
J. R. McNally, Jr.	"Spectroscopic Studies of Ultra-High Temperature Plasmas," College of William and Mary, Williamsburg, Va., Oct. 15, 1965.
H. Postma	"Controlled Thermonuclear Research: Progress Toward and Problems In Producing Fusion Plasmas (A)," Pennsylvania State University, University Park, Nov. 18, 1965.
H. Postma	"Controlled Thermonuclear Research: Progress Toward and Problems In Producing Fusion Plasmas (A)," University of Florida, Gainesville, Feb. 22, 1966.
H. Postma	"Controlled Thermonuclear Research: Progress Toward and Problems In Producing Fusion Plasmas (A)," Tulane University, Baton Rouge, La., Feb. 21, 1966.
H. Postma	"Controlled Thermonuclear Research: Progress Toward and Problems In Producing Fusion Plasmas (A)," University of South Florida, Tampa, Feb. 23, 1966.

ORNL-3989
UC-20 – Controlled Thermonuclear Processes

INTERNAL DISTRIBUTION

1. I. Alexeff
2. W. B. Ard
3. C. F. Barnett
4. C. O. Beasley
5. M. C. Becker
6–11. P. R. Bell
12. D. S. Billington
13. C. W. Blue
14. C. J. Borkowski
15. G. E. Boyd
16. R. L. Brown
17. E. H. Christy, Jr.
18. D. L. Coffey
19. R. J. Colchin
20. F. L. Culler
21. J. S. Culver
22. R. A. Dandl
23. R. C. Davis
24. S. M. DeCamp
25. R. A. Dory
26. J. L. Dunlap
27. H. O. Eason, Jr.
28. R. S. Edwards
29. K. R. Efferson
30. A. C. England
31. J. C. Ezell
32. J. L. Fowler
33. J. E. Francis, Jr.
34. J. H. Frye, Jr.
35. W. F. Gauster
36. D. A. Griffin
37. W. R. Grimes
38. G. E. Guest
39. E. Guth
40. G. M. Haas
41. W. Halchin
42. C. C. Harris
43. G. R. Haste
44. J. B. Hendricks
45. K. C. Hines
46. J. L. Horton
47. H. C. Hoy
48. R. P. Jernigan, Jr.
49. W. D. Jones
50. G. G. Kelley
51. M. T. Kelley
52. M. O. Krause
53. C. E. Larson
54. R. A. Langly
55. N. H. Lazar
56. G. F. Leichsenring
57. W. J. Leonard
58. J. Lewin
59. R. S. Livingston
60. J. N. Luton, Jr.
61. J. F. Lyon
62. H. G. MacPherson
63. F. C. Maienschein
64. J. R. McNally, Jr.
65. O. D. Matlock
66. O. B. Morgan
67. R. V. Neidigh
68. J. Neufeld
69. C. E. Parker
70–71. R. B. Parker
72. W. F. Peed
73. H. Postma
74. J. F. Potts
75. F. M. Rankin
76. J. A. Ray
77. R. G. Reinhardt
78. D. M. Richardson
79. M. Roberts
80. D. A. Ross
81. P. W. Rueff
82. W. K. Russell
83. H. E. Seagren
84. D. J. Sigmar
85. Y. Shima
86. E. D. Shipley
87. J. E. Simpkins
88. M. R. Skidmore
89. M. J. Skinner
90–110. A. H. Snell
111. W. L. Stirling
112. R. F. Stratton, Jr.
113. R. A. Strehlow
114. E. H. Taylor
115. H. A. Ullmaier
116. H. L. Watts
117. A. M. Weinberg
118. E. R. Wells

119. G. C. Williams
120. W. L. Wright
121. O. C. Yonts
122. Gale Young
123. Owen Eldridge (consultant)
124. J. W. Flowers (consultant)
125. D. C. Freeman, Jr. (consultant)
126. M. W. Garrett (consultant)
127. H. Grad (consultant)
128. E. G. Harris (consultant)
129. D. E. Harrison (consultant)
130. R. Hefferlin (consultant)
131. G. W. Hoffman (consultant)
132. J. W. Hooper (consultant)
133. V. W. Hughes (consultant)
134. D. W. Martin (consultant)
135. E. W. McDaniel (consultant)
136–137. D. R. Montgomery (consultant)
138. S. H. Neff (consultant)
139. C. E. Nielsen (consultant)
140. J. M. Reynolds (consultant)
141. H. S. Robertson (consultant)
142. H. E. Rorschach (consultant)
143. D. J. Rose (consultant)
144. L. P. Smith (consultant)
145. P. M. Stier (consultant)
146. T. H. Stix (consultant)
147. E. W. Thomas (consultant)
148. J. H. Wise (consultant)
149–169. Thermonuclear Division Library
170. Reactor Division Library
171. Biology Division Library
172–174. Central Research Library
175. Laboratory Shift Supervisor
176–251. Laboratory Records Department
252. Laboratory Records, ORNL R.C.
253–254. ORNL – Y-12 Technical Library Document Reference Section

EXTERNAL DISTRIBUTION

255. A. Bers, Mass. Institute of Technology
256. L. M. Branscomb, Joint Institute, Laboratory of Astrophysics, Boulder, Colorado
257. S. C. Brown, Massachusetts Institute of Technology
258. S. J. Buchsbaum, Bell Telephone Laboratories, Murray Hill, New Jersey
259. O. Buneman, Stanford Electronics Laboratories
260. Director, Technical Library, Defense Atomic Support Agency, Sandia Base, Albuquerque, New Mexico
261. F. W. Crawford, Stanford Electronics Laboratories
262. M. B. Gottlieb, Princeton University
263. W. W. Grigorieff, Assistant to the Executive Director, Oak Ridge Associated Universities
264. D. W. Kerst, University of Wisconsin
265. A. C. Kolb, Naval Research Laboratory
266. Morton A. Levine, Air Force Cambridge Research Laboratories
267. J. A. Phillips, Los Alamos Scientific Laboratory
268. R. F. Post, University of California, Lawrence Radiation Laboratory
269. John R. Roth, NASA Lewis Research Center (Mail Stop 301-1), 21000 Brookpark Road, Cleveland, Ohio 44135
270. A. E. Ruark, Division of Research, AEC, Washington
271. Russell Shelton, Chief, Nuclear and Plasma Physics Branch, Marshall Space Flight Center, Huntsville, Alabama 35812
272. L. D. Smullin, Massachusetts Institute of Technology
273. L. Spitzer, Princeton University
274. J. A. Swartout, 270 Park Avenue, New York 17, New York
275. R. F. Taschek, Los Alamos Scientific Laboratory
276. A. W. Trivelpiece, University of California, Berkeley, California
277. C. M. Van Atta, University of California, Lawrence Radiation Laboratory

278–279. Research and Development Division, AEC, ORO (1 copy each to H. M. Roth and R. B. Martin)
280–284. Controlled Thermonuclear Research Branch, AEC, Washington (A. S. Bishop)
285–295. USAEC, Division of Research, Controlled Thermonuclear Research Program Program (Stephen O. Dean)
296–607. Given distribution as shown in TID-4500 under Controlled Thermonuclear Processes category (75 copies – CFSTI)